



HAL
open science

Study of nuclear fission by spectrometry of the prompt gamma rays

Michal Rąpala

► **To cite this version:**

Michal Rąpala. Study of nuclear fission by spectrometry of the prompt gamma rays. Nuclear Experiment [nucl-ex]. Université Paris Saclay (COMUE), 2018. English. NNT : 2018SACLS390 . tel-01988955

HAL Id: tel-01988955

<https://theses.hal.science/tel-01988955>

Submitted on 22 Jan 2019

HAL is a multi-disciplinary open access archive for the deposit and dissemination of scientific research documents, whether they are published or not. The documents may come from teaching and research institutions in France or abroad, or from public or private research centers.

L'archive ouverte pluridisciplinaire **HAL**, est destinée au dépôt et à la diffusion de documents scientifiques de niveau recherche, publiés ou non, émanant des établissements d'enseignement et de recherche français ou étrangers, des laboratoires publics ou privés.

NNT: 2018SACLS390

Etude de la fission nucléaire par spectrométrie des rayons gamma prompts

Study of nuclear fission by spectrometry of the prompt gamma rays

Thèse de doctorat de l'Université Paris-Saclay
préparée à l'Université Paris-Sud

École doctorale n° 576 : particules hadrons énergie
et noyau : instrumentation, image, cosmos et
simulation (Pheniics)
Spécialité de doctorat : Structure et réactions nucléaires

Thèse présentée et soutenue à Saclay, le 15 octobre 2018, par

M. Michał Rapała

Composition du Jury :

M. Jonathan Wilson	Directeur de Recherche (IPN)	Président du jury
M ^{me} Louise Stuttgé	Directrice de Recherche (IPHC)	Rapporteuse
M. Igor Tsekhanovich	Professeur (CENBG)	Rapporteur
M. Mourad Ramdhane	Professeur (LPSC)	Examineur
M. Alain Letourneau	Ingénieur de Recherche (CEA)	Directeur de thèse
M. Thomas Materna	Ingénieur de Recherche (CEA)	Co-Directeur de thèse
M. Olivier Serot	Ingénieur de Recherche (CEA)	Co-Directeur de thèse

Contents

1	Introduction	1
1.1	History of a discovery	1
1.2	Fission process	3
1.2.1	Liquid Drop Model	3
1.2.2	Scission	4
1.2.3	Fission fragments mass distribution	5
1.2.4	Fission fragments de-excitation	8
1.3	Nuclear reactors	10
1.4	γ -heating process	12
1.5	Fission fragment de-excitation process simulation	14
1.6	Outline	15
2	FIFRELIN Monte-Carlo simulation code	17
2.1	Introduction	17
2.2	Characteristics of primary fission fragments	18
2.2.1	Mass, charge and kinetic energy	18
2.2.2	Spin and parity	20
2.2.3	Excitation energy	21
2.3	De-excitation process	26
2.3.1	Nuclear realization	26
2.3.2	Competition between neutron and γ -ray emission	27
2.4	Spin cutoff models	30
2.4.1	CONSTANT model	30
2.4.2	BSFG model	31
2.5	Level density	33
2.5.1	Constant temperature model	34

2.5.2	Fermi gas model	35
2.5.3	Composite Gilbert-Cameron model	36
2.5.4	Hartree-Fock-Bogoliubov	37
2.6	Photon strength functions	37
2.6.1	Introduction	37
2.6.2	Standard Lorentzian model	39
2.6.3	Enhanced Generalized Lorentzian model	40
2.7	Neutron transmission coefficients	42
2.8	Simulation with the FIFRELIN code	42
2.8.1	Elements selection	42
2.8.2	Models and free parameters selection	43
2.8.3	Results comparison	44
3	EXILL experiment	47
3.1	Introduction	47
3.2	EXILL campaign description	47
3.2.1	General information	47
3.2.2	Experiment setup	51
3.2.3	Data preprocessing	56
3.2.4	Detection system efficiency calibration	57
3.3	Triple- γ coincidence method	61
3.3.1	Introduction	61
3.3.2	Triple- γ coincidence requirements	62
3.3.3	γ - γ - γ cube	62
3.3.4	γ - γ - γ cube analysis	63
3.3.5	Limitations of the analysis method	69
4	New EXILL analysis technique	73
4.1	Introduction	73
4.2	Concepts of the new analysis method	74
4.3	Illustration on EXILL data	77
4.4	Semi-automatic spectra fitting process	79
4.4.1	Fitting procedure	79
4.4.2	Detection system response	83
4.5	Intensity calculation	86

4.5.1	Gate slices fitting	87
4.5.2	No contamination	87
4.5.3	Contamination in the horizontal slice	92
4.5.4	Contamination in both slices	94
4.5.5	Contamination anywhere in the plane	95
4.5.6	Other cases	96
4.6	Performance of the new analysis method	98
4.6.1	Motivations of the ^{142}Ba selection	98
4.6.2	Experimental data extraction	99
4.6.3	Analysis results	99
5	Studies on ^{100}Zr	111
5.1	Introduction	111
5.2	EXILL results and comparison with existing data	114
5.2.1	EXILL results	114
5.2.2	Comparison with existing data on $^{235}\text{U}(n_{th}, f)$	116
5.2.3	Comparison with existing data on spontaneous fission	117
5.2.4	Discussion based on FIFRELIN simulations	120
5.3	Evolution with the mass of the fission partner	123
5.3.1	EXILL results	124
5.3.2	Long-lived isomers in Te	127
5.3.3	The CONSTANT spin cut-off model	131
5.3.4	The BSFG spin cut-off model	133
5.4	Spin-distribution dependence	135
5.4.1	Selection of the best models in FIFRELIN	135
5.4.2	Influence of the spin-distribution	141
5.4.3	Comparison of the two models	147
5.5	Dependence with the temperature	149
5.6	Summary of the ^{100}Zr analysis	155
	General conclusions and perspectives	159
	Conclusions	159
	Perspectives	161
	Bibliography	170

Résumé	171
R.1 Introduction	171
R.1.1 Processus de fission	171
R.1.2 L'échauffement γ	172
R.1.3 Simulation du processus de désexcitation de fragments de fission	173
R.1.4 Plan du document	173
R.2 Le code de simulation Monte-Carlo FIFRELIN	174
R.2.1 Introduction	174
R.2.2 Caractéristiques des fragments de fission primaires	175
R.2.3 Le processus de désexcitation	176
R.2.4 Les différents modèles implémentés dans FIFRELIN	176
R.2.5 Multiplicité des neutrons prompts	177
R.3 L'expérience EXILL	178
R.3.1 Introduction	178
R.3.2 Description de la campagne EXILL	178
R.3.3 Méthode de coïncidence γ - γ - γ	179
R.4 Nouvelle technique d'analyse	181
R.4.1 Introduction	181
R.4.2 Concepts de la nouvelle méthode d'analyse	181
R.4.3 Analyse de ^{142}Ba	183
R.5 Études sur ^{100}Zr	185
R.5.1 Introduction	185
R.5.2 Résultats et interprétation	186
Appendix A	189
A.1 Experimental results - EXILL data analysis	189
A.1.1 ^{134}Te	190
A.1.2 ^{92}Kr	192
A.1.3 ^{142}Ba	194
A.1.4 ^{94}Sr	196
A.1.5 ^{140}Xe	198
A.1.6 ^{138}Xe	200
A.1.7 ^{104}Mo	202
A.1.8 ^{130}Sn	204

A.1.9	^{144}Ba	206
A.1.10	γ -ray intensity dependence with different fission bands of the fission partner	208
Appendix B		211
B.1	Uncertainty calculation	211
B.1.1	Uncertainty on an intensity from gate slices fitting	211
B.1.2	Uncertainty on a background from gate slices fitting	213
B.1.3	Uncertainty on a number of events coming from the desired γ -transition in the restricted 2D region of the central gate	213
B.1.4	Uncertainty on the absolute efficiency	214

List of Figures

1.1	Scheme of the neutron induced fission of ^{236}U [Gön14a].	3
1.2	(a) Potential energy surface of a deforming nucleus. (b) The potential energy along the most energetically favorable fission path. The red "x" marks the saddle point [BL80].	4
1.3	Potential energy as a function of deformation. Q is the nucleus potential energy at the ground state, S_n is the neutron separation energy, E_B is the fission barrier and ΔV is the potential energy difference between saddle and scission point [Gön14a].	5
1.4	Pre-neutron emission experimental fission fragment mass yield distribution following $^{235}\text{U}(n_{th}, f)$ [Oku+18].	6
1.5	Multimodal and total fission mass distribution following $^{235}\text{U}(n_{th}, f)$ at neutron energy $E_n=0.5$ MeV [Ham+03].	7
1.6	Multimodal fission mass distribution following $^{235}\text{U}(n_{th}, f)$ at neutron energy $E_n=0.5$ MeV [Möl+09].	8
1.7	Fission fragments de-excitation scheme with emission of the prompt and delayed particles [Lem15].	9
1.8	The design of the HTMR-100 generation IV reactor with a complex reflectors system [Boy15].	12
1.9	Sources of heating in the nuclear reactor as a function of the distance from the center of the core [Col+13].	13
1.10	Stages in a process of improvement of the generation IV nuclear reactors simulation.	14
2.1	An example of FIFRELIN input data. The pre-neutron emission distributions of: fission fragment mass yields (top), average kinetic energy (middle) and its standard deviation (bottom) [Lit+17].	19

2.2	The de-excitation scheme in $[E^*, J]$ representation [LS10; Lit+17]. . . .	23
2.3	Neutron emission probability as a function of energy E and angular momentum J of ^{144}Ba [Reg13].	23
2.4	Temperature ratio law $R_T(A)$. The deformation of the fission fragments is briefly presented by the pictographs above the boundary points [Lit+17].	25
2.5	Neutron/ γ -ray cascade simulated in FIFRELIN with the coupled approach. (a) shows three regions of the excitation energy with limits. (b) presents two different de-excitation paths: realized only by γ -rays (red) and with additional neutron emission (green) [Lit+17].	29
2.6	Spin distributions dependence on the spin cutoff value [Lit+17].	31
2.7	Average spin \bar{J} as a function of the fission fragment mass A using the BSFG or the CONSTANT spin cutoff models.	32
2.8	Cumulative number of levels for the ^{239}U compound nucleus. CTM is used to reproduce the known part of the nuclear level scheme (experimental level scheme). The final level scheme sampled by FIFRELIN combines the experimental level scheme at low energy with the theoretical level scheme coming from models at high energy. In the presented figure, the CTM spin cutoff model was used in the whole energy range for the FIFRELIN simulation [Lit+17].	35
2.9	Photon strength functions of ^{93}Rb calculated with different models: EGLO, QRPA with Hartree-Fock+Bardeen-Cooper-Schrieffer (HF+BCS+QRPA) and QRPA with Hartree-Fock-Bogoliubov (HFB+QRPA). The upper plot is a linear-linear representation. The lower plot is a log-log representation more adapted to see the differences between the models in the energy range involved in fission [Lit+17].	41
3.1	Fission fragments mass distribution coming from the neutron induced fission of ^{235}U and ^{241}Pu and the spontaneous fission of ^{248}Cm and ^{252}Cf . Data taken from [KBM09], graph taken from [Jen+17].	49
3.2	The detector configuration I used during the first reactor cycle of the EXILL campaign [Jen+17].	52
3.3	The target collimation system layout. It is followed by the target chamber surrounded by the detector array and the beam dump [Jen+17]. . .	53
3.4	The target chamber in a single wall configuration [Jen+17].	54

3.5	The detection system absolute efficiency curve fitted with the simple efficiency Equation 3.6 [Ra15]. The uncertainties on the experimental efficiency points are smaller than the marker size.	59
3.6	The detection system absolute efficiency curve fitted with the modified efficiency Equation 3.7. The absolute efficiency experiment data was corrected for the true coincidence effect.	60
3.7	Schematic presentation of the fission fragments de-excitation process. Fission fragment emits prompt γ -rays in the form of a cascade. The energies of these γ -rays are unique for each nucleus.	61
3.8	Prompt γ -ray spectrum without coincidence of $^{235}\text{U}(n_{th}, f)$ measured during the EXILL experiment after Compton rejection.	65
3.9	Schematic view of gates placement when "double gates" are used. Two gates are placed in the fission fragment A. In the coincidence spectrum one will see the complete de-excitation cascade of its fission partner B. Also cascades of other fission partners will be visible.	66
3.10	Schematic view of gates placement when "mixed gates" are used. The first gate is placed in the fission fragment A, the second one in its fission partner B. In the coincidence spectrum one will not see the complete de-excitation cascade of the fission partner B. Nevertheless, the spectrum will be much cleaner because no cascade of other fission partners will be present.	66
3.11	Level scheme of ^{92}Kr [RU+00]. The 769.0 keV γ -ray was selected as the first gate in the presented example.	67
3.12	Level scheme of ^{142}Ba [Urb+97]. The 359.5 keV γ -ray was selected as the second gate in the presented example.	67
3.13	Prompt γ -ray spectrum of $^{235}\text{U}(n_{th}, f)$ in coincidence with the 769.0 keV γ -transition from ^{92}Kr , with the background subtraction.	68
3.14	Prompt γ -ray spectrum of $^{235}\text{U}(n_{th}, f)$ in coincidence with the 769.0 keV and 359.5 keV γ -transitions from ^{92}Kr and ^{142}Ba , respectively, with the double subtraction of the background. The γ -rays with the highest intensities emitted by ^{92}Kr and ^{142}Ba can be easily identified.	69
3.15	First gate and background selection with standard γ - γ - γ coincidence method. The peak at 401.6 keV comes from the ^{90}Kr	70

-
- 3.16 Second gate and background selection with the standard γ - γ - γ coincidence method. The peak at 199.2 keV comes from the ^{144}Ba 70
- 3.17 Prompt γ -ray spectrum of $^{235}\text{U}(n_{th}, f)$ in coincidence with the 401.6 keV and 199.2 keV γ -transitions from ^{90}Kr and ^{144}Ba , respectively, with the double subtraction of the background. 71
- 4.1 Schematic representation of the standard way of analyzing the data. To obtain the intensity of a transition in coincidence with the transitions T_A and T_B , with energy E_A and E_B , one builds the spectrum of γ -rays in coincidence with a small region around (E_A, E_B) , then subtracts γ -rays in coincidence with the regions around (E'_A, E_B) and around (E_A, E'_B) and adds γ -rays in coincidence with a region around (E'_A, E'_B) 75
- 4.2 Schematic representation of the new way of 2D gate scanning around (E_A, E_B) . Each square corresponds to a 2D gate with (Δ_A, Δ_B) size. 77
- 4.3 2D scan of the gates in the Polish cube. Each dot denotes one pair of gates. The point at the intersection between the horizontal, the vertical and the diagonal slices (red dot) denotes the exact energies of the initially selected gates. Each number of counts comes from fitting the same γ -ray peak in the particular triple- γ coincidence spectrum. The measured γ -ray is at 475.0 keV in ^{142}Ba . The initial gates are the transition at 769.0 keV in ^{92}Kr and the transition at 359.5 keV in ^{142}Ba 78
- 4.4 2D scan of the gates in the GANIL cube. Each dot denotes one pair of gates. The point at the intersection between the horizontal, the vertical and the diagonal slices (red dot) denotes the exact energies of the initially selected gates. Each number of counts comes from fitting the same γ -ray peak in the particular triple- γ coincidence spectrum. The measured γ -ray is at 352.0 keV in ^{100}Zr . The initial gates were the transition at 212.6 keV in ^{100}Zr and the transition at 1279.3 keV in ^{134}Te 79
- 4.5 All the gated spectra generated with the scan of gates, zoomed on the γ -ray peak at 475.0 keV in ^{142}Ba . The central gate (E_A, E_B) is set around the 769.0 keV transition in ^{92}Kr and the 359.5 keV transition in ^{142}Ba 80

4.6	All the gated spectra generated with the scan of gates, zoomed on the γ -ray peak at 475.0 keV in ^{142}Ba . The central gate (E_A, E_B) is set around the 769.0 keV transition in ^{92}Kr and the 359.5 keV transition in ^{142}Ba . All γ -ray peaks were found and fitted. Blue triangles indicate the peak positions.	81
4.7	Peak positions in all triple- γ coincidence spectra generated with the 2D scan of gates. The initial gates were the γ -ray at 769.0 keV in ^{92}Kr and the γ -ray at 359.5 keV in ^{142}Ba . All γ -ray peaks were found and fitted in the region around the desired γ -ray at 475.0 keV in ^{142}Ba . Red lines are the (weighted) averaged energy of peaks. Gate pair 0 is the pair of central gates, gate pairs 1-14 are horizontal gates, gate pairs 15-28 are vertical gates, 29-42 are diagonal gates, starting from the lowest energy.	82
4.8	All triple- γ coincidence spectra generated with the 2D scan of gates. The initial gates were the γ -ray at 769.0 keV in ^{92}Kr and the γ -ray at 359.5 keV in ^{142}Ba . All γ -ray peaks were found and fitted in the region around the desired γ -ray at 475.0 keV in ^{142}Ba . The position of each peak is synchronized in all spectra based on their (weighted) averaged energy from the initial fit. Blue triangles indicate the synchronized peak positions. Green triangles indicate the peak positions from the first fit of the peaks (Figure 4.6).	83
4.9	Partial level scheme of ^{92}Zr with some of the transitions populated in the $^{91}\text{Zr}(n, \gamma)$ reaction.	84
4.10	Fit function shape used to fit the γ -transition peaks (black curve). It is composed of three Gaussian functions (red, green, blue curves) and, of a smooth step function that models the Compton tail (not represented). The black curve is the final response function.	85
4.11	Peak of ^{92}Zr at 1405.1 keV used to adjust the new fit function. The red curve is the fit function. The green curve is the fit function integrated over the bins. Experimental data are in dark blue, almost invisible due to relatively good fit.	86

4.12	Histogram visualizing the horizontal (a), vertical (b) and diagonal (c) slice in the Polish cube. Dark blue lines denote the data (partially covered by the green lines), red lines denote the fit function and green lines denote the fit function integrated over the single gate size. The fit was performed on the γ -ray transition at 475.0 keV in ^{142}Ba . The initial gates are the transition at 769.0 keV in ^{92}Kr and the transition at 359.5 keV in ^{142}Ba . The same peak areas in the form of a cross can be seen in Figure 4.3. This fit was used in the ^{142}Ba analysis in Section 4.6.	88
4.13	Schematic representation in the case of no contamination.	89
4.14	Coincidence matrix built from the fitted peak area at 475.0 keV. Details are explained in the text.	90
4.15	Schematic representation in the case of a contaminating peak in the horizontal slice.	92
4.16	Schematic representation in the case of contaminating peaks in the horizontal and the vertical slice.	94
4.17	Schematic representation in the case of a contaminating peak anywhere in the (E_1, E_2) plane.	95
4.18	Schematic representation in the case of a contaminating peak in the vertical slice and another one anywhere in the (E_1, E_2) plane.	97
4.19	Schematic representation in the case of three contaminating peaks: in the vertical slice, in the horizontal slice and the third one anywhere in the (E_1, E_2) plane.	97
4.20	The selection process of the first gate and the background with the standard technique. The gate is put at the γ -transition at 769.0 keV from ^{92}Kr . The horizontal axis is not placed at the zero counts.	102
4.21	The selection process of the second gate and the background with the standard technique. The gate is put at the γ -transition at 359.5 keV from ^{142}Ba . The horizontal axis is not placed at the zero counts.	103
4.22	The spectrum without coincidence. The first gate is put at the γ -transition at 359.5 keV from ^{142}Ba . The horizontal axis is not placed at the zero counts.	104

4.23	The spectrum in simple coincidence with the γ -transition at 359.5 keV (^{142}Ba) obtained with the standard technique. The second gate is put at the γ -transition at 769.0 keV from ^{92}Kr . The horizontal axis is not placed at the zero counts.	104
4.24	The triple- γ coincidence spectrum zoomed at the desired γ -ray at 706.8 keV (^{142}Ba). The selected gates are the γ -transitions at 769.0 keV (^{92}Kr) and at 359.5 keV (^{142}Ba). The horizontal axis is not placed at the zero counts.	105
4.25	The representation of the region of interest for the γ -transition at 706.8 keV (^{142}Ba). The main gates are the γ -transitions at 769.0 keV (^{92}Kr) and at 359.5 keV (^{142}Ba).	106
4.26	The fits of the region of interest for the γ -transition at 706.8 keV (^{142}Ba) for all spectra in triple coincidence. The main gates are the γ -transitions at 769.0 keV (^{92}Kr) and at 359.5 keV (^{142}Ba).	106
4.27	The fit of the horizontal (a), vertical (b), and diagonal (c) gate slices for the γ -transition at 706.8 keV (^{142}Ba). The main gates are the γ -transitions at 769.0 keV (^{92}Kr) and at 359.5 keV (^{142}Ba).	107
4.28	^{91}Kr level scheme taken from [RU+17a].	108
5.1	Level scheme of ^{100}Zr built with the data coming from the spontaneous fission of ^{252}Cf [Hwa+06].	113
5.2	Level scheme of ^{100}Zr built with the data coming from the EXILL experiment. Transition energies (in keV) and transition intensities (normalized to the 212.5 keV transition) are indicated on each arrow.	115
5.3	Ratio of γ -transition intensities in ^{100}Zr between the EXILL and the ^{252}Cf data [Hwa+06]. Fitted value is equal to 0.597(23).	119
5.4	Partial level scheme of ^{100}Zr built with the data coming from the FIFRELIN simulation using EGLO photon strength functions, CGCM level density model and CONSTANT spin cut-off model. Transition energies (in keV) and transition intensities (normalized to 100 on the 212.5 keV transition) are indicated on each arrow. Only the transitions with an intensity higher than 3.5% are shown.	121
5.5	The level scheme of ^{132}Te from [Hop+72].	124

5.6	The level scheme of ^{133}Te from [Bha+01]. Level energies are expressed relative to zero for the $11/2^-$ isomeric state which is at 334.26 keV.	124
5.7	Level scheme of ^{134}Te from [Sah+01].	125
5.8	Evolution of γ -transition intensities in ^{100}Zr with Te mass number obtained from the EXILL experiment data. The dashed lines show the fits with a first degree polynomials function.	126
5.9	Schematic view of gates placement when "mixed gates" are used and a nanosecond isomer is present. The first gate is placed in the fission fragment A below the long-lived isomer, the second one in its fission partner B. One can obtain correct intensities of the prompt γ -rays in both fission fragments A and B (marked in green).	128
5.10	Schematic view of gates placement when "double gates" are used and a nanosecond isomer is present. Two gates are placed in the fission fragment A, both below the nanosecond isomer. One can obtain correct intensities of the prompt γ -rays in the fragments B (marked in green).	128
5.11	Schematic view of gates placement when "double gates" are used and a nanosecond isomer is present. Two gates are placed in the fission fragment B. One cannot obtain correct intensities of the prompt γ -rays in fragments A (marked in red) because the intensities of the γ -transitions below the long-lived state is reduced due to used acceptance time window.	130
5.12	Schematic view of gates placement when "mixed gates" are used and a nanosecond isomer is present. The first gate is placed in the fission fragment A above the long-lived isomer, the second one in its fission partner B. One cannot obtain correct intensities of the prompt γ -rays in fragments A (marked in red) because the intensities of the γ -transitions below the long-lived state is reduced.	130
5.13	Evolution of simulated γ -transition intensities in ^{100}Zr with Te mass number when the CONSTANT spin cut-off model is used.	132
5.14	The process of neutron evaporation superposed on the ^{100}Zr level density $\rho(E, J)$. The gray line marks the mean value of the level density as a function of the excitation energy taken from RIPL-3.	133
5.15	Evolution of the simulated γ -transition intensities in ^{100}Zr with Te mass number when the BSFG spin cut-off model is used.	134

5.16	Light fragment neutron energy in the ^{100}Zr cascade when the CTM model is used.	139
5.17	Light fragment neutron energy in the ^{100}Zr cascade when the CGCM model is used.	139
5.18	Initial distribution of excitation energy (XE) and spin (J) for light fission fragments when the CONSTANT spin cut-off model is used and $\bar{\sigma}_L = \bar{\sigma}_H = 9.5$	142
5.19	Evolution of simulated γ -transition intensities in ^{100}Zr depending on the spin cut-off value. The CONSTANT spin cut-off model was used. Dashed lines show intensity values from the EXILL experimental data, dotted lines errors on them.	143
5.20	χ^2 values containing main band γ -ray transitions in ^{100}Zr for FIFRELIN simulations with different spin cut-off values. In each simulation $\bar{\sigma}_L$ was equal to $\bar{\sigma}_H$	144
5.21	χ^2 value containing main band γ -transitions in ^{100}Zr for FIFRELIN simulations with different scaling factor values (f_σ).	145
5.22	Initial distribution of excitation energy (XE) and spin (J) for light fission fragments when the BSFG spin cut-off model is used, $f_\sigma = 1.8$ and $R_{\text{T}}^{\text{max}} = 1.23$	146
5.23	Initial distribution of excitation energy (XE) and spin (J) for light fission fragments when the BSFG spin cut-off model is used, $f_\sigma = 1.15$ and $R_{\text{T}}^{\text{max}} = 1.23$	146
5.24	Evolution of simulated γ -ray transition intensities in ^{100}Zr depending on the spin cut-off value. The BSFG spin cut-off model was used. Dashed lines show intensity values from the EXILL experimental data, dotted lines errors on them.	147
5.25	$\bar{\nu}_L$ and $\bar{\nu}_H$ obtained with FIFRELIN simulations as a function of $R_{\text{T}}^{\text{max}}$ and for different $R_{\text{T}}^{\text{min}}$. Full lines show $\bar{\nu}_L$. Dashed lines show $\bar{\nu}_H$. Red lines show the experimental values. Only 3 different $R_{\text{T}}^{\text{min}}$ values are presented: minimum (0.5), maximum (0.95) and one from the analysis of the BSFG spin cut-off model (0.75).	150
5.26	Prompt-neutron multiplicity sawtooth as a function of a fission fragment mass number, coming from the published experimental data [Bat+05; MRC67; Nis+98; Vor+10].	151

5.27	$\bar{\nu}(100)$ obtained with FIFRELIN simulations as a function of R_T^{\max} and for different R_T^{\min} . Only 3 different R_T^{\min} values are presented: minimum (0.5), maximum (0.95) and one which was used in the previous analysis of the BSFG spin cut-off model (0.75). Dashed, red lines mark minimal and maximal $\bar{\nu}(100)$ coming from the published experimental data (Figure 5.26).	152
5.28	Temperature curve showing the relation between R_T^{\min} and R_T^{\max} . Dashed, red line marks a position of ^{100}Zr	152
5.29	χ^2 value containing main band γ -transitions in ^{100}Zr for FIFRELIN simulations with different scaling factor values (f_σ) for $R_T^{\max} = 1.0$	153
5.30	Initial distribution of excitation energy (XE) and spin (J) for light fission fragments when the BSFG spin cut-off model is used, $f_\sigma = 1.2$ and $R_T^{\max} = 1.0$	155
R.1	Représentation schématique de la méthode standard d'analyse des données. Pour obtenir l'intensité d'une transition en coïncidence avec les transitions T_A et T_B , avec l'énergie E_A et E_B , on construit le spectre des rayons γ en coïncidence avec une petite région autour de (E_A, E_B) , puis on soustrait les rayons γ en coïncidence avec les régions autour de (E'_A, E_B) et autour de (E_A, E'_B) et ajoute les rayons γ en coïncidence avec une région autour (E'_A, E'_B)	183
R.2	Représentation schématique de la nouvelle façon de scanner les portes 2D autour de (E_A, E_B) . Chaque carré correspond à une porte 2D avec la taille (Δ_A, Δ_B)	184
A.1	Level scheme of ^{134}Te from [Sah+01].	190
A.2	χ^2 value containing γ -transitions: 115.7 keV, 297.1 keV, 706.3 keV, 978.5 keV, 2322.0 keV in ^{134}Te , for the FIFRELIN simulations with different scaling factor values (f_σ). The χ^2 was calculated according to Equation 5.1. Models and free parameters set used in the simulations: EGLO photon strength functions, CTM level density model, BSFG spin cut-off model, $R_T^{\min} = 0.75$, $R_T^{\max} = 1.23$	190
A.3	Evolution of γ -transition intensities in ^{92}Kr with Ba mass number obtained from the EXILL experiment data. Lines show the fits with the constant function.	193

A.4	χ^2 value containing γ -transitions: 359.7 keV, 475.3 keV, 631.5 keV, 693.4 keV in ^{142}Ba , for the FIFRELIN simulations with different scaling factor values (f_σ). The χ^2 was calculated according to Equation 5.1. Models and free parameters set used in the simulations: EGLO photon strength functions, CTM level density model, BSFG spin cut-off model, $R_T^{\min} = 0.75$, $R_T^{\max} = 1.23$	194
A.5	Evolution of γ -transition intensities in ^{142}Ba with Kr mass number obtained from the EXILL experiment data. Lines show the fits with the constant function.	194
A.6	Level scheme of ^{94}Sr from [RU+09].	196
A.7	Evolution of γ -transition intensities in ^{94}Sr with Xe mass number obtained from the EXILL experiment data. Lines show the fits with the constant function.	197
A.8	Level scheme of ^{140}Xe from [Ham+97].	198
A.9	Evolution of γ -transition intensities in ^{140}Xe with Sr mass number obtained from the EXILL experiment data. Lines show the fits with the constant function.	198
A.10	Level scheme of ^{138}Xe from [Kor+00].	200
A.11	Level scheme of ^{104}Mo from [Jon+05]. Different fission bands are denoted by the numbers in brackets at the top of each band.	202
A.12	Level scheme of ^{90}Kr from [RU+17b].	206
A.13	Level scheme of ^{144}Ba from [Urb+97].	206
A.14	Level scheme of ^{87}Kr from [dAn07].	208
A.15	Level scheme of ^{146}Ba from [Urb+97].	208

List of Tables

2.1	Simulated numbers of γ -rays emitted by ^{100}Zr at the selected energies. Each simulation used a different random seed value thus different set of the nuclear realizations. Transition energies were taken from RIPL-3 database.	27
2.2	Models and free parameters used to simulate $^{235}\text{U}(n_{th}, f)$	44
2.3	Dependence of the prompt-neutron multiplicity values on the number of simulated events. In both simulations, models and free parameters are the same, see Table 2.2. The discrepancy between the simulated and experimental multiplicities are less than 1% for both simulations. . . .	44
3.1	Experiments performed during the EXILL campaign. The experiments marked in bold were analyzed in this work [Jen+17].	48
4.1	Relative intensities (I_γ) of the γ -ray transitions (keV) in ^{142}Ba , normalized to the $4_1^+ \rightarrow 2_1^+$ transition (475.0 keV). ^{248}Cm data comes from [Urb+97]. EXILL data analyzed with the standard technique (EXILL data old) comes from [Ra15]. The fission partner of ^{142}Ba for the EXILL data analyzed both with the standard and the new technique (EXILL data new) was ^{92}Kr , for [Urb+97] it was a complementary Zr fragment. To the intensities measured with the standard technique from the EXILL data additional 10% uncertainty has to be added due to the uncertainty of the background selection.	101
5.1	The most produced elements in the $^{235}\text{U}(n_{th}, f)$ reaction and their charge yields according to JEFF-3.3.	112

5.2	Relative intensities (I_γ) of the γ -ray transitions measured in ^{100}Zr obtained in this work at EXILL compared to the ones obtained at CIRUS [Muk+12]. Intensities are normalized on the 352.0 keV transition to 100. In both experiments the $^{235}\text{U}(n_{th}, f)$ was analyzed.	116
5.3	Relative intensities (I_γ) of the γ -ray transitions (keV) in ^{100}Zr , normalized to the strongest transition (212.5 keV). ^{252}Cf data coming from [Hwa+06], ^{248}Cm data coming from [Dur+95]. The fission partner of ^{100}Zr was not specified for [Hwa+06] and [Dur+95].	118
5.4	Models used to simulate $^{235}\text{U}(n_{th}, f)$ and $^{252}\text{Cf}(sf)$	120
5.5	Parameters used to simulate $^{235}\text{U}(n_{th}, f)$ and $^{252}\text{Cf}(sf)$	120
5.6	Relative intensities (I_γ) of the γ -ray transitions (keV) in ^{100}Zr , normalized to the strongest transition (212.5 keV). Data coming from the FIFRELIN simulation of the $^{235}\text{U}(n_{th}, f)$ and $^{252}\text{Cf}(sf)$. The analyzed fission fragment pairs are $^{100}\text{Zr} - ^{134}\text{Te}$ ($^{235}\text{U}(n_{th}, f)$), $^{100}\text{Zr} - ^{150}\text{Ce}$ ($^{252}\text{Cf}(sf)$)(2n) and $^{100}\text{Zr} - ^{148}\text{Ce}$ ($^{252}\text{Cf}(sf)$)(4n). The model/parameter setup used in these simulations can be found in Tables 5.4 and 5.5.	122
5.7	χ^2 values containing main band γ -transitions in ^{100}Zr for FIFRELIN simulations utilizing different models. The best results for the CONSTANT and BSFG spin cut-off models are written in bold text.	137
5.8	Relative intensities (I_γ) of the γ -ray transitions (keV) in ^{100}Zr , normalized to the strongest transition (212.5 keV). Comparison of the EXILL experimental data with the simulations using the EGLO and HFB photon strength functions, the CTM level density model and the CONSTANT spin cut-off model, without collective neutron behavior. These simulations give the correct neutron multiplicity.	138
5.9	Relative intensities (I_γ) of the γ -ray transitions (keV) in ^{100}Zr , normalized to the strongest transition (212.5 keV). Comparison of the EXILL experimental data with the simulations having the lowest χ^2 value, using CONSTANT ($\bar{\sigma}_L = \bar{\sigma}_H = 9.5$) and BSFG ($f_\sigma = 1.8$) spin cut-off models and the CTM level density model. These simulations give the correct neutron multiplicities ($\bar{\nu}_L, \bar{\nu}_H, \bar{\nu}_{Tot}$).	140
5.10	Parameters used to simulate $^{235}\text{U}(n_{th}, f)$ with the CONSTANT spin cut-off model giving the best agreement with the EXILL data for the γ -intensities and the correct $\bar{\nu}_{Tot}$	141

5.11	Parameters used to simulate $^{235}\text{U}(n_{th}, f)$ with the BSFG spin cut-off model giving the most accurate intensities and correct $\bar{\nu}_{Tot}$	144
5.12	Relative intensities (I_γ) of the γ -ray transitions (keV) in ^{100}Zr , normalized to the strongest transition (212.5keV). Comparison of the EXILL experimental data with the simulations scanning the spin cut-off value or f_σ which gives the lowest χ^2	148
5.13	Average prompt-neutron multiplicities for the simulations which give the lowest χ^2 value. For CONSTANT, the spin cut-off parameter is equal to 5.5. For BSFG, f_σ is equal to 1.15. The adopted experimental values are taken from [Nis+98].	149
5.14	Relative intensities (I_γ) of the γ -ray transitions (keV) in ^{100}Zr , normalized to the strongest transition (212.5 keV). Comparison of the EXILL experimental data with the simulations using BSFG which give the lowest χ^2 value for different R_T^{max}	154
A.1	Relative intensities (I_γ) of the γ -ray transitions (keV) in ^{134}Te , normalized to the $2_1^+ \rightarrow 0_1^+$ transition (1279.3 keV). ^{248}Cm data comes from [Sah+01]. The fission partner of ^{134}Te for the EXILL data was ^{100}Zr , for [Sah+01] it was ^{110}Ru , ^{111}Ru or ^{112}Ru . For ^{248}Cm data, except for the weakest lines, the intensities should be accurate within 20% [Sah+01]. Models and free parameters set used in the FIFRELIN simulation: EGLO photon strength functions, CTM level density model, BSFG spin cut-off model, $R_T^{\text{min}} = 0.75$, $R_T^{\text{max}} = 1.23$, $f_\sigma = 1.5$ (optimized, see Figure A.2). *The γ -transition intensities were not corrected to take into account that the excited state at 1692.1 keV is long-lived (164 ns).	191
A.2	Relative intensities (I_γ) of the γ -ray transitions (keV) in ^{92}Kr , normalized to the $2_1^+ \rightarrow 0_1^+$ transition (769.0 keV). The fission partner of ^{92}Kr for the EXILL data and the FIFRELIN data was ^{142}Ba . Models and free parameters set used in the FIFRELIN simulation: EGLO photon strength functions, CTM level density model, BSFG spin cut-off model, $R_T^{\text{min}} = 0.75$, $R_T^{\text{max}} = 1.23$, $f_\sigma = 1.8$. These parameters were used in the reference FIFRELIN simulation (Table 5.7) which gave the correct prompt-neutron multiplicity.	192

- A.3 Relative intensities (I_γ) of the γ -ray transitions (keV) in ^{142}Ba , normalized to the $2_1^+ \rightarrow 0_1^+$ transition (395.5 keV). ^{248}Cm data comes from [Urb+97]. The fission partner of ^{142}Ba for the EXILL data measured with the new analysis technique (EXILL data) was ^{92}Kr , for [Urb+97] it was a complementary Zr fragment. Models and free parameters set used in the simulations: EGLO photon strength functions, CTM level density model, BSFG spin cut-off model, $R_T^{\text{min}} = 0.75$, $R_T^{\text{max}} = 1.23$, $f_\sigma = 1.05$ (optimized, see Figure A.4). 195
- A.4 Relative intensities (I_γ) of the γ -ray transitions (keV) in ^{94}Sr , normalized to the $4_1^+ \rightarrow 2_1^+$ transition (1308.9 keV). ^{248}Cm data comes from [RU+09]. The fission partner of ^{94}Sr for the EXILL data measured with the new analysis technique (EXILL data) was ^{140}Xe . [RU+09] results were obtained from spectra doubly gated in ^{94}Sr on different γ -ray peaks. Models and free parameters set used in the simulations: EGLO photon strength functions, CTM level density model, BSFG spin cut-off model, $R_T^{\text{min}} = 0.75$, $R_T^{\text{max}} = 1.23$, $f_\sigma = 1.8$ 197
- A.5 Relative intensities (I_γ) of the γ -ray transitions (keV) in ^{140}Xe , normalized to the $4_1^+ \rightarrow 2_1^+$ transition (457.4 keV). ^{252}Cf data comes from [Ham+97], intensity uncertainties are around 15%. The fission partner of ^{140}Xe for the EXILL data measured with the new analysis technique (EXILL data) was ^{94}Sr , for [Ham+97] it was a complementary Ru fragment. Models and free parameters set used in the simulations: EGLO photon strength functions, CTM level density model, BSFG spin cut-off model, $R_T^{\text{min}} = 0.75$, $R_T^{\text{max}} = 1.23$, $f_\sigma = 1.8$ 199
- A.6 Relative intensities (I_γ) of the γ -ray transitions (keV) in ^{138}Xe , normalized to the $8_1^+ \rightarrow 6_1^+$ transition (729.6 keV). The fission partner of ^{138}Xe for the EXILL data and the FIFRELIN data was ^{96}Sr . Models and free parameters set used in the FIFRELIN simulation: EGLO photon strength functions, CTM level density model, BSFG spin cut-off model, $R_T^{\text{min}} = 0.75$, $R_T^{\text{max}} = 1.23$, $f_\sigma = 1.8$ 201

- A.7 Relative intensities (I_γ) of the γ -ray transitions (keV) in ^{104}Mo , normalized to the $2_1^+ \rightarrow 0_1^+$ transition (192.0 keV). ^{248}Cm data comes from [Gue+96; Smi+02]. The fission partner of ^{104}Mo for the EXILL data measured with the new analysis technique (EXILL data) was ^{130}Sn , for [Gue+96] it was ^{140}Xe . [Smi+02] results were obtained from spectra doubly gated in ^{104}Mo on different γ -ray peaks. Models and free parameters set used in the simulations: EGLO photon strength functions, CTM level density model, BSFG spin cut-off model, $R_T^{\text{min}} = 0.75$, $R_T^{\text{max}} = 1.23$, $f_\sigma = 1.8$ 203
- A.8 Relative intensities (I_γ) of the γ -ray transitions (keV) in ^{130}Sn , normalized to the $(4_1^+) \rightarrow (2_1^+)$ transition (774.4 keV). The fission partner of ^{130}Sn for the EXILL data measured with the new analysis technique (EXILL data) was ^{104}Mo . Models and free parameters set used in the simulations: EGLO photon strength functions, CTM level density model, BSFG spin cut-off model, $R_T^{\text{min}} = 0.75$, $R_T^{\text{max}} = 1.23$, $f_\sigma = 1.8$ 204
- A.9 Relative intensities (I_γ) of the γ -ray transitions (keV) in ^{144}Ba , normalized to the $4_1^+ \rightarrow 2_1^+$ transition (330.7 keV). ^{248}Cm data comes from [Urb+97]. The fission partner of ^{144}Ba was ^{90}Kr gated at 655.6 keV. Most of the transitions from [Urb+97] were measured in the spectra double-gated in ^{144}Ba . Models and free parameters set used in the simulations: EGLO photon strength functions, CTM level density model, BSFG spin cut-off model, $R_T^{\text{min}} = 0.75$, $R_T^{\text{max}} = 1.23$, $f_\sigma = 1.8$ 207
- A.10 Relative intensities (I_γ) of the γ -ray transitions (keV) in ^{146}Ba , normalized to the $4_1^+ \rightarrow 2_1^+$ transition (332.7 keV). The fission partner of ^{146}Ba was ^{87}Kr . In both presented measurements one of the gates was at 181.1 keV ($2_1^+ \rightarrow 0_1^+$) transition in ^{146}Ba , second either at 1577.5 keV or at 1419.8 keV in ^{87}Kr . Transitions at 1577.5 keV and at 1419.8 keV go to the ground state of ^{87}Kr but they belong to different bands, see Figure A.14. 209

Chapter 1

Introduction

According to Encyclopædia Britannica, the most basic definition of nuclear fission is: *subdivision of a heavy atomic nucleus, such as that of uranium or plutonium, into two fragments of roughly equal mass. The process is accompanied by the release of a large amount of energy* [Ste18]. In plain words, it is a split of an atomic nucleus into smaller parts (at least two lighter nuclei).

1.1 History of a discovery

In 1938, Otto Hahn, Lise Meitner, and Fritz Strassmann began performing an experiment during which uranium was bombarded with neutrons. After chemical analysis, O. Hahn concluded that some of the products of this bombardment was barium. L. Meitner interpreted it as an evidence of nuclear fission - split of an uranium nucleus into two lighter nuclei. She explained this behavior with the mass disappearance phenomenon. The combined mass of the two division products would be lighter than the original uranium nucleus by about one-fifth of the proton mass. This missing mass, according to Einstein's formula $E = mc^2$, would be equal to 200 MeV. L. Meitner predicted that about this amount of the repulsion energy would be needed to drive apart two nuclei after separation [MF39]. In this way, she created a theory which matched the observed phenomenon. The results were published in 1939 [MF39] and, in 1944, O. Hahn was granted the Nobel Prize in Chemistry for the discovery of the fission of heavy nuclei [Nob].

This discovery would not have been possible without earlier studies on the atom structure and radioactivity. Henri Becquerel in 1896 discovered radioactivity, while

working with phosphorescent materials. The uranium salts caused a blackening of the plate covered with a phosphorescent material. He identified it as a sort of invisible radiation. His further studies along with Pierre Curie and Maria Skłodowska Curie showed that the observed radioactivity was more complex than already known X-rays. In 1903, they received the Nobel Prize in Physics for the discovery and research on spontaneous radioactivity.

In 1900, Paul Villard observed a powerful ray while studying radiation emitted from radium. But only in 1903, Ernest Rutherford concluded that these rays are fundamentally different from already known types and he called them γ -rays.

In 1911, Ernest Rutherford presented a model which assumed that an atom consists of a tiny, dense and positively charged nucleus of protons and it is surrounded by orbiting, negatively charged electrons. In 1913, Niels Bohr developed this model by adding the quantum behavior of electrons creating the Bohr model.

Another event which led to the nuclear fission detection was the discovery of the neutron in 1932 by James Chadwick [Cha32]. He used the energetic alpha particles emitted from polonium to irradiate beryllium which led to the emission of a strongly penetrating radiation. He rejected the hypothesis that the observed effect was caused by γ -rays and proposed a new particle named neutron - uncharged, having a mass almost the same as the proton. He received the Nobel Prize in Physics for this discovery in 1935. Enrico Fermi quickly (1934) used the new particle to conduct an experiment on bombarding uranium with neutrons. He claimed to create new elements with 93 and 94 protons. Not all scientists were convinced with his discovery and later a very similar experiment was used to discover the nuclear fission.

In 1933, Leó Szilárd proposed the concept of a nuclear chain reaction, and in 1934 together with Enrico Fermi, patented the concept of a nuclear reactor (a chain reaction pile). After the discovery of the nuclear fission, Frédéric Joliot, Hans Von Halban and Lew Kowarski proved in 1938 that a nuclear chain reaction is possible by neutron multiplication in uranium. In 1939, they filed three patents: two describing power production from a nuclear chain reaction and one using it to create a bomb. This opened a road to harness the enormous amounts of the energy released during the nuclear fission for both peaceful and military purposes.

1.2 Fission process

Nowadays, our knowledge about the nuclear fission is much wider. Our interest in the process reaches much deeper than a simple energy exploitation and we try to understand and study all the phenomena which lead to fission and that occur after scission. In this work we analyze data coming from the thermal neutron induced fission of ^{236}U ($^{235}\text{U}(n_{th}, f)$ reaction).

1.2.1 Liquid Drop Model

The neutron induced fission process starts with the creation of the fissioning system. A nucleus (^{235}U) in the ground state captures a neutron and forms a compound nucleus (^{236}U). Its lifetime is close to a femtosecond [Vor+77]. The compound nucleus vibrates and deforms, obtaining a configuration where two groups of nucleons are connected by a neck, see Figure 1.1.

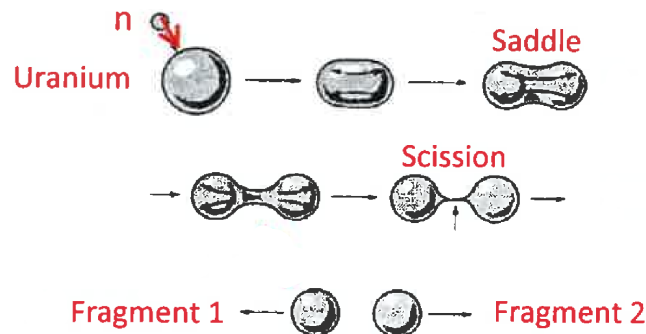


Figure 1.1: Scheme of the neutron induced fission of ^{236}U [Gön14a].

The deformation of the compound nucleus rises and it reaches the saddle point - the critical deformation of no return to the mono-nucleus. At this point the compound nucleus overcomes the potential barrier called "fission barrier".

The concept of the fission barrier was proposed by Bohr and Wheeler (1939). They created the theory of the electrically charged liquid drop - Liquid Drop Model (LDM). In LDM the nucleus is treated as a drop of very dense, incompressible fluid. The nucleons behave like the molecules in a drop of liquid.

In LDM the nuclear "fluid" is assumed to be incompressible thus when the liquid drop becomes deformed only the surface and the Coulomb energy are affected. The surface energy takes into account that the nucleons at the surface are less bounded

than the interior nucleons of the nucleus. The Coulomb energy accounts for the electric repulsion between protons inside the nucleus. Bohr and Wheeler succeeded to evaluate the potential energy of deformation as a function of the deformation parameters β_2 (the quadrupole deformation) and β_4 (the hexadecapole deformation). In the (β_2, β_4) plane (Figure 1.2) the saddle point is reached at specific β -parameter values. The fission proceeds along the energetically most favorable path (dashed line in Figure 1.2).

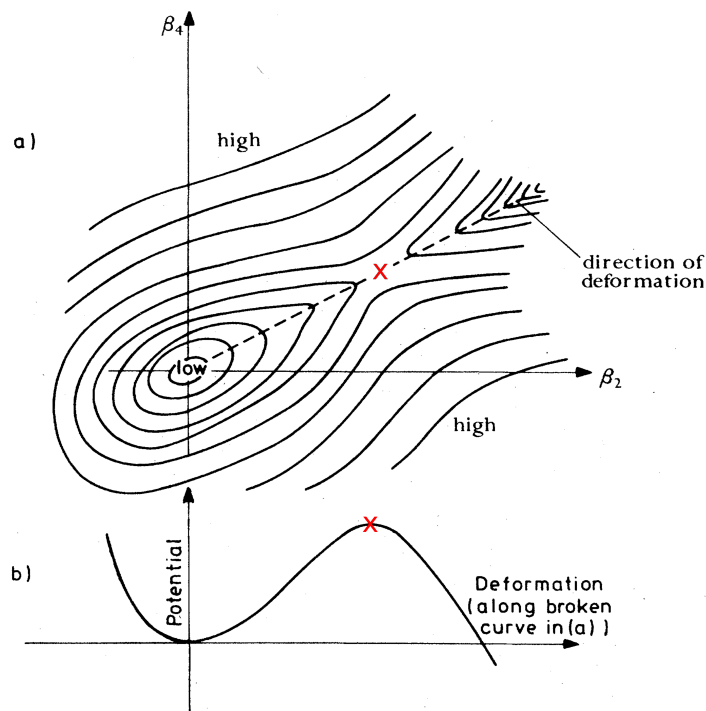


Figure 1.2: (a) Potential energy surface of a deforming nucleus. (b) The potential energy along the most energetically favorable fission path. The red "x" marks the saddle point [BL80].

1.2.2 Scission

Starting from the saddle point, the Coulomb repulsion force between protons starts to overcome the strong force - the attractive force that binds nucleons together. The deformation becomes even stronger and the neck more elongated, see Figure 1.3. Scission happens when the deformation is so strong that the neck joining the two nascent fragments becomes unstable and breaks apart. In the majority of cases, two excited nuclei, so called primary fission fragments, are created. The Coulomb repulsion force

accelerates them in the opposite direction (along the fission axis). This process is very fast, the fragments obtain 90% of their final velocity thus final kinetic energy in around $5 \cdot 10^{-21}$ s [Gön14a]. During acceleration deformed primary fission fragments are reorganized and obtain configurations close to their ground states. This process is called the relaxation phase. When the fission fragments obtain their final velocity, the sum of their kinetic energies is between 150 and 200 MeV, which is the essence of the energy released during the fission process. Additionally, each fission fragment has an excitation energy between 0 and 40 MeV [Reg13]. In solid nuclear fuel used in the conventional nuclear reactors such fragments can travel only microscopic distances. The kinetic energy is converted into heat and used to produce electricity.

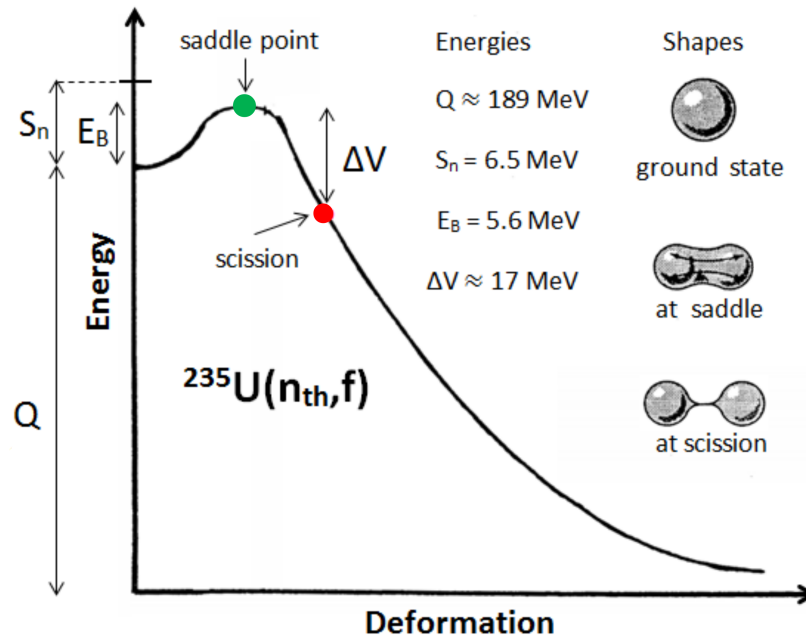


Figure 1.3: Potential energy as a function of deformation. Q is the nucleus potential energy at the ground state, S_n is the neutron separation energy, E_B is the fission barrier and ΔV is the potential energy difference between saddle and scission point [Gön14a].

1.2.3 Fission fragments mass distribution

The fission fragments created during scission have similar but not equal masses. Their experimental mass yields (Figure 1.4) show that very rarely two fission fragments have identical masses. This effect is caused by the influence of shell effects in the nascent fragments [Pom+18; MS71; CIZN16].

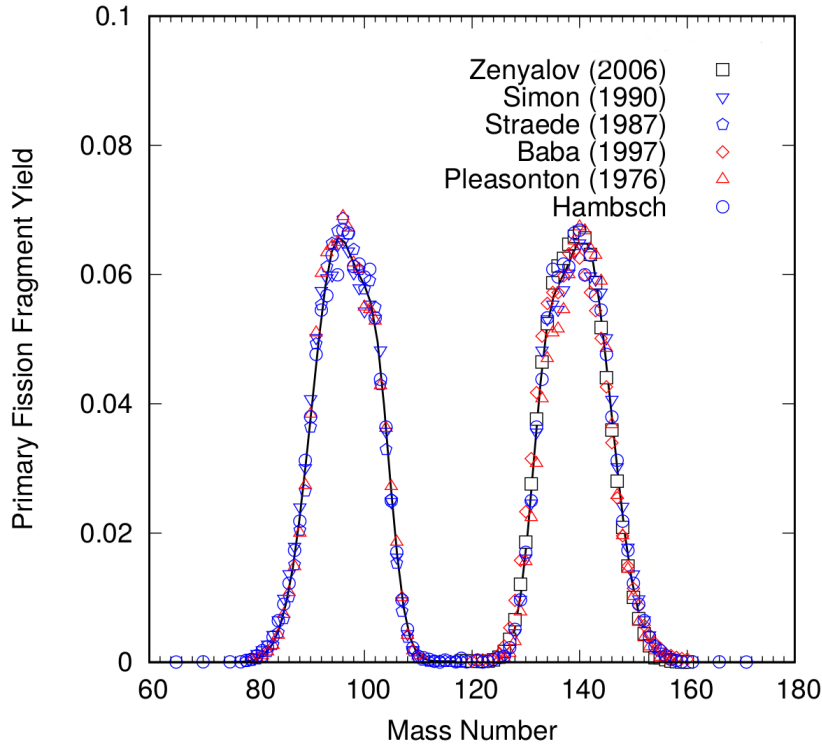


Figure 1.4: Pre-neutron emission experimental fission fragment mass yield distribution following $^{235}\text{U}(n_{th}, f)$ [Oku+18].

The asymmetry in charge or mass splits is proved to be a general feature in the (n, f) reactions and spontaneous fission of the actinides. For all of these reactions, the mass center of the heavy group stays about constant [Gön14b]. In this group the yields start to rise at the fission fragments mass of $A=130$ (Figure 1.4). This is associated with the magic charge $Z=50$. The mass center of the light group moves toward a higher mass with the increase of the compound nucleus mass [Gön14b]. This phenomenon is linked to the complex structures of the potential energy surfaces at the scission point [Paş+18].

A description of mass and energy distributions requires the introduction of different types of fission called fission modes. U. Brosa, S. Grossmann and A. Müller proposed a model of scission containing three modes [BGM90]. They are: the superlong symmetric mode (SL) and two asymmetric modes standard I (S1) and standard II (S2). The position of S1 is centered at the heavy mass $A=135$ and S2 at $A=142$. The S1 is driven by the doubly magic ^{132}Sn and S2 by the deformed neutron shell with $N=88$ [Gön14b]. Mass distributions for all three modes have a Gaussian shape, see Figure 1.5.

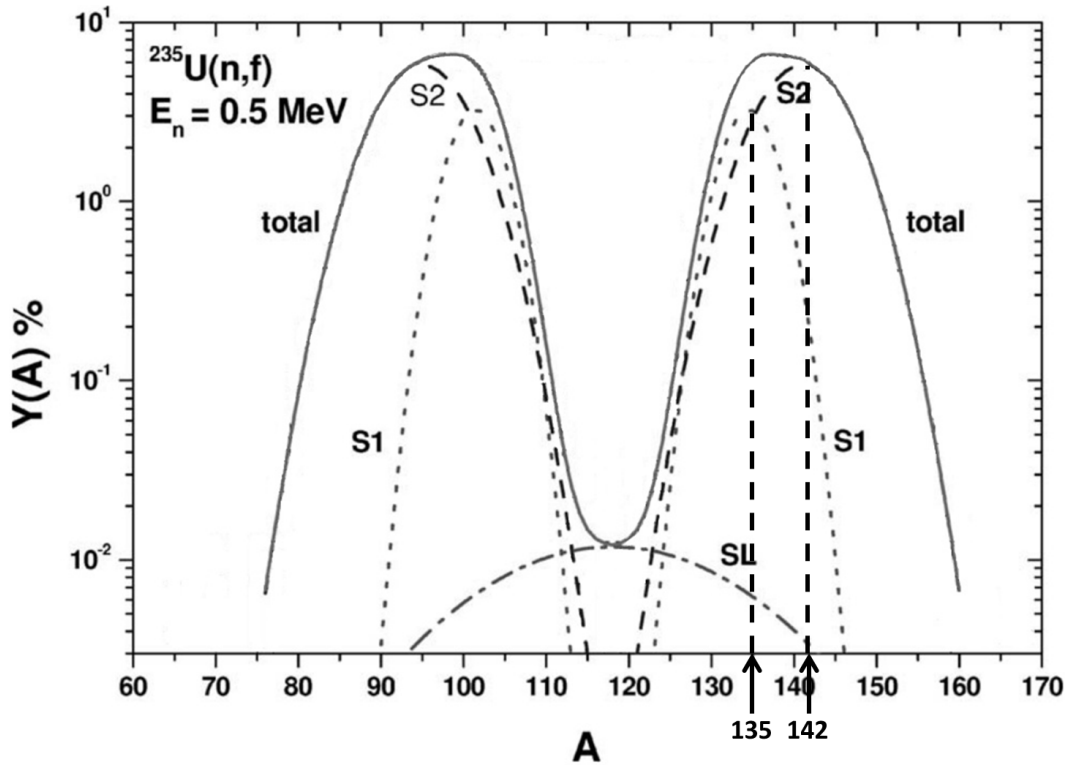


Figure 1.5: Multimodal and total fission mass distribution following $^{235}\text{U}(n_{th}, f)$ at neutron energy $E_n=0.5$ MeV [Ham+03].

The transformation from symmetric to asymmetric mode can be assigned to the interplay between the liquid-drop surface energy and the nucleus-nucleus interaction potential at the scission-point configurations. This interplay indirectly depends on the shell corrections [Bal+10]. The correlation of different fission modes depends on the configuration and position of the saddle and scission points on the energy surface [Pas89; FG94].

The fission barriers for the actinides are double-humped, see Figure 1.6. They emerge when both tri-axial and asymmetric deformations are taken into account. The symmetric and asymmetric modes follow the valleys of low potential toward scission. They are well separated by the ridges of high potential. The first barrier is symmetric. The asymmetry of the second barrier is considered to be the reason why the mass asymmetry occurs in the actinides [Gön14b]. The fission barrier for symmetric fission is higher than for asymmetric fission thus it is more energetically favorable to follow paths which lead to asymmetric fission.

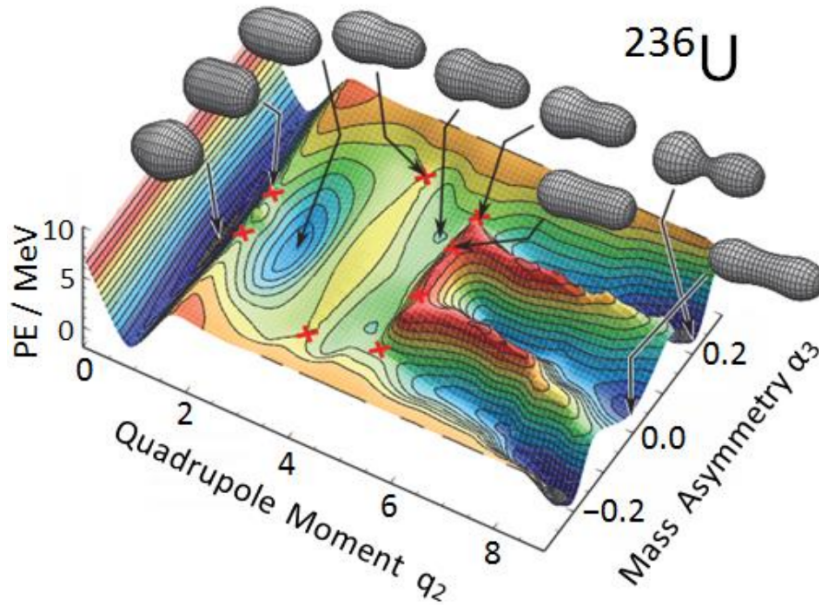


Figure 1.6: Multimodal fission mass distribution following $^{235}\text{U}(n_{th}, f)$ at neutron energy $E_n=0.5$ MeV [Möl+09].

1.2.4 Fission fragments de-excitation

The nuclear fission leads to the formation of the primary fission fragments. As mentioned earlier, during the relaxation phase most of the energy of the fission process is transferred into kinetic energy. The remaining energy is divided between the two nascent fragments in the form of excitation energy distributed between collective and individual excitations. Each primary fission fragment gains in this way from 0 up to 40 MeV. To remove this energy and de-excite to their ground states, fission fragments within picoseconds emit first prompt neutrons and then prompt γ -rays (Figure 1.7). When the excitation energy is above the neutron separation barrier (S_n), one can also observe a competition between neutron and γ -ray emission but this effect is negligible. Below S_n neutron emission becomes energetically impossible and a fission fragment de-excites further by γ -emission. The emitted γ -rays form a cascade, which can be arranged in different fission branches depending on the deformation of the fission fragment.

The created fission products are still unstable due to the excess of neutrons. This metastable state last microseconds, much longer than the previous processes. It is the time that fission products need for recombination. They decay by emitting β particles,

neutrons and γ -rays. These processes are labeled as delayed due to the fact that they occur much later during the de-excitation: β particles from microseconds, up to few months and neutrons in the range between milliseconds up to 55 seconds for the long-lived precursors. Even though, these neutrons represent only a very small fraction of the emitted neutrons (tenths of neutrons) during the nuclear fission process, they play the crucial role in the controlling of the chain reaction in nuclear reactors. It results in a long-term interest and numerous studies of these delayed processes, which translate into abundant and reliable data on the delayed neutrons and γ -rays.

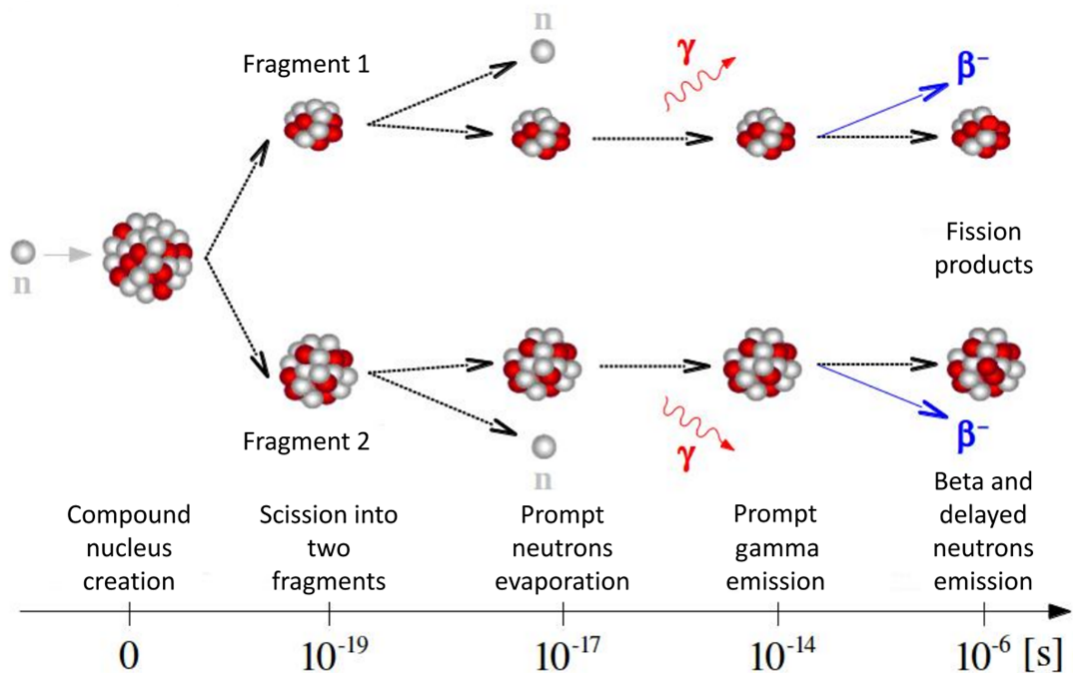


Figure 1.7: Fission fragments de-excitation scheme with emission of the prompt and delayed particles [Lem15].

Our understanding of the mechanisms responsible for the fission fragment creation occurring just after the scission point is incomplete. Many fundamental questions are left open:

- how are the excitation energy and the initial spin shared between primary fission fragments?
- what is the part of intrinsic and collective excitations in the excitation energy of the primary fission fragments?
- what is the process that generates high spins in the primary fission fragments?

The γ -spectroscopy is able to provide new experimental data on prompt γ -rays which can help to understand the fission process by answering these questions. γ -transitions are electromagnetic transitions created by the movement and rearrangement of nucleons in the excited nucleus thus the γ -ray cascade is sensitive to both collective and intrinsic excitation during the fission process. Studying the evolution of the prompt γ -ray cascade in a particular fission fragment as a function of different fission partners or different fissioning systems can address the issue of the spin distribution in the primary fission fragment. Part of my thesis is devoted to obtain such data by analyzing the de-excitation of the fission fragments in the $^{235}\text{U}(n_{th}, f)$ process.

1.3 Nuclear reactors

The undeniable success which was closely connected to the discovery of the nuclear fission and the nuclear chain reaction was the construction of a nuclear reactor. The first man-made nuclear reactor was Chicago Pile-1 which started to operate in 1942 under the supervision of Enrico Fermi. It was part of the military project called Manhattan Project, which aimed to create an atomic bomb.

Not long after World War II, the nuclear fission energy started to be used for civilian purposes. The first reactor which produced electricity was EBR-I near Arco in Idaho, USA, which in 1951 output about 100 kW. The first reactor which was intended to long-term electricity production and was connected to the power grid was AM-1 at the Obninsk Nuclear Power Plant in the USSR. It started to operate in 1954 and its electrical capacity was 6 MW.

The most common nuclear reactors use the nuclear fuel containing uranium. The fresh fuel is enriched to around 5% of ^{235}U content [Bla12; IAE15].

The energy of the nuclear fission, released as all sorts of radiations is converted into thermal energy in the irradiated materials of the nuclear fuel elements. Nowadays, in the majority of the operating reactors this energy is taken away by the coolant - light water. In the pressurized water reactors (PWR), which are the most widespread reactors around the World, this energy is transferred to the second loop via steam generators where the steam to drive turbines is created. The mechanical energy of the turbine movement is used to produce electricity in the generators.

During the last decades many types of reactors were developed but the newest ones completed at the time this thesis was written - generation III+ PWR reactors in Tais-

han, China (EPR reactor by Framatome) [Fra18] and in Sanmen, China (AP1000 by Westinghouse) [Wes18], still use thermal neutrons to induce fission in the fuel containing enriched uranium. Even though, the basics of the operation for this generation of reactors is the same as for the previous ones, their design features brought some new challenges. These reactors are designed to have a lifetime of around 50 (AP1000) or 60 (EPR) years [IAE15] and better fuel economy. The design life is considerable longer than the predicted 30 to 40 years for the generation II reactors [Far10]. This forced the designers to use parts which protect the core barrel and the reactor pressure vessel (RPV). RPV, that encapsulates the core barrel which houses the core, are both constantly irradiated by the neutrons and γ -rays. They are also considered to be irreplaceable. The RPV is one of the most significant parts which defines the safety of a nuclear reactor. Its aging due to the neutron radiation embrittlement is potentially the most important factor limiting the reactor lifetime. It has become an important question in the context of extending the operational time of existing nuclear reactors. Recently, the Nuclear Regulatory Commission has considered to extend it up to 80 years [FH18], which could be even twice the originally design lifetime of the reactor.

The solution which can extend the reactor's lifetime is adding a heavy reflector or in the case of AP1000 a specially designed core shroud which both have an additional radiation attenuation feature [IAE15]. The heavy reflector is made of stainless steel and placed inside the core barrel outside of the core. It has a double function: it decreases the neutrons leak and improves the fuel economy by redirecting neutrons back into the core. At the same time it reduces irradiation of the core barrel and the RPV, especially by the fast neutrons which are the most devastating for these parts. The placement of the heavy reflector just next to the core, exposes it to a constant, high flux of γ -radiation.

In 2014, the Generation IV International Forum (GIF) [NEA14] presented six new concepts of reactors. Generally, the new reactors should: provide better fuel economy and long-term operability, have a clear life-cycle cost and a low investment risk, sustain even a higher safety level and reliability than present reactors, and limit a risk of nuclear proliferation. Four out of the proposed designs operate with fast neutrons. Their core designs would need to be heavily modified in comparison to the conventional fast neutron reactors to meet all the new criteria. This emerges as replacing the UO_2 blankets placed around the core with steel or ceramic reflectors. The example of a concept of generation IV reactor with complex reflectors system is the High Temperature

Modular Reactor-100 (HTMR-100), see Figure 1.8.

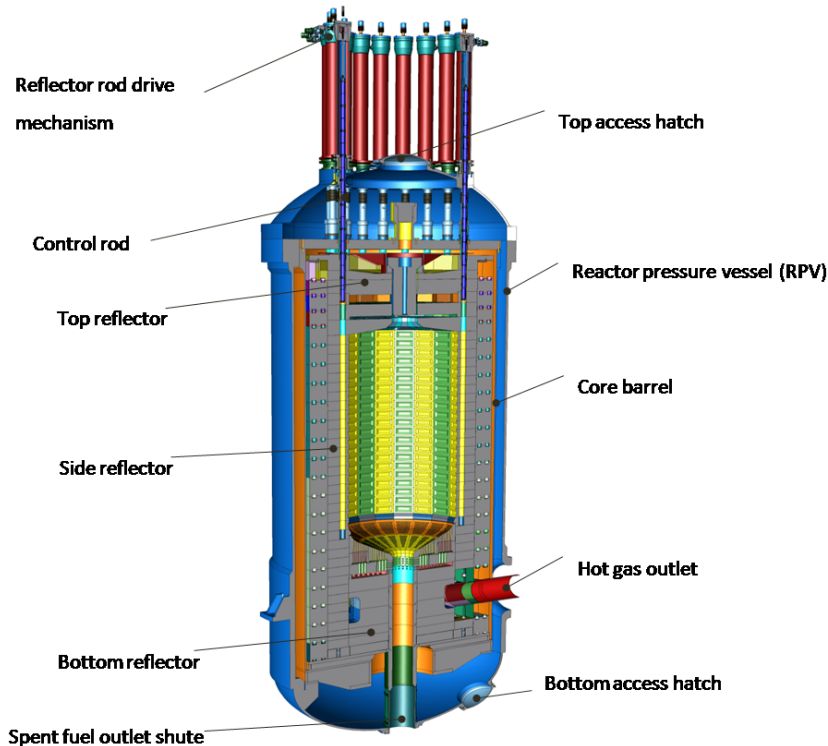


Figure 1.8: The design of the HTMR-100 generation IV reactor with a complex reflectors system [Boy15].

Like in the Gen III+ reactors, the reflectors in generation IV reactors will be exposed to a high flux of γ -radiation. In both cases it will cause a rise of temperature of these parts due to a process called γ -heating.

1.4 γ -heating process

γ -heating is a process of matter heating when γ -rays cross through it. It is caused by the γ -ray energy deposition via an electromagnetic interaction with materials. There are three main interactions considered to be the most important for the γ -heating: the photoelectric effect, the Compton effect (scattering) and pair production. All of them excite molecules of the material, which directly translates into its higher temperature. The contribution of γ -heating to the total heating in a reactor is illustrated in Figure 1.9. More than 90% of the total heating in the non-fuel regions of the reactor is caused

by γ -rays [Bla+08] thus a precise evaluation of the γ -ray spectrum is mandatory if one wants to correctly estimate this effect.

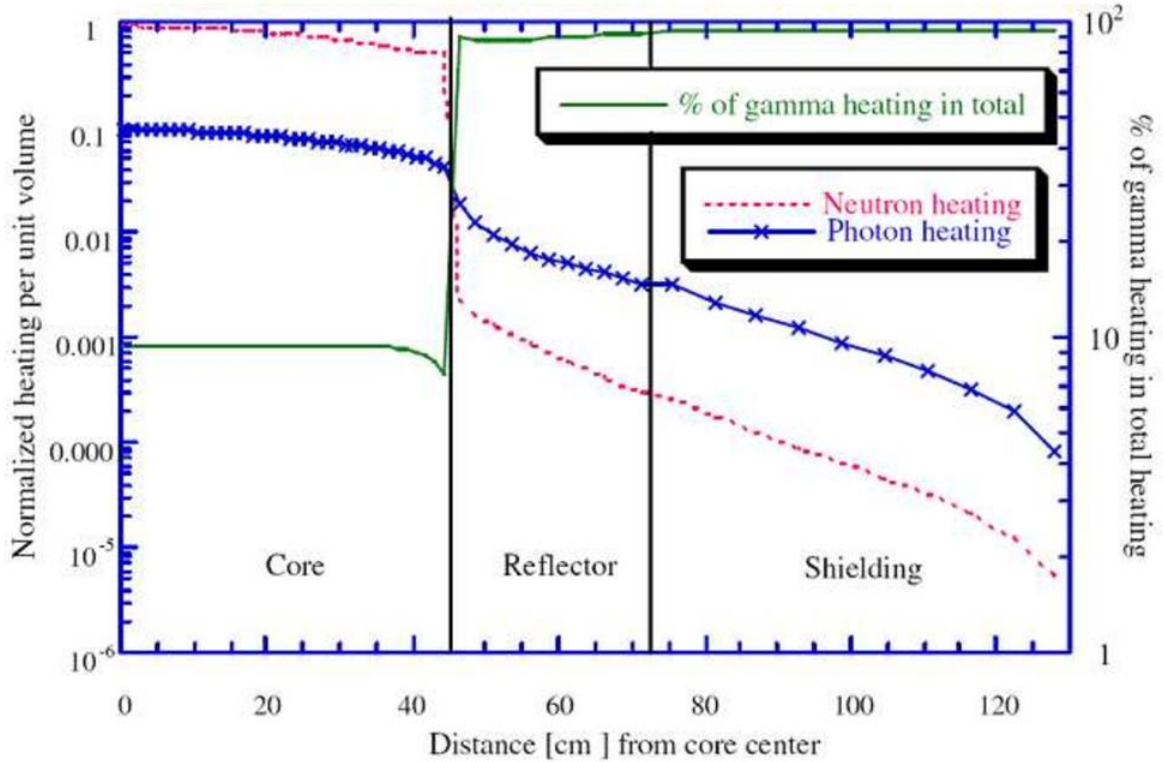


Figure 1.9: Sources of heating in the nuclear reactor as a function of the distance from the center of the core [Col+13].

To provide the highest possible safety level of new nuclear reactors, simulations of all nuclear processes especially those which take place around the reactor core need to be performed with high precision. Due to transient state in the working nuclear reactor which is changing the fuel composition (fuel burn-up), one needs to have precise data on different fission fragments produced in the fission process. This allows one to correctly simulate the γ -heating effect in every state of the reactor. To be sure that the new design solutions are safe, at most 7.5% uncertainty is permissible in the calculation of the energy deposition in non-fuel regions of the reactor [Rim05]. Present uncertainties on γ -heating calculations are in the range of 15-30%. They are caused mostly by lack of data on the γ -emission yields and spectra or their high uncertainties [Bla+08]. Nuclear-data libraries still provide values for γ -energy or multiplicity based on the experiments from early 70's where high uncertainties are expected. A second issue

is the mismodeling of functions and algorithms responsible for the γ -ray simulation, which is very often caused by not precise enough input data.

An accurate modeling of the prompt γ -rays emitted in the fission process is required to address problems related to the γ -heating in nuclear reactors. It requires precise experimental data on γ -rays, especially prompt γ -rays. Average spectra and multiplicities are available but more detailed information about prompt γ -rays emitted by individual elements (fission fragments) is missing. This should be the first step in a multistage process of designing a safe and reliable generation IV nuclear reactor (Figure 1.10).

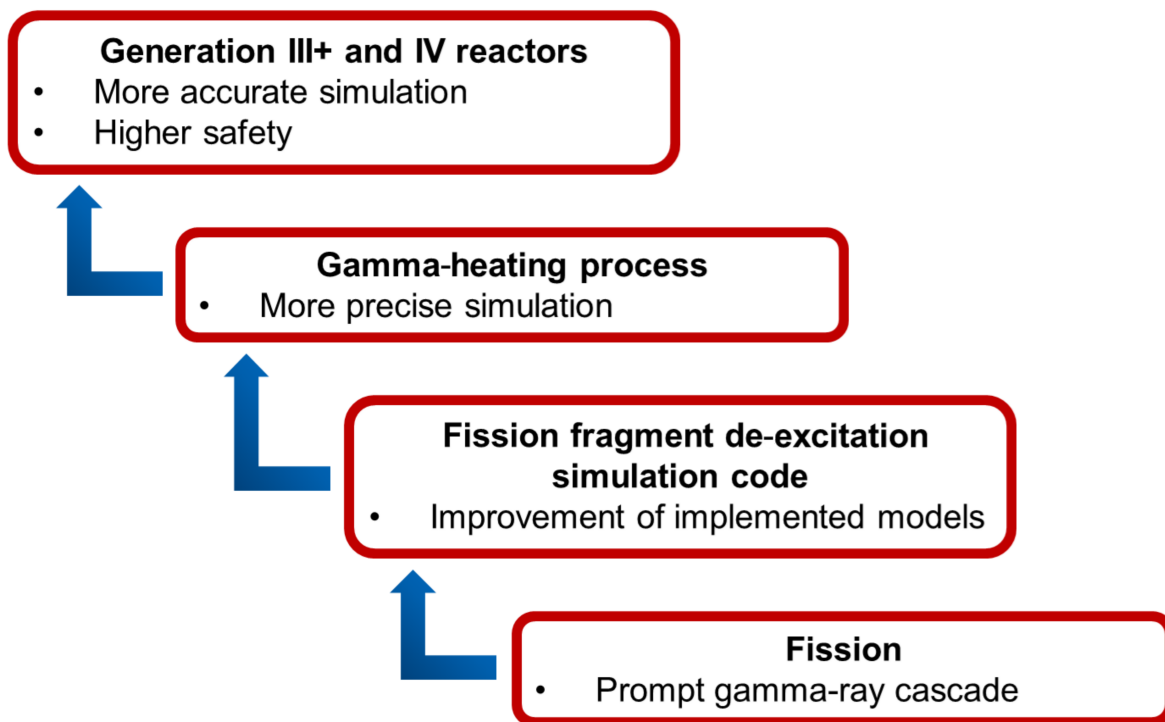


Figure 1.10: Stages in a process of improvement of the generation IV nuclear reactors simulation.

1.5 Fission fragment de-excitation process simulation

The issue with mismodeling of the γ -rays was addressed by scientists from the DEN/DER/SPRC/LEPH laboratory at CEA Cadarache. They have developed a Monte-Carlo simulation code on the de-excitation of fission fragments - FIFRELIN [LS10]. It is used to simulate the fission process and to estimate fission observables. It

can help to estimate γ -heating through simulating the prompt-neutron emission along with the complete prompt γ -ray cascade which occurs during de-excitation. Information on the prompt neutrons and γ -ray spectra and multiplicity, and on the released energy can be also used to estimate the radiation embrittlement of the reactor pressure vessel.

In this work, we test (benchmark) the FIFRELIN simulation code by comparing the simulated prompt γ -ray intensities to the ones coming from our experimental data based on the EXILL experiment. Since FIFRELIN provides a selection of models which can be used during simulation, we evaluated which setup gives results closest to experimental data. Our study also comprises the analysis of the influence of particular spin-distribution models and variables like the spin cutoff parameter, initial spin or initial excitation energy on the simulation results. This comparison will provide an important feedback for the code developers.

1.6 Outline

In this thesis work we have studied the possibility to use the high-resolution γ -spectroscopy of a fissile target to provide new experimental results which can be used to address key issues of our fundamental understanding and modelisation of the fission process. We used data coming from the neutron induced fission. A fissile target of ^{235}U was irradiated by a cold neutron beam. The target was surrounded by an array of germanium detectors (EXOGAM) which measured emitted γ -rays. It was a part of the EXILL campaign conducted at the research reactor of the Institut Laue-Langevin (ILL) in Grenoble, France. With the new data we could test and develop the methodology.

Part of this thesis is devoted to the Monte-Carlo simulation code FIFRELIN. It is used to study the fission process and the de-excitation of the fission fragments. The required input, the possible output, the used models and the functioning of this code are described in Chapter 2. It also contains an explanation of how the simulation is prepared and how we used the code.

The EXILL campaign and the experiment's set-up that we used (with its characteristics) are described in Chapter 3. It also contains information about data pre-processing (creation of γ - γ - γ cube) and the description of the basic γ - γ - γ coincidence method used to select the fission fragment pair by correlating the γ -rays coming from the de-excitation of these fragments.

In Chapter 4 we describe the new analysis method which allowed us to move from γ -spectroscopy to γ -spectrometry. In particular, we detail the treatment of the background and contamination rejection which is an improvement over the basic γ - γ - γ coincidence method. We describe the spectra fitting process and the calculation of prompt γ -ray intensities. The issues with their uncertainties are also addressed. In this chapter, the limitations of the γ -spectrometry method in terms of statistics and contamination is discussed.

In this work, we present our analysis of experimental data on $^{235}\text{U}(n_{th}, f)$ and study of prompt γ -ray intensities emitted during de-excitation of the most abundant fission fragments. A particular study of the (^{100}Zr - ^{134}Te) pair is presented in Chapter 5. ^{100}Zr is an even-even nucleus with a dominant rotational band. Its large deformation and a simple level-scheme allow us to validate the developed analysis methodology and to test the physical foundation of some models used in FIFRELIN, e.g. spin-distribution models. We could also compare our experimental data with the other available experimental data and with the FIFRELIN simulation results. We present and compare data on the prompt γ -ray intensities from the de-excitation cascade of ^{100}Zr coming from different fissioning systems. The origin of the observed discrepancies is also addressed. The comparison of our experimental data with the FIFRELIN simulation results allows us to test how accurate are the different models. The prompt γ -ray intensities generated with different model combinations are presented. We especially addressed the issue of the initial spin-distribution models. The evolutions of the prompt γ -ray cascade of ^{100}Zr as a function of different fission partners, obtained with different initial spin-distribution models, are demonstrated and compared.

Chapter 2

FIFRELIN Monte-Carlo simulation code

2.1 Introduction

FIFRELIN (FISSION FRAGMENT Evaporation Leading to an Investigation of Nuclear data) is a Monte-Carlo code which was developed in the DEN/DER/SPRC/LEPH laboratory at CEA Cadarache [LS10; LSB15; Lit+17]. It is used to simulate the fission process and the de-excitation of the fission fragments. For the neutron induced and spontaneous fission, it can simulate observables like: prompt neutrons and γ -rays spectra and multiplicities, post-neutron yields, released energy, γ -ray cascades in the fission fragments.

In this work we compare simulation results coming from FIFRELIN with experimental data from the EXILL experiment. FIFRELIN uses various models to describe the nuclear fission and de-excitation process. These models can be changed and chosen from the available pool. A closer look at the theories, assumptions, calculation methods and algorithms used in FIFRELIN is needed to understand how the code works and why the usage of different models changes simulation results. One of the aims of this thesis was to benchmark the simulation code FIFRELIN and to provide feedback to the code developers. I have not developed any of the tested models thus in this chapter, I used information coming from the FIFRELIN-1.0 user guide [Lit+17], which contains a wide description of FIFRELIN.

The main assumptions made in FIFRELIN are:

- fission is a binary process thus ternary fission is not taken into account;
- during acceleration, the fission fragments recover their ground state deformation (relaxation phase);
- there is no neutron emission at scission and during acceleration;
- after the acceleration phase, the fragments having their ground state deformation emit neutrons and γ -rays.

The simulation of the nuclear de-excitation process for a given fission fragment requires a large amount of nuclear data: nuclear level schemes, level densities, photon strength functions and neutron transmission coefficients.

2.2 Characteristics of primary fission fragments

To simulate the de-excitation cascade of a fragment, one first needs to know its mass A , nuclear charge Z , excitation energy E^* , spin J and parity π . At the beginning of the simulation process, these characteristics are sampled for the primary fission fragments and only after the decay of the fully characterized excited fragment is conducted.

2.2.1 Mass, charge and kinetic energy

In FIFRELIN, the mass and kinetic energy distributions before neutron evaporation are taken from experimental data or are provided by external codes like GEF [SJA14]. The binary fission hypothesis assumes a symmetry of the pre-neutron emission mass yields in reference to $A = A_{CN}/2$ (Figure 2.1). The mass of the light fragment (A_L) is sampled from the cumulative distribution calculated from the light peak. Afterwards, the heavy fragment mass (A_H) is deduced according to the mass conservation law:

$$A_H + A_L = A_{CN} \quad (2.1)$$

where A_{CN} is the mass of the compound nucleus.

The light fragment kinetic energy KE_L is sampled from a normal law with pre-neutron emission kinetic energy ($\langle KE \rangle$) and its standard deviation (σ_{KE}) (Figure 2.1). The heavy fragment kinetic energy (KE_H) is calculated from the momentum conservation law:

$$KE_H = \frac{A_L}{A_H} KE_L \quad (2.2)$$

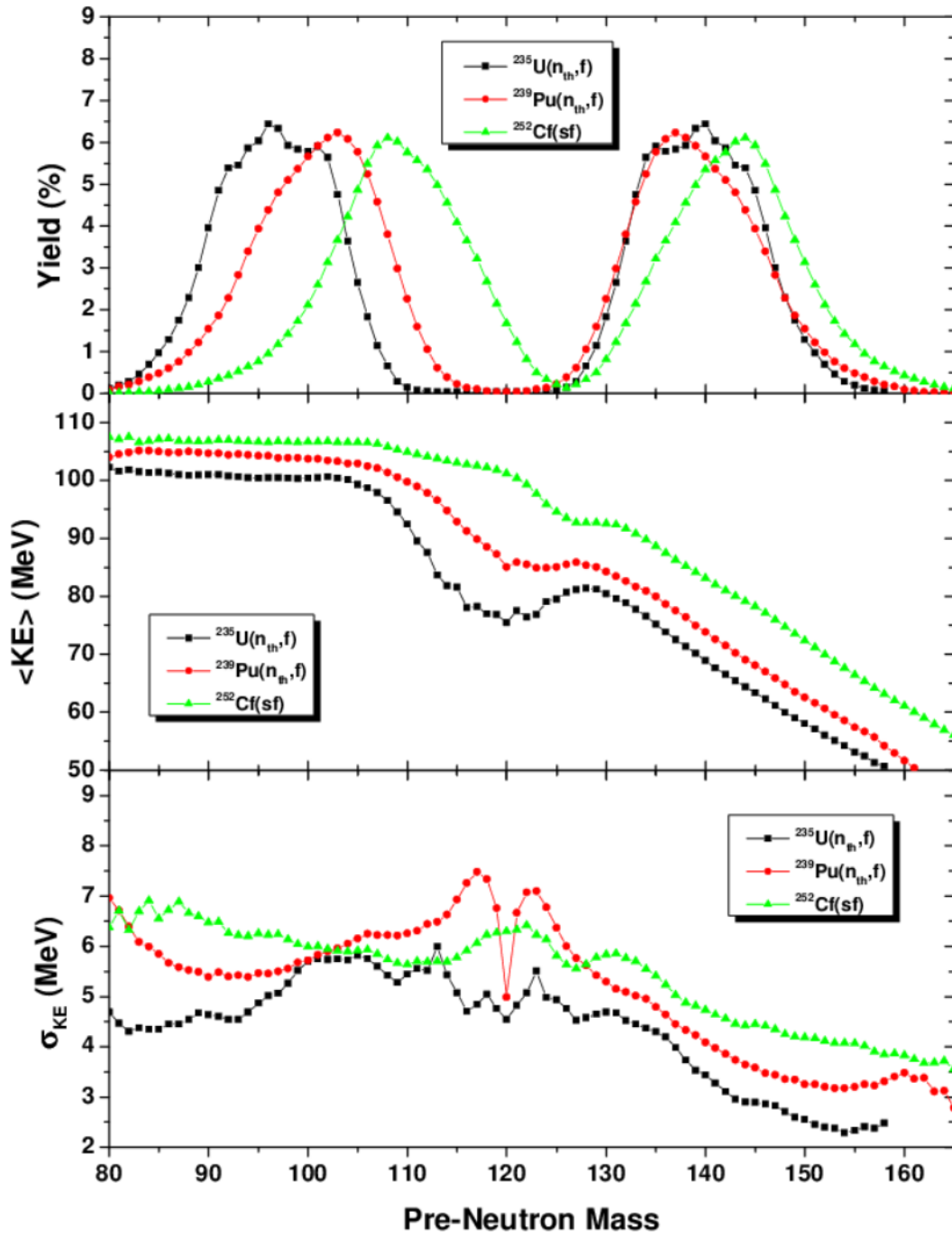


Figure 2.1: An example of FIFRELIN input data. The pre-neutron emission distributions of: fission fragment mass yields (top), average kinetic energy (middle) and its standard deviation (bottom) [Lit+17].

The nuclear charge (Z) is sampled from a "Gaussian" model:

$$P(Z) = \frac{1}{\sqrt{c\pi}} e^{-(Z-Z_p)^2/c} \quad (2.3)$$

with

$$c = 2\pi(\sigma_Z^2 + 1/12) \quad (2.4)$$

where Z_p is the most probable charge and σ_Z is a fissioning nucleus dependent charge dispersion parameter [Wah+62].

FIFRELIN adopts the Unchanged Charge Density (UCD) hypothesis modified by mass dependent polarization charge function [Wah88; BB89; Nai+97; NSI04]. The most probable charge is derived from:

$$\begin{aligned} Z_p^H &= Z^{UCD} + \Delta Z(A_H) \\ Z_p^L &= Z^{UCD} - \Delta Z(A_L) \end{aligned} \quad (2.5)$$

with

$$\frac{Z^{UCD}}{A^{UCD}} = \frac{Z_{CN}}{A_{CN}} = \frac{Z_H}{A_H} = \frac{Z_L}{A_L} \quad (2.6)$$

Finally, the Gaussian distribution is corrected by even-odd proton (F_Z) and neutron (F_N) factors following Wahl's model [Wah88].

2.2.2 Spin and parity

In FIFRELIN, one assumes that the probability of having a positive or a negative parity is the same in a first approximation. A spin distribution initially derived by Bethe [Bet36] is used to sample both: the initial spin of the primary fission fragments and the spins involved in the nuclear structure calculation. This distribution takes the form:

$$P(J|E) = \frac{J + 1/2}{\sigma^2} \exp\left\{ -\frac{(J + 1/2)^2}{2\sigma^2} \right\} \quad (2.7)$$

where σ^2 is the spin cutoff parameter.

The basic form of the spin cutoff parameter σ^2 is:

$$\sigma^2 = \langle m^2 \rangle > \frac{6}{\pi^2} aT \quad (2.8)$$

where T is the temperature, a is the level density parameter and $\langle m^2 \rangle$ is the average squared spin projection.

To calculate the spin cutoff parameter FIFRELIN uses a semi-classical approximation, which accounts for the moment of inertia of a spherical rigid body (\mathcal{I}_{rig}) in a Fermi gas model approach:

$$\sigma_F^2 = \mathcal{I}_{rig}T = \mathcal{I}_{rig}\sqrt{\frac{U}{a}} \quad (2.9)$$

where U is the effective excitation energy function $U = E - \Delta$. Δ is the pairing energy (pairing correction). The value σ^2/T changes under influence of shell effects. This has been proved both with the phenomenological [MD98] and microscopic approach [Gor96]. Under this condition Equation 2.9 can be reformulated:

$$\sigma_F^2 = \mathcal{I}_{rig}\frac{a}{\tilde{a}}\sqrt{\frac{U}{a}} \quad (2.10)$$

with the rigid spheroid moment of inertia defined as:

$$\mathcal{I}_{rig} = \frac{2}{5}AMR^2(1 + 0.31\beta_2 + 0.44\beta_2^2 + \dots) \quad (2.11)$$

where A , M , R , β^2 and \tilde{a} are the mass number, the nucleon mass, the nuclear radius ($R = 1.2A^{1/3} fm$), the quadrupole deformation parameter of the nucleus in its ground state and the asymptotic level density parameter.

This modifies Equation 2.10, giving it the form:

$$\sigma_F^2 = 0.01389\frac{A^{5/3}}{\tilde{a}}\sqrt{aU} \quad (2.12)$$

Due to insufficiently known characteristics of the primary fission fragments, the energy (temperature) dependent spin cutoff parameter calculated from Equation 2.12 was replaced by other models: a CONSTANT model ($\bar{\sigma}$), a linearly mass dependent model ($\sigma(A)$) or a rescaled, derived from Equation 2.12 BSFG model following RIPL-3 terminology [LS10; TLS16]. These models will be described later (Section 2.4) because some of them are strictly correlated with the nuclear realization used by FIFRELIN and the way it completes the nuclear level scheme, which needs to be defined beforehand (Section 2.3).

2.2.3 Excitation energy

The knowledge of the excitation energy is needed to perform the fission fragment de-excitation simulation. The basic form of the total excitation energy (TXE) equation at scission is:

$$TXE = E^{*,sc} + E^{def,sc} + E^{coll,sc} \quad (2.13)$$

where $E^{*,sc}$ is the intrinsic excitation energy, $E^{def,sc}$ is the deformation energy (difference between potential energies corresponding to the scission deformation and the ground state deformation) and $E^{coll,sc}$ is the excitation energy of collective modes (assumed to be rotational only in a first approximation). It is assumed that the total excitation energy is transformed into an intrinsic energy (E^*) and a collective rotational energy (E^{rot}) after full acceleration of the fission fragments (relaxation of the deformation energy). Afterwards, the total excitation energy can be derived separately for the light (L) and the heavy (H) fragments:

$$XE_L = E_L^* + E_L^{rot} \quad (2.14)$$

$$XE_H = E_H^* + E_H^{rot} \quad (2.15)$$

The total excitation energy takes the form:

$$TXE = E_L^* + E_H^* + E_L^{rot} + E_H^{rot} \quad (2.16)$$

According to [GTR07], the rotational energy is not drained from the intrinsic excitation energy available at scission because it exists due to angular momentum bearing collective modes like bending and wriggling. A rotating liquid drop approximation was used to express the rotational energy:

$$E^{rot} = \frac{\hbar^2 J(J+1)}{2\mathcal{I}} \quad (2.17)$$

where J is the total angular momentum and \mathcal{I} is the moment of inertia of the nucleus, which in FIFRELIN is replaced by the rigid spheroid moment of inertia (\mathcal{I}_{rig}) (Equation 2.11) modified by the parameter k_{rig} , which is a free parameter of FIFRELIN.

If we relate the rotational energy to the neutron/gamma de-excitation cascade, we will see that E^{rot} corresponds to the Yrast band (Figure 2.2), which is spin dependent. By adding the neutron separation energy S_n , we can determine a spin dependent energy (E_{lim}^*) which is the minimal excitation energy that the fission fragment needs to evaporate a neutron:

$$E_{lim}^* = S_n + E^{rot} \quad (2.18)$$

We can relate that to the probability of neutron emission during the de-excitation process. Any spin reduction will decrease the rotational energy (Equation 2.17) which will lower the limit energy (Equation 2.18). If the excitation energy stays the same,

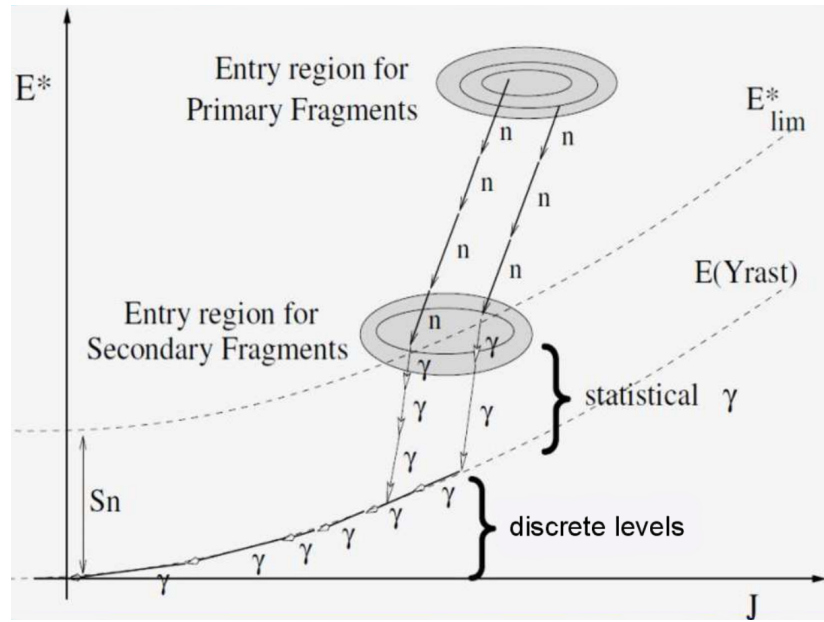


Figure 2.2: The de-excitation scheme in $[E^*, J]$ representation [LS10; Lit+17].

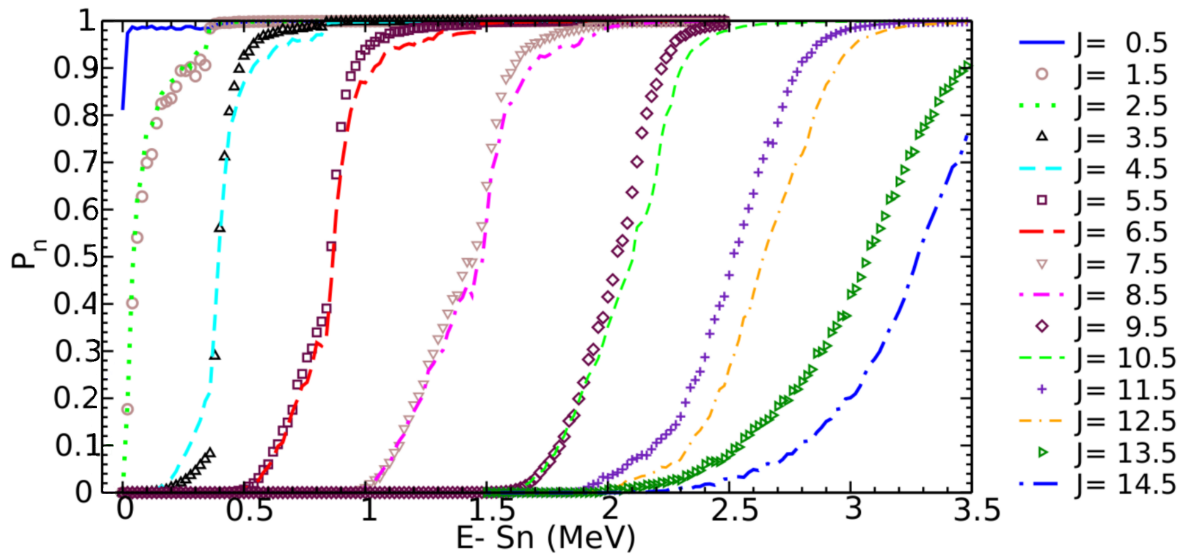


Figure 2.3: Neutron emission probability as a function of energy E and angular momentum J of ^{144}Ba [Reg13].

the neutron emission probability will increase. This behavior is presented in Figure 2.3.

FIFRELIN uses the kinetic energies of the fragments (taken from experimental data

as explained in Section 2.2.1) to calculate the total excitation energy:

$$TXE = Q - TKE + E_n + B_n \quad (2.19)$$

where Q , TKE , E_n and B_n are the energy released during the fission process, the total kinetic energy, the incident neutron energy and the neutron binding energy, respectively. The released energy is figured out from the Atomic Mass Evaluation AME2003 [AW95; WAT03] or AME2012 [Aud+12; Wan+12].

In order to calculate the intrinsic excitation energy E^* (equal to $TXE - E^{rot}$), Fifrelin uses the Fermi gas hypothesis:

$$E^* = aT^2 \quad (2.20)$$

where a and T are the level density parameter and the nuclear temperature. The fragment excitation energy is derived from an iterative process. The energy dependent level density parameter follows the Ignatyuk prescription [IST75; IGS79]:

$$a(E^*) = \tilde{a} \left\{ 1 + \frac{\delta W}{U^*} (1 - e^{-\gamma U^*}) \right\} \quad (2.21)$$

where \tilde{a} , δW , γ and U^* are the asymptotic level density parameter, the shell corrections, the damping factor and the effective excitation energy function ($U^* = E^* - \Delta$), respectively. The Megoni-Nakajima shell corrections are used. They allow a better description of the prompt fission neutron spectrum [SLC17]. δW is estimated from the difference between the measured and the calculated mass excess. Δ is the pairing correction:

$$\Delta = \chi \frac{12}{\sqrt{A}} \text{ [MeV]} \quad (2.22)$$

It uses the parity index χ equal to 0, 1 or 2 for odd-odd, even-odd or even-even nuclei, respectively.

A mass dependent temperature ratio law is then stated. It assumes a close coupling between the temperatures of both fission fragments:

$$R_T(A) = \frac{T_L}{T_H} \quad (2.23)$$

This law is based on the shell closure in the doubly spherical nuclei and it determines two linear functions presented in Figure 2.4. There are three main points defined by the temperature limits. The first one, R_T^{max} corresponds to the minimal temperature

of the heavy fission fragment associated with the minimum of the deformation energy (minimum in the excitation energy). This condition is fulfilled for the doubly closed spherical nucleus ^{132}Sn ($Z=50$, $N=82$). The second one, R_T^{\min} corresponds to the minimal temperature of the light fission fragment, which is the case for the doubly closed spherical shell nucleus ^{78}Ni ($Z=28$, $N=50$). The last point relates to symmetric fission where both fragments are identical and have the same temperature. R_T^{\max} and R_T^{\min} are free parameters of FIFRELIN.

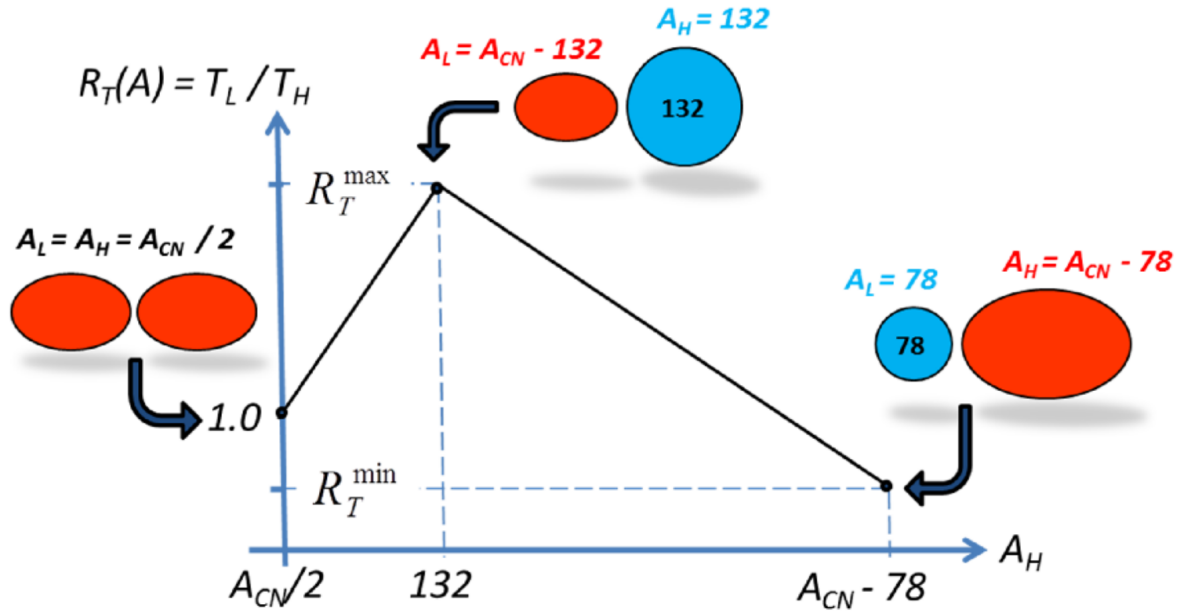


Figure 2.4: Temperature ratio law $R_T(A)$. The deformation of the fission fragments is briefly presented by the pictographs above the boundary points [Lit+17].

The iterative calculation of the complementary fission fragment excitation energies is based on the ratio law and already determined quantities:

$$\begin{cases} E_L^* = \frac{TXE - E^{rot}}{1 + \frac{a_H}{a_L R_T^2}} \\ E_H^* = \frac{TXE - E^{rot}}{1 + \frac{a_L R_T^2}{a_H}} \end{cases} \quad (2.24)$$

The intrinsic excitation energies are determined and used to calculate the total angular momentum. Its value is compared with the already determined total angular momentum, see Section 2.2.2. The intrinsic excitation energies are changed so that both total angular momentum values are close. This process is repeated until the intrinsic excitation energies meet the convergence criterion.

Afterwards, the total excitation energy is simply calculated from Equation 2.16. All the characteristics of the fission fragments (A , Z , KE , E^* , E^{rot} , J , π) are known and the simulation of the de-excitation process can begin.

2.3 De-excitation process

2.3.1 Nuclear realization

FIFRELIN uses the Hauser-Feshbach formalism to simulate the de-excitation process which is implemented using the notion of Nuclear Realization [Bec98]. A nuclear realization corresponds both to the complete level scheme (E , J , π values for every level) and the associated gamma partial widths (for every possible transition) for one nucleus. In FIFRELIN, this notion was extended to the case where several nuclei are involved in the decay chain [RLS16].

If the complete level scheme (the true nuclear realization) is known for all the fission fragments, the simulation would consist in a Monte Carlo de-excitation of the nuclei by the evaporation of neutrons and emission of gamma-rays.

However, the true nuclear realization is of course unknown. Most of the level schemes of the fragments are incomplete and anyway, no nuclear structure model is really able to reproduce correctly the properties of the nuclear states at high energy. In order to cope with that problem, a solution is to generate a large number of (virtual) nuclear realizations and then, to simulate the de-excitation cascade for each of them. The nuclear realization thus consists in the existing information on the nucleus added to a set of virtual levels produced accordingly to the level density (Section 2.5).

In practice, FIFRELIN records all the particles (neutrons or γ -rays) with their energies as well as all the nuclear states that are populated, until the fragments reach their ground state or a metastable state. The uncertainty of any observable can be linked to 1) the statistics of events 2) the lack of knowledge in the nuclear structure.

Since the nuclear realization has a statistical nature, the expectation value fluctuates from one realization to another. If the number of realizations is high enough, the mean value of an observable will be stable.

In order to illustrate that fact, I performed 7 simulations. Each simulation uses exactly the same models, the same free parameters, the same number of nuclear realizations (10^3) and the same number of events (10^3) per realization. The only difference

was the random seed value. I looked for the gamma-ray cascade emitted by ^{100}Zr and I extracted the number of times some particular γ -rays were emitted. Here, I chose the transitions in the ground state band of this element (Figure 5.2).

Table 2.1 shows the results. One observes that each simulation yields a very similar result. Moreover, the standard deviation of the seven simulation outputs is lower than the statistical uncertainty (\sqrt{N}). Here I concluded that: 1) the number of realizations and the number of events per realization I selected was sufficient to obtain a stable result 2) the statistical uncertainty (\sqrt{N}) is a good estimator of the simulation uncertainty.

The true nuclear realization is unknown. Even if the true realization occurs in the set of generated realizations, it is impossible to prove that the mean value of an observable (averaged over the set of realization) will converge to the output of the true realization. We can only assure that the mean value given by the simulation will be stable.

Energy [keV]	N1	N2	N3	N4	N5	N6	N7	mean	std	$\sqrt{\text{mean}}$
212.5	16148	16306	16117	16353	16354	16349	16182	16258	97	128
352.0	11237	11352	11203	11472	11442	11417	11324	11350	95	107
497.1	6268	6258	6111	6330	6371	6445	6352	6305	99	79
1082.3	629	631	693	657	644	702	663	660	27	26
1228.9	288	306	270	274	301	290	316	292	16	17
625.5	2074	2128	2130	2157	2078	2229	2007	2115	65	46
118.5	567	491	479	544	508	490	478	508	32	23

Table 2.1: Simulated numbers of γ -rays emitted by ^{100}Zr at the selected energies. Each simulation used a different random seed value thus different set of the nuclear realizations. Transition energies were taken from RIPL-3 database.

2.3.2 Competition between neutron and γ -ray emission

In FIFRELIN, the nuclear level scheme is divided in three energy regions (Figure 2.5). At low energy, the experimental level scheme is taken from RIPL-3 database [Cap+09; VC15]. More exactly, FIFRELIN takes the following data: level energy, spin and parity, γ -ray intensities between levels, level half-lives, conversion electron coefficients

and nature of the levels (β^- , β^-n , etc.). The first region is limited by a cutoff energy $E_{cutoff}^{RIPPL-3}$ where all the energies, spins and parities of the excited states are known. In this region, the experimental data determines the cascade till the ground state or an isomeric state.

The half-life is used to decide if a transition appears. If the cumulative time of emission is longer than the selected time-window (T_{max}), the transition is not counted.

The second region is set between $E_{cutoff}^{RIPPL-3}$ and an upper energy limit E_{bin} which corresponds to a threshold in the level density ($\sim 10^5$ MeV $^{-1}$). There are only few experimental levels in this energy range (the level scheme is incomplete). This information together with additional transitions, like the partial radiation widths (from photon strength functions (Section 2.6)) and supplementary nuclear states are determined from level density models (Section 2.5). The level scheme is completed according to them.

The third energy region is placed entirely above the upper energy limit. In this area, the excited states are no longer separated, they are treated as a continuum. The nuclear level scheme is described by average values which are calculated from the level density models. The levels are averaged over 10 keV bins (the value is modifiable by the user).

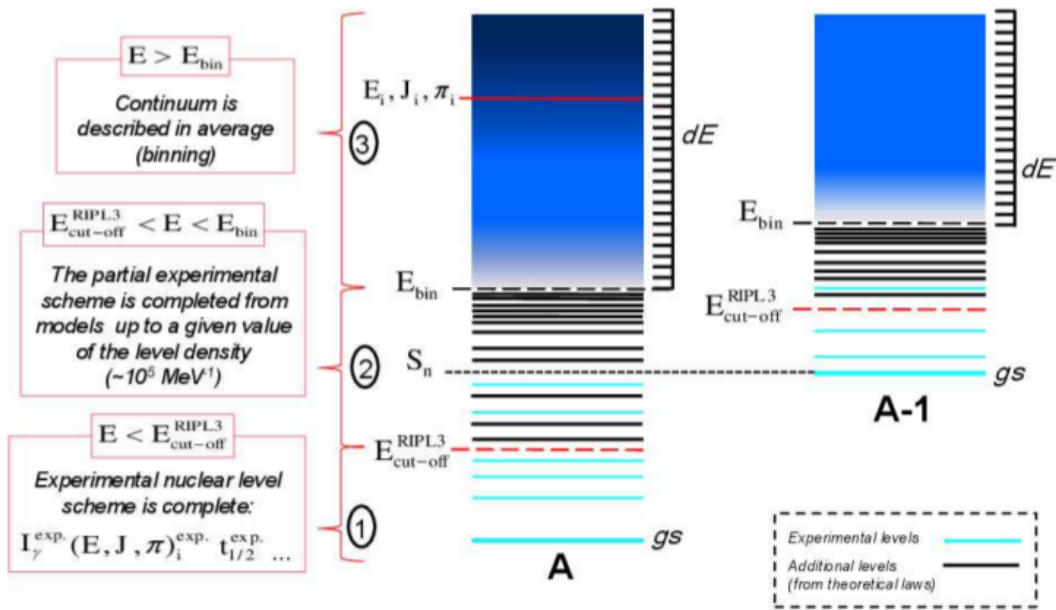
A competition between the emission of neutrons and γ -rays is considered from the beginning of the cascade. In coupled mode, the description of the transition zone between neutrons and γ -ray emission (in energy-spin-parity coordinates) assumes that it is possible to emit a γ -ray before the last neutron. In principle a γ -ray can be emitted at any excitation energy but the probability of such events starts to be relevant only very close to the E_{lim}^* (Section 2.2.3).

The ECIS code [Ray94] using various optical model potentials (Section 2.7) is responsible for calculating neutron transmission coefficients. They are tabulated and stored in a FIFRELIN-readable library. Average partial widths for γ -ray (Γ_γ) and neutron (Γ_n) emissions are estimated from neutron transmission coefficients $T_{l,j}$ and photon strength functions f_{XL} :

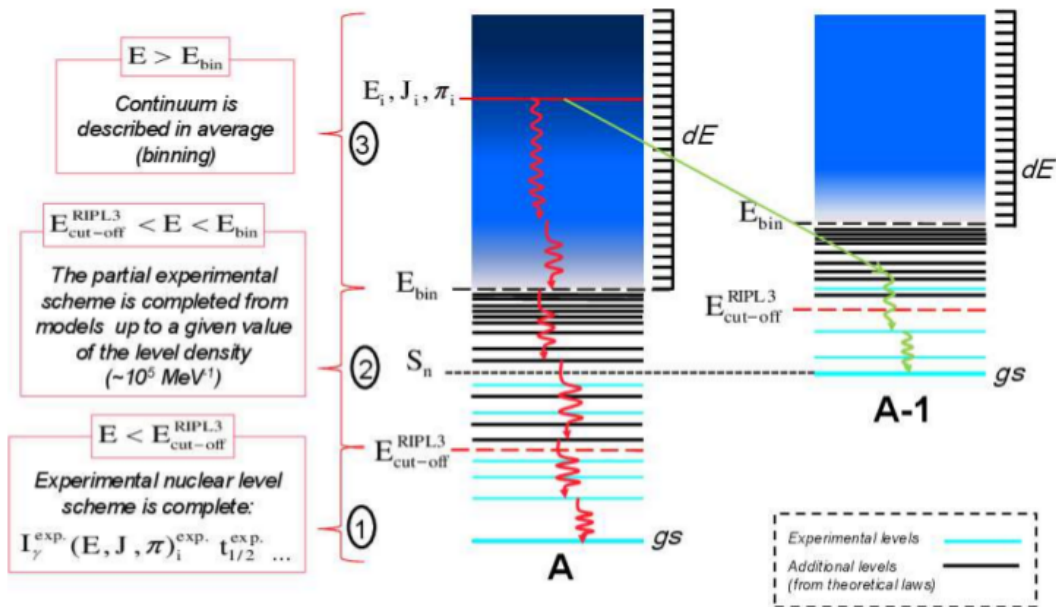
$$\langle \Gamma_\gamma(\epsilon_\gamma, XL) \rangle = \frac{f_{XL}(\epsilon_\gamma) \epsilon_\gamma^{2L+1}}{\rho(E_i, J_i, \pi_i)} \quad (2.25)$$

$$\langle \Gamma_n(\epsilon_n, l, j) \rangle = \frac{T_{l,j}(\epsilon_n)}{2\pi\rho(E_i, J_i, \pi_i)} \quad (2.26)$$

where n denotes neutron and γ denotes γ -ray, ϵ_γ and ϵ_n are the energies of γ -ray and



(a) Nuclear level scheme.



(b) Cascades.

Figure 2.5: Neutron/ γ -ray cascade simulated in FIFRELIN with the coupled approach. (a) shows three regions of the excitation energy with limits. (b) presents two different de-excitation paths: realized only by γ -rays (red) and with additional neutron emission (green) [Lit+17].

neutron, XL denotes multipole character, l and j are quantum numbers associated with the orbital angular momentum and total angular momentum of a neutron and ρ is the level density at the energy E , spin J and parity π . In order to apply Equations 2.25 and 2.26 ρ , $T_{l,j}$ and f_{XL} need to be described. In FIFRELIN, appropriate models are used to do that. They will be described later in this work (level density models - Section 2.5, neutron transmission coefficients - Section 2.7 and photon strength functions Section 2.6). The probability of a particle emission from an initial excited state i is:

$$P_{n,\gamma}([E, J, \pi]_i) = \frac{\Gamma_{n,\gamma}^{tot}([E, J, \pi]_i)}{\Gamma_{\gamma}^{tot}([E, J, \pi]_i) + \Gamma_n^{tot}([E, J, \pi]_i)} \quad (2.27)$$

When the total partial width for neutron and γ -ray emission is equal to the sum of all partial widths (Equations 2.25 and 2.26) over all transitions:

$$\bar{\Gamma}_p^{tot}([E, J, \pi]_i) = \sum_{[E,J,\pi]_{f,\alpha}} \Gamma_p([EJ\pi]_i \rightarrow [EJ\pi]_{f,\alpha}) \quad (2.28)$$

where $p = n, \gamma$ denotes neutron (n) or γ -ray (γ) emission and $\alpha = XL; l, j$. In FIFRELIN, the probabilities of emitting n or γ are calculated by accounting for conservation of energy, spin and parity between initial (i) and final (f) states.

2.4 Spin cutoff models

FIFRELIN uses the spin cutoff models to complete the insufficiently known characteristics (spin and parity) of the primary fission fragments.

2.4.1 CONSTANT model

For the CONSTANT model the calculation of spin involves two constant average spin cutoff parameters $\bar{\sigma}_L^2$ and $\bar{\sigma}_H^2$, for the light and heavy fission fragment groups, respectively. When this model is used, these are two free parameters of the FIFRELIN simulation. The influence of the spin cutoff parameter on the spin distribution is presented in Figure 2.6.

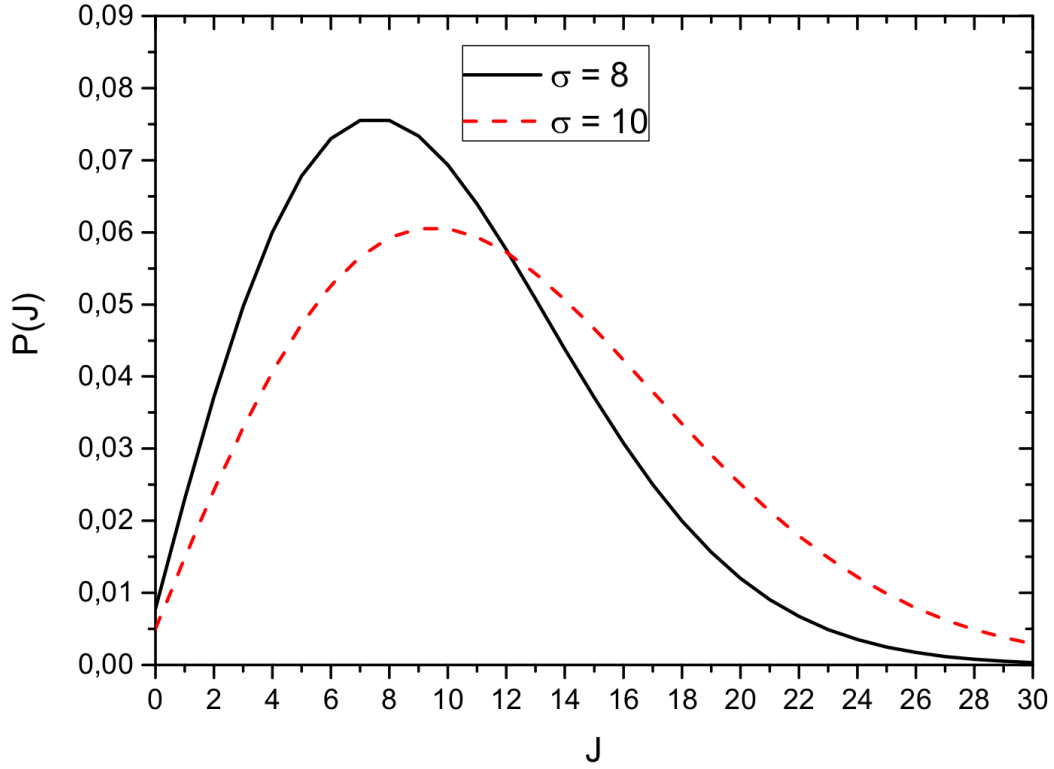


Figure 2.6: Spin distributions dependence on the spin cutoff value [Lit+17].

In this model the entry states of the initial fission fragment are distributed around the average initial spin and the average initial excitation energy values (Figure 5.18, in Section 5.4.2). The spin comes from sampling the distribution described by Equation 2.7 when the fixed spin cutoff value is used. This means that in this model the spin distribution is not excitation energy dependent.

2.4.2 BSFG model

In the Back-Shifted Fermi Gas (BSFG) spin cutoff model the two free parameters $\bar{\sigma}_L^2$ and $\bar{\sigma}_H^2$ are replaced by one free parameter called the scaling factor (f_σ). This parameter modifies the energy dependent spin cutoff parameter used to calculate the initial spin. It has different behaviors in different energy regions:

$$\sigma_{BSFG}^2(E) = \begin{cases} \sigma_d^2 & \text{for } E < E_d \\ \sigma_d^2 + \frac{E-E_d}{S_n-E_d} \left(f_\sigma^2 \cdot \sigma_F^2(S_n) - \sigma_d^2 \right) & \text{for } E_d \leq E < S_n \\ f_\sigma^2 \cdot \sigma_F^2(E) & \text{for } S_n \leq E \end{cases} \quad (2.29)$$

where σ_d^2 is the spin cutoff parameter following the RIPL-3 recommendation, in the energy region (up to E_d) where all discrete nuclear states are known. E_d is the energy equal to the average between E_{low} and E_{up} (where the level scheme is fully known) present in the RIPL-3 database. FIFRELIN also uses numbers of levels N_{low} and N_{up} , which correspond to the mentioned energies. Between E_d and the neutron separation energy (S_n) a linear interpolation is used. Above S_n the spin cutoff parameter (σ_F^2) in the Fermi gas model approach (Equation 2.12) is applied. The spin cutoff parameter (σ_d^2) for the discrete part is:

$$\sigma_d^2 = \frac{1}{\sum_{i=N_{low}}^{N_{up}} (2J_i + 1)} \sum_{i=N_{low}}^{N_{up}} J_i(J_i + 1)(2J_i + 1) \quad (2.30)$$

where J_i is the spin of discrete level i . The difference in generated spins between CONSTANT and BSFG models can be seen in Figure 2.7.

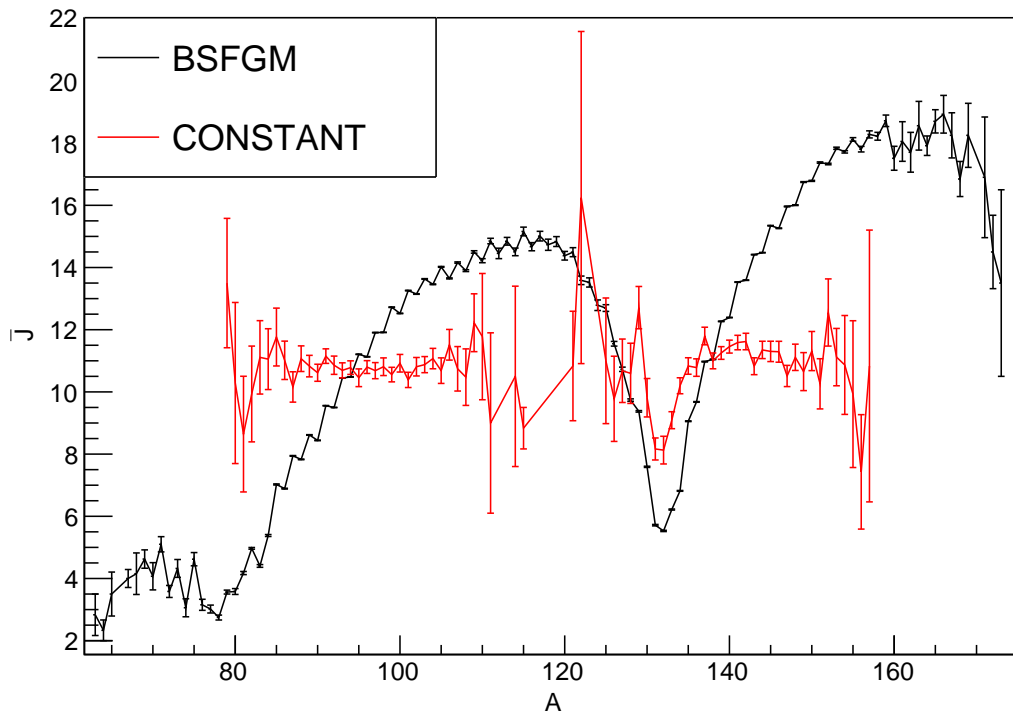


Figure 2.7: Average spin \bar{J} as a function of the fission fragment mass A using the BSFGM or the CONSTANT spin cutoff models.

2.5 Level density

The experimental nuclear level scheme is not fully known. To complete it FIFRELIN utilizes level density models, photon strength functions and neutron transmission coefficients. The level density models are related to the energy, spin and parity dependent level density thus the general level density equation takes the form:

$$\rho(E, J^\pi) = \rho(E)P(J|E)P(\pi|E) \quad (2.31)$$

Both positive and negative parities are equally likely in a first approximation. The most important term is the spin distribution. When the level scheme is unknown or partially incomplete (missing spin and/or parity) this term is used to sample the spin of unknown nuclear levels. It is the most complicated task at the beginning of the de-excitation process where fission fragments have their initial states. There is no experimental data or a theoretical model to determine the spin in this region. Spin is still sampled from Equation 2.7 and the particular form (recommended in RIPL-3) of the Back-Shifted Fermi Gas (BSFG) model is used by default in FIFRELIN to determine the spin cutoff parameter involved in the level density calculation:

$$\sigma^2(E) = \begin{cases} \sigma_d^2 & \text{for } E < E_d \\ \sigma_d^2 + \frac{E-E_d}{S_n-E_d}(\sigma_F^2(S_n) - \sigma_d^2) & \text{for } E_d \leq E < S_n \\ \sigma_F^2(E) & \text{for } S_n \leq E \end{cases} \quad (2.32)$$

where σ_d^2 and σ_F^2 are the spin cutoff parameters described by Equation 2.30 and 2.12, respectively. E_d , E_{low} , E_{up} are the energies and N_{low} , N_{up} are corresponding numbers of levels, all present in the RIPL-3 database. S_n is the neutron separation energy. The formulation of the spin from Equation 2.32 is described in previous Section 2.4 in the paragraph about BSFG.

The spin in level density models is sampled from Equation 2.7, the same as the initial spin (Section 2.2.2) and the spin cutoff parameter is calculated from the BSFG-like spin cutoff model (Equation 2.32). So, when the BSFG spin cutoff model with f_σ close to 1 is used to determine the initial spin, the entry state of the primary fission fragment will be close to the mean value of the level density thus close to the most probable excited states.

The total level density $\rho(E)$ corresponds to the total number of levels per MeV in

vicinity of energy E :

$$\rho(E) = \sum_J \sum_{\pi} \rho(E, J^{\pi}) \quad (2.33)$$

2.5.1 Constant temperature model

An exponential law can describe the energy dependence of a cumulative number of low-lying nuclear levels:

$$N(E) = \exp\left(\frac{E - E_0}{T}\right) \quad (2.34)$$

where $N(E)$ is the number of levels up to an energy E . The parameters E_0 and T are adjusted on experimental data. The number of levels in the energy bin $[E, E + \Delta E]$ defines the level density ρ at energy E :

$$\rho(E) = \frac{N(E + \Delta E) - N(E)}{\Delta E} \xrightarrow{\Delta E \rightarrow 0} \frac{dN}{dE} \quad (2.35)$$

For the Constant Temperature Model (CTM) it takes the form:

$$\rho_{CTM}(E) = \frac{1}{T} \exp\left(\frac{E - E_0}{T}\right) \quad (2.36)$$

It refers to the so-called constant temperature formula included in CTM. This model is based on the assumption that the temperature T is constant over the whole energy range. CTM is also adopted at the low excitation energy range when the Gilbert-Cameron model 2.5.3 is used.

CTM is adjusted on experimental data and needs to reproduce them in the restricted energy range E_{low}, E_{up} . In this region the energies of excited states are known. E_{low} and E_{up} (where the level scheme is fully known) as well as the related number of excited states (N_{low} and N_{up}) are provided by the RIPL-3 database. Figure 2.8 shows the energy limits and how much different is the level density generated with CTM in comparison to the experimental one for the ^{239}U compound nucleus.

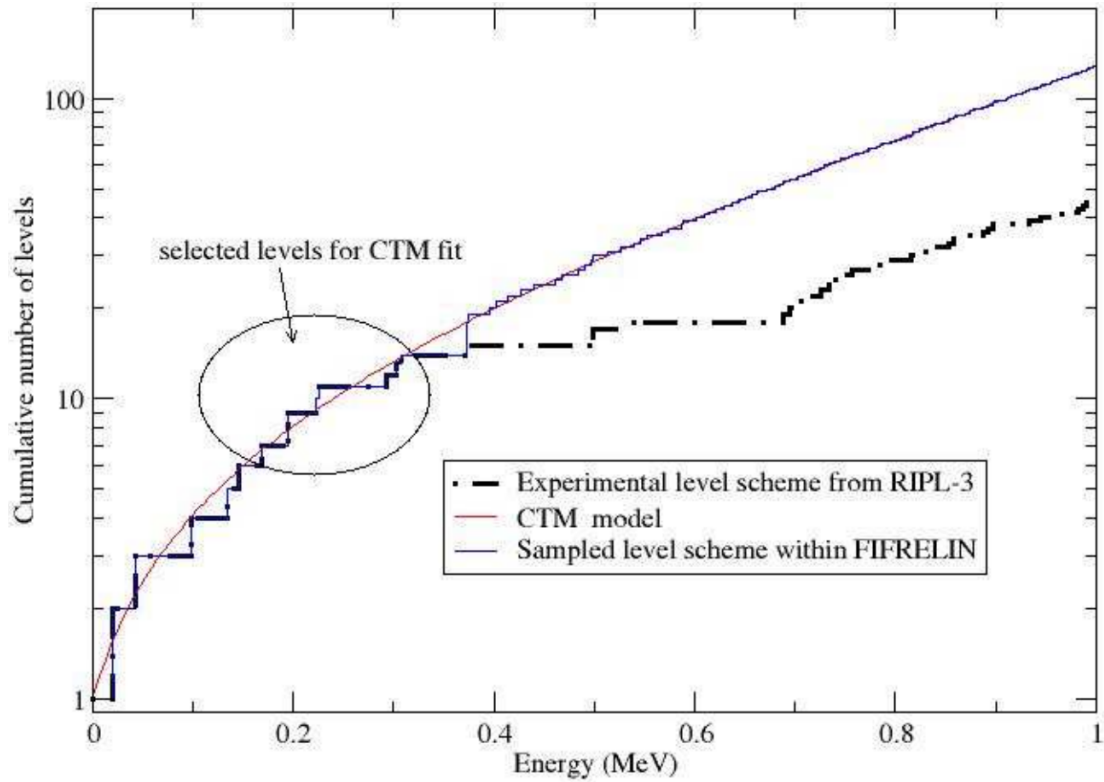


Figure 2.8: Cumulative number of levels for the ^{239}U compound nucleus. CTM is used to reproduce the known part of the nuclear level scheme (experimental level scheme). The final level scheme sampled by FIFRELIN combines the experimental level scheme at low energy with the theoretical level scheme coming from models at high energy. In the presented figure, the CTM spin cutoff model was used in the whole energy range for the FIFRELIN simulation [Lit+17].

2.5.2 Fermi gas model

Within the Fermi gas model, the level density equation takes the form:

$$\rho_F(E) = \frac{\sqrt{\pi}}{12} \frac{1}{\sqrt{2\pi\sigma}} \frac{\exp(2\sqrt{aU})}{a^{1/4}U^{5/4}} \quad (2.37)$$

where a , σ and U are the level density parameter, the spin cutoff parameter and the effective excitation energy.

2.5.3 Composite Gilbert-Cameron model

Gilbert and Cameron [GC56] proposed to combine the low-energy region description by CTM (Equation 2.36) with the energy dependence predicted by the Fermi gas model in the high-energy region:

$$\rho_{CGCM}(E) = \begin{cases} \rho_{CTM}(E) & \text{for } E < E_M \\ \rho_F(E) & \text{for } E \geq E_M \end{cases} \quad (2.38)$$

where E_M is the matching energy. In FIFRELIN, the Gilbert-Cameron model uses the level density parameter $a(E)$ which follows the Ignatyuk's prescription 2.21 [IST75; IGS79]. Such solution was proposed in RIPL-3 [Cap+09].

The differences of level densities for even-even, odd-even and odd-odd are taken into account by the effective excitation energy ($U = E - \Delta$). The pairing shift based on the average pairing shift $\frac{12}{\sqrt{A}}$ is:

$$\Delta = n \frac{12}{\sqrt{A}} \quad (2.39)$$

where n is equal to 0, 1 and 2 for odd-odd, odd-A and even-even nuclei, respectively.

The most important parameter which links CTM with the Fermi gas model is the matching energy E_M . It is found by imposing continuity of the level density function and its first derivative:

$$E_0 = E_M - T \ln(T \rho_F(E_M)) \quad (2.40)$$

$$T^{-1} = \left. \frac{\partial \rho_F(E)}{\partial E} \right|_{E=E_M} \quad (2.41)$$

Another condition is based on the evaluated level scheme from the RIPL-3 database. In the restricted energy range where the level scheme is fully known [E_{low}, E_{up}], the nuclear levels predicted by the constant temperature model must be coherent with the experimental discrete levels from RIPL-3. This condition is written:

$$N_{up} = N_{low} + \int_{E_{low}}^{E_{up}} \rho_{CTM}(E) dE \quad (2.42)$$

after inserting Equation 2.36 it takes the form:

$$N_{up} = N_{low} + \left[\exp\left(\frac{E_{up} - E_0}{T}\right) - \exp\left(\frac{E_{low} - E_0}{T}\right) \right] \quad (2.43)$$

Then thanks to the combination of Equations 2.40, 2.41 and 2.43 the T , E_0 and E_M can be determined. Finally:

$$N_{up} = N_{low} + T\rho_F E_M \left[\exp\left(\frac{E_{up} - E_M}{T}\right) - \exp\left(\frac{E_{low} - E_M}{T}\right) \right] \quad (2.44)$$

from which E_M can be solved iteratively. In FIFRELIN a bisection method is used to calculate it [Reg13].

2.5.4 Hartree-Fock-Bogoliubov

The level scheme is composed of the known (experimental) excited states and the virtual excited states. The microscopic approach allows one to quickly access this information thus also the level densities, which can be tabulated over the excitation energy grid up to 50 MeV. 50 first values of the spin and parity dependent level density (for both positive and negative parities) can be also tabulated by using the spin grid. The Hartree-Fock-Bogoliubov and combinatorial level densities [GHK08] are calculated, tabulated and available in the RIPL-3 database. This calculation uses the single-particle level scheme and the tuned pairing interaction at the ground state deformation based on the effective interaction of Skyrme (BSk14) [GSP07].

2.6 Photon strength functions

2.6.1 Introduction

To fully describe photon strength functions, first we need to study the relation between the photo-absorption cross-section and photon radiation widths. The average absorption cross section for any multipole excitation in the continuum region (level density above 10^5 MeV⁻¹) is strongly influenced by the giant dipole resonances (GDR): E1, M1 and E2 [Lon85]. The photon capture cross-section for an isolated resonance synthesized with the Breit and Wigner formula [Reg13]:

$$\bar{\sigma}_{XL}(\epsilon_\gamma) = \frac{2\pi}{k^2} \left(\frac{2J_e + 1}{2J_{GS} + 1} \right) \frac{\Gamma_0}{\Gamma_\gamma^{tot}} \frac{1}{[2(\epsilon_\gamma - E_R)/\Gamma_\gamma^{tot}]^2 + 1} \quad (2.45)$$

where $\epsilon_\gamma = \hbar ck$ is the energy of the absorbed photon (\hbar is the reduced Planck constant, c is the speed of light and k is the wavenumber), J_e and J_{GS} are the total angular momenta of the excited state and the ground state (GS), Γ_γ^{tot} is the total γ -width of

the excited state, Γ_0 is the partial width associated with the de-excitation till the GS by a γ -ray and E_R is the appropriate resonance energy. XL denotes the multipole character.

The additional assumptions made by P. Axel [Axe62] allow him to determine an energy integral of the photon capture cross-section for an isolated resonance. He concluded that the total photo-absorption cross-section XL (no matter towards which excited state) can be expressed by the approximation equal to the sum of all the cross-sections of the excited states heading towards this level [Reg13]. The new relation established by Lone [Lon85] was built based on this assumption:

$$\bar{\sigma}_{XL}(\epsilon_\gamma) = (\pi\hbar c)^2 \sum_{J_e \text{ possible with } XL} \frac{\rho(E = \epsilon_\gamma, J_e, \pi_e) \bar{\Gamma}_\gamma(XL, J_e)}{\epsilon_\gamma^2} \left(\frac{2J_e + 1}{2J_{GS} + 1} \right) \quad (2.46)$$

where $\bar{\Gamma}_\gamma(XL, J_e)$ is an average of the partial widths of the levels with the angular momentum J_e and excitation energy around ϵ_γ going to the GS. If one assumes that the fraction of the density by the γ -width is independent from the angular momentum J_e , and one uses selection rules, it can be written [Reg13] :

$$\bar{\Gamma}(XL, J_e) = \frac{1}{(\pi\hbar c)^2(2L + 1)} \frac{\epsilon_\gamma^2 \bar{\sigma}_{XL}(\epsilon_\gamma)}{\rho(\epsilon_\gamma, J_e, \pi_e)} \quad (2.47)$$

With the use of the experimental capture cross-section, through this equation, it is possible to determine the approximated partial widths decaying to the ground state [Reg13]. Nonetheless, to do that selection rules need to be applied:

$$\begin{aligned} |J_i - J_f| &\leq L \leq J_i + J_f \\ M_i &= M_f + M \end{aligned} \quad (2.48)$$

The second selection rule allows determining if the emitted radiation is of the electric or magnetic type. The photon transitions are none zero if:

$$\begin{aligned} \pi_i \pi_f &= (-1)^{L+1} \text{ for electrical transitions} \\ \pi_i \pi_f &= (-1)^L \text{ for magnetic transitions} \end{aligned} \quad (2.49)$$

To simulate the de-excitation cascade the partial radiation widths between the initial level and all other attainable levels (including the ground states) are needed [Reg13]. An estimation of the γ -emission between simulated levels is performed with the photon strength functions (PSF) or radiative strength functions (RSF). PSF are

differentiated according to their type (electric E or magnetic M) and multipolarity (L). In excited nuclei at high energy, the most important electromagnetic radiations are dipole-electric $E1$. All other transitions ($M1, E2, M3 \dots$) are defined in relation to $E1$ transition. If we generalize Equation 2.47 by replacing the ground state by all the excited levels f (final) reachable from the other excited levels i (initial), the strength function f_{XL} can be calculated from the relation:

$$f_{XL}(\epsilon_\gamma) = \frac{\rho(E_i, J_i, \pi_i) \bar{\Gamma}_{i \rightarrow f}^{XL}}{\epsilon_\gamma^{2L+1}} \quad (2.50)$$

where X , L and ϵ_γ are the type of transition, the multipolarity ($L = 1$ for dipole, $L = 2$ for quadrupole. . .) and the γ -transition energy, respectively.

To describe γ -ray transition rates FIFRELIN uses one of the models based on the Giant Dipole Resonance concept (GDR). GDR can be seen as collective dipole vibrations of proton and neutron fluids in the nucleus.

2.6.2 Standard Lorentzian model

One of the easiest cross-section to measure is the photo-absorption cross-section between the ground state and a considered level. A very important ingredient is the $E1$ photo-absorption cross-section. For a spherical nucleus it has a Lorentzian shape and forms Giant Dipole Resonances (GDR). They have been already observed in the 40's in the cross section of photo-nuclear reactions [GT48]. The GDR can be interpreted as dipole vibrations of proton and neutron fluids in the nucleus. Additionally, in Brink's hypothesis [Bri55] one can find that the giant resonances built on an excited state or on the ground state have the same shape (and intensity) because collective and intrinsic excitation energies are independent. Most of the experimental data related to GDR can be modeled by a strength function having a Lorentzian shape. It means that the absorption cross-section of a photon going to a particular excitation level has a Lorentzian shape with the same width and amplitude as the absorption cross-section of a photon going to the ground state.

To describe the $E1$ transition Brink and Axel [Axe62; Bri63] proposed the Standard Lorentzian (SLO) model:

$$f_{SLO}(\epsilon_\gamma) = \frac{1}{(2L+1)(\pi\hbar c)^2} \frac{1}{10} \sigma_r \Gamma_r \frac{\epsilon_\gamma \Gamma_r}{(\epsilon_\gamma^2 - E_r^2)^2 + \epsilon_\gamma^2 \Gamma_r^2} [MeV^{-3}] \quad (2.51)$$

where E_r , Γ_r , σ_r are GDR characteristics (position and width in MeV, and peak cross-section in mb). For $E1$ transitions ($L = 1$), the constant term has the form:

$$\frac{1}{3(\pi\hbar c)^2} \frac{1}{10} \sim 8.68 \cdot 10^{-8} [mb^{-1} MeV^{-2}] \quad (2.52)$$

where $\hbar c \sim 197 MeV fm$.

2.6.3 Enhanced Generalized Lorentzian model

The Enhanced Generalized Lorentzian (EGLO) model is an empiric model based on the Standard Lorentzian model. It was proposed by Kopecky, Uhl and Chrien [KU90; KUC93]. The strength function describing $E1$ transitions in this model is γ -ray energy and temperature dependent:

$$f^{EGLO}(\epsilon_\gamma, T) = \frac{1}{(2L+1)(\pi\hbar c)^2} \frac{1}{10} \sigma_r \Gamma_r \left[\frac{\epsilon_\gamma \Gamma(\epsilon_\gamma, T)}{(\epsilon_\gamma^2 - E_r^2)^2 + \epsilon_\gamma^2 \Gamma(\epsilon_\gamma, T)^2} + \frac{0.7\Gamma(0, T)}{E_r^3} \right] [MeV^{-3}] \quad (2.53)$$

with the width of the Lorentzian being energy and temperature dependent:

$$\Gamma(\epsilon_\gamma, T) = \frac{\Gamma_r}{E_r^2} \mathcal{K}(\epsilon_\gamma) (\epsilon_\gamma^2 + 4\pi^2 T^2) \quad (2.54)$$

with

$$\mathcal{K}(\epsilon_\gamma) = \left(k + (1-k) \frac{\epsilon_\gamma - 4.5}{E_r - 4.5} \right) \quad (2.55)$$

and

$$k = \begin{cases} 1 & \text{for } A < 148 \\ 1 + 0.09(A - 148)^2 \exp(-0.18(A - 148)) & \text{for } A \geq 148 \end{cases} \quad (2.56)$$

For non-spherical (deformed) nuclei the γ -absorption cross-section does not have the form of a simple Lorentzian. In axially deformed nuclei the cross-section should be considered as a sum of two Lorentzians with independent parameters.

FIFRELIN also gives an option to use the pre-tabulated strength function values obtained from a microscopic approach like Quasi particle Random Phase Approximation (QRPA) with a Hartree-Fock + Bradeen-Cooper-Schrieffer model (HF+BCS) or Hartree-Fock-Bogoliubov equations (HFB) [GK02; GKS04]. The behavior of EGLO in comparison to the models based on the microscopic approach (QRPA+HF+BCS) or (QRPA+HFB) is presented in Figure 2.9.

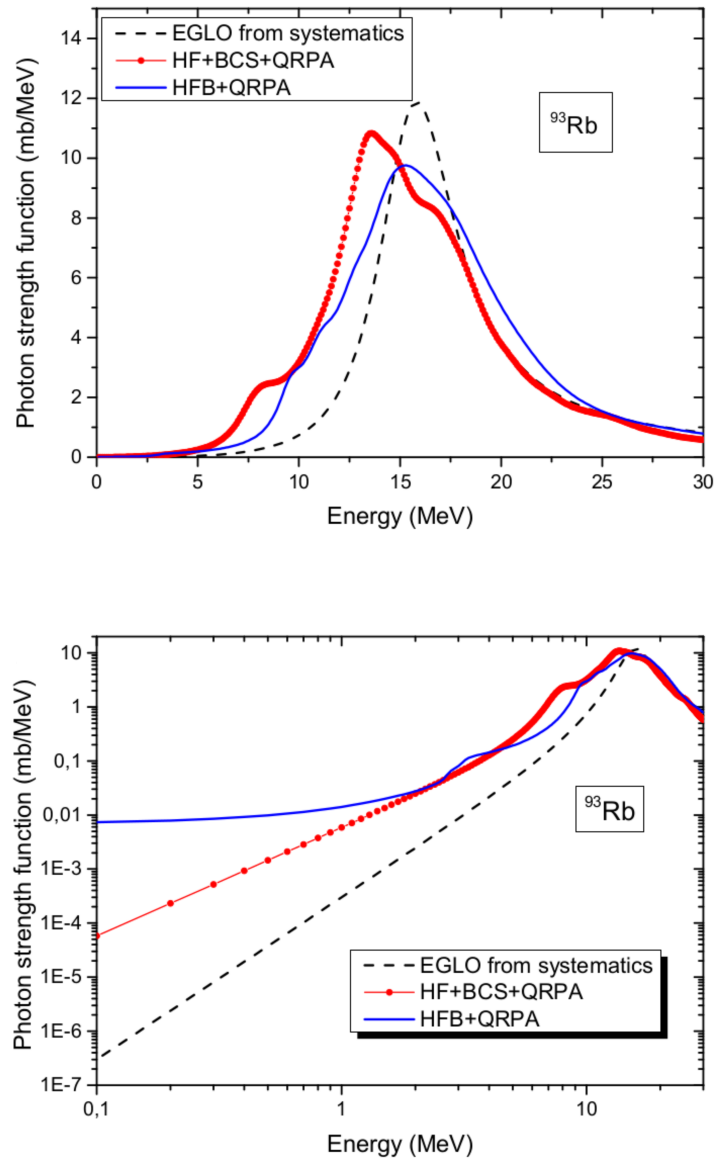


Figure 2.9: Photon strength functions of ^{93}Rb calculated with different models: EGLO, QRPA with Hartree-Fock+Bardeen-Cooper-Schrieffer (HF+BCS+QRPA) and QRPA with Hartree-Fock-Bogoliubov (HFB+QRPA). The upper plot is a linear-linear representation. The lower plot is a log-log representation more adapted to see the differences between the models in the energy range involved in fission [Lit+17].

2.7 Neutron transmission coefficients

During the de-excitation process of the fission fragments, most of the excitation energy is removed by prompt-neutrons emission. To simulate this part of de-excitation (Equation 2.26) we need to know neutron transmission coefficients. They are calculated with the ECIS [Ray94] or the TALYS codes [KHD08] using various optical model potentials such as Becchetti-Greenlees [BG69], Koning-Delaroche [KD03] or Jeukenne-Lejeunce-Mahaux [JLM74]. The neutron transmission coefficients are tabulated and stored in a library for 1000 points with an energy grid which varies from 1 eV to 20 MeV, around 600 nuclei and 20 values of the total angular momentum ($j = l \pm s$) and corresponding orbital angular momentum (l) and spin angular momentum (s) of a neutron. This library can be read and used by FIFRELIN during simulation performing.

2.8 Simulation with the FIFRELIN code

The FIFRELIN code can simulate the de-excitation of fission fragments created after fission ((n_{th}, f) or spontaneous fission) of a compound nucleus. Before starting the simulation process a selection of models and free parameters (R_T^{min} , R_T^{max} , $\bar{\sigma}_L^2$ and $\bar{\sigma}_H^2$ for the CONSTANT spin cutoff model or f_σ for the BSFG spin cutoff model) need to be chosen by the user. This information is provided to FIFRELIN in the form of an input file. Apart from it, at least two additional sets of data containing initial (pre-neutron emission) fission fragment mass and kinetic energy have to be supplied to FIFRELIN, see Section 2.2.1. Each simulation can provide many observables for a variety of fission fragments. For us the most important are the prompt-neutron multiplicities and the normalized prompt- γ transition intensities.

2.8.1 Elements selection

The basic information that needs to be provided to FIFRELIN is the nuclear mass (A_{CN}) and charge (Z_{CN}) of the compound nucleus. In our case, most of the results have been compared to the experimental data coming from the $^{235}\text{U}(n_{th}, f)$ fission (EXILL experiment) (Section 5.4.1). We simulated this fission process. We have also compared our experimental data to data on spontaneous fission of ^{252}Cf (Section 5.2.3). Therefore, we simulated this process as well with FIFRELIN.

Another option in FIFRELIN, is the capability to simulate the de-excitation of a given excited nucleus. The initial state of this fragment (spin and excitation energy) is then fixed. We used this option to study how the γ -ray intensity varies when different nuclear realizations are used in FIFRELIN.

2.8.2 Models and free parameters selection

The photon strength functions model (Section 2.6), the level density model (Section 2.5) and the spin cutoff model (Section 2.2.2) need to be defined for each FIFRELIN simulation. Each simulation primary goal is to correctly reproduce the average prompt-neutron multiplicities ($\bar{\nu}_L, \bar{\nu}_H, \bar{\nu}_{Tot}$). To fulfill this objective we need to adjust the free parameters values for each models setup.

Prompt-neutron multiplicity

The prompt-neutron multiplicity is the most important observable of a FIFRELIN simulation. We can distinguish the average multiplicity for the light ($\bar{\nu}_L$) and heavy ($\bar{\nu}_H$) fission fragment groups, and integrated over all ($\bar{\nu}_{Tot}$) fission fragments (total). $\bar{\nu}_L$ and $\bar{\nu}_H$ are known only for few fissioning systems and $\bar{\nu}_{Tot}$ is known for a bit more compound nuclei. We have done many simulations for $^{235}\text{U}(n_{th}, f)$. For this nucleus the average multiplicities are $\bar{\nu}_L=1.41$, $\bar{\nu}_H=1.01$ and $\bar{\nu}_{Tot}=2.42$ with uncertainties close to 1% [Nis+98; LSB15]. These are the values that we expected the FIFRELIN simulation to give. We verify the simulations by checking the discrepancies between experimental and simulated prompt-neutron multiplicities. The free parameters need to be optimized so that these discrepancies do not exceed 1% what is equal to the uncertainty of the experimental data. This condition is the default constraint for FIFRELIN simulations. It has been chosen by the code developers from the DEN/DER/SPRC/LEPH laboratory at CEA Cadarache because the multiplicities are ones of the few simulation observables which are also experimentally known with a good precision for the fissioning systems with uranium, plutonium, californium or curium. These four elements are important because they are often used in the nuclear fission studies and also due to the high content of the first two elements in the currently used or future nuclear fuel. Only if the condition of the prompt-neutron multiplicity discrepancies lower than 1% is fulfilled, analysis of such a simulation is continued.

Test simulations

Looking for a correct set of the free parameters is done with the support of so-called "test" simulations. A regular simulation which we make, has 10^6 events. We believe that this is a good combination between the statistics (low γ -ray intensity uncertainty) and the computation time. We observed that when the same models and free parameters are used (see Table 2.2), the difference between the prompt-neutron multiplicity values for 10^4 and for 10^6 is not significant (Table 2.3). This allows us to conduct so called "test" simulations with only 10^4 events. Their aim is to check if the prompt-neutron multiplicity values are correct for the particular set of free parameters and for a given model setup. Due to a much shorter computation time we are able to check many more combinations.

Model	Used model
Strength Function	EGLO
Level Density	CTM
Spin Cutoff	BSFG
Free parameter	Used value
R_T^{\min}	0.48
R_T^{\max}	1.35
f_σ	1.75

Table 2.2: Models and free parameters used to simulate $^{235}\text{U}(n_{th}, f)$.

Target observable	10^4 events	10^6 events	Experimental values
$\bar{\nu}_L$	1.414	1.417	1.41
$\bar{\nu}_H$	1.011	1.009	1.01
$\bar{\nu}_{Tot}$	2.426	2.426	2.42

Table 2.3: Dependence of the prompt-neutron multiplicity values on the number of simulated events. In both simulations, models and free parameters are the same, see Table 2.2. The discrepancy between the simulated and experimental multiplicities are less than 1% for both simulations.

2.8.3 Results comparison

After finding the free parameters that allow the simulation to fulfill the condition of the prompt-neutron multiplicity discrepancies lower than 1%, the complete (10^6 events) simulation is conducted. Then, we calculate the prompt γ -ray intensities and we compare them to experimental data coming from the EXILL experiment. We check how good the agreement between corresponding intensities is and also how well the

whole level scheme is reproduced. Depending on the statistics of the experimental data, most of the time, we were able to compare the intensities of the transitions coming from different bands including the ground state band, as well as the cross transitions between bands.

Chapter 3

EXILL experiment

3.1 Introduction

γ -spectroscopy is able to provide precise experimental data on the prompt γ -ray cascades in fission fragments. It can be used to understand the structure of the nuclei but it can help as well to study the fission process. The information we want to extract will be used to test (benchmark) the different models implemented in FIFRELIN.

An innovative experiment was conducted at the research reactor of the ILL. It produces a large amount of useful data on the de-excitation of the fission fragments. In this chapter, I will describe in detail the experiment and the various techniques that were performed to preprocess the raw data. Then I will explain the method we used in first instance to extract the cascade of γ -rays emitted by the fragments and the limits of this method.

3.2 EXILL campaign description

3.2.1 General information

The EXILL (**EXOGAM at ILL**) experiment was conducted in years 2012 and 2013 at the research reactor of the Laue-Langevin institute (ILL) in Grenoble, France. It was divided into several campaigns which used four different detector configurations. Three of them were used in γ -ray spectroscopy and one for fast-timing measurements (Table 3.1).

In the EXILL campaign an array of high-purity germanium (HPGe) detectors was

used. The array was placed at the intense cold neutron facility PF1B at the ILL for two reactor cycles (50 days each), what gave a cumulative beam time of 100 days devoted to the whole EXILL campaign.

Beam Time	Campaign	Target	Detector Configuration	Reactor cycle
7 days	beam test	BaCl ₂ , ¹⁵² Eu, ⁶⁰ Co		
14 days	(<i>n, γ</i>)	⁴⁸ Ca, ⁷⁷ Se, ⁹⁶ Zr, ¹⁶⁷ Er, ¹⁹⁴ Pt		
16 days	(<i>n, f</i>)	²³⁵U on Zr backing	I	I
6 days	(<i>n, f</i>)	²³⁵U on Be backing		
7 days	(<i>n, γ</i>)	⁹⁶ Zr, ^{155,157} Gd, ¹⁶¹ Dy, ²⁰⁹ Bi		
10 days	(<i>n, γ</i>) fast timing	⁴⁶ Ca, ⁹⁶ Zr, ²⁰⁹ Bi ⁴⁸ Ti		
13 days	(<i>n, f</i>) fast timing	²³⁵ U on Be backing	II	
1 day	(<i>n, γ</i>)	¹⁹⁵ Pt		
10 days	(<i>n, f</i>) fast timing	²⁴¹ Pu on Be backing		II
1 day	(<i>n, γ</i>)	⁹⁵ Mo	III	
1 day	(<i>n, γ</i>)	¹⁴³ Nd	IV	
14 days	(<i>n, f</i>)	²⁴¹ Pu on Be backing		

Table 3.1: Experiments performed during the EXILL campaign. The experiments marked in bold were analyzed in this work [Jen+17].

Combined arrays of HPGe detectors have been used in nuclear spectroscopy since the 1980s [ES08]. Thanks to their high efficiency and relatively high energy resolution it is possible to build coincidences between detected γ -rays thus high isotopic selectivity can be obtained and even nuclei with complex level schemes can be precisely studied. The HPGe detectors array can provide information on angular correlation or polarization of γ -rays which can be used to assign spins and parities to nuclear states [Jen+17].

The ILL provides one of the most intense neutron source in the world. The PF1B cold neutron beam facility is fed by a ballistic super mirror guide which gives the most intense neutron beam at the ILL ($2.2 \cdot 10^{10} \text{ cm}^{-2} \text{ s}^{-1}$ of a thermal neutron capture equivalent flux at a nominal reactor power of 58.3 MW). PF1B is also equipped with dedicated shielding which minimizes the γ -ray and neutron background coming from

the neighboring instruments and neutron guides [Jen+17].

More recent experiments (1990s) with EUROGAM/EUROBALL [AP95] and GAMMASPHERE [Ham+95; Lee97] on spontaneous fission of ^{248}Cm and ^{252}Cf showed the capability to perform precise study of the prompt γ -rays coming from fission products. The EXILL campaign embraces both (n, γ) and neutron induced fission (n, f) experiments (Table 3.1). The targets for the (n, f) experiments were ^{235}U and ^{241}Pu . Neutron induced fission with such targets gives a better access to the neutron-rich nuclei towards mass 80 where their yields are much higher in comparison to spontaneous fission of ^{248}Cm and ^{252}Cf , see Figure 3.1. In this way, the EXILL campaign provides access to the precise spectroscopic data on exotic nuclei. For the mass regions already studied through spontaneous fission, it gives the possibility to use different complementary fission fragments which may help to identify new, weak γ -transitions and to confirm the ones already measured [Jen+17]. In this way, the EXILL campaign data can complete the results coming from the experiments with spontaneous fission.

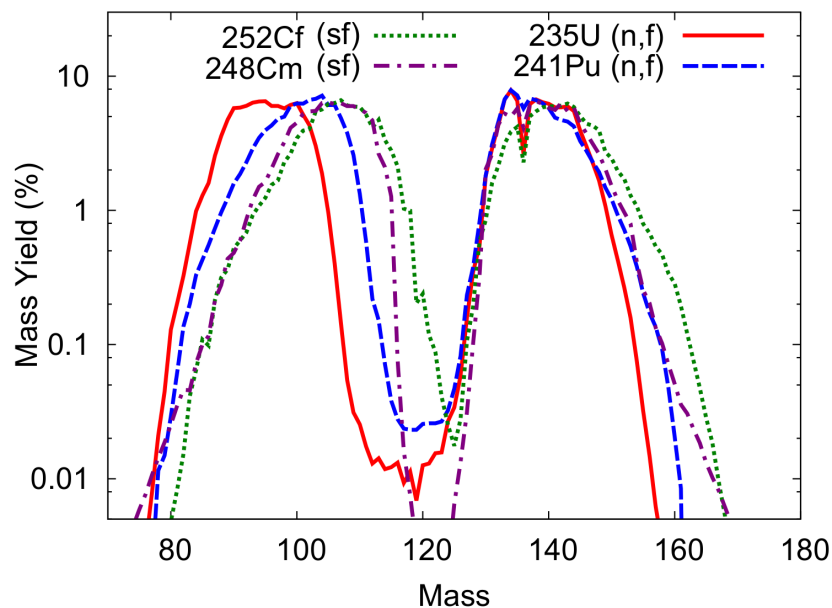


Figure 3.1: Fission fragments mass distribution coming from the neutron induced fission of ^{235}U and ^{241}Pu and the spontaneous fission of ^{248}Cm and ^{252}Cf . Data taken from [KBM09], graph taken from [Jen+17].

A wide group of experiments during the EXILL campaign was devoted to (n, γ) reactions. Their measurement with the array of HPGe detectors gives detailed spectroscopic information close to the line of stability [Jen+17]. In comparison to exper-

iments made so far with crystal spectrometers and a single HPGe, nuclei with much more complex level schemes could be studied and their transitions could be identified and arranged with much higher confidence.

Another motivation to perform the EXILL campaign was that, with the use of a complementary detectors array of lanthanum bromide scintillators (FATIMA array), it was possible to measure short lifetimes with a fast-timing technique [Jen+17].

Our lab (IRFU, DRF, CEA Saclay) in cooperation with colleagues from CEA Cadarache (DEN, DER) proposed to study the fission process and the prompt γ -ray cascade occurring in the fission fragments. The idea was to extract two kinds of information from the EXILL data. The first one concerns the fission fragment pair distribution $Y(Z1,A1,Z2,A2)$. The post-neutron evaporation fragment pair yields are directly related to the prompt neutron evaporation thus to the excitation energy of the fragments at scission. The γ -yield measurement can help to determine how the excitation energy is shared between the primary fission fragments. Pair yields can as well be directly used to benchmark codes like GEF or FIFRELIN.

The second point was linked to the possibility to extract precisely the cascade of discrete γ -rays emitted by the fragments. The level scheme (level energies, spins and parities) of many nuclei is well known. One can use a spectrometric method to obtain the intensities of the γ -ray transitions between these levels, as populated by the fission process. One can test whether the γ -ray cascade changes with the fissioning system ($^{235}\text{U}(n_{th}, f)$, $^{252}\text{Cf}(sf)$, $^{248}\text{Cm}(sf)$) and even test whether the cascade in a fragment changes with its fission partner.

According to FIFRELIN, the γ -ray cascade depends on the excitation energy and the angular momentum of the primary fragment thus its analysis can give the opportunity to benchmark the variety of models implemented in FIFRELIN and to choose their best combination.

In this work we concentrate on γ -ray spectroscopy of the fission products produced in $^{235}\text{U}(n_{th}, f)$ reactions. Data comes from the first reactor cycle and is a sum of 16 days of measurements with ^{235}U on Zr backing and 6 days of measurements with ^{235}U on Be backing (marked in bold in Table 3.1). We have analyzed the γ -ray cascades occurring in the fission fragments with the highest fission yields.

3.2.2 Experiment setup

Detectors and shields

During the whole EXILL campaign, four different detector setups were used. In this work we have only analyzed data coming from the configuration I.

In the past, only arrays with many small germanium detectors or small amount of HPGe detectors were used to study neutron-capture induced reactions (n, γ). For the EXILL experiment the detectors array was extended to 16 HPGe detectors. Three types of detectors were used: 8 EXOGAM Clover detectors, 2 Clover detectors from the ILL instrument LOHENGRIN and 6 GASP detectors.

EXOGAM detectors came from the laboratory of the Grand Accelérateur National d'Ions Lourds (GANIL). Each consisted of four segmented closed-ended coaxial n-type Ge crystals (60 mm diameter, 90 mm length, with the front side tapered at the length of 30 mm), each having 38% of relative efficiency, giving a combined efficiency of the whole detector in add-back mode of about 220% [Aza99; Sim+00].

The Clover detectors from ILL also consisted of four segmented closed-ended coaxial n-type Ge crystals (50 mm diameter, 80 mm length, non tapered). These detectors had a 1.5 mm thin Al entrance window which improves the detection efficiency of low-energy γ -rays. The relative efficiency of each crystal was about 25% and the combined efficiency of one detector in add-back mode was about 150% [Duc+99].

GASP detectors came from the Legnaro National Laboratory (LNL). They were large volume HPGe detectors each containing a single closed ended coaxial n-type Ge crystal (70 mm diameter, 80 mm length with the front side tapered at the length of 30 mm). The relative efficiency of one detector was about 80% [Alv93].

The whole array used in this configuration summed up to 46 germanium crystals. All detectors were mounted on a dedicated support structure. 8 EXOGAM Clover detectors were arranged in a regular octagon perpendicular to the beam axis. The two LOHENGRIN Clover detectors were placed at 45° with respect to the beam axis, below the beam axis, on both sides of the the target. The GASP detectors were placed at the 6 remaining positions at 45° with respect to the beam axis [Jen+17]. The configuration I is presented in Figure 3.2.

All Ge detectors, except for the LOHENGRIN Clovers, were equipped with an active bismuth germanate (BGO) Compton-suppression shield. Signals from all the Ge crystals were recorded in list mode together with the daisy-chained signals from the

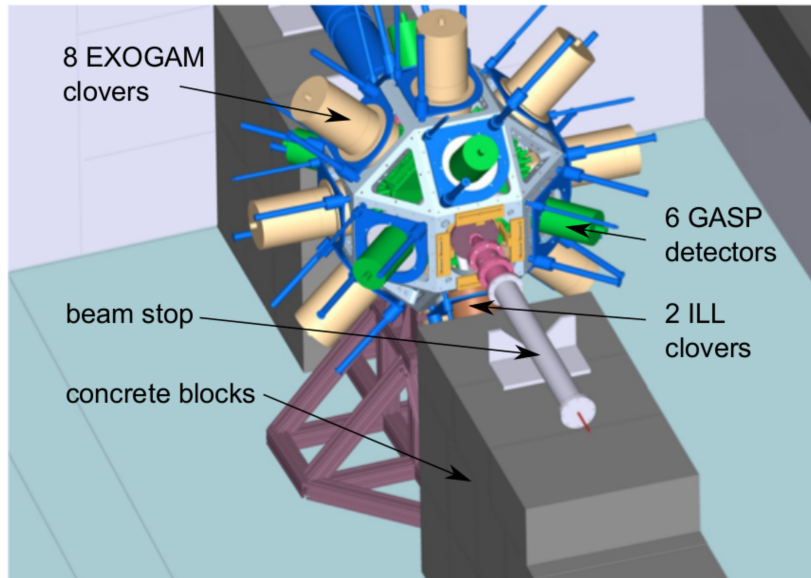


Figure 3.2: The detector configuration I used during the first reactor cycle of the EXILL campaign [Jen+17].

BGO surrounding each particular Ge detector [Jen+17]. Anti-coincidence discrimination was performed off-line. To remove γ -rays coming from the target which directly hit the BGO shield and to decrease cross-talk between adjacent detectors, tungsten collimators were placed in front of the BGO shield. The addback process was used to increase the efficiency and reduce Compton background: when two or more γ -rays were detected in coincidence in the crystals of the same detector, the reconstruction software sum their energies and attribute the sum to the whole detector [Ra15].

The detectors were placed about 13 cm away from the target.

Collimation system

During the EXILL campaign a dedicated collimation system was used. The neutron beam has been shaped to a pencil beam with a diameter of 1 cm five meters downstream from the the end of the neutron guide. The collimated neutron flux was around 10^8 n/cm²/s which translated into about 10^5 fission per second with the uranium targets. The neutron energy was about 4.5 meV. The precisely shaped beam was needed for angular correlation measurements which require a geometrically well defined source [Jen+17]. The collimation system consisted of a sequence of circular apertures made from absorbing materials: sintered natural boron carbide and sintered enriched ⁶LiF.

To reduce the γ -ray background produced by boron, the apertures were shielded with 5 cm thick lead absorbers. The apertures were placed inside a cylindrical aluminum tube with a neutron absorbing inner layer of 1-cm thick borated plastic. The tube segments were assembled together with the mechanical transversal misalignment not larger than 1 mm over the entire length of the collimation system [Jen+17].

The first two collimators (the closest to the beam guide) were made of machined 1 cm thick B_4C ceramics, each mounted on a 5 cm thick lead aperture. The next three collimators were made of 5 mm thick 6LiF ceramics, each mounted on 3 cm thick borated polyethylene, supported by 5 cm thick lead apertures [Jen+17]. Presented in Figure 3.3 the aperture sequence was about 4 m in length. The target chamber was connected to it through the 1 m free flight path section. The beam dump pipe with a 5 mm thick 6LiF beam stop was connected to the target chamber by the vacuum tube lined with 2 cm boron loaded rubber sheet [Jen+17]. This layer absorbed neutrons backscattered from the beam dump.

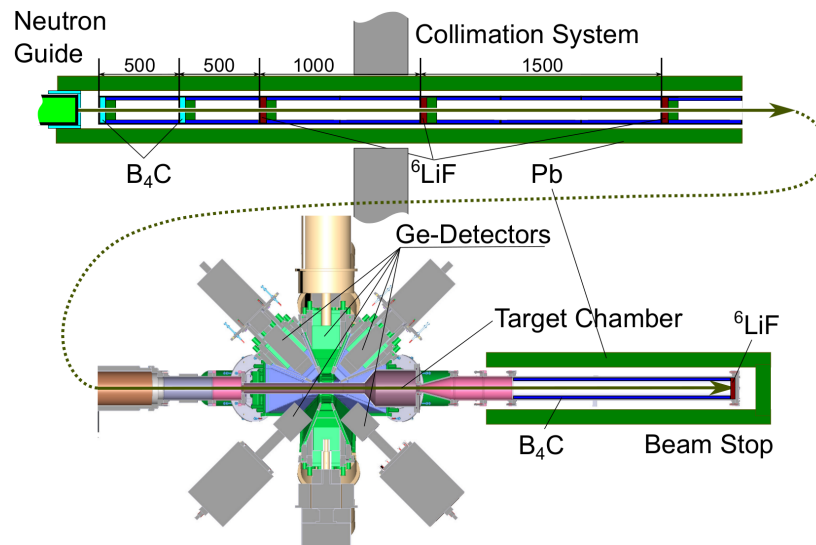


Figure 3.3: The target collimation system layout. It is followed by the target chamber surrounded by the detector array and the beam dump [Jen+17].

Target chamber

To provide optimal conditions for γ -ray spectroscopy a dedicated target chamber was designed and used. Such a chamber needs to fulfill several requirements: materials which absorb or scatter γ -rays emitted from the target should be avoided, it should

produce low γ -background by neutrons scattered by the target, it should be placed close to the target and should allow easy target change [Jen+17]. An additional condition for the EXILL campaign was the ability to safely use a highly radio-toxic ^{241}Pu target thus the chamber was designed as a double wall containment. Nevertheless, the data analyzed in this work comes from the detector configuration I. It only used the outer shell of the chamber, which is presented in Figure 3.4.

The chamber was made of an aluminum pipe having 50 mm diameter and 2 mm thick walls and it was directly connected to the collimation and beam stop vacuum systems [Jen+17]. Samples were held in teflon bags fixed with teflon wires to a small metal frame [Jen+17]. The outer layer of the chamber was surrounded with a 1 mm thick ^6LiF rubber sheet to remove scattered neutrons.

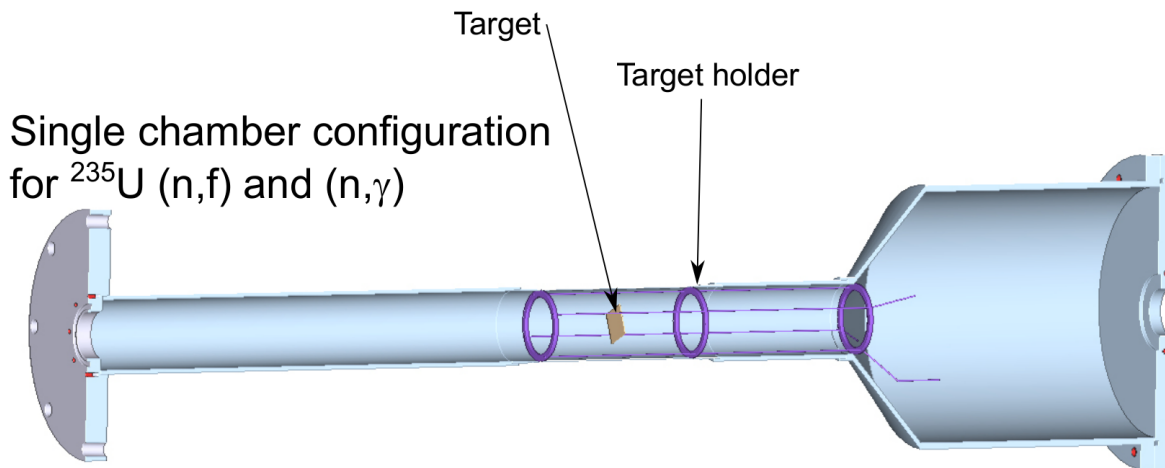


Figure 3.4: The target chamber in a single wall configuration [Jen+17].

Target

Many different targets were used during the EXILL campaign, see Table 3.1. In this work only data from the experiments with ^{235}U is used and only uranium targets will be discussed. The neutron induced fission process produces fission fragments with a recoil energy in the range from 50 to 110 MeV which need to be stopped very soon after scission to reduce Doppler broadening of the emitted γ -rays [Jen+17]. This was obtained by using sandwich targets where uranium was placed between two pieces of material which stop fission products but do not attenuate γ -ray emission.

^{235}U was enriched to 99.7%. One target was made by depositing $^{235}\text{UO}_2$ layers by

the multiple painting technique [TEKS99] on a 2 μm thin Zr foil and was sandwiched between two 15 μm thick nuclear grade Zr foils. Additionally, they were cold-rolled with a few mg/cm^2 metallic tin as filling material. The fission products stopping power in uranium oxide, tin and zirconium are very close thus such sandwich can be treated as a homogeneous stopper [Jen+17]. In total, the target consisted of three of such sandwich layers. The total mass was equal to 525 μg . This target has been irradiated, and the emitted γ -rays has been measured for 16 days, see Table 3.1 (bold text).

The second ^{235}U target, which has been measured for 6 days, see Table 3.1 (bold text), was made by depositing a $^{235}\text{UO}_2$ layer by the multiple painting technique on a thick graphite sheet. Afterwards, the top graphite layer was removed and $^{235}\text{UO}_2$ was glued between two 25.4 μm thick beryllium foils [Jen+17]. The total mass of the target was equal to 675 μg .

The two targets were used because one of the ideas had been to test the Doppler effect influence on the results. The stopping power of Be is lower than for Zr. During the experiment, no difference was observed between the targets, which was partially caused by the low energy resolution of the detector that made it impossible to observe small differences.

Acquisition system

During the EXILL campaign, the data acquisition system managed up to 72 channels depending on the detector configuration. The analogue signals coming from detector preamplifiers were transformed into digital signals by digitizers. To obtain the proper timing information the internal clock of each digitizer was phase locked to an external clock source (master clock) [Jen+17]. The digitizers had been implemented with a specific Digital Pulse Processing (DPP) algorithm which allowed them to extract the amplitude and the arrival time of the detected pulses. A trigger starting the pulse conversion was used. It had the form of a programmable digital threshold. Whenever a voltage step exceeded it, the conversion started.

The numerical information about the amplitude of the analogue signals and their arrival time were collected by board computers (data concentrators) and recorded on a computer hard disk. The implemented real-time processing algorithm analyzed each pulse, converted it to a list-mode event and produced the relevant histograms. Afterwards, such events were transferred to the external mass storage where the histograms were accessible [Jen+17].

Due to high count rates, each experiment was subdivided into time intervals of 7 to 15 minutes, which produced data files of about 2 Gbyte in size. Between different experiments, calibration runs were performed. For low energies ^{133}Ba , ^{60}Co and ^{152}Eu sources were used. For high energies ^{35}Cl (n, γ) and ^{36}Cl were used. Moreover, (n, γ) lines from the target backing and chamber materials were used for energy calibration monitoring during experiments [Jen+17].

During the whole EXILL campaign about 60 Tbytes of data have been recorded.

3.2.3 Data preprocessing

Energy alignment

For the detector configuration I the calibration spectra were obtained with a 420 kBq ^{152}Eu source. A standard gain matching gave a full width at half maximum (FWHM) resolution of around 3.7 keV at 1408 keV [Jen+17].

γ -rays with a well-known accuracy of at least 0.02 keV had been chosen to perform the periodical energy calibration monitoring. Due to changes of external conditions the gain matching was performed for each run [Jen+17]. For the $^{235}\text{U}(n, f)$ measurements about 3500 runs were recorded and an automatized procedure has been developed to perform the alignment run by run. After the gain matching, the add-back procedure and the sorting of the data into a histogram, the final energy calibration was done by fitting a single, second-order polynomial to γ -rays with well-known energies [Jen+17].

Time alignment

At the beginning of each run the master clock was set to zero. This provided time synchronization of all electronic channels every 7 to 15 minutes. Nevertheless, offline time alignment was needed due to differences in detector types, cable lengths, preamplifier performances. Without the precise time measurement it would not have been possible to analyze the data using the γ -coincidence method. To counteract the different arrival times of the detector signals, the time-difference spectra between the time responses of the reference detector and all other detectors were produced [Jen+17]. All the spectra were aligned so that the differences between prompt γ -ray peaks were smaller than 10 ns. It was small enough value in comparison to the used during analyses acceptance time window of about 200 ns and would not disturb γ -ray cascades measurements.

The width of the peak was about 120 ns due to relatively weak time resolution of some detectors.

3.2.4 Detection system efficiency calibration

The detection efficiency of a germanium detector is energy dependent. The detectors used during the first reactor cycle of the EXILL campaign had various efficiencies (Section 3.2.2). The detection efficiency of an array of such detectors needs to be calibrated. This process was described in details in my Master's thesis [Rq15]. The calibration source was the γ -emitter ^{152}Eu . It decays to ^{152}Gd (β^-) and to ^{152}Sm (electron capture) with the emission of several γ -rays with well known energies in the range between 100 to 1500 keV. Additional corrections of the detection efficiency were added in this work e.g. correcting for the true coincidence effect.

Coincidence detection efficiency

In this work, as well as in my Master's thesis [Rq15] γ - γ - γ coincidences were used to analyze the spectroscopic data from the EXILL experiment on $^{235}\text{U}(n, f)$. This method, to be efficient, needs a simplified estimation of the total efficiency of all detectors in coincidence ($\epsilon_{\text{coinc}}(E_1, E_2, E_3)$). The regular formula takes the form:

$$\epsilon_{\text{coinc}}(E_1, E_2, E_3) = \sum_{i=1}^N \sum_{\substack{j \neq i \\ j=1}}^N \sum_{\substack{k \neq i \\ k \neq j \\ k=1}}^N \epsilon_i(E_1) \epsilon_j(E_2) \epsilon_k(E_3) \quad (3.1)$$

where E_1, E_2, E_3 are the energies of the γ -rays, $\epsilon_i, \epsilon_j, \epsilon_k$ are the detection efficiencies of the i, j, k detectors, respectively, N is the number of detectors. If one assumes that all detectors have an identical detection efficiency Equation 3.1 can be simplified to:

$$\epsilon_{\text{app}}(E_1, E_2, E_3) = N(N-1)(N-2)\epsilon(E_1)\epsilon(E_2)\epsilon(E_3) \quad (3.2)$$

The detectors used in the configuration I of the EXILL campaign did not have the same detection efficiencies. We made an assumption that the total detection efficiency ($\epsilon_T(E)$) at the energy E of N same detectors is equal to the sum of the detection efficiencies of N different detectors:

$$\epsilon_T(E) = \sum_{i=1}^N \epsilon_i(E) = N \cdot \epsilon(E) \quad (3.3)$$

After applying Equation 3.3 to Equation 3.2 the approximated coincidence detection efficiency takes the form:

$$\epsilon_{app}(E_1, E_2, E_3) = \frac{(N-1)(N-2)}{N^2} \epsilon_T(E_1) \epsilon_T(E_2) \epsilon_T(E_3) \quad (3.4)$$

We verified these assumptions by calculating the coincidence detection efficiencies with the basic Equation 3.1 and the approximated Equation 3.4 for some γ -rays coming from the calibration source ^{152}Eu . The relative differences have been found lower than 1.5% [Ra15], which was an acceptable discrepancy. We have used the approximated formula for further analysis.

Source activity

A correct determination of the detection system absolute efficiency (Equation 3.5) demands a precise source activity value. I used the already determined coincidence efficiencies thus the activity was calculated for a number of γ -rays in coincidence coming from the calibration source ^{152}Eu [Ra15]. Results were not uniform. Some peaks were higher than the others. It was caused by the false coincidence effects which occurred due to the high count rate (high source activity) and high detector efficiencies. In such conditions it is possible that two γ -rays from different cascades come to the detector within one output pulse and they will not be recognized as separated events. After correcting for this effect, activities were calculated once again and the calculated values were averaged, taking into account their uncertainties. The determined source activity was equal to 416.0(7) kBq [Ra15] which was not far from the activity of 420 kBq given by the source manufacturer [Jen+17]. This discrepancy is much lower than the uncertainty on the manufacturer's source activity value.

Absolute efficiency

All of the previously calculated values allowed me to determine the absolute efficiency of the detection system for the γ -ray energies emitted by the calibration source ^{152}Eu :

$$\epsilon(E) = \frac{V(E)}{I(E) \cdot A \cdot T} \quad (3.5)$$

where $V(E)$ is the volume of the γ -ray peak at energy E , $I(E)$ is the absolute intensity of the γ -ray at energy E (taken from the NNDC or LNHB/CEA database), A is the source activity and T is the acquisition time.

The calculated activities for particular energies were then fitted with the calibration curve [Ra15]:

$$\epsilon(E) = \exp^{\ln(A)+B \cdot \ln(E)} \quad (3.6)$$

where A and B are the independent constants. Figure 3.5 presents the absolute efficiency curve coming from [Ra15]. One can see that the curve does not fit well the points which are displaced and have only minimal uncertainties (covered by the graph markers). This problem was investigated in this work.

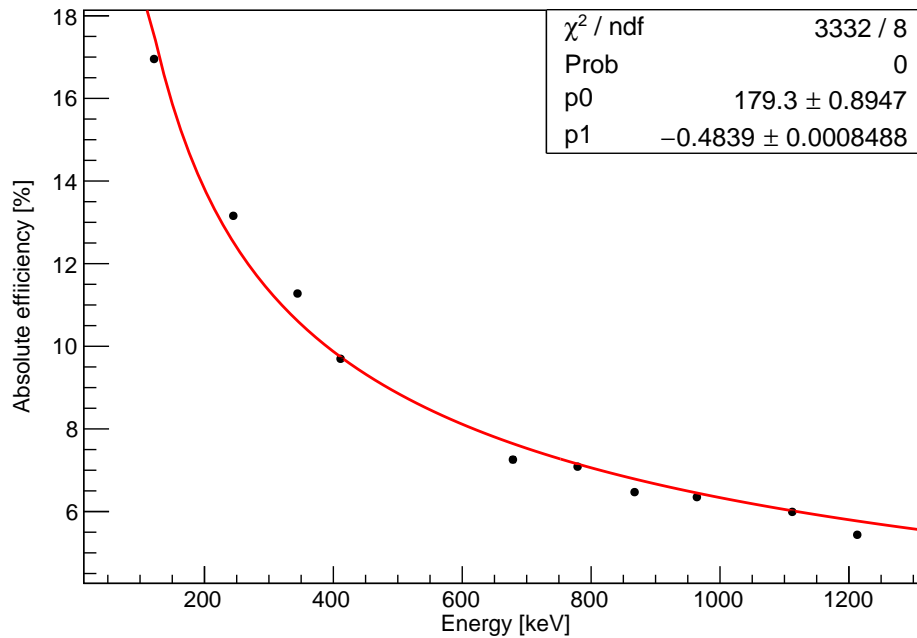


Figure 3.5: The detection system absolute efficiency curve fitted with the simple efficiency Equation 3.6 [Ra15]. The uncertainties on the experimental efficiency points are smaller than the marker size.

The true coincidence effect was identified as the cause of the experimental efficiency points displacement. This is the result of recording as a one event two or more γ -rays detected in the same detector at the same time. Their energy is summed together. The number of counts of each one of the summed transitions is decreased. Assuming that the sum energy is identical to the energy of the known γ -ray of the same de-excitation cascade, the number of counts of this transition is increased. This effect is also intensified by the addback process. To face this issue the TrueCoinc software [Sud02]

developed at the University of Debrecen in Hungary was used. It uses information coming from existing databases (e.g. nuclear levels) and detector parameters supplied by the user to determine the true coincidence influence on experimental data and to generate correction factors by looking for the γ -rays which sum energy is close to the transition energy of the other γ -ray and how strong is this effect when the detection efficiency is taken into account.

To perform this correction, data from the EXILL experiment were divided between three detector groups according to their types: EXOGAM Clovers, Clovers from LOHENGRIN, and GASP.

Based on provided detector parameters, the true coincidence effect was calculated with the TrueCoinc software and the experimental data was corrected and summed. The new efficiency curve was fitted with the function:

$$\epsilon(E) = \exp^{A+B \cdot \ln(E)+C \cdot \ln^2(E)} \quad (3.7)$$

where A, B and C are the independent constants.

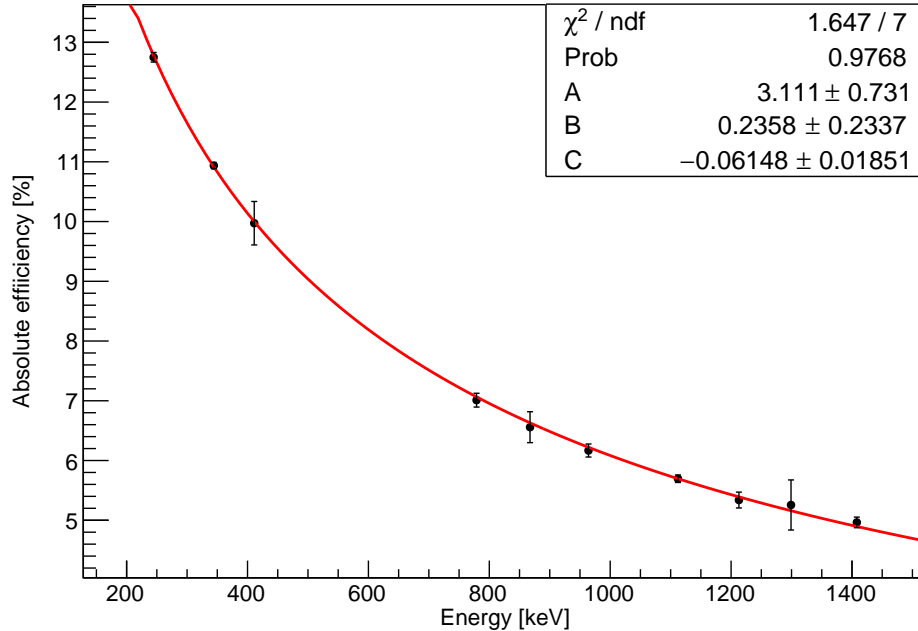


Figure 3.6: The detection system absolute efficiency curve fitted with the modified efficiency Equation 3.7. The absolute efficiency experiment data was corrected for the true coincidence effect.

In Figure 3.6 one can see that the new efficiency curve fits much better the modified experimental data. The uncertainties of some experimental data points in Figure 3.6 are much higher than in Figure 3.5. It is the result of correcting the γ -ray intensities for the true coincidence effect. The transitions where the effect was the strongest (the correction was the biggest) have the highest uncertainties.

3.3 Triple- γ coincidence method

3.3.1 Introduction

At the beginning of our studies we used a classical triple- γ coincidence method. This γ -ray spectroscopy technique is based on the fact that during the de-excitation process of one fission fragment nucleus (Figure 3.7), all prompt γ -rays are emitted in a limited time (often within picoseconds or nanoseconds).

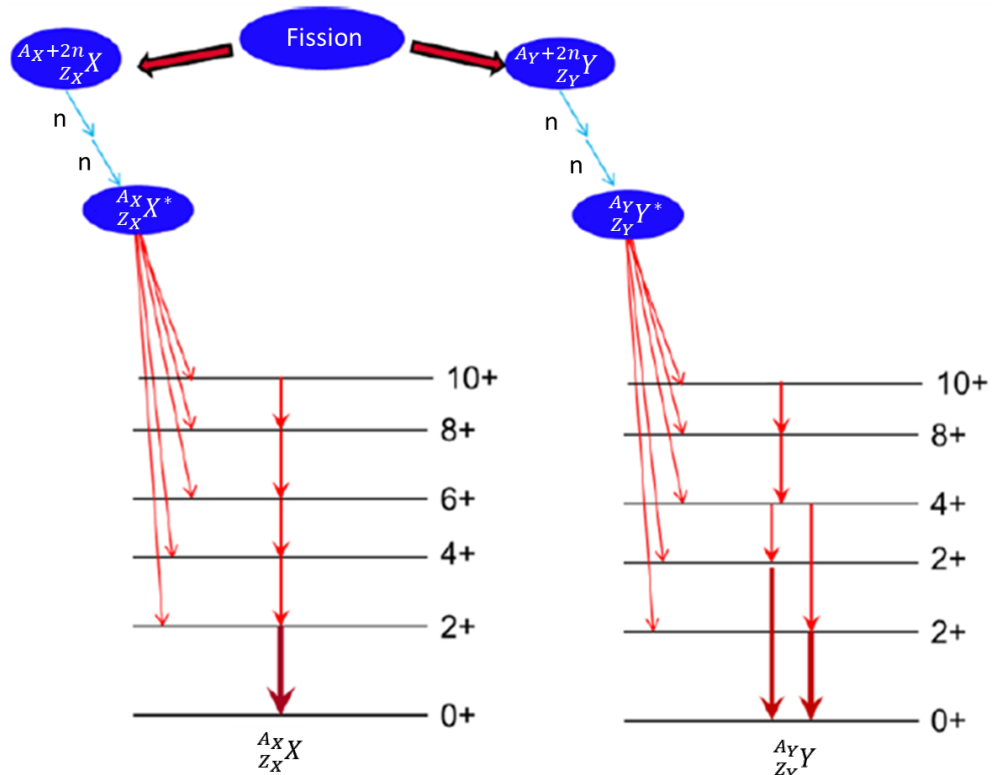


Figure 3.7: Schematic presentation of the fission fragments de-excitation process. Fission fragment emits prompt γ -rays in the form of a cascade. The energies of these γ -rays are unique for each nucleus.

Their energies are unique for a particular element and their emission depends on the fission fragment entry state (excitation energy, spin and parity). By selecting a γ -ray in a fission fragment de-excitation cascade and looking on the other γ -rays in coincidence within a short time window, one is able to filter experimental data and find out transitions coming from the same cascade or from the fission partner cascade. One can build a level scheme which contains these γ -rays and excited levels in the form of a cascade (Figure 3.7).

3.3.2 Triple- γ coincidence requirements

It is only possible to use the triple- γ coincidence method to analyze experimental data if the setup of the experiment fulfills specific conditions. First of all, it needs to be able to detect at least three γ -rays at the same time (within the prompt γ -ray cascade lifetime and between two consecutive fission events) thus multiple detectors need to be used. Second, the relative or absolute detection times of γ -rays need to be precisely recorded. Moreover, the detection efficiency and statistics need to be high because the detection efficiency in triple- γ coincidence is the result of multiplying efficiencies of three detectors, see Equation 3.4. We have the absolute detection efficiency of around 10% at 400 keV (Figure 3.6) thus the number of detected transitions in the triple- γ coincidence will be 100 times lower than without coincidence. The energy resolution of the detection system must be high enough to allow distinguishing individual γ -ray peaks. The HPGe detectors array used during the EXILL campaign (detector configuration I) fulfilled these requirements.

3.3.3 γ - γ - γ cube

The crude experimental data (events in list mode) are used to build a three-dimensional histogram called γ - γ - γ cube. It contains the information about coincidences between all the events measured during the experiment and allows one to easily use the triple- γ coincidence method. The creation of the cube starts with choosing an acceptance coincidence time window. In the case of the EXILL experiment data, this window needs to be longer than the time resolution of the detection system. When we take into account that the width of the peak was about 120 ns, the time window should have around 200 ns. A smaller window would reduce the number of counts which was tested in [Rą15]. A too long time window can cause γ -rays coming from other cascades to be

erroneously recognized as events in coincidence. γ - γ - γ cubes built with the EXILL data typically have an acceptance time window fixed to a couple of hundred nanoseconds thus an intensity of the γ -ray coming from the long lived state (e.g. nanoseconds isomers) cannot be correctly estimated with the triple- γ coincidence method.

The fission rate of about 10^5 fission per second translates into on average a single fission every $10 \mu\text{s}$. It means that all the prompt γ -rays coming from the de-excitation cascade (not taking into account longer living states) were theoretically emitted and detected between subsequent fissions. For every detected fission, within the acceptance coincidence time window all γ -rays are associated to each other by creating all possible combination containing three events. These triplets are placed in a three-dimensional γ -ray histogram (γ - γ - γ cube) with the γ -ray energies along the axis.

3.3.4 γ - γ - γ cube analysis

To analyze the de-excitation cascade of a fission fragment, one needs to select a γ -ray (called gate) which belongs to its cascade or to the cascade of its fission partner. The size of the gate can be changed and normally it corresponds to the width of the γ -ray peak which depends on the energy resolution of the detection system. Based on this gate, a histogram with all γ -rays in coincidence is built. One can identify and fit the peaks of the desired γ -rays to obtain the amount of such photons in coincidence with the previously selected γ -ray.

ANA cube and software

The first cube that we have used, had been created at the University of Warsaw under the supervision of Waldemar Urban. The cube has a dedicated analysis software called ANA which is equipped with a user interface. It allows one to select gates and background, to produce and visualize spectra in double and triple coincidences and to fit γ -ray peaks.

GASP cube and software

The second cube that we have used, had been created at GANIL by Caterina Michelagnoli. It also has a dedicated analysis software called GASP with similar functions to the ANA software. The advantage of GASP over ANA is an easier access to spectra and to the terminal which allows one to use dedicated commands to analyze spectra.

This makes it possible to write a script which quickly generates a huge amount of spectra with different gates which was very important in further analysis made in this work.

Triple γ -coincidence for the EXILL data analysis

In principle, to extract the γ -ray cascade in a fission fragment, a simple (double) coincidence is sufficient: one uses as a gate a strong transition in the fission partner, generates the γ -ray spectrum in coincidence and analyses it to find out transitions and fit their intensities.

In the case of the EXILL data, the use of the triple- γ coincidence method is required due to the strong contamination of the spectra by: 1) the prompt γ -rays produced after neutron capture by the setup or target elements (Al, Zr) 2) the γ -rays that follow β -decay of the fission fragments 3) the Compton background (Figure 3.8). Spectra in simple coincidence have so many peaks that it is impossible to correctly identify and fit desired γ -rays. Theoretically, with the triple- γ coincidence method we are able to create a spectrum which contains only the γ -rays which we are interested in.

Gates selection

Normally, in the standard triple- γ coincidence method, to observe the de-excitation cascade in a fission fragment (B), the best way is to select two gates in its fission partner (A). The problem with this type of gating is that one sees as well the transitions that occur in all the possible fission partners of (A). It means that in the triple coincidence spectra we will see many γ -rays emitted by many fission fragments which can hinder the wanted transitions or contaminate them. But the advantage of this type of gating is that one sees the complete de-excitation cascade of a fission fragment and hence it can be entirely analyzed. We call this type of gates "double gates", see Figure 3.9.

To have the highest possible statistics, the gates are two subsequent γ -rays from the de-excitation cascade having the highest intensities. One of them is the γ -ray going to the ground state (or the long living excited state with the lowest energy).

In our analysis we have used double gates only to measure the main transition going to the ground state and some others from the same fission branch (transitions with the highest intensities). We could not analyze the whole cascade with double gates because peaks of the γ -rays with similar energies are hard to separate due to

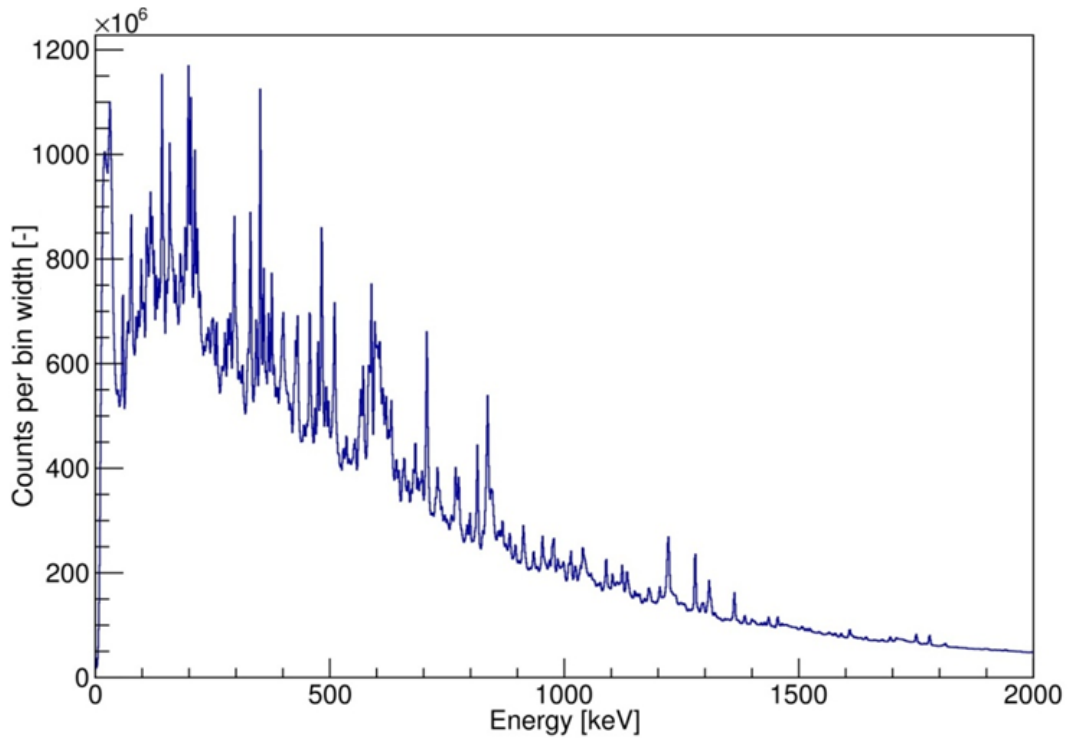


Figure 3.8: Prompt γ -ray spectrum without coincidence of $^{235}\text{U}(n_{th}, f)$ measured during the EXILL experiment after Compton rejection.

relatively weak energy resolution thus we are unable to distinguish which event belongs to which transition. Also, the amount of peaks is so huge that it is impossible to fit the peaks of the transitions with lower intensities because they are contaminated by the Compton tails of the transitions with higher energies. This significantly rises the results uncertainty.

To reduce the number of peaks in the spectrum and to decrease the possibility of contaminating any of them we have used "mixed" gates. The first gate is placed in the fission fragment (A) and the second one in its fission partner that one wants to analyze (B), see Figure 3.10. We normally select γ -rays having the highest intensities (going to the ground state). Such gating allows us to define exactly the fission fragment pair that we want to analyze. In this way we will theoretically build a coincidence spectrum which contains only γ -rays emitted by the two fragments A and B. Such a coincidence spectrum is much cleaner than the one built with double gates, there are less γ -ray peaks thus it is easier to identify and fit them.

With mixed gates it is impossible to normalize the γ -ray intensities to the transition

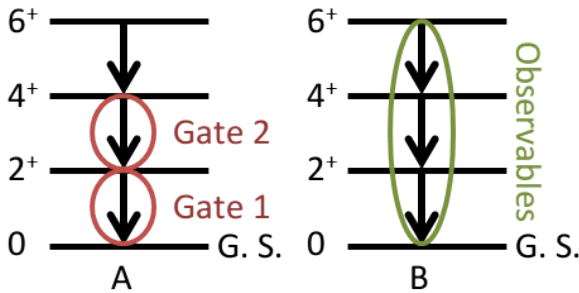


Figure 3.9: Schematic view of gates placement when "double gates" are used. Two gates are placed in the fission fragment A. In the coincidence spectrum one will see the complete de-excitation cascade of its fission partner B. Also cascades of other fission partners will be visible.

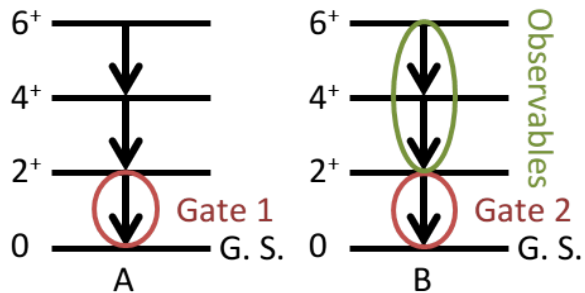


Figure 3.10: Schematic view of gates placement when "mixed gates" are used. The first gate is placed in the fission fragment A, the second one in its fission partner B. In the coincidence spectrum one will not see the complete de-excitation cascade of the fission partner B. Nevertheless, the spectrum will be much cleaner because no cascade of other fission partners will be present.

going to the ground state (with the highest intensity). Normally, it is our gate. To solve this issue, we need to renormalize the results with data coming from double gates spectra. Renormalization rises the uncertainties but in this way we are able to measure the complete de-excitation cascade and to normalize it to the transition going to the ground state.

Gating and fitting process

As an example how the triple- γ coincidence works with mixed gates, I will show gating on ^{92}Kr and its fission partner ^{142}Ba . This fission fragment pair has one of the highest yields out of the fission fragments produced in the $^{235}\text{U}(n_{th}, f)$ process. An additional advantage of these two fragments is that they have relatively simple level schemes, each having only one strong γ -ray going to the ground state, see Figures 3.11 and 3.12.

To start with, we place the first gate in the spectrum without coincidence (Figure

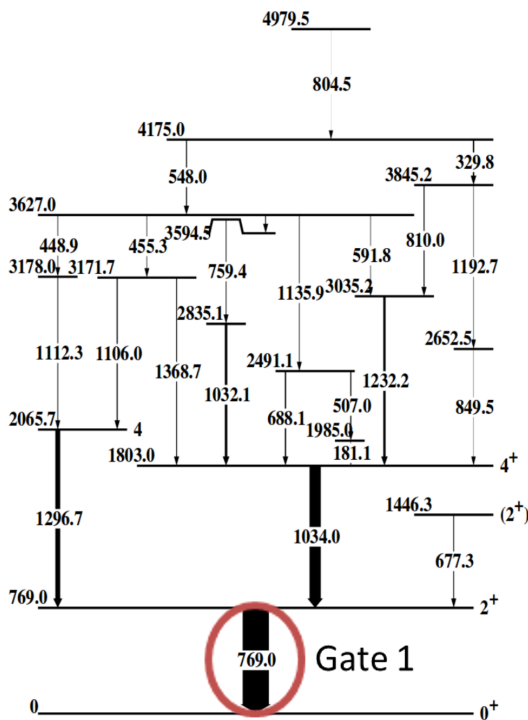


Figure 3.11: Level scheme of ^{92}Kr [RU+00]. The 769.0 keV γ -ray was selected as the first gate in the presented example.

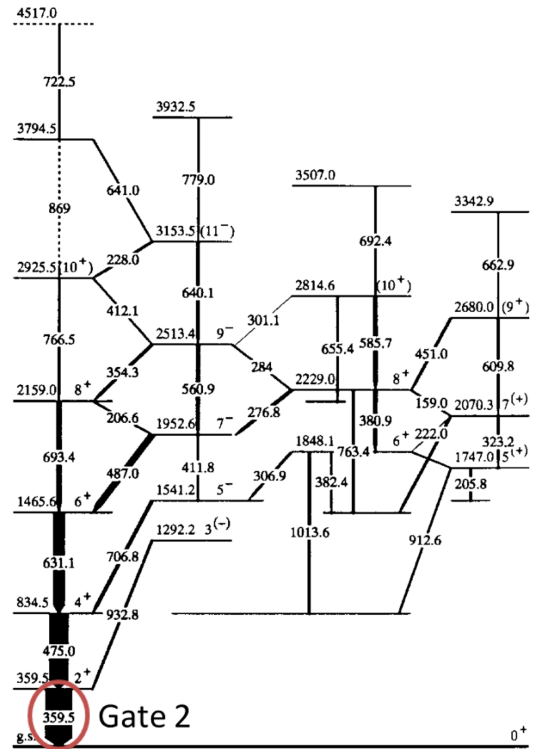


Figure 3.12: Level scheme of ^{142}Ba [Urb+97]. The 359.5 keV γ -ray was selected as the second gate in the presented example.

3.8). We select the γ -ray transition at 769.0 keV going to the ground state of ^{92}Kr and we subtract the appropriate background. The gate itself can have a couple of keV (depending on the detector energy resolution) which means that we also select some part of other γ -ray peaks with energies around 769.0 keV. The spectrum in simple coincidence is built, see Figure 3.13. The new spectrum is not clean enough to be analyzed. There are still many γ -rays emitted by other bariums than ^{142}Ba . We also see γ -ray cascades coming from other fission fragments which contain γ -rays with energies close to 769.0 keV.

Since the first gate comes from ^{92}Kr , we select the second gate in ^{142}Ba (mixed gates). Once again we choose the γ -ray going to the ground state, which is the photon having the energy equal to 359.5 keV, see Figure 3.12. We place this gate in the single coincidence spectrum and we select the appropriate background. The result is a

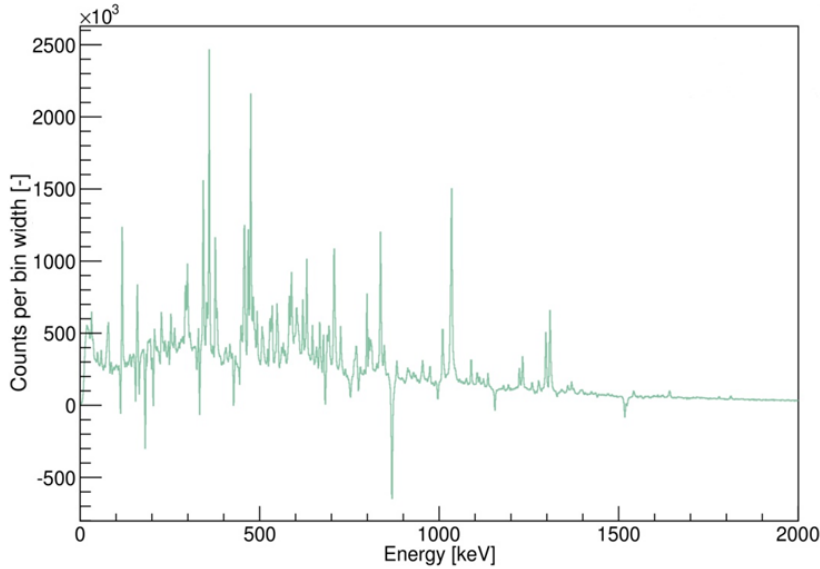


Figure 3.13: Prompt γ -ray spectrum of $^{235}\text{U}(n_{th}, f)$ in coincidence with the 769.0 keV γ -transition from ^{92}Kr , with the background subtraction.

spectrum in triple coincidence with subtracted background, see Figure 3.14. It is much cleaner than the spectra in single coincidence. The background is low and the peaks can be easily associated with known transitions. In Figure 3.14, I marked the γ -rays with the highest intensities emitted by ^{92}Kr and ^{142}Ba .

After identifying the peaks we chose the appropriate background for each peak we want to analyze and we fit it. The peak volume corresponds to the number of measured γ -rays having the particular energy. After applying the absolute efficiency of the detection system in triple coincidence, we obtain the number of these γ -rays emitted by the chosen fission fragment pair (^{92}Kr and ^{142}Ba). Then the relative intensity of a transition is calculated by normalizing it to the intensity of the chosen γ -ray. Most of the time, this normalizing γ -ray has a very high intensity and is emitted between $4^+ \rightarrow 2^+$ excited states.

We need to bare in mind that with selected gates we are unable to measure the intensity of the transitions going to the ground state. To get them we need to build two separated triple coincidence spectra with double gates only in ^{92}Kr or only in ^{142}Ba (in the analyzed fission fragment pair). Double gates in ^{92}Kr give us access to all γ -rays in ^{142}Ba , and vice versa. Eventually, the intensities measured with mixed gates are renormalized and can be e.g. compared with data coming from other experiments.

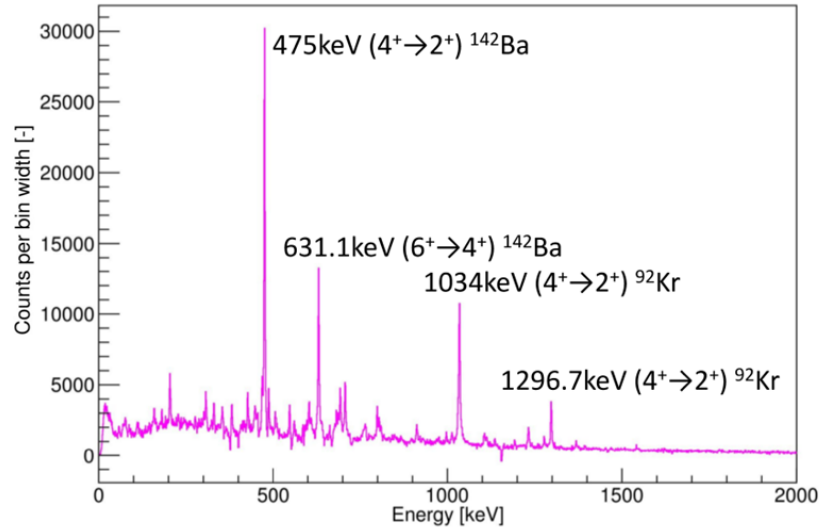


Figure 3.14: Prompt γ -ray spectrum of $^{235}\text{U}(n_{th}, f)$ in coincidence with the 769.0 keV and 359.5 keV γ -transitions from ^{92}Kr and ^{142}Ba , respectively, with the double subtraction of the background. The γ -rays with the highest intensities emitted by ^{92}Kr and ^{142}Ba can be easily identified.

3.3.5 Limitations of the analysis method

In the standard triple- γ coincidence method the appropriate background is chosen and subtracted along with the selection of each gate. The standard practice is to select the gate wide enough to contain the whole γ -ray peak. In our case, due to particular energy resolution, caused by the low energy resolution of some detectors, peaks were rather wide. Gating on the full width of the peak would also include part of many other peaks which would contaminate the coincidence spectrum. Our solution was to gate only on the central part of the peak. This reduced the statistics but also gave us the confidence that our coincidence spectra contains mostly γ -rays emitted by the desired fission fragment pair. We tested various widths of gates. Finally, it was reduced to just 1 keV - the smallest size possible with the binning used during the EXILL experiment.

Normally, the background is put close to the peak in the place where no peaks are present. With the spectrum without coincidence presented in Figure 3.8 it was really hard to find such a place. We decided to set the background adjacent to the gate. In this way we removed part of the selected γ -ray peak itself but we are sure that any other peaks hidden in the tails are also suppressed. Figure 3.15 presents the described way of gating and background selection.

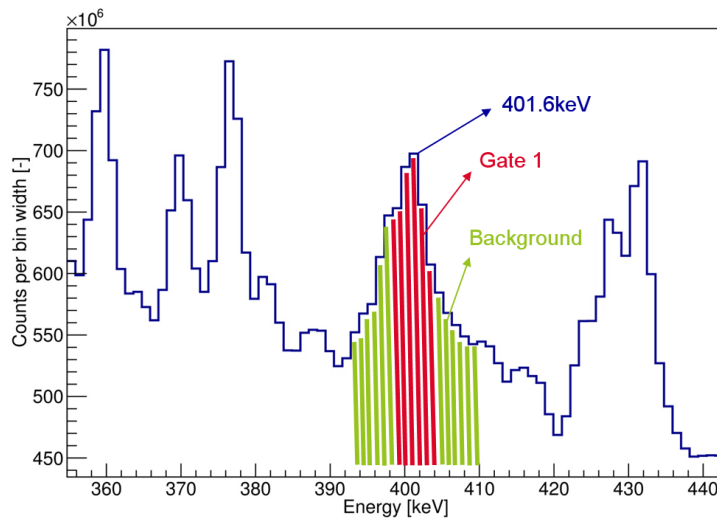


Figure 3.15: First gate and background selection with standard γ - γ - γ coincidence method. The peak at 401.6 keV comes from the ^{90}Kr .

Already in Figure 3.16, which presents the spectrum in simple coincidence, the first problem with this method is visible. The background subtraction during gating generates negative peaks. If the second gate is placed near the negative peak the new adjacent background can be negative too.

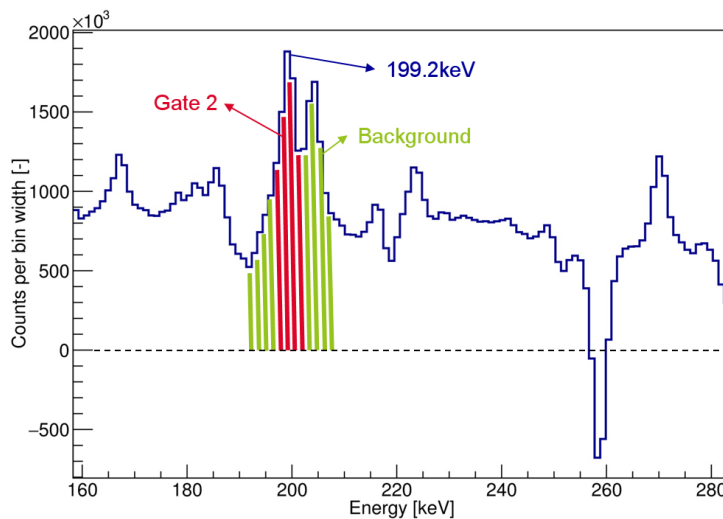


Figure 3.16: Second gate and background selection with the standard γ - γ - γ coincidence method. The peak at 199.2 keV comes from the ^{144}Ba .

This becomes much more relevant at the final phase of the measurement when the

γ -ray peak is fitted and the background is chosen, see Figure 3.17. As one could see in Figure 3.17 there are a few possible locations of the background close to the peak 330.7 keV. The problem is, where is the true background and which peak is negative (lower than the true background). Around 400 and 420 keV we obviously have negative peaks but it is not clear around 315 or 350 keV.

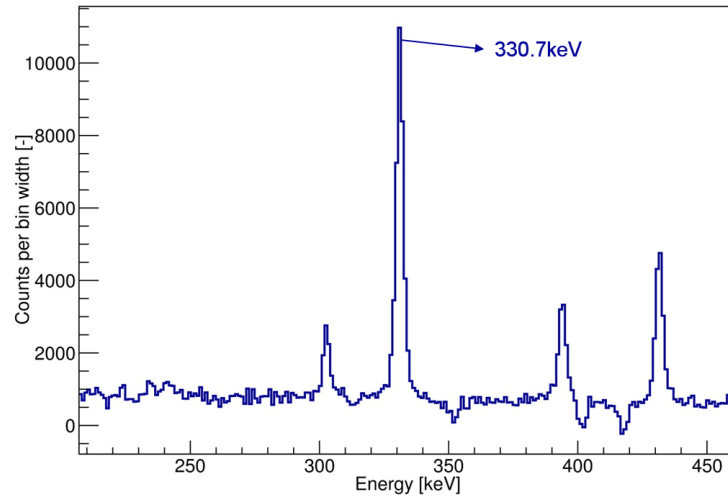


Figure 3.17: Prompt γ -ray spectrum of $^{235}\text{U}(n_{th}, f)$ in coincidence with the 401.6 keV and 199.2 keV γ -transitions from ^{90}Kr and ^{144}Ba , respectively, with the double subtraction of the background.

Depending on the chosen background the measured number of counts changes thus the calculated intensities of the γ -ray also vary. Results were not reproducible and the discrepancy between measurements with different backgrounds was up to 10%. Such an additional uncertainty on the results would make it impossible to observe a phenomenon like the dependence of the de-excitation cascade in a fission fragment with its fission partner.

Chapter 4

New EXILL analysis technique

4.1 Introduction

I have shown in the previous chapter in Section 3.3.5 that the standard way of extracting transition intensities from the γ - γ - γ cube was problematic when applied to the EXILL data. The large number of possible nuclei produced in fission and thus the huge amount of detected γ -ray transitions and the incomplete detection of the whole energy of these transitions due to Compton scattering complicate the selection of the background used in the gating process. As a result, extracted intensities may fluctuate by 10% depending on the chosen background or gating. It made some studies impossible as e.g. the expected variation of the transition intensities as a function of the fission partner were of that order.

I have tested different ways of analyzing the data and we finally decided to develop a new analysis scheme that takes into account the background in a more correct way. In a sense, the standard way can be seen as a "spectroscopic" method with the main goal of finding new transitions and new excited states in nuclei. To study the fission fragment de-excitation, we want to measure precisely the intensity of some known transitions with the best estimated uncertainties. Generally speaking, we need a "spectrometric" method.

In the next section, I will describe the general idea and analysis scheme used in this new method. Section 4.3 presents analysis procedure differences depending on the used γ - γ - γ cube. Section 4.4 will briefly explain how we automatized the fitting of a large amount of peaks and spectra and how we calibrated the response function (or fit function) of the detection system. Section 4.5 explains in detail the algorithms

used to extract the transition intensity in triple coincidence, especially in the case of contaminants. The last section provides the performances and limits of this new method by showing the extracted γ -ray cascades in ^{142}Ba .

4.2 Concepts of the new analysis method

In the standard method, the difficulty of peak fitting can be attributed to the fact that the gated spectrum is obtained by subtraction of spectra.

To formalize the concept, let's consider a simple case with the standard method. We want to study the discrete cascade of γ -rays in a fission fragment F_2 . F_1 is one of its fission partners. As gates, we use transition T_A , belonging to the cascade of F_1 and transition T_B , which e.g. populates the ground state of fragment F_2 . The goal is to measure the intensity of a γ -ray transition in the cascade of F_1 , which we call T_X , in coincidence with T_A and T_B . Transitions T_A , T_B and T_X have respectively the energy E_A , E_B and E_X .

We build the coincidence spectrum. It is the spectrum of γ -rays in coincidence with a small region of γ -rays around T_A with energy (E_A) and a small region of γ -rays around T_B with energy (E_B); or in the short form around (E_A, E_B).

The problem is that, when doing so, we take as well events in coincidence with γ -rays from the background i.e. with γ -rays that belong to the small region around (E_A, E_B) but which are not related to transitions T_A and T_B .

This background comes from Compton scattering of high energy transitions and one can expect some portion to come from higher energy transitions belonging to fragment F_1 or F_2 . The standard method consists in subtracting an equivalent portion of events in coincidence with a small region around an energy E'_A a bit higher than E_A and the same small region unchanged around E_B . Then, symmetrically, an equivalent portion of events in coincidence with the same small region around E_A and a small region around an energy E'_B a bit higher than E_B is subtracted.

The background below the peak of T_A and T_B however consists also of γ -rays that have nothing to do with the nuclei A and B : Compton scattering of other fragments, (n, γ) reactions in the target or γ -rays from the surrounding environment. Since we subtract it twice in the previous process, we have to compensate it by adding an equivalent portion of events in coincidence with the (same) small region of γ -rays around (E_A, E_B).

The process is illustrated in Figure 4.1. Δ_A is the width of the regions (gates) around respectively E_A and E'_A . Δ_B is the width of the regions (gates) around respectively E_B and E'_B .

Let's call $C(E_1, E_2, E_3)$ our cube, the 3D distribution of γ -rays in coincidence. The process of gating the cube on a region around (E_A, E_B) consists in building the histogram of events in coincidence in the following way:

$$GS(E_3) = \int_{E_A - \frac{\Delta_A}{2}}^{E_A + \frac{\Delta_A}{2}} \int_{E_B - \frac{\Delta_B}{2}}^{E_B + \frac{\Delta_B}{2}} C(E_1, E_2, E_3) dE_1 dE_2 \quad (4.1)$$

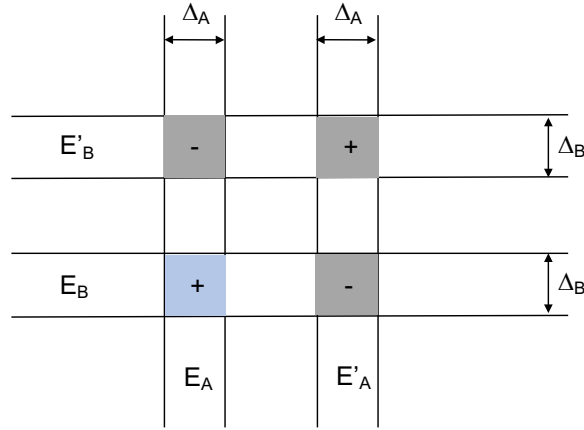


Figure 4.1: Schematic representation of the standard way of analyzing the data. To obtain the intensity of a transition in coincidence with the transitions T_A and T_B , with energy E_A and E_B , one builds the spectrum of γ -rays in coincidence with a small region around (E_A, E_B) , then subtracts γ -rays in coincidence with the regions around (E'_A, E_B) and around (E_A, E'_B) and adds γ -rays in coincidence with a region around (E'_A, E'_B) .

To keep track of the gating parameters, I use the following notation: $GS(E_3; E_A, E_B, \Delta_A, \Delta_B)$. The final spectrum, after the explained background correction, is given by:

$$S(E_3) = GS(E_3; E_A, E_B, \Delta_A, \Delta_B) + GS(E_3; E'_A, E'_B, \Delta_A, \Delta_B) - GS(E_3; E'_A, E_B, \Delta_A, \Delta_B) - GS(E_3; E_A, E'_B, \Delta_A, \Delta_B) \quad (4.2)$$

The final spectrum $S(E_3)$ contains all the transitions in coincidence with T_A and T_B , and among them, the wanted transition T_X . We can fit it to extract its area. The

spectrum contains as well, due to imperfect subtraction, some remaining peaks that are not in coincidence with T_A and T_B , and some negative peaks (valleys) if e.g. the background region is not well selected. The addition of a region around (E'_A, E'_B) (last term of Equation 4.2) brings new contaminating peaks and the subtractions (second and third terms) bring new contaminating valleys. As a consequence, $S(E_3)$ contains peaks and valleys, which makes it difficult to analyze.

The standard way may be more refined with several background gates in order to find a better estimation of the background below the peak, E'_A may be chosen more carefully to avoid contamination, etc. Nevertheless, the conclusion stays valid: the goal of the process is well adapted to find new transitions but the drawback is that their intensity may be difficult to estimate with a good precision.

The new method that we developed is based on the idea that one should scan the gates in 2D in order to better estimate the background and that one should avoid subtraction of spectra.

We perform gate scans in three directions: along the first axis E_1 , it defines a set of horizontal gates; along the second axis E_2 , the vertical gates and along both axes E_1 and E_2 at the same time, the diagonal gates, see Figure 4.2.

As before, each "gating" is done on a small 2D region of energies with sizes (Δ_A, Δ_B) . For this method, however, the gate size must be smaller than the detector resolution. Such narrow gates allow scanning the shape and detecting possible contaminants.

Gating on a small region around (E_1, E_2) yields a spectrum with peaks, that one can fit to extract their area. This spectrum contains only "positive" peaks since there are no spectra subtraction. The process consists in finding the peak associated to transition T_X in each gated spectrum and to fit its area. At the end of this process, we will have horizontal, vertical and diagonal sets of areas (or counts) associated to transition T_X for the different gates defined in Figure 4.2.

We could at this stage apply a similar formula as Equation 4.2 but using the peak area. However, we can improve the results by finding a better estimation of the background: one can fit the horizontal set of areas, the vertical one and the diagonal one and correct the γ -rays in triple coincidence with T_A and T_B in the following way:

$$N_{corr}(E_A, E_B) = N(E_A, E_B) - B_{HORIZ} - B_{VERT} + B_{DIAG} \quad (4.3)$$

where $N(E_A, E_B)$ is the area of the peak associated to transition T_X in the gated

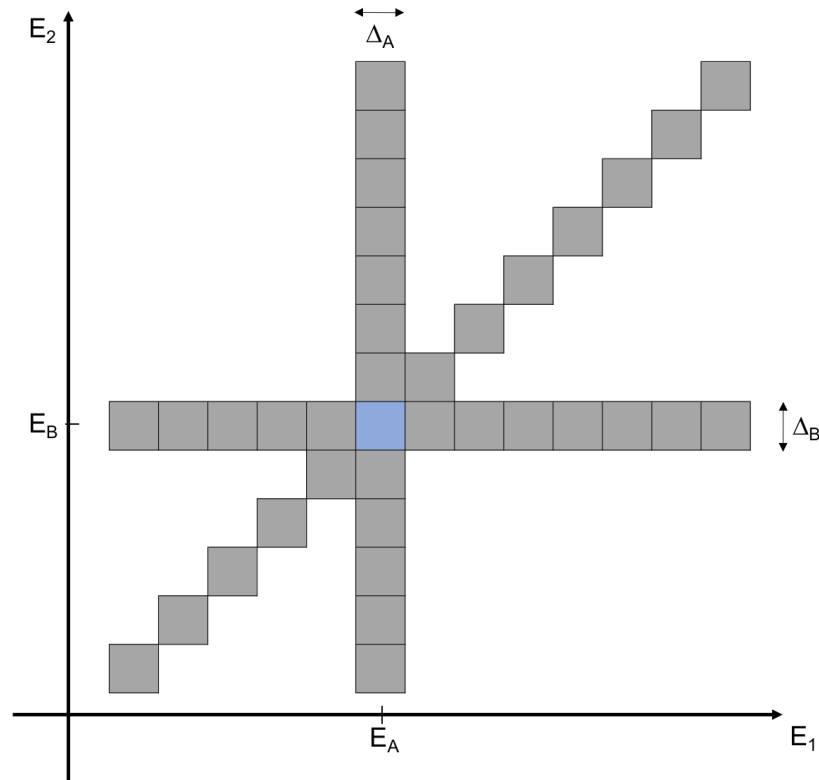


Figure 4.2: Schematic representation of the new way of 2D gate scanning around (E_A, E_B) . Each square corresponds to a 2D gate with (Δ_A, Δ_B) size.

spectrum on the region around (E_A, E_B) , B_{HORIZ} is the fitted background using the set of peak areas associated to T_X but in the horizontal gated spectra, B_{VERT} and B_{DIAG} are the same quantities for the vertical and diagonal gates.

The exact formalism will be detailed in Section 4.5.

4.3 Illustration on EXILL data

The new method was developed using the cube generated by the Warsaw group. As explained in Chapter 3, this cube was only readable with a specific software. Generation of gated spectra could only be done manually, in a interactive mode. So scanning over a large number of gates was tedious. In this chapter, I will illustrate the new method with my study on the cascade in ^{142}Ba (Section 4.6). This study was done with the Polish cube. The number of horizontal, vertical and diagonal gates was set to 15. One of the gates is common to the three scans, thus the total number of gates is 43, their

arrangement is presented in Figure 4.3. The size of the gates is around 2 keV x 2 keV. In fact, the Polish group adopted a non-linear binning: the bin size varies with energy in order to compensate for the decrease of statistics with energy and to keep a rather low size of the cube in memory (4096^3 bins).

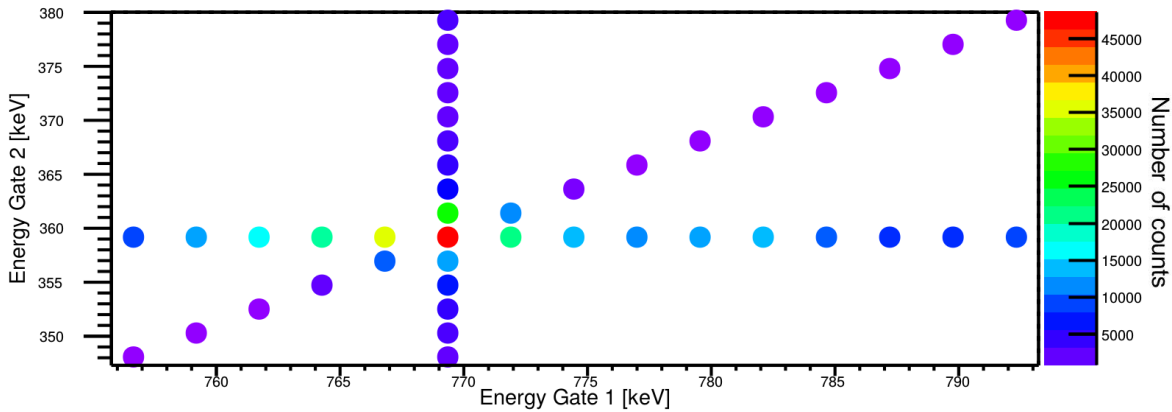


Figure 4.3: 2D scan of the gates in the Polish cube. Each dot denotes one pair of gates. The point at the intersection between the horizontal, the vertical and the diagonal slices (red dot) denotes the exact energies of the initially selected gates. Each number of counts comes from fitting the same γ -ray peak in the particular triple- γ coincidence spectrum. The measured γ -ray is at 475.0 keV in ^{142}Ba . The initial gates are the transition at 769.0 keV in ^{92}Kr and the transition at 359.5 keV in ^{142}Ba .

Later on, we received another cube, built by GANIL, that was readable with a GASP macro. Gating this cube on a large number of regions was easier and the macro was included in the EXILLANA software. The energy binning of this cube is more conventional: 1 bin = 1 keV. The GANIL cube was used to analyze all the other fragments and especially ^{100}Zr which I will present in the next chapter. With the GANIL cube, the number of horizontal, vertical and diagonal gates was set to 31. The width of the gates were set to 1 keV x 1 keV. Such a width decreases statistics in the gated spectra and the peak area by a factor of 4 but improves the detection of contaminants. The total number of gates equals $3 \times 30 + 1 = 91$, their arrangement is presented in Figure 4.4.

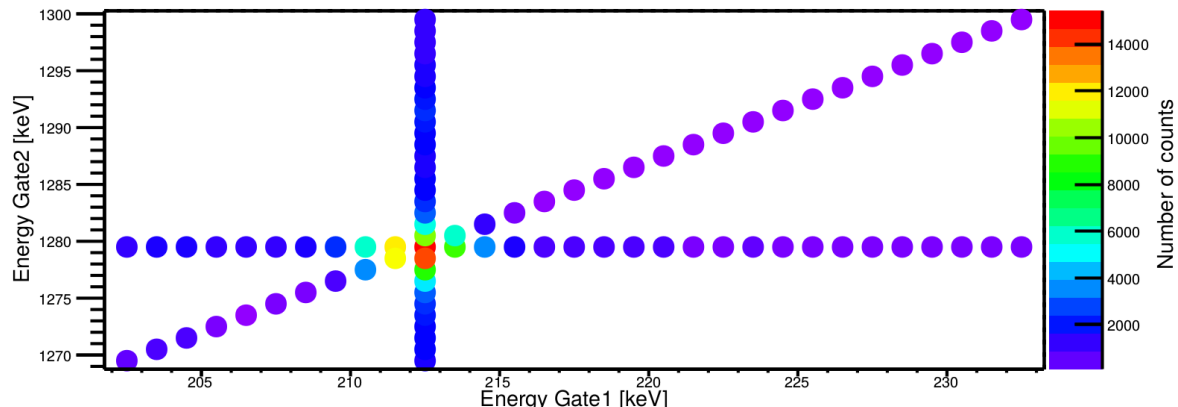


Figure 4.4: 2D scan of the gates in the GANIL cube. Each dot denotes one pair of gates. The point at the intersection between the horizontal, the vertical and the diagonal slices (red dot) denotes the exact energies of the initially selected gates. Each number of counts comes from fitting the same γ -ray peak in the particular triple- γ coincidence spectrum. The measured γ -ray is at 352.0 keV in ^{100}Zr . The initial gates were the transition at 212.6 keV in ^{100}Zr and the transition at 1279.3 keV in ^{134}Te .

4.4 Semi-automatic spectra fitting process

The intensity of the γ -ray transitions must be extracted (fitted) in all 43 (or 91) gated spectra. Doing it interactively for each spectrum would take a long time and kill finally the method (and the user eyes). It is done in a semi-automated way with an algorithm written in C++ using ROOT libraries, that mimics somehow the standard way of doing it interactively.

4.4.1 Fitting procedure

The first step is to find a region of interest (ROI) that contains the wanted peak(s) and any close peaks that may interfere during the fitting process. One has to choose the same ROI for all the 91 spectra for a given T_X . It simplifies hugely the algorithm. The best ROI is found visually by looking at the 43 (91) spectra at the same time, see Figure 4.5. Since for all the spectra the ROI is the same, as a consequence, the ROI may become large. It is caused by the fact that one has to find such limits of the ROI so they do not overlap any peak. A possible future improvement of the code may be to implement an algorithm that finds the best ROI for each of the 91 spectra separately.

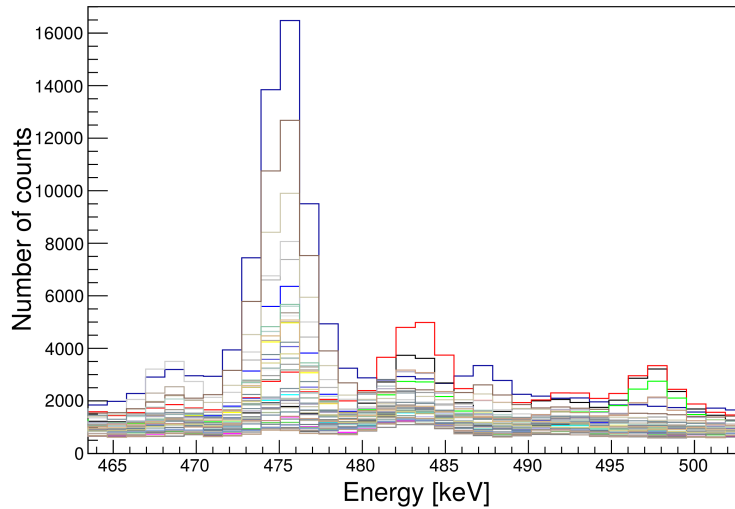


Figure 4.5: All the gated spectra generated with the scan of gates, zoomed on the γ -ray peak at 475.0 keV in ^{142}Ba . The central gate (E_A, E_B) is set around the 769.0 keV transition in ^{92}Kr and the 359.5 keV transition in ^{142}Ba .

The next step is applied to every spectrum independently. In the ROI, we use the TSpectrum library to find all the peak positions. Then the portion of the spectrum defined by the ROI is fitted (with the Minuit library) using a defined function which describes the detection system response and the background and which uses all the peak positions as input parameters. It allows to find a better estimation of the peak positions and their area.

To be sure that all peaks are found and treated, even those with low statistics, an iterative procedure is applied by comparing the experimental spectrum and its fit. We build the residual spectrum (a difference spectrum in unit of σ) and new peaks are searched in it, again using the TSpectrum library. The process ends when no new peak is found.

If a new peak is observed in the residue, it is added to the list of peaks only if it is not too close to any of the peaks on the list (considering the detection system resolution). The algorithm is complex to tune because it can generate artificial peaks when the fitting function does not perfectly reproduce the detection system response. Artefacts occur in particular in the tails of large peaks and should be removed in a later stage by the user. Other complications are linked to parameters that one could set free, fixed or constrained like the width of the peaks, fitting error handling, etc.

Finally, this process is rather long, e.g. in the cases where there are many peaks in the ROI (up to few tens of minutes per spectrum); so we parallelized it - one job per spectrum - on the IN2P3 computing center.

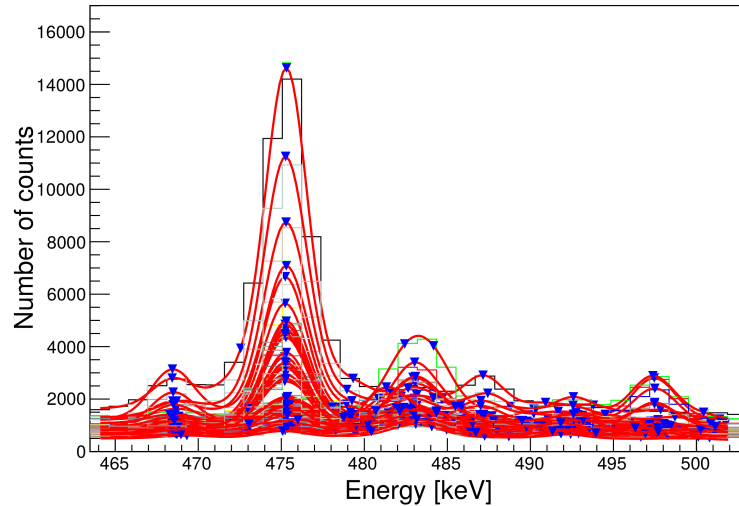


Figure 4.6: All the gated spectra generated with the scan of gates, zoomed on the γ -ray peak at 475.0 keV in ^{142}Ba . The central gate (E_A, E_B) is set around the 769.0 keV transition in ^{92}Kr and the 359.5 keV transition in ^{142}Ba . All γ -ray peaks were found and fitted. Blue triangles indicate the peak positions.

At the end of the previous process, we have, for each of the 43 (91) gated spectra, the position and the area of all the peaks found in the common ROI, see Figure 4.6. Some of the peaks appear in all 43 (91) spectra, others appear only in the horizontal or vertical gated spectra. The last case occurs e.g. when the peak is in coincidence with a strong, high energy transition and one gates on the Compton scattering tail of this transition.

The next step consists in associating the different peaks to the same transitions. This process is done automatically and the result must be validated by the user. In principle, a transition has the same energy in all the different gated spectra and this is of course valid for the desired transition and any contaminant. However, the scan over the gates is large. The desired transition can appear in all the gates but it is not necessarily the case for the contaminants. A peak area may as well decrease quite a lot far from its optimal gates. It has an impact on its uncertainty and the estimation of its energy by the fitting process. The association algorithm is rather complex, and I will

only explain the main ideas. It starts by sorting the peaks with the lowest uncertainty then step by step, one associates a peak to a "transition" by checking if its energy differs less than its relative uncertainty to the best estimation of the transition energy. The transition energy is at each step updated to the (uncertainty-) weighted average energy of all associated peaks. The result is illustrated in Figure 4.7.

In some cases, the transition energy is known from other experiments more precisely and it is better to fix its value. It can be done at this point.

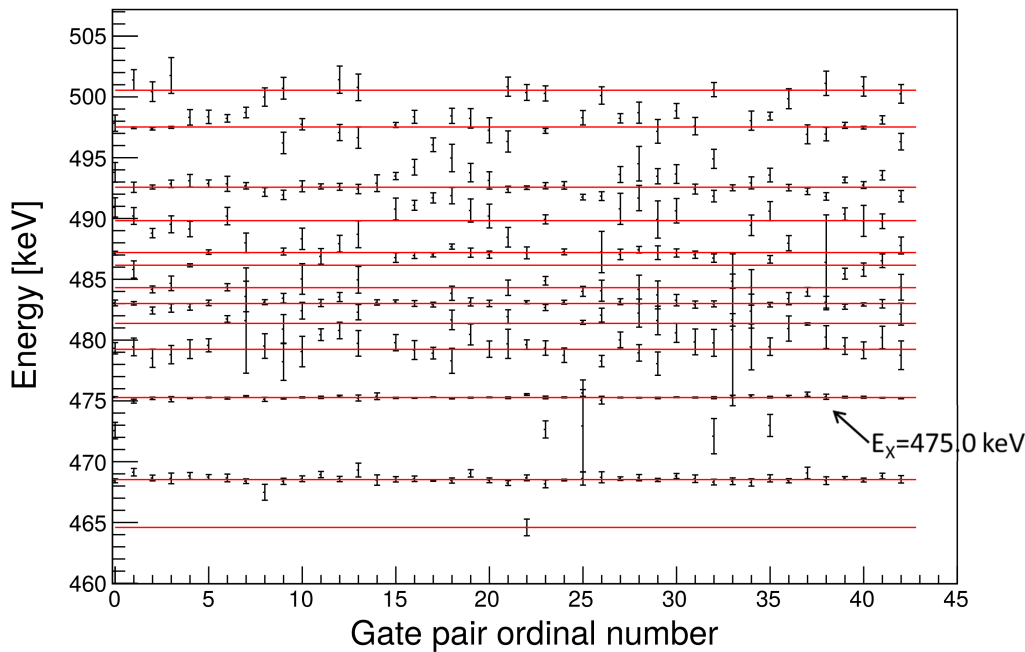


Figure 4.7: Peak positions in all triple- γ coincidence spectra generated with the 2D scan of gates. The initial gates were the γ -ray at 769.0 keV in ^{92}Kr and the γ -ray at 359.5 keV in ^{142}Ba . All γ -ray peaks were found and fitted in the region around the desired γ -ray at 475.0 keV in ^{142}Ba . Red lines are the (weighted) averaged energy of peaks. Gate pair 0 is the pair of central gates, gate pairs 1-14 are horizontal gates, gate pairs 15-28 are vertical gates, 29-42 are diagonal gates, starting from the lowest energy.

At this stage, we perform a final fit of all the spectra with the same list of peak energies used as input. The advantage of the last fit is that one can fit very small peaks that were not detected in one spectrum but appear in the others, see Figure 4.8. The

drawback is that the list of peaks is often so big that one cannot let any freedom to the energy of the peaks in the fitting process. It may impact the uncertainty estimation.

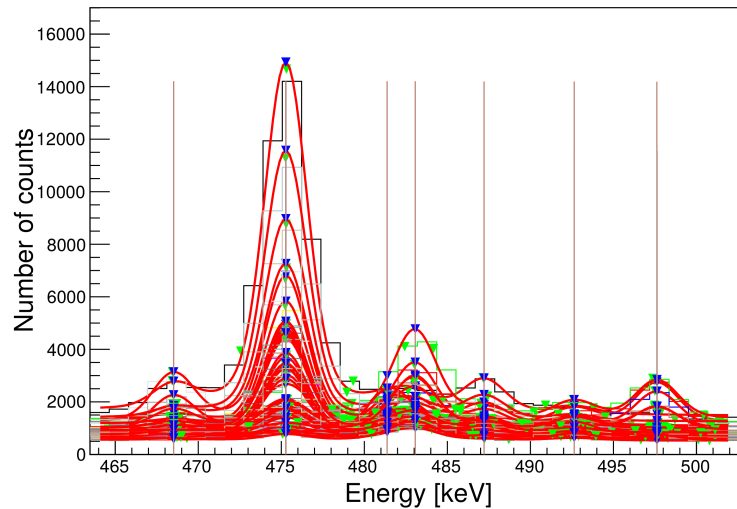


Figure 4.8: All triple- γ coincidence spectra generated with the 2D scan of gates. The initial gates were the γ -ray at 769.0 keV in ^{92}Kr and the γ -ray at 359.5 keV in ^{142}Ba . All γ -ray peaks were found and fitted in the region around the desired γ -ray at 475.0 keV in ^{142}Ba . The position of each peak is synchronized in all spectra based on their (weighted) averaged energy from the initial fit. Blue triangles indicate the synchronized peak positions. Green triangles indicate the peak positions from the first fit of the peaks (Figure 4.6).

The final output of all these steps is the area of the wanted peak(s) in the ROI for all the 43 (91) spectra, which is used in the next step of the analysis.

4.4.2 Detection system response

As explained previously, peaks have to be fitted in an automatic way. It requires a good knowledge of the detection system response function. Ideally, the fit function should have two free parameters, the peak position and its area. Peak width and tails should be fixed and known for the whole energy range.

Due to 1) different performances of the detectors (different energy resolutions) and 2) small variations of the calibration during the rather long EXILL experiment, which could not be corrected perfectly before summing all the contributions, the final peak

shape is not as Gaussian as the one expected from a HPGe detector.

We have adjusted the fitting function using the events coming from the $^{91}\text{Zr}(n, \gamma)$ and $^{92}\text{Zr}(n, \gamma)$ reactions. These events result from the interaction of the thermal neutron beam with the target backing material (made of Zr). ^{91}Zr and ^{92}Zr are two stable isotopes of Zr (natural abundance of respectively 11.2% and 17.1%) with a relatively large capture cross-section for thermal neutrons (σ_{th} respectively of 1.2 barns and 0.2 barns).

The energy of the γ -rays emitted during the de-excitation process of the compound nuclei (^{92}Zr and ^{93}Zr) are well known. Several transitions are at very high energy (primary γ -rays) what makes their peaks very clean in the spectra. Figure 4.9 shows some useful transitions populated in the $^{91}\text{Zr}(n, \gamma)$ reaction. Gating on the 6294.81 keV transition and the 934.46 keV transitions yields a very clean spectrum with e.g. a strong 1405.06 keV peak.

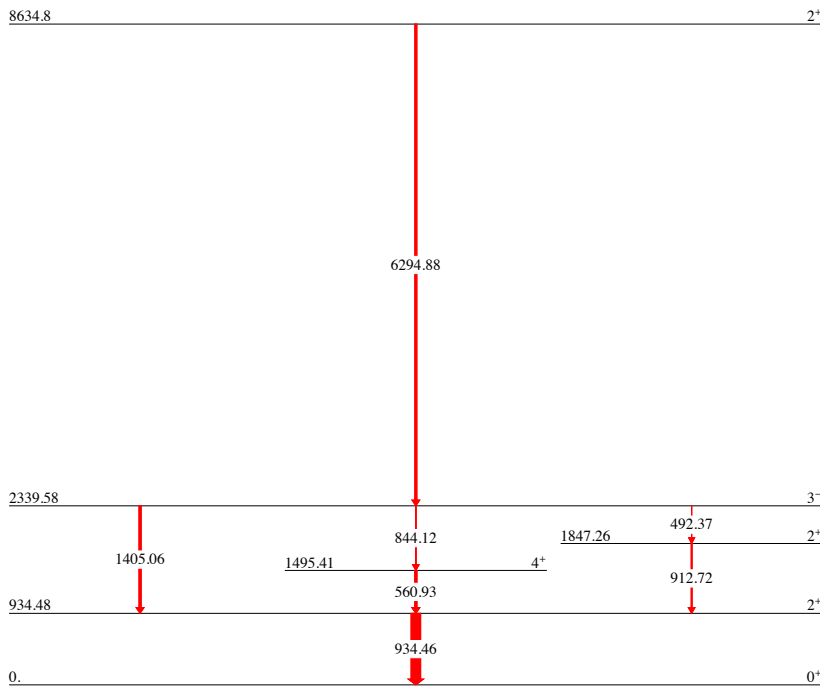


Figure 4.9: Partial level scheme of ^{92}Zr with some of the transitions populated in the $^{91}\text{Zr}(n, \gamma)$ reaction.

The optimal fitting function was found to be the sum of three Gaussian functions, with the same center but different widths and a smoothed step function (to take into account Compton scattering):

$$R(E) = A (p_1 G(c, \sigma_1; E) + p_2 G(c, \sigma_2; E) + p_3 G(c, \sigma_3; E) + p_{cs} S(c, \sigma_S, \sigma_W; E)) \quad (4.4)$$

where A is the peak area; p_1 , p_2 and p_3 are the proportions of each Gaussian, with $p_1 + p_2 + p_3 = 1$; p_{cs} is the proportion of Compton scattering. The background is modeled by a first order polynomial function of the energy.

The Gaussian function is defined in the usual way as:

$$G(c, \sigma; E) = \frac{1}{\sqrt{2\pi} \sigma} \exp\left(-\frac{(E - c)^2}{2 \sigma^2}\right) \quad (4.5)$$

The smoothed step function was defined as:

$$S(c, \sigma_S, \sigma_W; E) = \frac{\pi}{2} + \arctan\left(-\sigma_W \frac{E - c}{\sqrt{2} \sigma_S}\right) \quad (4.6)$$

The response function and its decomposition is shown in Figure 4.10.

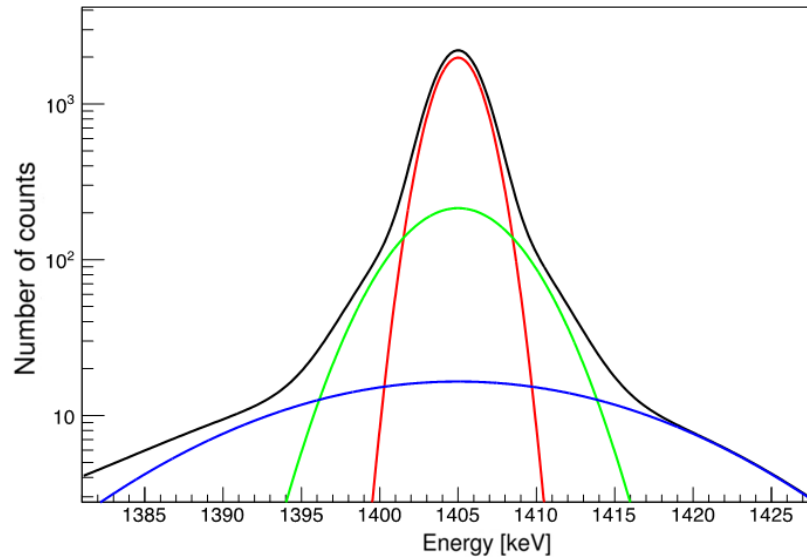


Figure 4.10: Fit function shape used to fit the γ -transition peaks (black curve). It is composed of three Gaussian functions (red, green, blue curves) and, of a smooth step function that models the Compton tail (not represented). The black curve is the final response function.

The idea was therefore to fix all the parameters of the fitting function using the transitions emitted by the $^{91}\text{Zr}(n, \gamma)$ and $^{92}\text{Zr}(n, \gamma)$ reactions because those reactions took place during a quite long part of the experiment, with the first target. Their peaks are a much better reference than the peaks obtained during the very short calibration runs with radioactive sources (such as ^{60}Co , ^{152}Eu).

The fitting results on the peak at 1405.06 keV is e.g. shown in Figure 4.11.

Best values of p_1 , p_2 and p_3 were found to be 0.75, 0.20 and 0.05 and do not seem to vary with energy. σ_1 is a first order polynomial function of the energy. Optimal σ_2 and σ_3 are proportional to σ_1 . The parameter p_{cs} is best fitted with a first order polynomial function of the energy. The best solution was found for $\sigma_W = \sigma_S$.

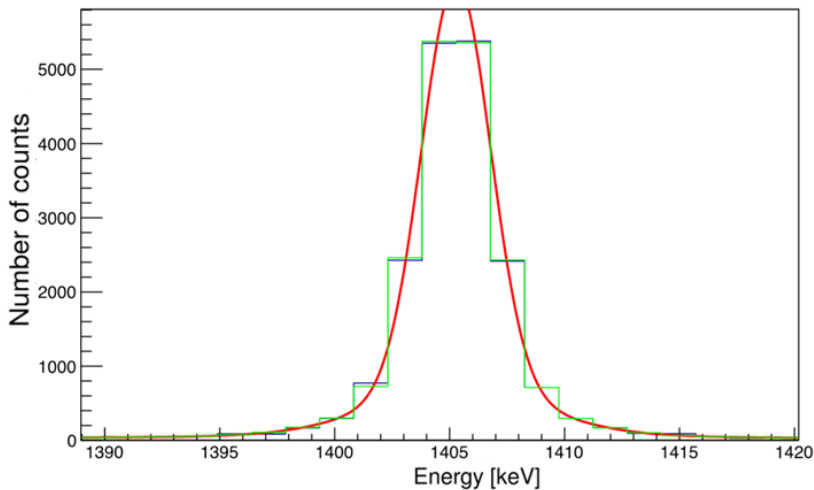


Figure 4.11: Peak of ^{92}Zr at 1405.1 keV used to adjust the new fit function. The red curve is the fit function. The green curve is the fit function integrated over the bins. Experimental data are in dark blue, almost invisible due to relatively good fit.

4.5 Intensity calculation

This section will describe in a more formal way the method used to calculate the intensity of a transition from the 3 sets (horizontal, vertical and diagonal) of count numbers. The method depends on the existence of contaminants, their position and intensities.

4.5.1 Gate slices fitting

First we put the 3 sets (horizontal, vertical and diagonal) of count numbers in separated histograms, see Figure 4.12. To find a good estimation of the desired γ -ray peak volume and the correct background, a fit of the set of areas across each slice is performed. This is an essential part of the new analysis technique and provides the values used in the basic concept equation (Equation 4.3).

The histograms give us also a possibility of finding and estimating contaminants. We use the response function described in the previous section to fit all the peaks that we find in the histogram and a constant function to fit the background. Small contaminating peaks on both sides of the desired γ -ray peak and their fit can be seen in the horizontal slice (a) in Figure 4.12.

In this way for each slice (horizontal, vertical and diagonal) we obtained: the area of the desired peak, the background and the area of any contaminating peak. These values are used in the next step to calculate the correct volume of the desired γ -ray peak. Based on the contamination position and area, we decide which calculation scheme is used. The calculation schemes are established by extending the basic concept equation (Equation 4.3).

4.5.2 No contamination

Let's take the same fission fragments F_1 and F_2 with their transitions T_A and T_B at energies E_A and E_B . Our goal is to calculate the intensity of transition T_X at energy E_X in coincidence with the transition T_A and T_B . Scanning the gates in three directions in the $E_1 \times E_2$ plane (horizontal, vertical and diagonal) around the region (E_A, E_B) gave us a large number of gated spectra, in which we fitted the peak associated to transition T_X . Let's call this fitted peak area $N(E_1, E_2)$. This situation with no contamination in the vicinity of the main gate is schematically represented in Figure 4.13

$N(E_1, E_2)$ is nothing else than the γ - γ matrix of events in coincidence with the transition T_X . If the values were available for all the positions around (E_A, E_B) , plotting $N(E_1, E_2)$ would display a 2D peak, quasi-Gaussian in both dimensions and centered on (E_A, E_B) . Our goal is to find the volume of this peak having in our hand the values across three slices. In reality, the difficulty does not lie really in finding the peak volume itself but to estimate the background below the peak.

Since $N(E_1, E_2)$ is a coincidence matrix, it is relatively easy to model the shape

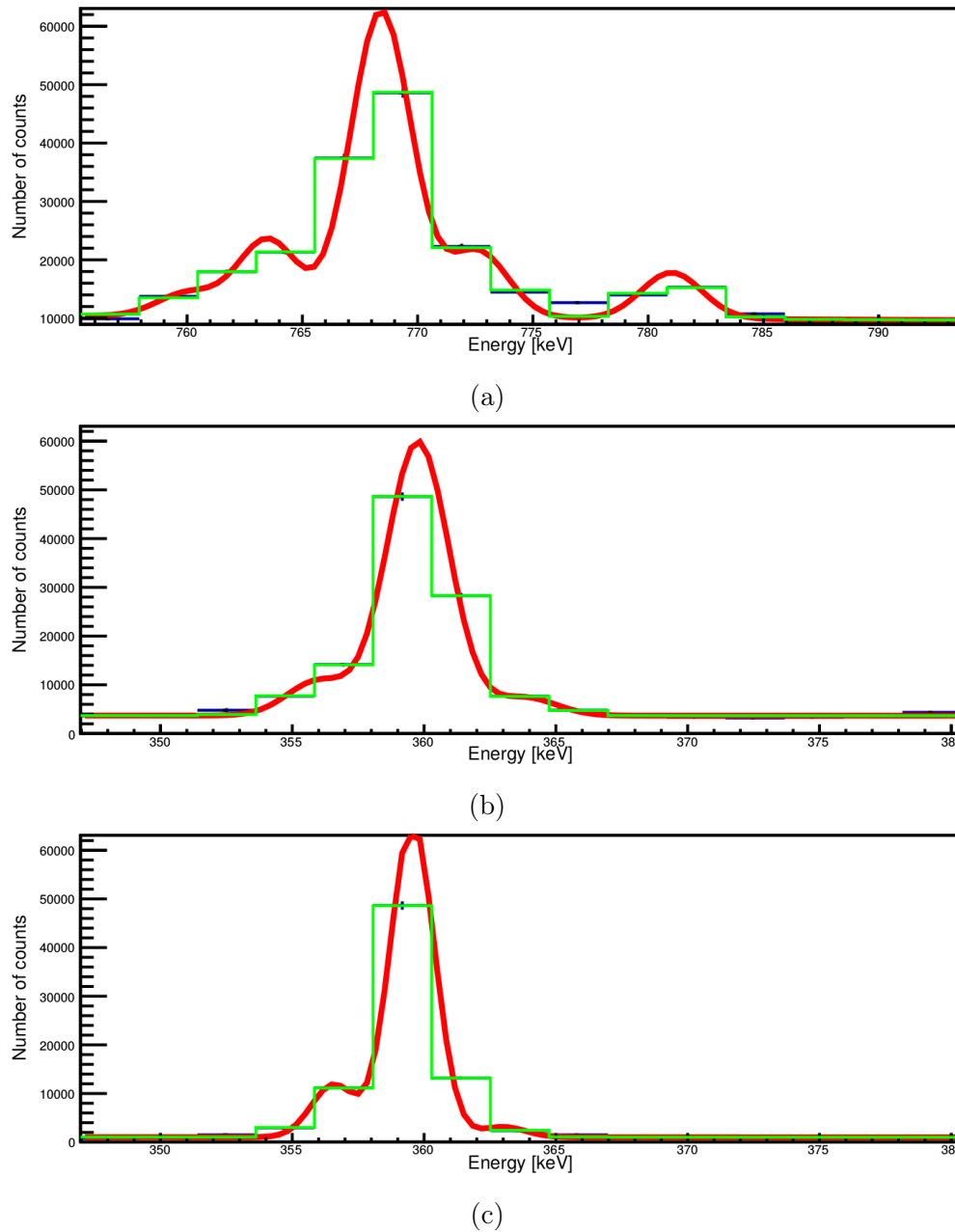


Figure 4.12: Histogram visualizing the horizontal (a), vertical (b) and diagonal (c) slice in the Polish cube. Dark blue lines denote the data (partially covered by the green lines), red lines denote the fit function and green lines denote the fit function integrated over the single gate size. The fit was performed on the γ -ray transition at 475.0 keV in ^{142}Ba . The initial gates are the transition at 769.0 keV in ^{92}Kr and the transition at 359.5 keV in ^{142}Ba . The same peak areas in the form of a cross can be seen in Figure 4.3. This fit was used in the ^{142}Ba analysis in Section 4.6.

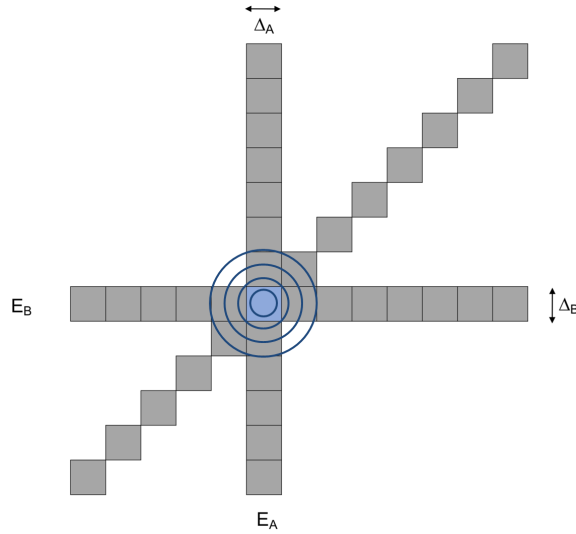


Figure 4.13: Schematic representation in the case of no contamination.

of a peak and its background using the response function of the detection system and some basic considerations of the coincidence process.

We described the response of the detection system in section 4.4.2 by Equation 4.4. It has a quasi-Gaussian shape, with a smoothed step function that models the incomplete detection of the transition energy in the detector. In this section, we slightly change the notation and we write $G_A(E_1)$ which is the response of the system to a transition with energy E_A .

The 2D distribution $N(E_1, E_2)$ in case of no contamination and no background is simply $N(E_1, E_2) = V G_A(E_1) G_B(E_2)$ where V is the volume of the peak. Here, to simplify the demonstration, we consider an infinitely small gate size.

In case of no contamination, in the vicinity of the peak, the γ -ray background from other fission fragments than F_1 and F_2 can be considered mostly constant. Compton scattering from higher energy transitions in the fragments F_1 will appear as a Gaussian horizontal tunnel. Indeed, such transitions are by construction in coincidence with T_B and their coincidence forms a peak on the right side of our peak, at the position (E'_A, E_B) with E'_A much larger than E_A . If that peak is away, then only the Compton tail is visible and its distribution along the horizontal axis is constant. Its distributions along the vertical axis follows the response of the system to T_B transition and it is quasi-Gaussian. There are often many transitions at high energy in fission fragments; the tunnel can be quite strong, especially at low energy. The same is valid for Compton

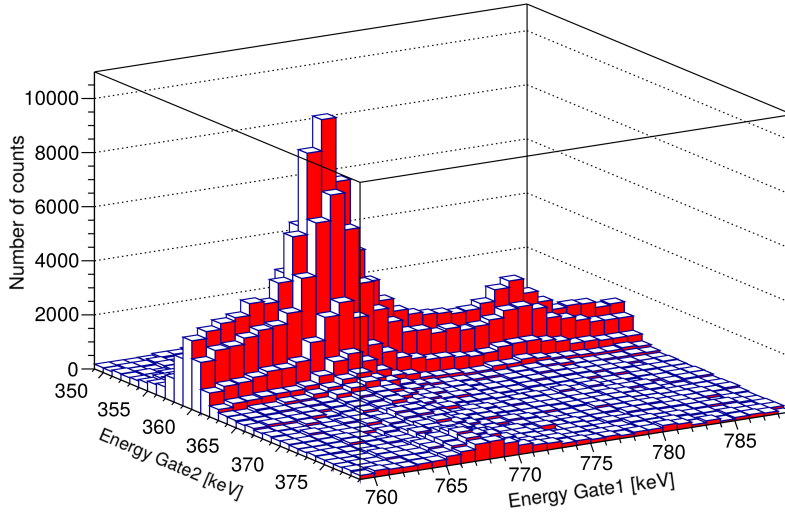


Figure 4.14: Coincidence matrix built from the fitted peak area at 475.0 keV. Details are explained in the text.

scattering from higher energy transitions in the fragments F_2 . Their coincidence with transition T_A appears as a vertical Gaussian tunnel.

Such horizontal and vertical lines are quite common in experimental coincidence matrices. To illustrate the shape of the peak and the tunnels, I calculated the 2D distribution $N(E_1, E_2)$ obtained for the 475.0 keV transition in ^{142}Ba for a large set of gates around the ^{142}Ba transition at 359.5 keV and the one in ^{92}Kr at 769.0 keV. It is shown in Figure 4.14. The peak at (769, 359) and the Gaussian tunnel $(-, 359)$ are quite strong. The tunnel at (769, -) is much weaker. A contaminant is visible around (781, 359). It can be related to the 781.4 keV transition in ^{91}Kr , in coincidence with the 359.5 keV and 475.0 keV transitions in ^{142}Ba .

Finally, $N(E_1, E_2)$ in case of no contamination in the vicinity of (E_A, E_B) can be modeled by:

$$N(E_1, E_2) = VG_A(E_1)G_B(E_2) + B_HG_B(E_2) + B_VG_A(E_1) + B_D \quad (4.7)$$

On the vertical slice, where $E_1 = E_A$, the distribution becomes:

$$N(E_A, E_2) = \underbrace{[VG_A(E_A) + B_H]}_{A'_V} G_B(E_2) + \underbrace{B_VG_A(E_A) + B_D}_{B'_V} \quad (4.8)$$

Fitting the experimental $N(E_A, E_2)$ with a simple quasi-Gaussian function (plus a constant background) gives the best estimation of A'_V and B'_V .

Similarly for the horizontal slice, where $E_2 = E_B$:

$$N(E_1, E_B) = \underbrace{[VG_B(E_B) + B_V]}_{A'_H} G_A(E_1) + \underbrace{B_H G_B(E_B) + B_D}_{B'_H} \quad (4.9)$$

and fitting the horizontal values gives A'_H and B'_H .

The diagonal slice is more complicated but it can still be approximated by the sum of a quasi-Gaussian function and a constant:

$$\begin{aligned} N(E, E) &= VG_A(E)G_B(E) + B_H G_B(E) + B_V G_A(E) + B_D \\ &\approx V'G(E) + B_D \end{aligned} \quad (4.10)$$

The product of two Gaussians with the same center but different σ is a Gaussian with $\frac{1}{\sigma} = \frac{1}{\sigma_A} + \frac{1}{\sigma_B}$. The width of the quasi-Gaussian varies with the energy of the peak, thus σ_A differs from σ_B . Therefore, the fit of the diagonal slice is usually not as good as the other ones but we will see that we are only interested in finding the best estimation of the constant value B_D .

Instead of trying to extract the volume V of the peak, we found more useful to estimate the equivalent quantity $N_X = VG_A(E_A)G_B(E_B)$.

The value of the distribution at the position (E_A, E_B) can be written as:

$$\begin{aligned} N(E_A, E_B) &= VG_A(E_A)G_B(E_B) + B_H G_B(E_B) + B_V G_A(E_A) + B_D + B_D - B_D \\ &= VG_A(E_A)G_B(E_B) + B'_H + B'_V - B_D \end{aligned} \quad (4.11)$$

And finally, we find:

$$N_X = N(E_A, E_B) - B'_H - B'_V + B_D \quad (4.12)$$

The volume of the peak V is the number of events in coincidence between the transitions T_X , T_A and T_B . N_X is the number of events in coincidence between the same transitions but for the restricted 2D region of energies with size $\Delta_A \times \Delta_B$. It has no impact on the rest of the process because one always deals with the relative number of counts by taking the ratio of the intensity of two transitions in the same gated spectrum.

One can observe that equation 4.12 is identical to equation 4.3. Taking into account the width of the gates requires averaging the fit function over the gate size. The fit of the slices are done in the EXILLANA code using ROOT with Minuit libraries. This option was already used to fit peaks in the gated spectra.

4.5.3 Contamination in the horizontal slice

When a contamination (contaminating peak) occurs in the vicinity of the peak at (E_A, E_B) , we need to consider its contribution to eventually remove it. We will at first consider a simple case. The contamination comes from a transition T_F that is emitted in coincidence with T_B and T_X and its energy E_F is close to E_A . Such a contamination happens e.g when T_F belongs to the fragment F_1 or another fission partner of F_2 . Its peak appears in the horizontal slice at (E_F, E_B) . This situation is schematically represented in Figure 4.15

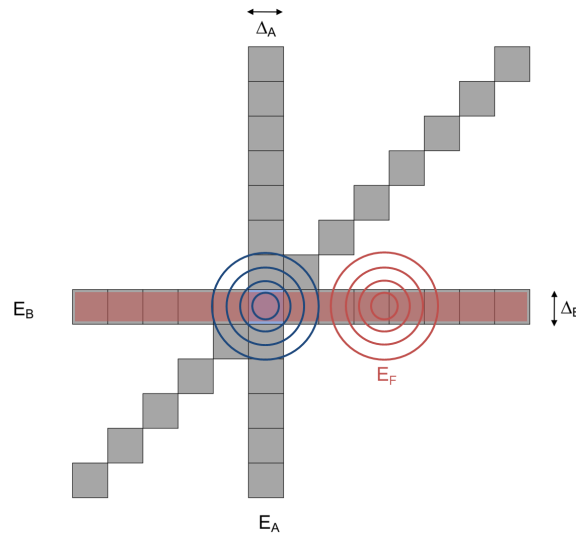


Figure 4.15: Schematic representation in the case of a contaminating peak in the horizontal slice.

The matrix $N(E_1, E_2)$ becomes:

$$N(E_1, E_2) = VG_A(E_1)G_B(E_2) + B_H G_B(E_2) + B_V G_A(E_1) + B_D + V_F G_B(E_2)G_F(E_1) \quad (4.13)$$

where V_F is the volume of the peak at (E_F, E_B) .

We try, like in the previous subsection, to estimate $N_X = VG_A(E_1)G_B(E_2)$.

On the vertical slice ($E_1 = E_A$) we have:

$$N(E_A, E_2) = \underbrace{[VG_A(E_A) + B_H + V_F G_F(E_A)]}_{A'_V} G_B(E_2) + \underbrace{B_V G_A(E_A) + B_D}_{B'_V} \quad (4.14)$$

For the horizontal slice ($E_2 = E_B$):

$$N(E_1, E_B) = \underbrace{[VG_B(E_B) + B_V]}_{A'_H} G_A(E_1) + \underbrace{V_F G_B(E_B)}_{C'_H} G_F(E_1) + \underbrace{B_H G_B(E_B) + B_D}_{B'_H} \quad (4.15)$$

For the value at (E_A, E_B), one can reorganize the terms in two different ways:

$$N(E_A, E_B) = \underbrace{[VG_B(E_B) + B_V]G_A(E_A)}_{N_H} + \underbrace{V_F G_B(E_B)G_F(E_A)}_{N_F} + \underbrace{B_H G_B(E_B) + B_D}_{B'_H} \quad (4.16)$$

$$= \underbrace{VG_A(E_A)G_B(E_B) + B_V G_A(E_A)}_{N_X} + N_F + B'_H \quad (4.17)$$

Then, by comparing 4.16 and 4.17, one obtains:

$$N_H + \cancel{N_F} + \cancel{B'_H} = N_X + \underbrace{B_V G_A(E_A) + B_D - B_D}_{B'_V} + \cancel{N_F} + \cancel{B'_H} \quad (4.18)$$

$$N_H = N_X + B'_V - B_D$$

and finally one can estimate N_X from:

$$N_X = N_H - B'_V + B_D \quad (4.19)$$

with $N_H = A'_H G_A(E_A)$. The value of B_D is obtained as before from the fit of the diagonal slice, B'_V from the fit of the vertical slice.

One should now consider the size of the gate in the calculation of N_H . It is done by averaging its value over the gate. It becomes:

$$N_H = \frac{1}{\Delta_A} \int_{E_A - \frac{\Delta_A}{2}}^{E_A + \frac{\Delta_A}{2}} A'_H G_A(E) dE \quad (4.20)$$

The whole process is applied only when the contaminant is close to the main peak and it is strong enough to disturb its area. Otherwise, the "no contamination" algorithm is used. This condition is checked by comparing the impact of the contamination with the uncertainty on N_X .

A similar analysis can be developed when the contamination appears in the vertical slice. It results in an analog result: $N_X = N_V - B'_H + B_D$

4.5.4 Contamination in both slices

We will now consider the case of contamination peaks in both: the horizontal and vertical slices. Let's take the same horizontal contaminant transition T_F as in the previous example and we add a contaminant transition T_E at E_E in the vertical slice. This situation is schematically represented in Figure 4.16

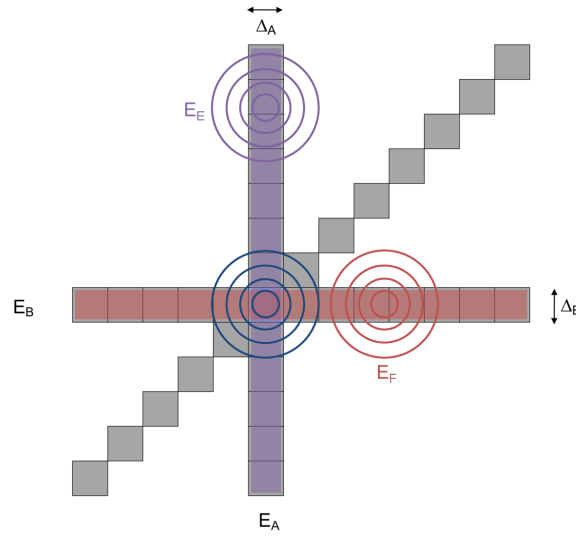


Figure 4.16: Schematic representation in the case of contaminating peaks in the horizontal and the vertical slice.

The equation describing $N(E_1, E_2)$ takes the form:

$$N(E_1, E_2) = VG_A(E_1)G_B(E_2) + B_H G_B(E_2) + B_V G_A(E_1) + B_D + V_F G_B(E_2)G_F(E_1) + V_E G_A(E_1)G_E(E_2) \quad (4.21)$$

For the vertical slice ($E_1 = E_A$):

$$N(E_A, E_2) = \underbrace{[VG_A(E_A) + B_H + V_F G_F(E_A)]}_{A'_V} G_B(E_2) + \underbrace{V_E G_A(E_A)}_{C'_V} G_E(E_2) + \underbrace{B_V G_A(E_A) + B_D}_{B'_V} \quad (4.22)$$

The contribution of the transition T_C with

$$N(E_1, E_2) = VG_A(E_1)G_B(E_2) + B_H G_B(E_2) + B_V G_A(E_1) + B_D + V_C G_{C1}(E_1)G_{C2}(E_2) \quad (4.25)$$

For vertical gates ($E_1 = E_A$):

$$N(E_A, E_2) = \underbrace{[VG_A(E_A) + B_H]}_{A'_V} G_B(E_2) + \underbrace{B_V G_A(E_A) + B_D}_{B'_V} + \underbrace{V_C G_{C1}(E_A)}_{C'_V} G_{C2}(E_2) \quad (4.26)$$

For horizontal gates ($E_2 = E_B$):

$$N(E_1, E_B) = \underbrace{[VG_B(E_B) + B_V]}_{A'_H} A'_H G_A(E_1) + \underbrace{B_H G_B(E_B) + B_D}_{B'_H} + \underbrace{V_C G_{C2}(E_B)}_{C'_H} G_{C1}(E_1) \quad (4.27)$$

The process is similar to the previous cases, and the same results are obtained either from:

$$N_X = N_V - B'_H + B_D \quad (4.28)$$

or from:

$$N_X = N_H - B'_V + B_D \quad (4.29)$$

with $N_H = A'_H G_A(E_A)$ and $N_V = A'_V G_B(E_B)$.

Because the fits are not perfect and N_X calculated from each of the Equations 4.28 or 4.29 is a bit different, we use the weighted average of two N_X values to calculate the final N_X .

4.5.6 Other cases

More complicated contaminants were considered in the EXILLANA code (see Figure 4.18 and Figure 4.19). I will not give their detailed calculations.

I want to emphasize that for all the cases, I derived uncertainties and I have implemented them in the software.

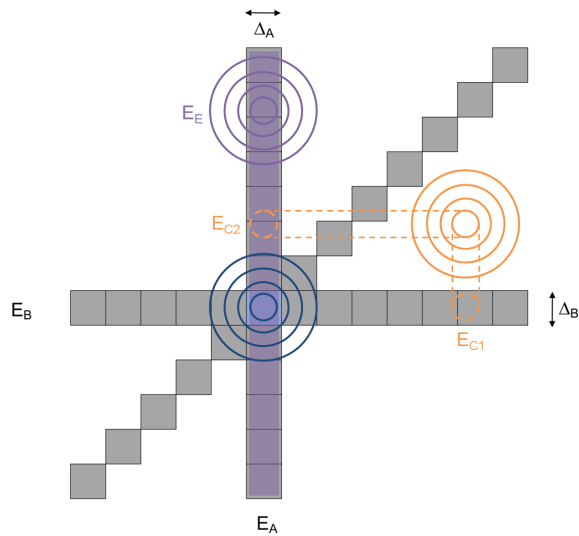


Figure 4.18: Schematic representation in the case of a contaminating peak in the vertical slice and another one anywhere in the (E_1, E_2) plane.

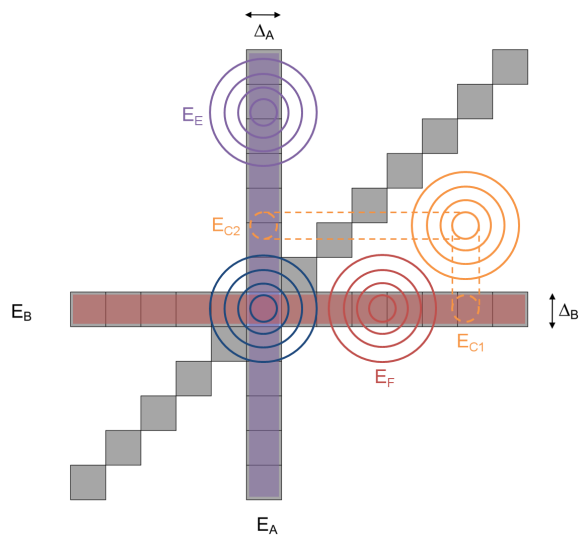


Figure 4.19: Schematic representation in the case of three contaminating peaks: in the vertical slice, in the horizontal slice and the third one anywhere in the (E_1, E_2) plane.

4.6 Performance of the new analysis method

To evaluate the new analysis technique, I will compare the intensities of the discrete γ -ray transitions of ^{142}Ba , well produced in the $^{235}\text{U}(n_{th}, f)$ process, extracted with this new analysis technique (with the EXILLANA software) and with the standard technique. Both sets of results will be compared with the existing experimental data coming from the spontaneous fission of ^{248}Cm [Urb+97].

4.6.1 Motivations of the ^{142}Ba selection

There are several reasons why ^{142}Ba seems to be a good candidate for studying the new analysis technique. Firstly, ^{142}Ba and its fission partners (the isotopes of krypton) belong to the most produced fragments in the $^{235}\text{U}(n_{th}, f)$ reaction (see Table 5.1 in Chapter 5). γ -transition peaks in the gated spectra should thus have a very high statistics, which will allow us to keep low uncertainties. Secondly, ^{142}Ba is an even-even nucleus having a relatively simple nuclear structure. Its level scheme is simpler in comparison to even-odd or odd-odd nuclei. ^{142}Ba was already well studied with other reactions. In particular, a well detailed level scheme was obtained using EUROGAM2 at Strasbourg [Urb+97]. It is reproduced in Figure 3.12. Most of the transitions are larger than 200 keV and they appear in our spectra far away from the region of low energies (below about 100 keV) dominated by Compton background. This makes them less prone to contamination. Additionally, there is only one known γ -transition (359.5 keV) going directly to the ground state which is produced in fission, see Figure 3.12. It simplifies the analysis and the normalization process. All other γ -rays emitted in the de-excitation cascade of ^{142}Ba are thus feeding this state. The other known transitions to the ground state, which were observed e.g. after β -decay [Sco+80], do not seem to be produced in fission.

The most produced fission partner of ^{142}Ba in $^{235}\text{U}(n_{th}, f)$ is ^{92}Kr because two neutrons are emitted in total by this pair, which is close to 2.42 - the average total prompt-neutron multiplicity of ^{235}U [Nis+98; LSB15]. In addition, the level scheme of ^{92}Kr is well determined and there is only one well known γ -transition (769.0 keV) going directly to the ground state that is populated in fission, see Figure 3.11. This was helpful during the gating procedure and facilitated our analysis.

4.6.2 Experimental data extraction

To validate our new analysis methodology of intensity extraction performed with the EXILLANA software and to see how precise it is, we compared our data on ^{142}Ba with the published results of the transitions measurement obtained in the $^{248}\text{Cm}(sf)$ reaction [Urb+97]. In that study, most of the transitions were extracted from the spectrum double-gated on ^{142}Ba : on the $4^+ \rightarrow 2^+$ transition at 475.0 keV and on the $2^+ \rightarrow 0^+$ transition at 359.5 keV. Missing transitions were then measured by using one gate in a Zr fragment. The exact Zr isotope was not indicated in [Urb+97] but we suppose that it was ^{102}Zr because ($^{102}\text{Zr} - ^{142}\text{Ba}$) has the highest yield among the (Zr - ^{142}Ba) fission fragment pairs for $^{248}\text{Cm}(sf)$.

We extracted from the EXILL data all the transitions that we could identify and measure. In comparison to the $^{248}\text{Cm}(sf)$ data [Urb+97] some transitions are missing due to either very low statistics or a contamination which makes their precise measurement impossible. For both analysis techniques, the standard one, using the Polish software, and the new one, using the EXILLANA code, triple coincidence spectra were created with the same transitions. We chose ^{92}Kr as the (post-neutron-evaporation) fission partner by gating on the $2^+ \rightarrow 0^+$ transition at 769.0 keV, which has the highest intensity in the ^{92}Kr de-excitation cascade. The second gate was placed on the $2^+ \rightarrow 0^+$ transition at 359.5 keV in ^{142}Ba , which is also the most intense transition. From the triple- γ coincidence spectra with such gates I extracted all transition intensities of ^{142}Ba presented in Table 4.1 (EXILL data old - data obtained with the standard technique, EXILL data new - data obtained with the new technique) except for $2^+ \rightarrow 0^+$ transition at 359.5 keV which was measured from the spectrum double-gated in ^{92}Kr (gated at 769.0 keV and 1034.0 keV). All intensities were normalized to the $4^+ \rightarrow 2^+$ transition at 475.0 keV.

4.6.3 Analysis results

The result of my analysis is summarized in Table 4.1 where I present the measured transitions and their intensities with uncertainties. Some transitions measured with the standard technique (at 412.1 keV, 706.8keV and 912.6 keV, see Table 4.1) showed a large discrepancy in comparison to the experimental data coming from the spontaneous fission of ^{248}Cm [Urb+97]. If we compare the $^{235}\text{U}(n_{th}, f)$ to the $^{248}\text{Cm}(sf)$ process, in first instance, there is no reason which could explain strong discrepancies. The

initial state of ^{142}Ba in both fissioning systems seems to be similar. The prompt-neutron multiplicity for fission fragments with mass around $A = 142$ is close to 1.2 for $^{235}\text{U}(n_{th}, f)$ [Nis+98] and close to 1.5 for ^{248}Cm [Kal+02]. This suggests that the initial excitation energy of ^{142}Ba and thus its de-excitation cascade may be similar and the intensities of γ -rays should not differ much between both fissioning systems. On the other hand, other factors, like the distribution of primary fragment spins may have an impact and explain the observed difference. The verification of discrepancies with the new analysis technique was an additional factor that encouraged us to analyze ^{142}Ba .

Comparison with the standard technique

A common feature of almost all intensities in Table 4.1 is that, with the new technique, their values have been reduced. A simple explanation is that with much smaller gates and a considerably better control over the contamination detection and elimination, counts coming from contaminating peaks have been removed. It is especially visible with γ -rays at 412.1 keV, 706.8 keV and 912.6 keV. Their huge overestimation in the EXILL data coming from the analysis with the standard technique have been radically decreased.

Worth noting is also the fact that for the γ -rays with relatively high intensities, thus high count rates, differences between intensities obtained with the two methods stay lower than uncertainties. It can be seen for transitions at 487.0 keV and 631.1 keV.

We analyzed the fission fragments pair which has one of the highest yields for $^{235}\text{U}(n_{th}, f)$ reaction thus we can assume that the most intense γ -ray peaks of ^{142}Ba are not especially vulnerable to contamination because there are not many other peaks having comparably high statistics. Less intense transitions are proportionally much more exposed to contamination because their statistics is lower than the statistics of the most intense transitions of many other fission fragments. It means that, large Compton tails coming from the Compton scattering of γ -rays at higher energy can be by mistake associated to the measured peaks. This can explain the higher intensities measured with the standard technique where gates are multiple times wider than for the new technique. Much more events associated to the Compton scattering can be then falsely included in the measured peaks.

E_γ (keV)	E_i^{level} (keV)	E_f^{level} (keV)	Transition	I_γ			I_γ Relative difference [%]	
				^{248}Cm data	EXILL data old	EXILL data new	EXILL old to ^{248}Cm	EXILL new to ^{248}Cm
276.8	2229.06	1952.64	$8_2^+ \rightarrow 7_1^-$	2.7(4)	3.1(3)	2.2(5)	13.7	-17.1
306.9	1848.05	1541.12	$6_2^+ \rightarrow 5_1^-$	4.7(5)	6.7(4)	5.9(5)	41.6	25.1
323.2	2069.98	1746.96	$7_1^{(+)} \rightarrow 5_1^{(+)}$	1.8(4)	2.0(2)	1.8(8)	11.9	3.8
354.3	2513.52	2159.15	$9_1^- \rightarrow 8_1^+$	6.0(5)	4.7(3)	5.6(6)	-22.3	-7.5
359.5	359.50	0.00	$2_1^+ \rightarrow 0_1^+$	118(6)		125(5)		6.3
380.9	2229.06	1848.05	$8_2^+ \rightarrow 6_2^+$	7.7(9)	11.0(4)	5.0(8)	43.5	-34.2
412.1	2925.63	2513.52	$(10_2^+) \rightarrow 9_1^-$	1.2(2)	5.1(6)	1.8(9)	333.9	52.5
475.0	834.50	359.50	$4_1^+ \rightarrow 2_1^+$	100	100	100	0.0	0.0
487.0	1952.64	1465.70	$7_1^- \rightarrow 6_1^+$	21(2)	10.1(8)	9(1)	-52.2	-55.4
560.9	2513.52	1952.64	$9_1^- \rightarrow 7_1^-$	5.3(5)	7.5(4)	5.0(6)	41.2	-5.7
585.7	2814.64	2229.06	$(10_1^+) \rightarrow 8_2^+$	6.5(6)	5.5(5)	5(1)	-14.7	-21.2
609.8	2679.92	2069.98	$(9_1^+) \rightarrow 7_1^{(+)}$	4.5(9)	6.9(5)	4(1)	53.2	0.7
631.1	1465.70	834.50	$6_1^+ \rightarrow 4_1^+$	47(4)	50.8(8)	52(2)	7.8	11.0
640.1	3153.62	2513.52	$(11_1^-) \rightarrow 9_1^-$	5.9(1)	7.1(8)	3(2)	20.1	-51.3
693.4	2159.15	1465.70	$8_1^+ \rightarrow 6_1^+$	15(2)	18.6(9)	15(1)	21.9	-3.2
706.8	1541.12	834.50	$5_1^- \rightarrow 4_1^+$	7.1(7)	17.6(9)	13(1)	149.3	81.8
766.5	2925.63	2159.15	$(10_2^+) \rightarrow 8_1^+$	2.7(4)	4.4(4)	3.0(9)	61.3	8.9
912.6	1746.96	834.50	$5_1^{(+)} \rightarrow 4_1^+$	4.1(6)	7.6(4)	5.7(6)	84.7	39.4
932.8	1292.30	359.50	$3_1^{(-)} \rightarrow 2_1^+$	2(1)	1.9(3)	1.4(5)	-19.6	-41.4
1013.6	1848.05	834.50	$6_2^+ \rightarrow 4_1^+$	3.4(5)	4.5(3)	4(1)	33.1	6.4

Table 4.1: Relative intensities (I_γ) of the γ -ray transitions (keV) in ^{142}Ba , normalized to the $4_1^+ \rightarrow 2_1^+$ transition (475.0 keV). ^{248}Cm data comes from [Urb+97]. EXILL data analyzed with the standard technique (EXILL data old) comes from [Ra15]. The fission partner of ^{142}Ba for the EXILL data analyzed both with the standard and the new technique (EXILL data new) was ^{92}Kr , for [Urb+97] it was a complementary Zr fragment. To the intensities measured with the standard technique from the EXILL data additional 10% uncertainty has to be added due to the uncertainty of the background selection.

Contamination detection with the new technique

Let's take the γ -transition at 706.8 keV in ^{142}Ba which showed clear discrepancy in the intensity measurement between the standard and the new analysis technique, see Table 4.1. I will try to look for the contamination with both techniques. Starting with the standard technique we need to select the first gate and the first background to be subtracted. We chose the γ -transition at 769.0 keV from ^{92}Kr and we put a two-bins gate and two background regions adjacent to the gate, see Figure 4.20.

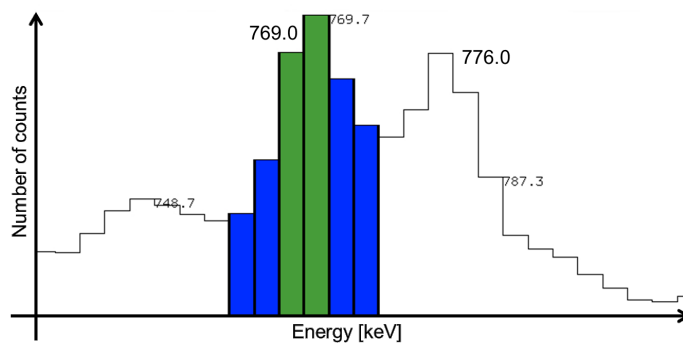


Figure 4.20: The selection process of the first gate and the background with the standard technique. The gate is put at the γ -transition at 769.0 keV from ^{92}Kr . The horizontal axis is not placed at the zero counts.

One can see that the two-bins gate which we selected is not visibly contaminated. There can be only some traces of the peak at 776.0 keV included. After the gating procedure and the background subtraction we obtain a spectrum in single coincidence. From this spectrum we select the second gate and the second background. We chose the γ -transition at 359.5 keV in ^{142}Ba and again two adjacent backgrounds, see Figure 4.21. As before, the gate is not contaminated or there are only very small traces of the peak at 348.2 keV included.

To be sure that there is no contamination hidden in the peak we reversed the procedure by gating first at 359.5 keV (Figure 4.22) and than at 769.0 keV (Figure 4.23). The new spectra do not show any γ -ray peaks that contaminate the gates. The transitions at 753.3 keV and 781.0 keV in Figure 4.23 are too small and too far to contaminate the core of the selected peak (2 keV in the middle of the peak which is selected during gating). No matter in what order I have selected the gates, peaks are not deformed what allows me to assume that the gates are not contaminated by the

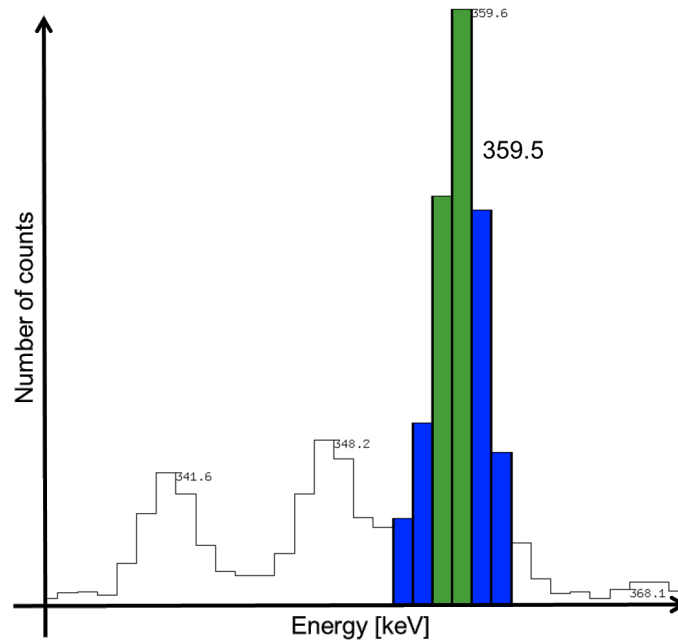


Figure 4.21: The selection process of the second gate and the background with the standard technique. The gate is put at the γ -transition at 359.5 keV from ^{142}Ba . The horizontal axis is not placed at the zero counts.

peaks which are placed within the gate width.

The γ -transition peak in triple coincidence at 706.8 keV (^{142}Ba) does not show any contamination content, see Figure 4.24. The peak is not deformed and the background is clearly visible. Small traces of the peaks at 693.4 keV and at 715.3 keV can be easily fitted and removed. During the analysis with the standard technique the γ -transition at 706.8 keV and the gates seem to be clean and there are no signs of possible problems with intensity values.

Let's analyze the same case with the new technique. As said in Section 4.2 we need to scan the gates and to do so we create many spectra which are shifted in reference to the main gates at 769.0 keV and 359.5 keV. After creating the triple- γ coincidence spectra without subtracted background, we need to select the region of interest, see Figure 4.25. It needs to contain the γ -transition at 706.8 keV and the region limits have to be the same for each spectrum. We selected a region between 671 keV and 715 keV. The peak at 706.8 keV is clearly separated from other peaks. Afterwards, I used the EXILLANA software to perform the fits for all spectra. The results of the fits and found peaks are presented in Figure 4.26. One can see that the closest peaks are at

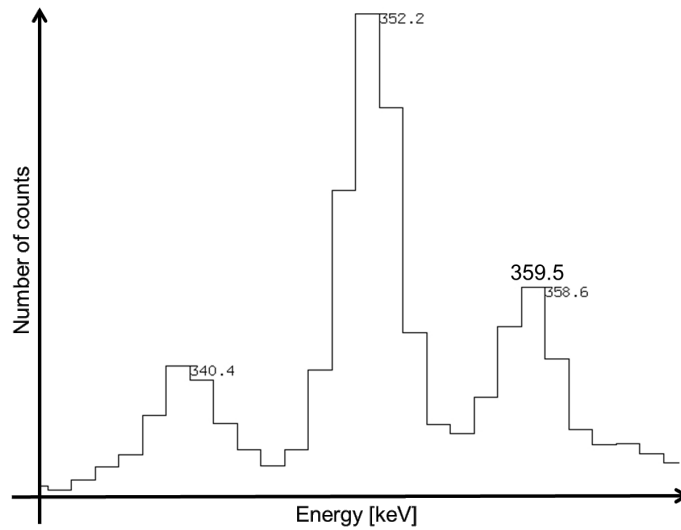


Figure 4.22: The spectrum without coincidence. The first gate is put at the γ -transition at 359.5 keV from ^{142}Ba . The horizontal axis is not placed at the zero counts.

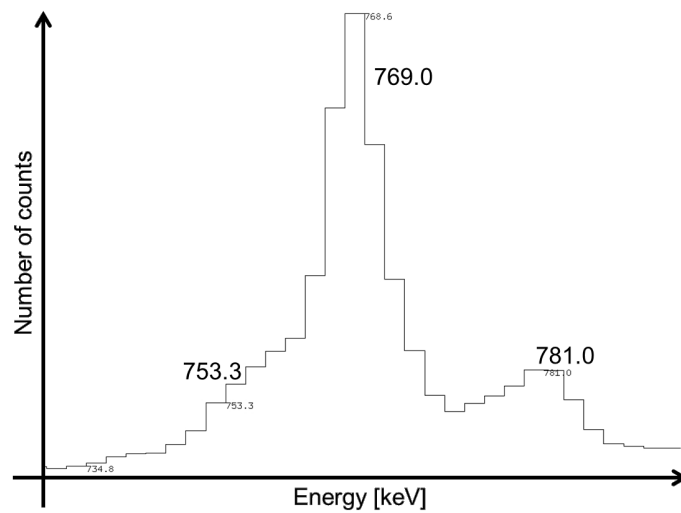


Figure 4.23: The spectrum in simple coincidence with the γ -transition at 359.5 keV (^{142}Ba) obtained with the standard technique. The second gate is put at the γ -transition at 769.0 keV from ^{92}Kr . The horizontal axis is not placed at the zero counts.

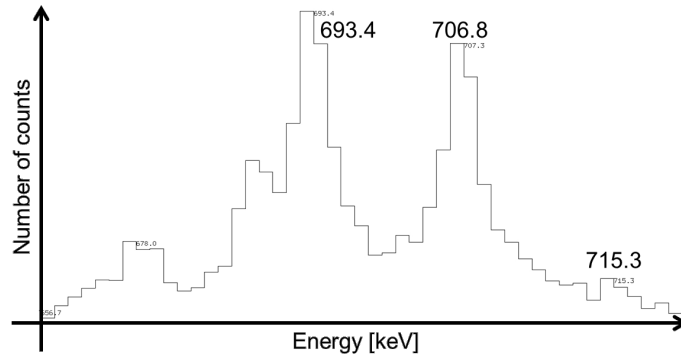


Figure 4.24: The triple- γ coincidence spectrum zoomed at the desired γ -ray at 706.8 keV (^{142}Ba). The selected gates are the γ -transitions at 769.0 keV (^{92}Kr) and at 359.5 keV (^{142}Ba). The horizontal axis is not placed at the zero counts.

around 703 keV and 713 keV. These peaks are too far and too weak to contaminate the 706.8 keV peak.

Finally, we need to build histograms with the numbers of counts from the fits for three gate slices and then fit them, see Section 4.5. Vertical and diagonal slices are clean but the peak in the horizontal slice is contaminated, see Figure 4.27. There is a clear contaminant at around 772 keV where the transition at 706.8 keV has a higher intensity than in the main gate at 769.0 keV. Its influence can be easily anticipated and the correct intensity of the γ -transition at 706.8 keV can be calculated by using the derived calculated schemes accounting for the contamination placement and strength, see Section 4.5.3.

This example clearly shows that by using the new technique, one has much better control over the background, and the contamination detection is much easier. As can be seen in Table 4.1, due to the correct contamination removal the γ -transition intensity at 706.8 keV is reduced by more than 25%. In the standard technique, during the first background subtraction (close to 769.0 keV), I removed part of the contamination at 772 keV but I was not able to see or evaluate if any traces are left in the gate. The new technique allowed me to treat the contamination in the correct way, to find the appropriate background and to find the correct intensity.

The found contamination is the γ -transition at 771.4 keV from ^{91}Kr . It is a transition with a relatively strong intensity according to [RU+17a]. ^{91}Kr is the fission partner of ^{142}Ba in the $^{235}\text{U}(n_{th}, f)$ process and the number of the emitted neutrons is 3. It is

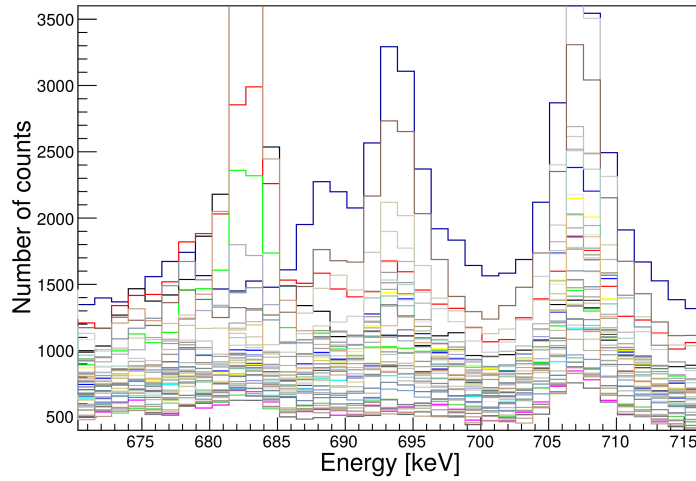


Figure 4.25: The representation of the region of interest for the γ -transition at 706.8 keV (^{142}Ba). The main gates are the γ -transitions at 769.0 keV (^{92}Kr) and at 359.5 keV (^{142}Ba).

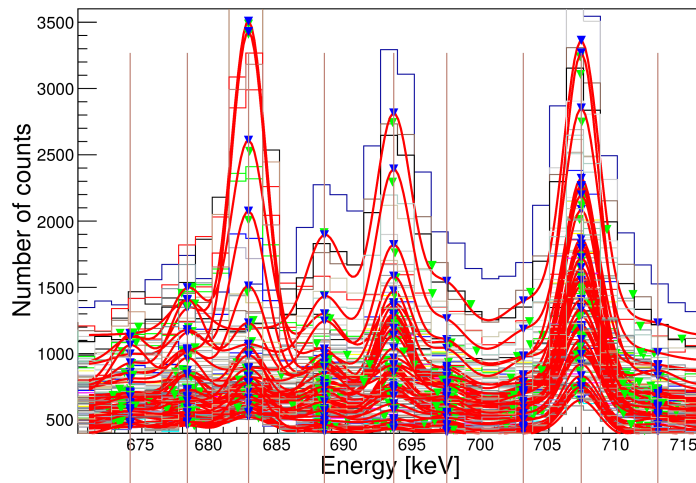
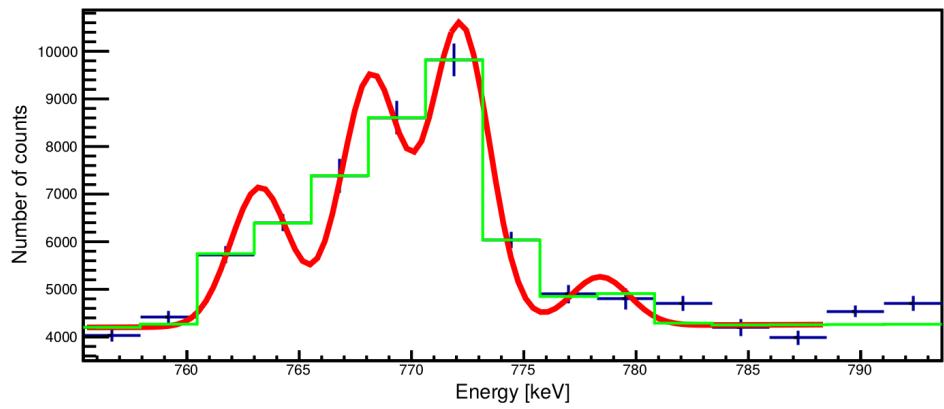
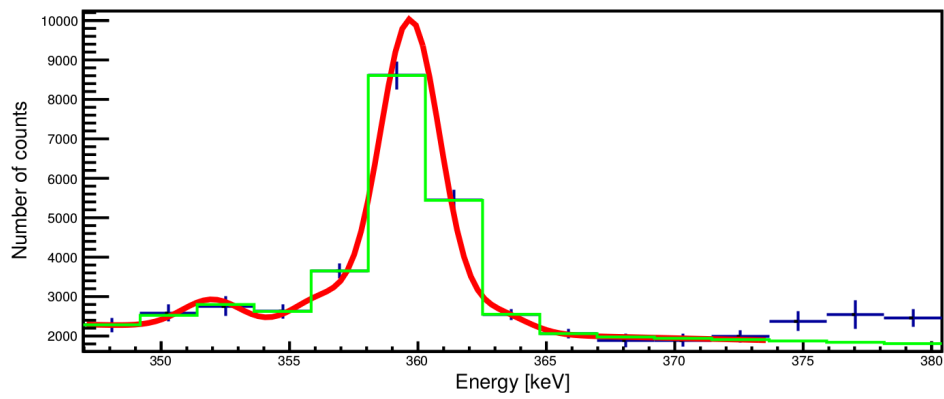


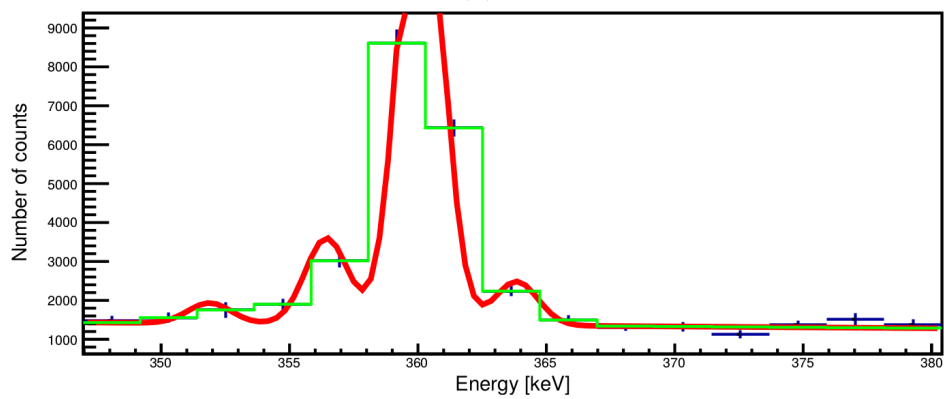
Figure 4.26: The fits of the region of interest for the γ -transition at 706.8 keV (^{142}Ba) for all spectra in triple coincidence. The main gates are the γ -transitions at 769.0 keV (^{92}Kr) and at 359.5 keV (^{142}Ba).



(a)



(b)



(c)

Figure 4.27: The fit of the horizontal (a), vertical (b), and diagonal (c) gate slices for the γ -transition at 706.8 keV (^{142}Ba). The main gates are the γ -transitions at 769.0 keV (^{92}Kr) and at 359.5 keV (^{142}Ba).

Comparison to the ^{248}Cm data

Both observations are well summarized by a χ^2 comparison. We calculated two reduced χ^2 values. The first one compares the EXILL results obtained with the standard method and the $^{248}\text{Cm}(sf)$ results. The second one compares the EXILL results obtained with the new analysis technique and the $^{248}\text{Cm}(sf)$ results. We considered the intensities of all measured γ -rays listed in Table 4.1 except the γ -transition at 359.0 keV and 475.0 keV. The first one was not analyzed with the standard technique, the second one is the normalization. The reduced χ^2 calculated for the intensities measured with the new technique is equal to 2.91 and is significantly lower than 12.93 obtained for the standard technique. The relative differences between the intensities, presented in Table 4.1, are lower with the new technique. Unfortunately, this comes at the cost of an increase of uncertainty for the new technique. The lower statistics caused by the much smaller gate-size and the contamination removal process, which inherently has some uncertainty level, contribute to the increase of the overall uncertainty on the γ -ray intensity. Nevertheless, we are much more confident about the results and their uncertainties obtained with the new analysis method because they take into account much more factors than the standard technique. Moreover, there is, as already mentioned in Section 3.3.5, up to 10% uncertainty on the results obtained with the standard analysis method due to difficulties with the background selection.

The γ -ray intensity comparison has shown an additional problem with the standard technique using wide gates. It is very vulnerable to contamination and there is no method to predict how much it influences the measured values. Therefore, there is an additional uncertainty on this analysis technique, not currently included, which is impossible to estimate. This basically limits the usage of the standard analysis technique with the EXILL data to measurements of only some γ -ray transitions with the highest intensities.

In conclusion, the ^{142}Ba analysis has shown a direct impact of the new analysis technique on the results and their physical interpretation.

Chapter 5

Studies on ^{100}Zr

5.1 Introduction

This chapter presents our study of the discrete γ -ray cascade in a well produced fission fragment, ^{100}Zr , and the dependence of its γ -ray cascade with its fission partner (with the number of evaporated neutrons). Transition intensities were extracted from the EXILL data using the method explained in Chapter 4 and were compared to the results from the FIFRELIN calculations.

As detailed in Chapter 2, FIFRELIN is a living code and the developers implemented different options for the primary fission fragments entry states, several models for the nuclear level densities, for the photon strength functions, etc. This reflects of course the current lack of knowledge on the fission process and the de-excitation of the fission fragments as well as on the nuclear structure itself. One of the initial purposes of the study was to benchmark FIFRELIN, to find the models that fit our data and to optimize their parameters. At the end, we believe that we reached some conclusions on the processes themselves. Several models in FIFRELIN were tested to see which one best reproduces experimental data and a particular study was done on the spin-distribution models to test the dependence of the initial spin-distribution of the primary fission fragment with the excitation energy.

There are several reasons why ^{100}Zr was finally the best candidate to make this study. The first one is that ^{100}Zr and its fission partners (the isotopes of Tellurium) belong to the most produced fragments in the $^{235}\text{U}(n_{th}, f)$ reaction (see Table 5.1). The next ones are related to the nuclear structure of ^{100}Zr . It is an even-even nucleus and its level scheme is simpler (in comparison to even-odd or odd-odd nuclei). ^{100}Zr was

already well studied with other reactions. In particular, a well detailed level scheme was obtained at LBNL using Gammasphere [Hwa+06]. It is reproduced in Figure 5.1. One observes that most of the transitions are larger than 200 keV. They appear in our spectra far away from the region of low energies (below about 100 keV) dominated by Compton background. One sees also that there is only one γ -transition (212.6 keV) going directly to the ground state in the level scheme in Figure 5.1 and all the γ -ray cascades are thus feeding this state. It simplifies tremendously the analysis and the normalization process. The other known transitions to the ground state, which were observed e.g. after β -decay [Woh+86], do not seem to be emitted by the de-exciting fission fragment in the prompt γ -ray cascade. Finally, the level schemes of the fission partners of ^{100}Zr (Te isotopes) are also well determined, what was helpful during our analysis.

Z1 - Z2	Elements	Y(Z)
38 - 54	Sr - Xe	19.7
40 - 52	Zr - Te	18.1
36 - 56	Kr - Ba	15.6
39 - 53	Y - I	12.0
37 - 55	Rb - Cs	11.4
41 - 51	Nb - Sb	7.4
35 - 57	Br - La	5.7
34 - 58	Se - Ce	4.3
42 - 50	Mo - Sn	3.9
33 - 59	As - Pr	0.9

Table 5.1: The most produced elements in the $^{235}\text{U}(n_{th}, f)$ reaction and their charge yields according to JEFF-3.3.

In this work, our intention was not to study the structure of ^{100}Zr and we did not try to find new transitions or levels or to improve any branching ratio. On the other hand, the nuclear structure of ^{100}Zr plays an important role in our interpretation. A major feature is that ^{100}Zr is a deformed nucleus and when it is produced by fission, its de-excitation proceeds mainly through the ground state band, which is a rotational band.

Another interesting feature of ^{100}Zr is that it exhibits a clear coexistence of two

deformed shapes at low excitation energy [Hwa+06]. The ground state band (band (1) in Figure 5.1) is interpreted as the rotational band of a well deformed prolate shape. A slightly oblate shape is associated to band (4) built on top of the 331.1 keV. Other bands could possibly be associated to a triaxial shape. This feature was not exploited in this work although we made some tentative study. The reason is that the oblate shape is not strongly populated in fission and the transitions belonging to this band could barely be measured when e.g. we wanted to study their evolution as a function of the fission partner.

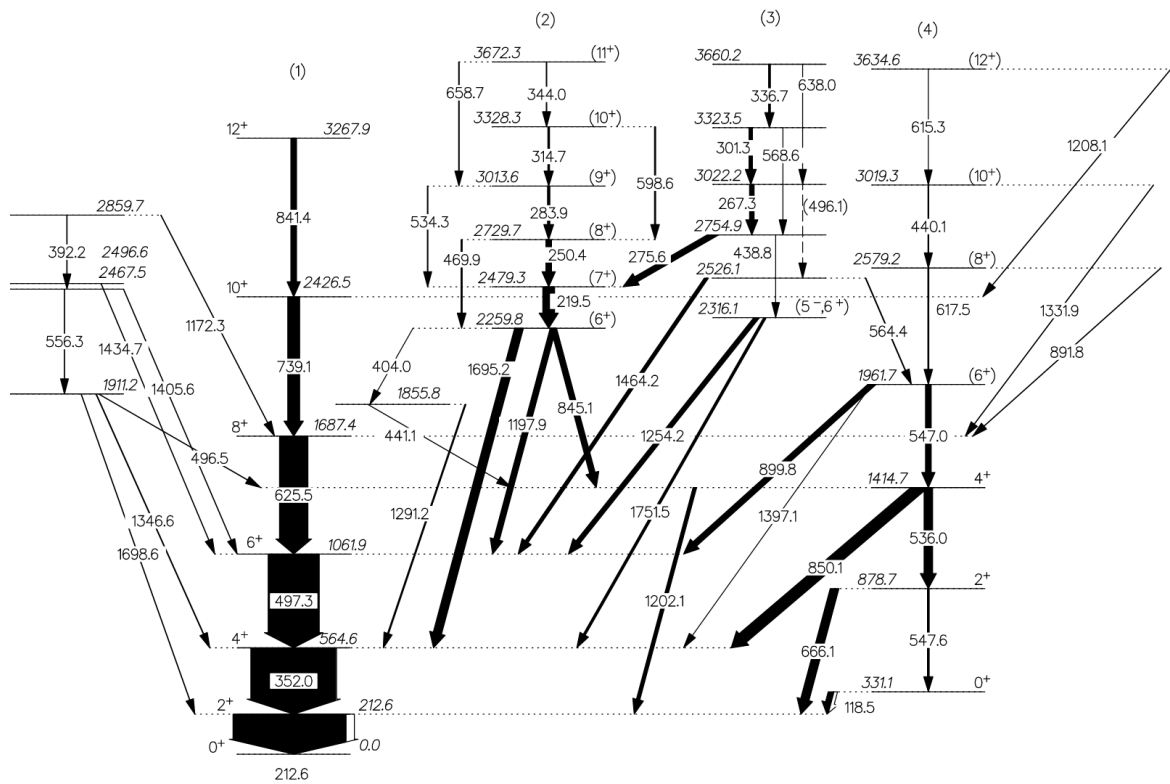


Figure 5.1: Level scheme of ^{100}Zr built with the data coming from the spontaneous fission of ^{252}Cf [Hwa+06].

In Section 5.2, I will present a comparison of our results on the $^{235}\text{U}(n_{th}, f)$ reaction obtained from the EXILL experiment with existing data on the same fissioning system and on two different fissioning systems: $^{248}\text{Cm}_{152}$ and $^{252}\text{Cf}_{154}$ spontaneous fissions. A comparison of the $^{235}\text{U}(n_{th}, f)$ reaction and $^{252}\text{Cf}_{154}$ spontaneous fission is also performed with the FIFRELIN simulations in the same section. In Section 5.3, the evolution of the γ -ray cascade in $^{100}\text{Zr}_{60}$ with its fission partner is discussed and

compared with the FIFRELIN simulations using different models and parameter values. This study allows us to propose an optimization of the model to describe the spin-distribution of the primary fragment in Section 5.4. The optimized simulations do not provide the correct average prompt-neutron multiplicity values. In Section 5.5, I will present the results of the prompt-neutron multiplicity optimization by changing the parameters ($R_{\text{P}}^{\text{min}}$ and $R_{\text{P}}^{\text{max}}$) responsible for the fission fragment temperature. In section 5.6 we conclude.

5.2 EXILL results and comparison with existing data

To validate our methodology of intensity extraction and to see how precise it is, we compared our data on ^{100}Zr with the published results of a measurement on the same fissioning system ($^{235}\text{U}(n_{\text{th}}, f)$). We also compared the γ -ray transitions of ^{100}Zr obtained in $^{235}\text{U}(n_{\text{th}}, f)$ to the transitions obtained in $^{248}\text{Cm}(sf)$ and $^{252}\text{Cf}(sf)$. Data on californium provided a very precise cascade description. This extensive comparison work was mainly driven by the basic idea of testing and validating our methodology of intensity extraction but also to check in the data if the cascade could depend on the fissioning system. Indeed, even if the average prompt-neutron multiplicity of the light fission fragments group is higher for $^{252}\text{Cf}(sf)$ than for $^{235}\text{U}(n_{\text{th}}, f)$ (respectively 2.05 [Vor+05] and 1.41 [Nis+98]), the prompt-neutron multiplicity for mass $A = 100$ is almost the same, close to 1.5 for both fissioning systems. Moreover, in both cases, the average emitted prompt-neutron energy is close to 1.3 MeV per neutron. We can then assume that the initial excitation energy of ^{100}Zr is about the same in the two fissioning systems. As a consequence, if in a first approximation, the ^{100}Zr de-excitation cascade only depends on the excitation energy, it should be almost the same for both systems.

5.2.1 EXILL results

We extracted from the EXILL data the intensity of as many as possible transitions in ^{100}Zr to have a complete view of the γ -ray cascade. In the data analysis, we chose ^{134}Te as the (post-neutron-evaporation) fission partner. This was done, as explained in Chapter 3 by taking the strongest transition in ^{134}Te ($2^+ \rightarrow 0^+$ transition at 1279 keV) in the set of γ -rays in triple coincidence. The ($^{100}\text{Zr} - ^{134}\text{Te}$) fission fragment pair has indeed the highest yield of all the (Zr - Te) isotopes in the fission of $^{235}\text{U}(n_{\text{th}}, f)$.

For this fission fragment pair, during de-excitation process, two neutrons are emitted in total. This is close to the average total prompt-neutron multiplicity of ^{236}U equal to 2.42 [Nis+98; LSB15].

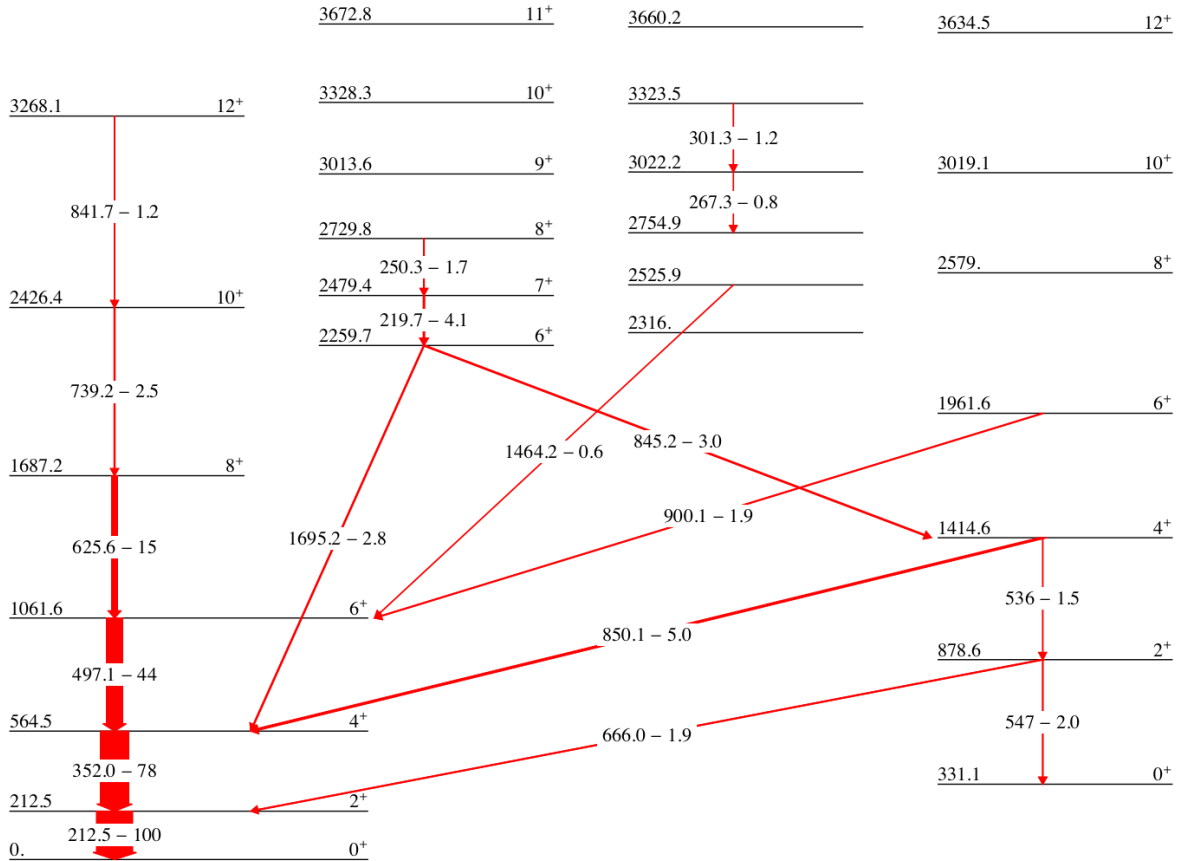


Figure 5.2: Level scheme of ^{100}Zr built with the data coming from the EXILL experiment. Transition energies (in keV) and transition intensities (normalized to the 212.5 keV transition) are indicated on each arrow.

The result of our analysis is summarized in Figure 5.2 where I show the measured transitions and their intensities. The same information and the uncertainties are detailed in Table 5.3. The first observation is that we could measure much less transitions in the EXILL data than what was done at LBLN with ^{252}Cf (Figure 5.1). This is partly due to the lower statistics in the EXILL data but also due to a different way of analysing the data. In [Hwa+06], the goal was to discover new transitions and to improve the level scheme. The analysis was more focused on the spectroscopy and on the nuclear structure of ^{100}Zr . In our case, the analysis aims to provide the best estimation of

the transition intensities with their uncertainty in a controlled way. We want to be sure that the post-evaporation fission partner of ^{100}Zr was ^{134}Te . It is more a kind of a spectrometric study. It is important to add that in [Hwa+06], the authors do not precise the fission partner.

5.2.2 Comparison with existing data on $^{235}\text{U}(n_{th}, f)$

At first, we compare in Table 5.2 our results with the few intensities obtained in an experiment performed at the CIRUS reactor facility in Mumbai (India) and published in 2012 [Muk+12]. Their setup consisted of two clovers placed around a 3 mm thick target made of low enriched pellets of UAl_3 in a thermal neutron flux of about $4 \cdot 10^7 \text{ n}\cdot\text{cm}^{-2}\cdot\text{s}^{-1}$. Having two detectors only, they could just analyze their data in γ - γ coincidence. The rather thick target most probably explains why they could not provide the 212.5 keV transition intensity. In their article, it is not mentioned what was the fission partner they selected in coincidence with ^{100}Zr ; however, it would be surprising that they made another choice than us (^{134}Te) because the other isotopes have lower yields thus the peaks in coincidence have lower statistics.

E_γ (keV)	Transition	I_γ	
		EXILL data	CIRUS data
212.5	$2_1^+ \rightarrow 0_1^+$	133(4)	>100
352.0	$4_1^+ \rightarrow 2_1^+$	100	100
497.1	$6_1^+ \rightarrow 4_1^+$	56(2)	62(3)
625.6	$8_1^+ \rightarrow 6_1^+$	19(1)	17.0(9)
739.2	$10_1^+ \rightarrow 8_1^+$	3.2(8)	9.6(5)

Table 5.2: Relative intensities (I_γ) of the γ -ray transitions measured in ^{100}Zr obtained in this work at EXILL compared to the ones obtained at CIRUS [Muk+12]. Intensities are normalized on the 352.0 keV transition to 100. In both experiments the $^{235}\text{U}(n_{th}, f)$ was analyzed.

In Table 5.2, one can see that all prompt γ -rays intensities, except for the transition at 739.2 keV, are compatible. The intensity of the 739.2 keV transition coming from

[Muk+12] seems to be overestimated. This hypothesis is supported by the $^{252}\text{Cf}(sf)$ data and the $^{248}\text{Cm}(sf)$ data that I will show in the next subsection.

5.2.3 Comparison with existing data on spontaneous fission

I will compare our results to the published results of two experiments with spontaneous fission sources. The first one was performed at LBNL using GAMMASPHERE, a γ -ray spectrometer with one hundred and two Ge detectors and their Anti-Compton shield, placed around a target made of the spontaneously fissile ^{252}Cf [Hwa+06]. The second one was done with ^{248}Cm in the center of the Argonne-Notre Dame with the γ -ray facility which consisted of ten BGO-suppressed Ge detectors, two LEPS (low-energy photon spectrometers) and an array of fifty bismuth germanate detectors used as a multiplicity filter [Hot+91].

In both cases, the fission partner used to extract the transitions in ^{100}Zr was not mentioned in the article. In comparison to $^{235}\text{U}(n_{th}, f)$, $^{252}\text{Cf}(sf)$ is characterized by a much higher prompt-neutron multiplicity equal to 3.75 [Vor+05]. It means that the strongest yield is expected for fission fragment pairs that evaporate together 4 neutrons. This condition is fulfilled when ^{100}Zr is associated with ^{148}Ce . The most probable fission partner of ^{100}Zr in $^{248}\text{Cm}(sf)$ is ^{145}Ba [Hot+91].

In Table 5.3, the γ -ray transition intensities extracted from the EXILL data are compared to the results obtained from the spontaneous fission of ^{252}Cf and ^{248}Cm . One observes that the intensities extracted from the EXILL data - $^{235}\text{U}(n_{th}, f)$ reaction - and from the ^{248}Cm data do not differ significantly and the discrepancies are smaller than the uncertainties. This is not the case when the EXILL data is compared with the ^{252}Cf data. Rather big differences can be seen already in the ground state band.

As explained before, the initial excitation energy of the fragment that deexcites to ^{100}Zr is expected to be almost the same in $^{252}\text{Cf}(sf)$ and in $^{235}\text{U}(n_{th}, f)$. One can wonder if the discrete γ -ray cascade should not be the same. This hypothesis seems however contradictory with the large difference observed in the transition intensities.

We have calculated the ratios between intensities of the corresponding γ -rays coming from the EXILL data and the ^{252}Cf data (Figure 5.3).

At first, the ratios show a global deviation of about 0.6 between the two sets of data. This could be explained by a normalization problem in the ^{252}Cf data on the measured intensity of the 212.5 keV transition. This is the only known γ -ray emitted

E_γ (keV)	Transition	I_γ		
		EXILL data	^{252}Cf data	^{248}Cm data
Deformed Ground State Band (1)				
212.5	$2_1^+ \rightarrow 0_1^+$	100	100	100
352.0	$4_1^+ \rightarrow 2_1^+$	78(3)	84(4)	81(8)
497.1	$6_1^+ \rightarrow 4_1^+$	44(2)	65(3)	49(5)
625.6	$8_1^+ \rightarrow 6_1^+$	15(1)	26(1)	14(3)
739.2	$10_1^+ \rightarrow 8_1^+$	2.5(6)	5.2(3)	4(1)
841.7	$12_1^+ \rightarrow 10_1^+$	1.2(5)	2.1(6)	
Band (2)				
219.8	$(7_1^+) \rightarrow (6_3^+)$	4.1(6)	5.5(3)	
250.3	$(8_3^+) \rightarrow (7_1^+)$	1.8(4)	2.4(7)	
Band (3)				
267.3	$?^? \rightarrow ?^?$	0.8(4)	1.0(3)	
301.3	$?^? \rightarrow ?^?$	1.2(6)	0.8(2)	
Band (4)				
536.0	$4_2^+ \rightarrow 2_2^+$	1.5(8)	6.8(3)	
547.0	$(6_2^+) \rightarrow 4_2^+$	2.0(4)	3.0(9)	
Transitions between Bands				
845.2	$(6_3^+) \rightarrow 4_2^+$	3.0(6)	8.8(4)	
1695.2	$(6_3^+) \rightarrow 4_1^+$	2.8(4)	5(1)	
1464.2	$?^? \rightarrow 6_1^+$	0.6(3)	1.80(54)	
665.98	$2_2^+ \rightarrow 2_1^+$	1.9(7)	7.0(4)	
850.1	$4_2^+ \rightarrow 4_1^+$	5.0(6)	9.5(5)	
900.1	$(6_2^+) \rightarrow 6_1^+$	1.9(3)	2.3(7)	

Table 5.3: Relative intensities (I_γ) of the γ -ray transitions (keV) in ^{100}Zr , normalized to the strongest transition (212.5 keV). ^{252}Cf data coming from [Hwa+06], ^{248}Cm data coming from [Dur+95]. The fission partner of ^{100}Zr was not specified for [Hwa+06] and [Dur+95].

by ^{100}Zr produced in the fission process that goes to the ground state and thus it is used as normalization. If it is too high, all other intensities will be artificially lowered. Another argument that supports this hypothesis is that no significant differences are observed between the EXILL data ($^{235}\text{U}(n_{th}, f)$) and the $^{248}\text{Cm}(sf)$ data.

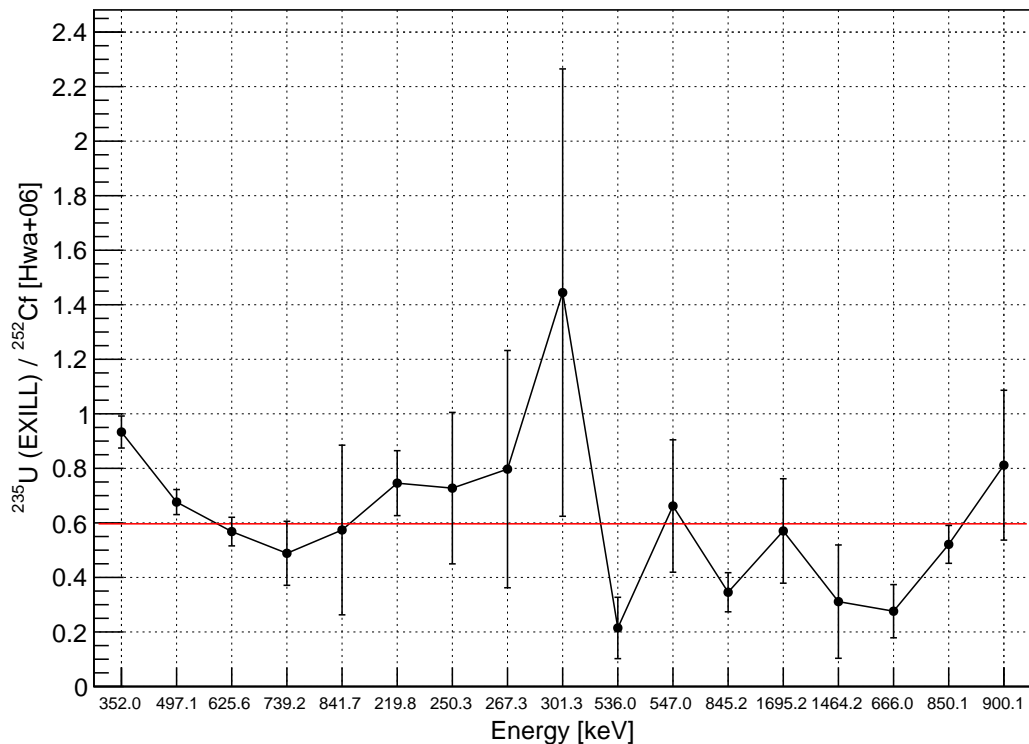


Figure 5.3: Ratio of γ -transition intensities in ^{100}Zr between the EXILL and the ^{252}Cf data [Hwa+06]. Fitted value is equal to 0.597(23).

On the other hand, Figure 5.3 also shows a slight slope for the ground state band transitions (352.0 keV, 497.1 keV, 625.6 keV, 739.2 keV). Such a trend could point out a different population before neutron evaporation, with much higher spin states in the fission of $^{252}\text{Cf}(sf)$ compared to the fission of $^{235}\text{U}(n_{th}, f)$. This conclusion is also supported by the $^{248}\text{Cm}(sf)$ data where we see also a small decrease as a function of the high-spin states population in the main band even if this trend is not significant due to the huge uncertainties.

5.2.4 Discussion based on FIFRELIN simulations

We used the FIFRELIN simulation to explore this trend and to compare with data. We simulated the intensities of the prompt γ -rays of ^{100}Zr emitted in the $^{235}\text{U}(n_{th}, f)$ and $^{252}\text{Cf}(sf)$ reactions with the FIFRELIN code. In both simulations the same default models were used: the EGLO model for the photon strength functions; the CGCM model for the level density and the CONSTANT model for the primary fission fragments spin cut-off. Simulations were constraint to reproduce the average prompt-neutron multiplicities of $^{235}\text{U}(n_{th}, f)$ and $^{252}\text{Cf}(sf)$. The models and their parameters are summarized in Tables 5.4 and 5.5.

Function	Used model
Strength Function	EGLO
Level Density	CGCM
Spin Cut-off	CONSTANT

Table 5.4: Models used to simulate $^{235}\text{U}(n_{th}, f)$ and $^{252}\text{Cf}(sf)$.

Parameter	Used values	
	$^{235}\text{U}(n_{th}, f)$	$^{252}\text{Cf}(sf)$
R_T^{\min}	0.35	0.35
R_T^{\max}	1.4	1.4
$\bar{\sigma}_L$	9.5	11.0
$\bar{\sigma}_H$	9.5	10.5

Table 5.5: Parameters used to simulate $^{235}\text{U}(n_{th}, f)$ and $^{252}\text{Cf}(sf)$.

For $^{235}\text{U}(n_{th}, f)$ we analyzed the $^{100}\text{Zr} - ^{134}\text{Te}$ fission fragment pair. When these fission fragments are created, the average number of emitted neutrons is equal to 2. For $^{252}\text{Cf}(sf)$ we chose the $^{100}\text{Zr} - ^{148}\text{Ce}$ pair where 4 neutrons are emitted. For $^{252}\text{Cf}(sf)$, we also analyzed the $^{100}\text{Zr} - ^{150}\text{Ce}$ pair to study if a lower number of evaporated neutrons, equal to 2, influences the de-excitation cascade in ^{100}Zr .

Results are given in Table 5.6 and the calculated level scheme for the $^{235}\text{U}(n_{th}, f)$ reaction in Figure 5.4. When comparing the measured (Figure 5.2) and the simulated level schemes we observe that the main rotational band is much more populated in the FIFRELIN simulation than in the EXILL data. In Table 5.6, it translates into a higher intensity of high-spin states in the deformed rotational band whereas other transitions are in a quite good agreement. This conclusion is also valid for the $^{252}\text{Cf}(sf)(4n)$ simulation and the discrepancy is even higher for $^{252}\text{Cf}(sf)(2n)$.

This overestimation of the high-spin states is probably caused by the high spin cut-off parameter values ($\bar{\sigma}_L$, $\bar{\sigma}_H$) used in the default simulation (Table 5.5) to correctly reproduce the average prompt-neutron multiplicity, the main constraint of the

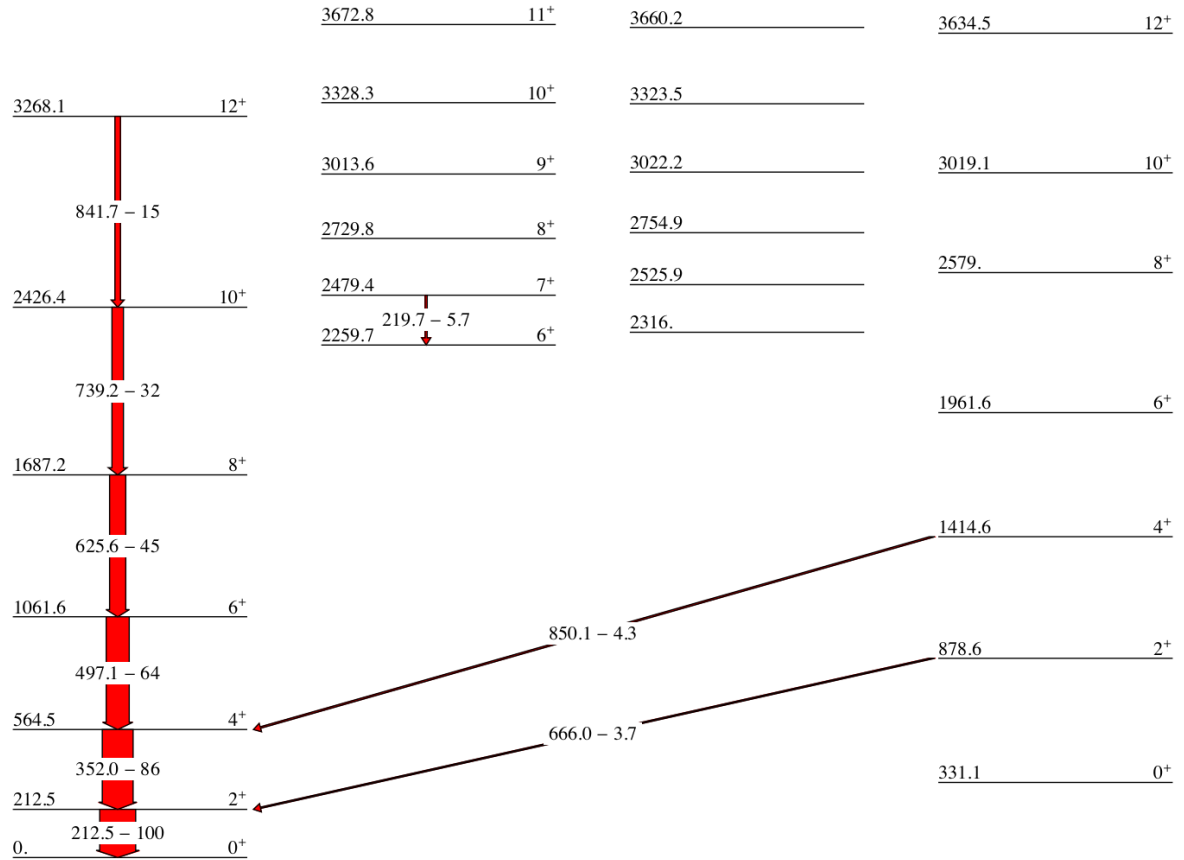


Figure 5.4: Partial level scheme of ^{100}Zr built with the data coming from the FIFRELIN simulation using EGLO photon strength functions, CGCM level density model and CONSTANT spin cut-off model. Transition energies (in keV) and transition intensities (normalized to 100 on the 212.5 keV transition) are indicated on each arrow. Only the transitions with an intensity higher than 3.5% are shown.

simulation. Indeed, as we will see in the following sections, a high spin cut-off value increases the initial spin of the fission fragment and thus the population of high-spin states. Moreover, the CONSTANT spin cut-off model forces the initial spin of ^{100}Zr to be the same no matter what is the fission partner. As each emitted neutron removes some spin from the fission fragment, when only two neutrons are evaporated the post-neutron emission fragment will have a higher spin (see Section 5.3) than when four are emitted. This is what we observe when comparing $^{252}\text{Cf}(sf)(2n)$ and $^{252}\text{Cf}(sf)(4n)$ simulations.

An interesting point is that, despite these disagreements between experimental

E_γ (keV)	Transition	I_γ		
		FIFRELIN simulation data ^{235}U	FIFRELIN simulation data $^{252}\text{Cf}(2\text{n})$	FIFRELIN simulation data $^{252}\text{Cf}(4\text{n})$
Deformed Ground State Band (1)				
212.5	$2_1^+ \rightarrow 0_1^+$	100	100	100
352.0	$4_1^+ \rightarrow 2_1^+$	86(1)	93(1)	86.9(9)
497.1	$6_1^+ \rightarrow 4_1^+$	64.0(9)	82(1)	72.0(8)
625.6	$8_1^+ \rightarrow 6_1^+$	44.9(7)	71(1)	56.4(6)
739.2	$10_1^+ \rightarrow 8_1^+$	31.9(6)	58.8(9)	42.1(5)
841.7	$12_1^+ \rightarrow 10_1^+$	15.4(4)	41.5(7)	26.4(4)
Band (2)				
219.8	$(7_1^+) \rightarrow (6_3^+)$	5.7(2)	2.5(2)	2.6(1)
250.3	$(8_3^+) \rightarrow (7_1^+)$	2.4(1)	1.3(1)	1.34(8)
Band (3)				
267.3	$?^? \rightarrow ?^?$	2.3(1)	0.40(6)	0.29(4)
301.3	$?^? \rightarrow ?^?$	0.21(4)	0.26(5)	0.17(3)
Band (4)				
536.0	$4_2^+ \rightarrow 2_2^+$	2.9(1)	1.4(1)	1.49(8)
547.0	$(6_2^+) \rightarrow 4_2^+$	0.89(8)	0.47(6)	0.48(5)
Transitions between Bands				
845.2	$(6_3^+) \rightarrow 4_2^+$	3.5(2)	1.9(1)	1.67(9)
1695.2	$(6_3^+) \rightarrow 4_1^+$	2.1(1)	1.0(1)	1.00(7)
1464.2	$?^? \rightarrow 6_1^+$	0.55(6)	0.53(7)	0.43(4)
665.98	$2_2^+ \rightarrow 2_1^+$	3.7(2)	2.1(1)	2.3(1)
850.1	$4_2^+ \rightarrow 4_1^+$	4.3(2)	2.1(1)	1.9(1)
900.1	$(6_2^+) \rightarrow 6_1^+$	0.73(7)	0.36(6)	0.43(4)

Table 5.6: Relative intensities (I_γ) of the γ -ray transitions (keV) in ^{100}Zr , normalized to the strongest transition (212.5 keV). Data coming from the FIFRELIN simulation of the $^{235}\text{U}(n_{th}, f)$ and $^{252}\text{Cf}(sf)$. The analyzed fission fragment pairs are $^{100}\text{Zr} - ^{134}\text{Te}$ ($^{235}\text{U}(n_{th}, f)$), $^{100}\text{Zr} - ^{150}\text{Ce}$ ($^{252}\text{Cf}(sf)(2\text{n})$) and $^{100}\text{Zr} - ^{148}\text{Ce}$ ($^{252}\text{Cf}(sf)(4\text{n})$). The model/parameter setup used in these simulations can be found in Tables 5.4 and 5.5.

data and simulations, the same decreasing trend observed in the data is also visible in the simulation when comparing the ratios between the $^{235}\text{U}(n_{th}, f)$ and $^{252}\text{Cf}(sf)$ reactions. Such observation points towards the conclusion from the previous section that the initial spin distribution of the pre-neutron fragment leading to ^{100}Zr may be different from one system to another and probably depends on the spin-distribution of the fission-fragment partner.

5.3 Evolution with the mass of the fission partner

It has been already stated that ^{100}Zr is a good candidate to study the influence of the fission partner on the prompt γ -ray cascade. It has been seen in the previous section that FIFRELIN predicts a large variation of the intensity of the high spin transitions in ^{100}Zr when its fission partner changes from ^{148}Ce to ^{150}Ce . This is a systematic feature of some FIFRELIN simulations and it depends on the choice of the model that describes the primary fission fragment entry states.

In fact, the related physics question is the dependence of the spin-distribution of the primary fission fragments with their excitation energy. Since the number of evaporated neutrons is quasi a linear function of the excitation energy, this question could be studied by looking at the evolution of the high spin transitions as a function of the number of evaporated neutrons. In practice, however, in our data, one can only access the total number of neutrons emitted by the two fragments because we select the post-neutron-evaporation fission pair by their discrete γ -ray cascades.

In a first approximation, one can make the hypothesis that the cascade in a fission fragment depends on its own excitation energy and not on the excitation energy of its fission partner. Anyway, to take correctly into account that point, experimental data are compared to the same observables in the simulations and simulated intensities are extracted in the most similar way to the real data.

In other words, in this section, we will present the evolution of the discrete γ -rays cascade in ^{100}Zr as a function of its fission partner (after neutron evaporation). The mass of the fission partner will fix the total number of evaporated neutrons (because $\nu_T = A_{CN} - A_1 - A_2 = 236 - 100 - A_2$). Comparing FIFRELIN simulations to our results will allow us to test the different reference models for the (excitation energy, spin) distribution of the primary fission fragments.

5.3.1 EXILL results

In the EXILL data, we analyzed the strongest transitions in ^{100}Zr with the following three partners: ^{132}Te (see Figure 5.5), ^{133}Te (see Figure 5.6) and ^{134}Te (see Figure 5.7). The result is plotted in Figure 5.8. The transitions are the ones at 212.5 keV, 352.0 keV, 497.1 keV, 625.6 keV and 841.7 keV and all of them belong to the ground-state band. The uncertainties on the transition intensity at 739.2 keV coming from the EXILL experiment obtained with the ^{132}Te , ^{133}Te partners were too high to be considered in the evolution studies.

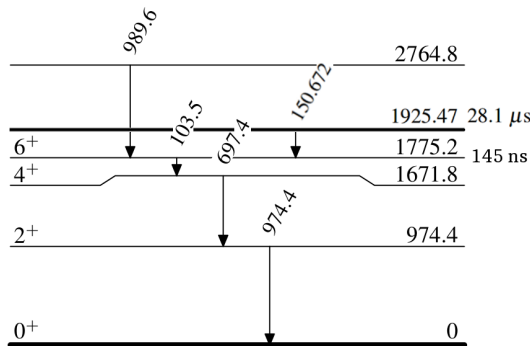


Figure 5.5: The level scheme of ^{132}Te from [Hop+72].

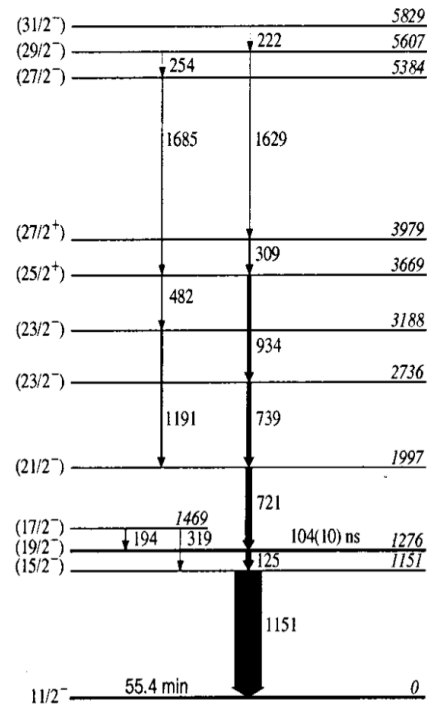


Figure 5.6: The level scheme of ^{133}Te from [Bha+01]. Level energies are expressed relative to zero for the $11/2^-$ isomeric state which is at 334.26 keV.

In order to keep the uncertainty of the values as low as possible, we avoid a double normalization. As explained in Chapters 3 and 4, the analysis is performed in two steps. In the first step, one gate is taken in Te and the other one in ^{100}Zr (here the 212.5 keV transition to the ground state). The gate for ^{132}Te was the transition at

This fragmentation is of course not so well produced; the total number of emitted neutrons is already equal to 4.

The problem with the 212.5 keV transition is linked to the second step in the analysis where two gates are taken in ^{132}Te (we chose the transitions at 974.08 keV and 697.05 keV, see Figure 5.5) and the goal is to find the ratio between the 212.5 keV and the 352.0 keV intensities. We believe that the peak at 352.0 keV may be partially contaminated by the transition at 353.69 keV belonging to ^{132}Te (emitted from the level at 2764.37 keV). This leads to the decrease of the 212.5 keV relative intensity and this is indeed what we observe in Figure 5.8.

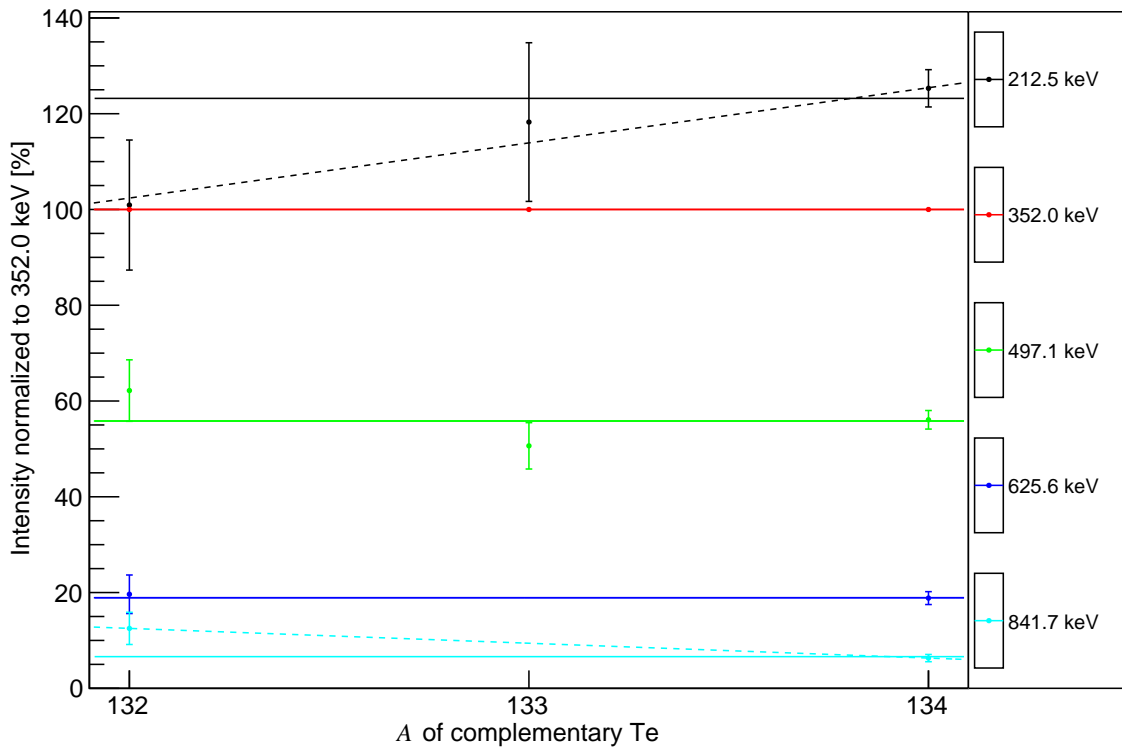


Figure 5.8: Evolution of γ -transition intensities in ^{100}Zr with Te mass number obtained from the EXILL experiment data. The dashed lines show the fits with a first degree polynomials function.

The problem with the 841.7 keV transition occurs in the first analysis step where a gate is taken in ^{100}Zr (on the 212.5 keV transition) and the other is taken in ^{132}Te . We believe that the peak at 841.7 keV may be contaminated by the transition 841.1 keV from the level 4534.1 keV in ^{132}Te .

One should add that contamination of the normalization peak (at 352.0 keV) by the 353.69 keV transition may have an impact on the other transitions but it should be much weaker. In the analysis step with the two gates in ^{132}Te , the transition at 353.69 keV is produced in coincidence with all the possible isotopes of Zr. In the analysis step with one gate in ^{100}Zr and the other in ^{132}Te , the transition at 353.69 keV can only be produced in coincidence with ^{100}Zr . Its effect is thus weaker in that case. We therefore do not expect the 497.1 keV and 625.6 keV to be strongly affected.

Finally, removing the two contaminated values makes all the curves compatible with a constant function. It seems reasonable to conclude that the discrete γ -ray cascade does not change with the fission partner.

5.3.2 Long-lived isomers in Te

When the γ - γ - γ coincidence cube is created a specific acceptance window is used (see Section 3.3.3). The cube which we used, had it set to around 200 ns. This means that the nano- and microsecond isomers can influence the results of our analysis. Such long-lived isomers occur in every Tellurium that we gated on. In the ^{132}Te there are a 145 ns isomer at 1775.2 keV and a 28 μs isomer at 1925.47 keV, see Figure 5.5. In the ^{133}Te a 104 ns isomer is at 1610.4 keV, see Figure 5.6. Furthermore, a 164 ns isomer occurs in ^{134}Te at 1691.3 keV, see Figure 5.7. We always selected for the gates γ -rays emitted from the levels below the long-lived isomers. For ^{132}Te they were transitions at 974.4 keV and 697.4 keV, for ^{133}Te transitions at 1150.6 keV and 125.5 keV, and for ^{134}Te transitions at 1297.4 keV and 297.1 keV. We believe that this way of gating provided us with the intensities in ^{100}Zr which were not disturbed by the presence of the long-lived isomers in the Tellurium isotopes.

In the standard analysis without long-lived isomers we are able to correctly measure intensities of the γ -rays in element A and B no matter where we place the gates. It is a bit more complicated when a long-lived isomer is present. Let's assume that we have two simple cascades in coincidence which belong to fragments A and B (fission partners). Both cascades are presented in Figure 5.9.

I will consider the situation when a nanosecond isomer is present in the element A. The acceptance time window is 200 ns. If we want to analyze the γ -ray cascade in the fragment B we can put the gate above or below the nanosecond isomer in the cascade A. It works for both "mixed gates" (see Figure 5.9) and "double gates" (see

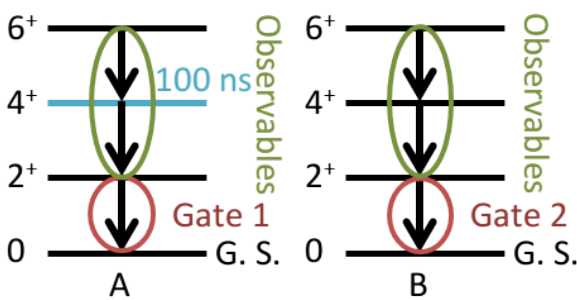


Figure 5.9: Schematic view of gates placement when "mixed gates" are used and a nanosecond isomer is present. The first gate is placed in the fission fragment A below the long-lived isomer, the second one in its fission partner B. One can obtain correct intensities of the prompt γ -rays in both fission fragments A and B (marked in green).

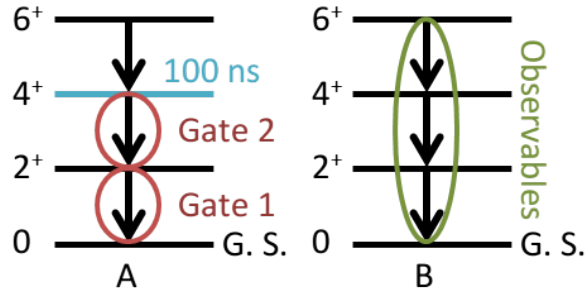


Figure 5.10: Schematic view of gates placement when "double gates" are used and a nanosecond isomer is present. Two gates are placed in the fission fragment A, both below the nanosecond isomer. One can obtain correct intensities of the prompt γ -rays in the fragments B (marked in green).

Figure 5.10) and it will not change the γ -transition intensities but it will influence the statistics. Gating below the long-lived isomer reduces the number of registered γ -rays because part of them will not be included in the acceptance time window. The sum of the lifetimes of the cascade and the nanosecond isomer can exceed the size of the acceptance time window in the significant number of events. As a result the cascade will not be in coincidence with the nanosecond isomer and such events will not be counted in. It means a loss of statistics which translates into higher uncertainty but the intensity values should be correct. If the two transitions from different cascades are not in coincidence we lose all the events from both of these cascades. If we adapt this example to our measurements; the fragment A is Tellurium, the fragment B is Zirconium. Since we used exactly the same method of gating, it can be assumed that our measurements of the γ -ray intensities in ^{100}Zr are correct.

In the EXILL data, there can be a small aberration in intensities caused by the relatively low time resolution ($\sim 120\text{ns}$). This effect is stronger at lower energies. The

result can be a partial acceptance of the cascade. It would be the case at the border of the acceptance time window. Its position is not ideal and it fluctuates a bit regarding the beginning of the cascade. Some of the transitions can be artificially delayed in relation to the rest of the cascade, which would make them miss the acceptance time window. We consider that this effect does not have a strong influence on intensities because on average the fraction of different γ -rays that miss the acceptance time window is similar. It can be more visible if the statistics is low. This could explain the behaviour of the γ -ray intensities of ^{100}Zr with the partner of ^{132}Te in Figure 5.8. The statistics of the γ -ray peaks in the coincidence spectrum of ^{132}Te and ^{100}Zr is relatively low. We can see that for ^{132}Te the intensity of the transition at 212.5 keV is lower in comparison to other Tellurium isotopes. Due to higher Compton tails at the lower energies, this peak can be a bit wider in terms of energy and can have a bit lower time resolution. The moment when the acquisition system registers it can vary more than for peaks at the higher energy. With the nanosecond isomer lifetime of 145 ns and the acceptance time window of around 200 ns this can result in less registered events than for the rest of the γ -rays belonging to the cascade. Additional factor which reduces the statistics in the ^{100}Zr - ^{132}Te fission fragment pair is a microsecond isomer at 1925.47 keV. Almost every transition which gets through this level is lost because its lifetime is 28 μs which is about 100 times more than the acceptance time window.

Let's consider our example once again. This time, we want to analyze the cascade in the fragment A (with the nanosecond isomer). In such a case, we need to pay more attention to the gate selection. If we put one of the gates below the nanosecond isomer and the second one in the fragment B (see Figure 5.9) the situation is similar to the one already presented - the intensities should be correct but their uncertainties will be higher due to lower statistics. We can measure simultaneously the intensities of the γ -rays above and below the nanosecond isomer because the coincidence spectrum is build based on the coincidence between the cascade B and the transition below the nanosecond isomer in the cascade A. Two statements are valid for this case. The transitions below the nanosecond isomer are always in coincidence, and the cascade B is always in coincidence with the cascade A above the nanosecond isomer. As a result, if Gate 1 and Gate 2 are in coincidence they will be always in coincidence with the whole cascade A (above and below the nanosecond isomer). There are no such events visible in the coincidence spectrum where Gate 1 is in coincidence with only the γ -transitions below the nanosecond isomers because Gate 1 must be in coincidence

with Gate 2 which directly indicates its coincidence with the cascade A above the nanosecond isomer.

This example presents the situation which would have taken place if we had measured the γ -ray intensities in mentioned Tellurium isotopes. The measurements of ^{132}Te and ^{133}Te would be relatively simple because there are almost no transitions which does not go through the nanosecond isomers. In ^{134}Te one can see at least three strong transitions at: 979 keV, 1151 keV, and 1404 keV (Figure 5.7) which directly feed the γ -ray (1297.4 keV) where the gate is placed. It means that these γ -rays are always in coincidence with both gates, whereas other transitions which are a part of branches going through the long-lived isomer are partially rejected. It can be simplified and adapted to other situations.

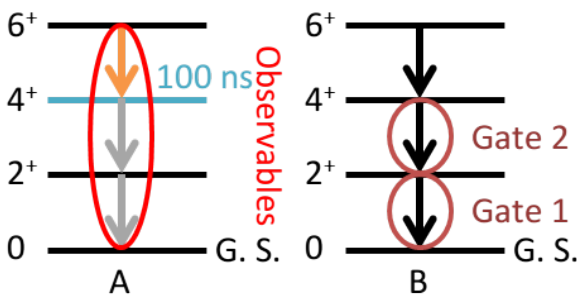


Figure 5.11: Schematic view of gates placement when "double gates" are used and a nanosecond isomer is present. Two gates are placed in the fission fragment B. One cannot obtain correct intensities of the prompt γ -rays in fragments A (marked in red) because the intensities of the γ -transitions below the long-lived state is reduced due to used acceptance time window.

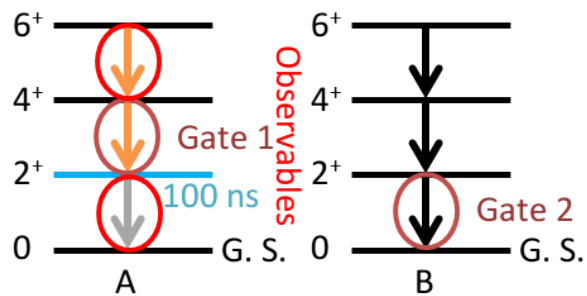


Figure 5.12: Schematic view of gates placement when "mixed gates" are used and a nanosecond isomer is present. The first gate is placed in the fission fragment A above the long-lived isomer, the second one in its fission partner B. One cannot obtain correct intensities of the prompt γ -rays in fragments A (marked in red) because the intensities of the γ -transitions below the long-lived state is reduced.

Let's consider a second example. We will concentrate on the cases when the gates are placed only in the cascade B, where there are no nanosecond isomers (Figure 5.11) or when the gate is put above the nanosecond isomer (Figure 5.12). In such cases,

in the coincidence spectrum, we will see all the events above the nanosecond isomer and only a part of them below it. The visible events are ones that were registered in the acceptance time window and since the cumulative lifetime of the cascade and the nanosecond isomer can exceed the length of the acceptance time window, part of the events below the nanosecond isomer will be missing. This means that we will measure the full intensities of the γ -rays above the nanosecond isomer and only partial intensities below the nanosecond isomer. We cannot compare the intensities of the γ -rays above and below the nanosecond isomer. They need to be considered as separated cases or we need to use a factor which takes into account how much counts we lose. The factor is based on the comparison of the isomer's lifetime to the length of the acceptance time window.

Another very specific case is "double gates" in the fragment A to measure the intensities of the cascade in A. We have never used it in our analysis. If one puts the first gate below and the second above the nanosecond isomer, the intensities of all the transitions will be correct, just the statistics will be lower. Due to coincidence between Gate 1 and Gate 2 we are sure that the coincidence between the cascade below and above the nanosecond isomer is preserved. Intensities of the γ -transitions in cascade A above and below the nanosecond isomer cannot be compared when both gates are placed in the cascade A above or under the nanosecond isomer. This always results in measuring the full intensities for one part of the cascade and the partial intensities for the second part.

5.3.3 The CONSTANT spin cut-off model

We first tested the CONSTANT spin cut-off model, which is the default model in FIFRELIN. The evolution of the strongest γ -ray transitions in ^{100}Zr with mass number of its partner is shown in Figure 5.13. We kept the same convention as in experimental results: the intensities are normalized to the transition at 352.0 keV.

One clearly observes a linear evolution of the intensity. All intensities increase with Te mass number (decrease with the total number of evaporated neutrons) except the one at 352.0 keV (because it is the normalization transition - its value is 100%) and the one at 212.5 keV (which is between the levels with lower spins $2^+ \rightarrow 0^+$ than the normalization transition at 352.0 keV $4^+ \rightarrow 2^+$).

This trend is quite systematic in the simulation with the CONSTANT spin cut-off

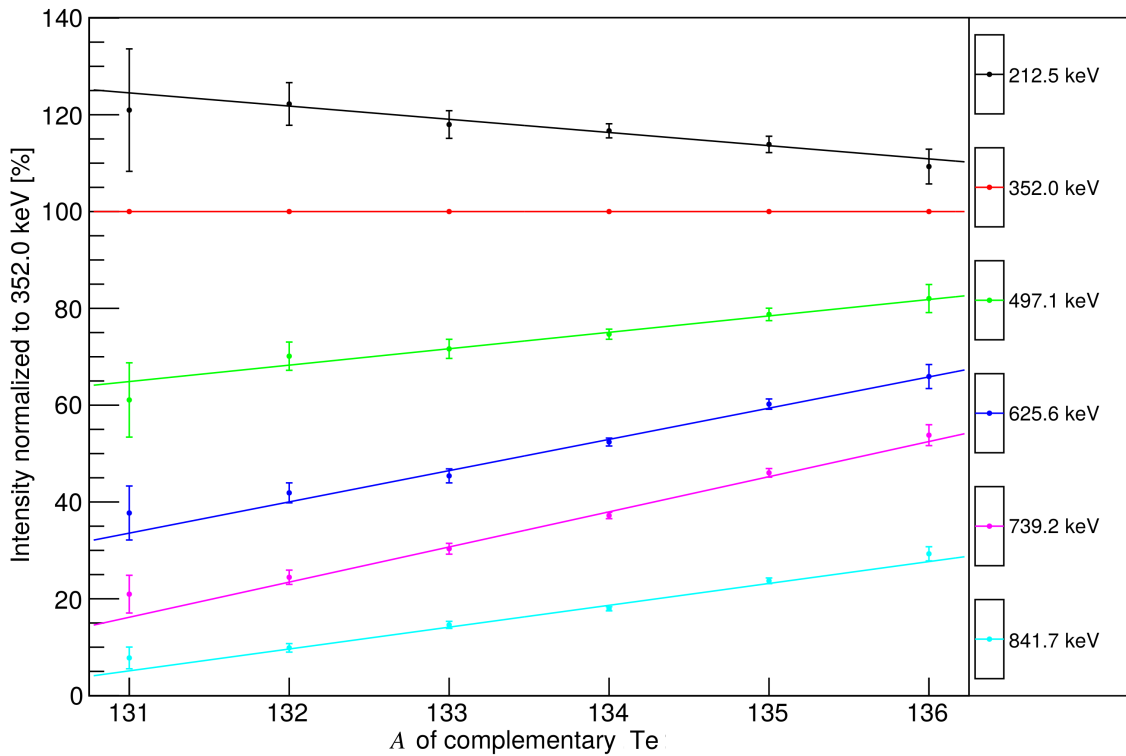


Figure 5.13: Evolution of simulated γ -transition intensities in ^{100}Zr with Te mass number when the CONSTANT spin cut-off model is used.

model and not only for ^{100}Zr . We will try to explain its origin.

As explained in Chapter 2, the CONSTANT spin cut-off model is a very simple model where one considers that the initial spin distribution of the primary fission fragments does not change with the excitation energy. Figure 5.18 shows the distribution of entry states $P(E, J)$ of the fragments that decay to ^{100}Zr according to this model.

Let us consider that the initial spin distribution can be reduced to its mean value (J_F). The entry state is then reduced to a vertical curve at $J = J_F$. Then let us superpose that curve on the level density of the Zr nucleus. This is presented in Figure 5.14. On average, and at a first approximation, the emission of a neutron does not change the spin of the fission fragment because the fragment can either gain or lose the spin of the neutron. In this naive view, in Figure 5.14, the fission fragments follow the vertical line down to the Yrast line. In a less naive view and looking at the level density, by emitting a neutron, the fission fragments will prefer to decay to a region with a higher density and on average always lose some amount of spin.

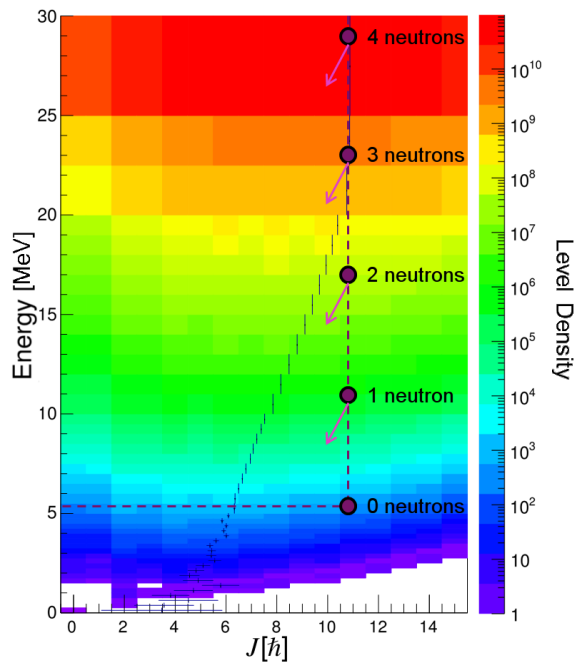


Figure 5.14: The process of neutron evaporation superposed on the ^{100}Zr level density $\rho(E, J)$. The gray line marks the mean value of the level density as a function of the excitation energy taken from RIPL-3.

A fission fragment with a very high initial excitation energy will emit many neutrons and loose at the end more spin than a fragment at a lower energy which can emit only one neutron. Since in the constant model, they start with the same initial spin, at the end, the fission fragment that emits many neutrons has a lower spin. This is what we see in Figure 5.14 and it explains the simulation results in Figure 5.13.

The phenomenon observed in the simulations is not confirmed by the experimental data. Even if we assume that the contaminated intensities are correct it does not change the situation, because the experimental trend goes in the other direction.

We can conclude that the CONSTANT model is too simple and should be rejected.

5.3.4 The BSFG spin cut-off model

The experimental data did not confirm the observation made with the simulations using the CONSTANT spin cut-off model. We decided to test another possible spin cut-off model to check if the intensities dependence with the fission partner can be avoided in FIFRELIN. We performed a simulation with the BSFG spin cut-off model

(Section 2.2.2). Results are shown in Figure 5.15. We do not take into account the cases when the fission partner for ^{100}Zr is ^{131}Te and ^{136}Te due to low statistics causing high uncertainty for the simulation with 1000000 events that we analyzed. No strong dependence with the fission partner is observed. The exceptions are the 739.2 keV and 841.7 keV transitions. We believe that the slopes are caused by too high initial spin of the primary fission fragments.

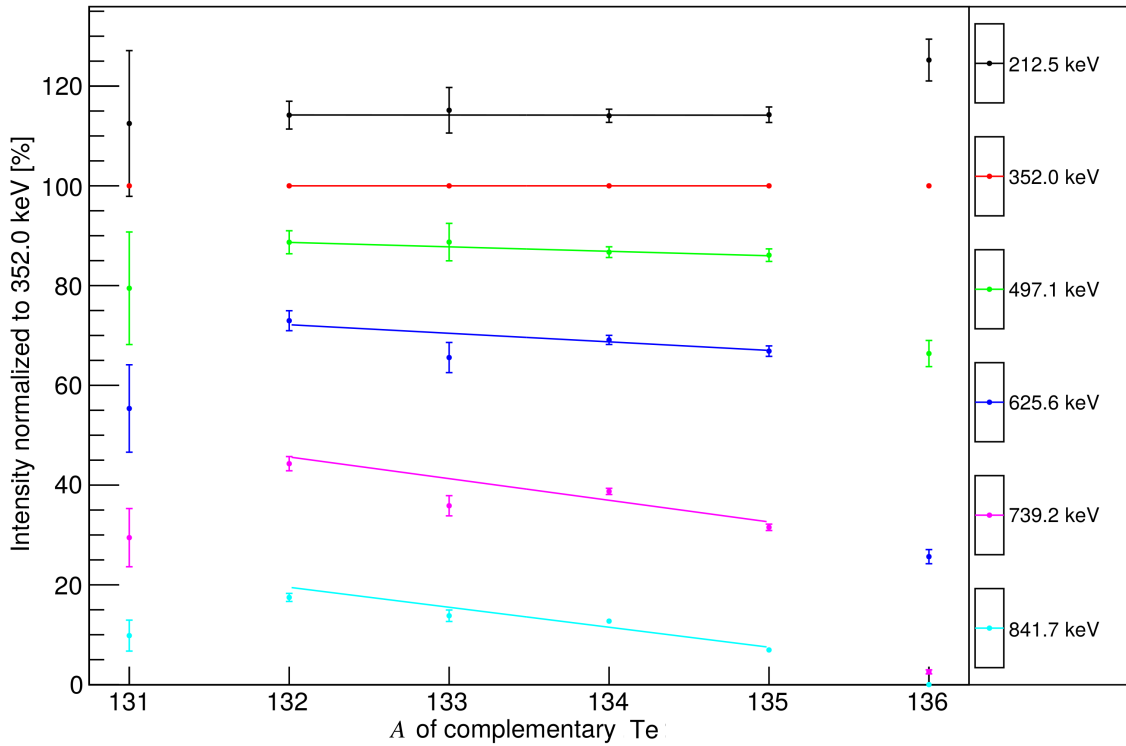


Figure 5.15: Evolution of the simulated γ -transition intensities in ^{100}Zr with Te mass number when the BSFG spin cut-off model is used.

As explained in Chapter 2, the BSFG spin cut-off model has an energy dependent spin cut-off parameter. In the BSFG model currently used in FIFRELIN, due to problems with implementation, there is no distribution of the initial spin of the primary fission fragments spin for each excitation energy. The initial spin of the primary fission fragments is reduced to just one value per excited state thus the initial level density distribution of the primary fission fragments is restricted to a simple curve (Figure 5.22). The initial spin of the primary fission fragments $J(E)$ is linked to the mean value of the level density by: $J(E) = f_{\sigma} \cdot J_{mean}(E)$, where $J_{mean}(E)$ is the mean spin

value of the level density (E, J) distribution at energy E . The curve is thus tilted relatively to the curve of $J_{mean}(E)$ and the user parameter f_σ defines the inclination. It can be assumed that $J_{mean}(E)$ is close to reality because the level density is adjusted on the experimental values from RIPL-3, see Section 2.5.

The scaling factor f_σ (Section 2.4) used in the simulation is much higher than 1 hence the initial spin curve is shifted a lot to high spin in comparison to the $J_{mean}(E)$ curve. Obviously, with such a model, the shift to a higher spin increases with the excitation energy. This causes an overpopulation of the high-spin states when the initial excitation energy is high (when many neutrons are evaporated), which can be seen in Figure 5.15. Probably, if a value closer to 1 had been used for f_σ , these slopes would have been significantly reduced or even nonexistent. We can conclude that the initial spin-distribution of the simulation using the BSFG model fits much better to the trend seen in the experimental data.

5.4 Spin-distribution dependence

A common feature of the previously presented simulations is the relatively high value of the initial spin of the pre-neutron fission fragment which induces an overpopulation of the high-spin excited states. It is mainly due to an overestimation of the initial spin distribution in the FIFRELIN default models. In this section, we describe more specifically how the spin-distribution in the simulations could influence the γ -cascade.

5.4.1 Selection of the best models in FIFRELIN

Before going further in the analysis, we tried to find which combination of models better fits the data. One of the ways to test the different simulation models and see how well they reproduce the experimental data is to use a χ^2 test. The χ^2 test measures the distance between two sets of data taking into account the possibility for this distance to vary within its uncertainty. It tests the probability for these two sets of data to be compatible within their uncertainties. It preconceives Gaussian distributions for uncertainties. That is the reason why we consider only strong transitions from the ground state band: 212.5 keV, 352.0 keV, 497.1 keV, 625.6 keV, 739.2 keV and 841.7 keV, for which statistics are sufficient so that the uncertainties can be considered to be Gaussian. In addition, it has been already shown that FIFRELIN reproduces quite

badly the other bands. The reason is probably an incomplete level scheme.

The χ^2 was defined as:

$$\chi^2 = \sum_i^{\text{mixed gates}} \frac{(N_i^{\text{data}} - \alpha N_i^{\text{simu}})^2}{(\sigma_i^{\text{data}})^2 + (\alpha \sigma_i^{\text{simu}})^2} + \sum_i^{\text{double gates}} \frac{(N_i^{\text{data}} - \beta N_i^{\text{simu}})^2}{(\sigma_i^{\text{data}})^2 + (\beta \sigma_i^{\text{simu}})^2} \quad (5.1)$$

where N_i^{data} is the experimental number of counts in the transition i and σ_i^{data} its uncertainty; N_i^{simu} is the simulated number of counts in the transition i and σ_i^{simu} its uncertainty; α and β are two normalization factors that are obtained by minimization.

The reason for using the two sums is that a transition intensity is obtained in two steps as already explained before. In the first step, with the mixed gates, we measured the number of counts of the transitions at 352.0 keV, 497.1 keV, 625.6 keV, 739.0 keV and 841.7 keV. In the second step, with double gates in Te, we measured the number of counts in the transitions at 212.4 keV and 352.0 keV. The degree of freedom equals $5 + 2 - 2 = 5$.

Table 5.7 shows the different models and parameters tested and the last column the resulting χ^2 value. In this approach, the χ^2 test was used only to quantify the distance between experimental and simulated transition values by looking for a combination of models which minimizes the distance. No statistical interpretation of the χ^2 value was done as the distances for all simulations are much larger than the uncertainties, leading to the simple conclusion that in principle all the simulations could be rejected with a good confidence level.

Here, I recall that the parameters were adjusted so that the simulation gives the correct average neutron multiplicities. One can see in the table that simulations using the EGLO model for the strength function and the CTM model for the level density (Table 5.7) show the lowest χ^2 value. Then, among those, the CONSTANT spin cut-off model looks like the best choice. If one considers the BSFG model, the best models would be EGLO and CTM as well.

In all cases, simulations with the EGLO model to calculate the photon strength functions (PSF) gives a lower χ^2 value than the simulations using Hartree-Fock-Bogoliubov (HFB) to calculate the PSF. In the EGLO model, a Lorentzian shape strength function models the experimental data accordingly to the Giant Dipole Resonances concept (GDR). It seems that HFB gives higher strength functions values than EGLO at the γ -ray energies involved in fission (0.1÷10 MeV) (Figure 2.9 in Section 2.6). This is probably the reason why for the HFB based simulations we see a bit stronger feeding

Strength function model	Level Density model	Spin cut-off model	R_T^{\min}	R_T^{\max}	$\bar{\sigma}_L$ or f_σ	$\bar{\sigma}_H$	χ^2 value
EGLO	CGCM	BSFG	0.48	1.35	1.75	-	1061.73
EGLO	CGCM	BSFG	0.9	1.19	1.75	-	1046.42
EGLO	CGCM	CONSTANT	0.35	1.40	9.5	9.5	1026.09
EGLO	CTM	BSFG	0.75	1.23	1.80	-	626.19
EGLO	CTM	CONSTANT	0.63	1.26	9.5	9.5	440.05
HFB	CGCM	CONSTANT	0.82	1.19	9.0	9.5	1072.82
HFB	CTM	CONSTANT	0.75	1.20	9.5	10.0	490.43

Table 5.7: χ^2 values containing main band γ -transitions in ^{100}Zr for FIFRELIN simulations utilizing different models. The best results for the CONSTANT and BSFG spin cut-off models are written in bold text.

of the levels in the ground state band of ^{100}Zr , see Table 5.8. However, the difference is not significant. Further adjustment of the free parameters is likely to improve the χ^2 value for the simulations using HFB.

It seems that the relatively simple CTM model reproduces the experimental data more accurately than the CGCM model. CTM uses an exponential law to describe the energy dependence of the cumulative number of low-lying nuclear levels. Its parameters are adjusted on experimental data. As explained in Chapter 2, CGCM is more complicated. As a matter of fact it uses the CTM model in the low energy region and the Fermi gas model above some matching energy.

It is possible to explain why the CTM model gives a lower χ^2 value. If we look on the energy distribution of the neutrons emitted by the primary fission fragments in their initial state (Figures 5.16 and 5.17), we see that more energetic neutrons are emitted in the simulation using the CGCM model. In CTM the number of levels is larger at high excitation energies than in CGCM [RLS12]. It translates into more available ways to follow the de-excitation process and on average a smaller energy gap between the states. The neutrons need thus to be less energetic in the CTM model to go from one state to another. The same is true for the γ -ray transitions. It is more probable to

E_γ (keV)	Transition	I_γ		
		EXILL data	FIFRELIN simulation EGLO	FIFRELIN simulation HFB
Deformed Ground State Band (1)				
212.5	$2_1^+ \rightarrow 0_1^+$	100	100	100
352.0	$4_1^+ \rightarrow 2_1^+$	78(3)	82(1)	82(1)
497.1	$6_1^+ \rightarrow 4_1^+$	44(2)	62.5(8)	63.7(8)
625.6	$8_1^+ \rightarrow 6_1^+$	15(1)	34.8(6)	37.5(6)
739.2	$10_1^+ \rightarrow 8_1^+$	2.5(6)	17.2(4)	18.3(4)
841.7	$12_1^+ \rightarrow 10_1^+$	1.2(5)	6.5(2)	6.1(2)
Band (2)				
219.8	$(7_1^+) \rightarrow (6_3^+)$	4.1(6)	2.0(1)	1.8(16)
250.3	$(8_3^+) \rightarrow (7_1^+)$	1.8(4)	1.12(9)	0.87(8)
Band (3)				
267.3	$?^? \rightarrow ?^?$	0.8(4)	0.27(4)	0.27(4)
301.3	$?^? \rightarrow ?^?$	1.2(6)	0.10(3)	0.11(3)
Band (4)				
536.0	$4_2^+ \rightarrow 2_2^+$	1.5(8)	1.5(1)	1.7(1)
547.0	$(6_2^+) \rightarrow 4_2^+$	2.0(4)	0.55(6)	0.47(5)
Transitions between Bands				
845.2	$(6_3^+) \rightarrow 4_2^+$	3.1(6)	1.3(1)	1.4(1)
1695.2	$(6_3^+) \rightarrow 4_1^+$	2.8(4)	0.85(8)	0.63(6)
1464.2	$?^? \rightarrow 6_1^+$	0.6(3)	0.34(5)	0.31(4)
665.98	$2_2^+ \rightarrow 2_1^+$	1.9(7)	2.6(1)	2.8(1)
850.1	$4_2^+ \rightarrow 4_1^+$	5.0(6)	1.9(1)	2.2(1)
900.1	$(6_2^+) \rightarrow 6_1^+$	1.9(3)	0.30(5)	0.39(5)

Table 5.8: Relative intensities (I_γ) of the γ -ray transitions (keV) in ^{100}Zr , normalized to the strongest transition (212.5 keV). Comparison of the EXILL experimental data with the simulations using the EGLO and HFB photon strength functions, the CTM level density model and the CONSTANT spin cut-off model, without collective neutron behavior. These simulations give the correct neutron multiplicity.

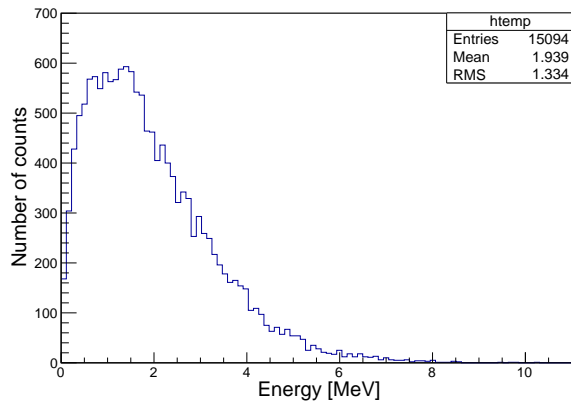


Figure 5.16: Light fragment neutron energy in the ^{100}Zr cascade when the CTM model is used.

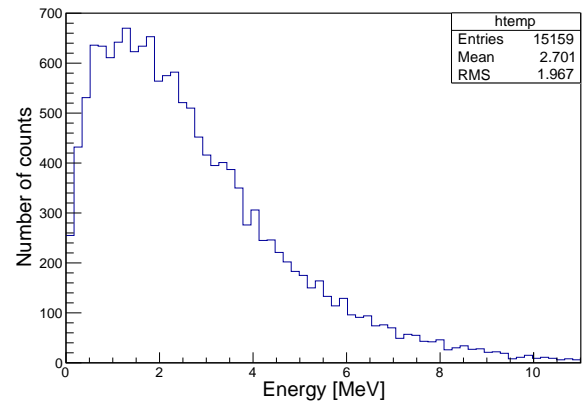


Figure 5.17: Light fragment neutron energy in the ^{100}Zr cascade when the CGCM model is used.

find an optimal de-excitation path which quickly reduces the spin of a fission fragment if the level density is high thus the overfeeding of the high-spin states will be lower for the CTM model.

Using the CTM model indeed brings simulation results ($^{235}\text{U}(n_{th}, f)$) closer to the experimental data for the transitions in the main band of ^{100}Zr . This is especially true for the γ -rays emitted between the high-spin states: $12^+ \rightarrow 10^+$, $10^+ \rightarrow 8^+$ and $8^+ \rightarrow 6^+$. When one compares the output of the simulation with the CTM model (fourth column of Table 5.9) and with the CGCM model (third column of Table 5.6), one sees that the intensities of some overpopulated transitions are reduced even by a factor of 2 for CTM. On the other hand, the feeding of the states outside the main band is also reduced. These transitions are reproduced more accurately with the CGCM model.

In conclusion, the two simulations using the EGLO strength function, the CTM level density model and CONSTANT or BSFG spin cut-off model are considered to be the best combinations of models to reproduce the EXILL data. These models will be used in the following sections to study the effect of the spin-distribution dependence of the γ -cascade.

E_γ (keV)	Transition	I_γ		
		EXILL data	FIFRELIN simulation CONSTANT	FIFRELIN simulation BSFG
Deformed Ground State Band (1)				
212.5	$2_1^+ \rightarrow 0_1^+$	100	100	100
352.0	$4_1^+ \rightarrow 2_1^+$	78(3)	82(1)	88(1)
497.1	$6_1^+ \rightarrow 4_1^+$	44(2)	62.5(8)	80(1)
625.6	$8_1^+ \rightarrow 6_1^+$	15(1)	34.8(6)	50.8(7)
739.2	$10_1^+ \rightarrow 8_1^+$	2.5(6)	17.2(4)	21.8(4)
841.7	$12_1^+ \rightarrow 10_1^+$	1.2(5)	6.5(2)	5.7(2)
Band (2)				
219.8	$(7_1^+) \rightarrow (6_3^+)$	4.1(6)	2.0(1)	2.7(1)
250.3	$(8_3^+) \rightarrow (7_1^+)$	1.8(4)	1.12(9)	1.9(1)
Band (3)				
267.3	$?^? \rightarrow ?^?$	0.8(4)	0.27(4)	0.18(4)
301.3	$?^? \rightarrow ?^?$	1.2(6)	0.10(3)	0.10(3)
Band (4)				
536.0	$4_2^+ \rightarrow 2_2^+$	1.5(8)	1.5(1)	0.91(8)
547.0	$(6_2^+) \rightarrow 4_2^+$	2.0(4)	0.55(6)	0.34(5)
Transitions between Bands				
845.2	$(6_3^+) \rightarrow 4_2^+$	3.0(6)	1.3(1)	1.7(1)
1695.2	$(6_3^+) \rightarrow 4_1^+$	2.8(4)	0.85(8)	0.88(8)
1464.2	$?^? \rightarrow 6_1^+$	0.6(3)	0.34(5)	0.27(4)
665.98	$2_2^+ \rightarrow 2_1^+$	1.9(7)	2.6(1)	1.7(1)
850.1	$4_2^+ \rightarrow 4_1^+$	5.0(6)	1.9(1)	1.4(1)
900.1	$(6_2^+) \rightarrow 6_1^+$	1.9(3)	0.30(5)	0.23(4)

Table 5.9: Relative intensities (I_γ) of the γ -ray transitions (keV) in ^{100}Zr , normalized to the strongest transition (212.5 keV). Comparison of the EXILL experimental data with the simulations having the lowest χ^2 value, using CONSTANT ($\bar{\sigma}_L = \bar{\sigma}_H = 9.5$) and BSFG ($f_\sigma = 1.8$) spin cut-off models and the CTM level density model. These simulations give the correct neutron multiplicities ($\bar{\nu}_L, \bar{\nu}_H, \bar{\nu}_{Tot}$).

5.4.2 Influence of the spin-distribution

In FIFRELIN so far, there is no free parameter set (Section 2.8.2) which correctly reproduces both the average prompt-neutron multiplicity and the discrete γ -ray cascade. FIFRELIN simulations are constrained on the average prompt-neutron multiplicities for the light fission fragment group ($\bar{\nu}_L$), for the heavy fission fragment group ($\bar{\nu}_H$) and total ($\bar{\nu}_{Tot}$). The maximum accepted discrepancy between experimental and simulated prompt-neutron multiplicities is equal to the uncertainties on the experimental neutron-multiplicities which are around a few percents (Section 2.8.2). Otherwise, a simulation is considered to be faulty. To explore the influence of the spin-distribution, we remove this condition.

CONSTANT model

As a starting point we used the CONSTANT model coupled to the EGLO model for the strength function and CTM for the level density. The optimized parameters which give the lowest χ^2 value (Table 5.7) are given in Table 5.10. This simulation will be referred in the following as the reference simulation. In the new simulation we changed only the spin cut-off parameter, other free parameters stayed identical. An example of an initial spin-distribution for light fragments using the CONSTANT model is shown in Figure 5.18.

Parameter	Used values
R_{Γ}^{\min}	0.63
R_{Γ}^{\max}	1.26
$\bar{\sigma}_L$	9.5
$\bar{\sigma}_H$	9.5

Table 5.10: Parameters used to simulate $^{235}\text{U}(n_{th}, f)$ with the CONSTANT spin cut-off model giving the best agreement with the EXILL data for the γ -intensities and the correct $\bar{\nu}_{Tot}$.

In Figure 5.19, the intensities coming from the simulations with the reduced spin cut-off parameter are compared to the EXILL experimental data for ^{100}Zr . We decided to use the same spin cut-off parameter for the light and for the heavy fission fragment

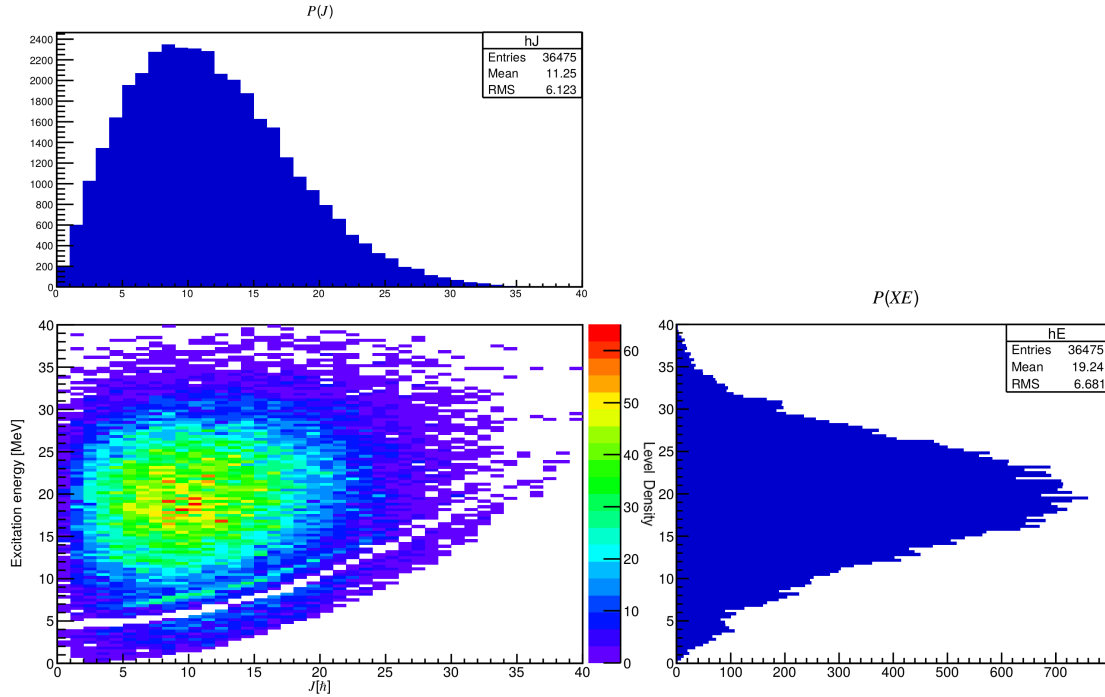


Figure 5.18: Initial distribution of excitation energy (XE) and spin (J) for light fission fragments when the CONSTANT spin cut-off model is used and $\bar{\sigma}_L = \bar{\sigma}_H = 9.5$.

groups, like in the reference simulation (see Table 5.10). The new spin cut-off parameter values span from 5.0 to 9.5 with a step of 0.5. We chose such a wide range to guarantee that production of the high-spin states is visibly reduced. The steps of 0.5 were optimal, smaller ones would be problematic because of the amount of resources and computing time needed for each simulation. The experimental data coming from EXILL are presented as dashed lines, with the dotted lines marking the envelop of their uncertainties. As can be seen in Figure 5.19, there was no need to use a lower spin cut-off than 5. Each experimental prompt γ -ray transition intensity has a corresponding simulation which correctly reproduces its value. We can see a dependence between the spin of the excitation state and the spin cut-off value. For γ -ray at 351.96 keV which comes from the 4^+ state the simulation that is the closest to the experimental data uses a spin cut-off parameter equal to 8.5. If we move to the transition 497.14 keV which comes from the 6^+ state the corresponding simulation has a spin cut-off parameter equal to 6.0 or 6.5. For the transitions coming from the states with even higher spins equal to 10^+ (734.2 keV) and 12^+ (841.7 keV), the corresponding simulation uses a spin cut-off parameter equal to only 5.5.

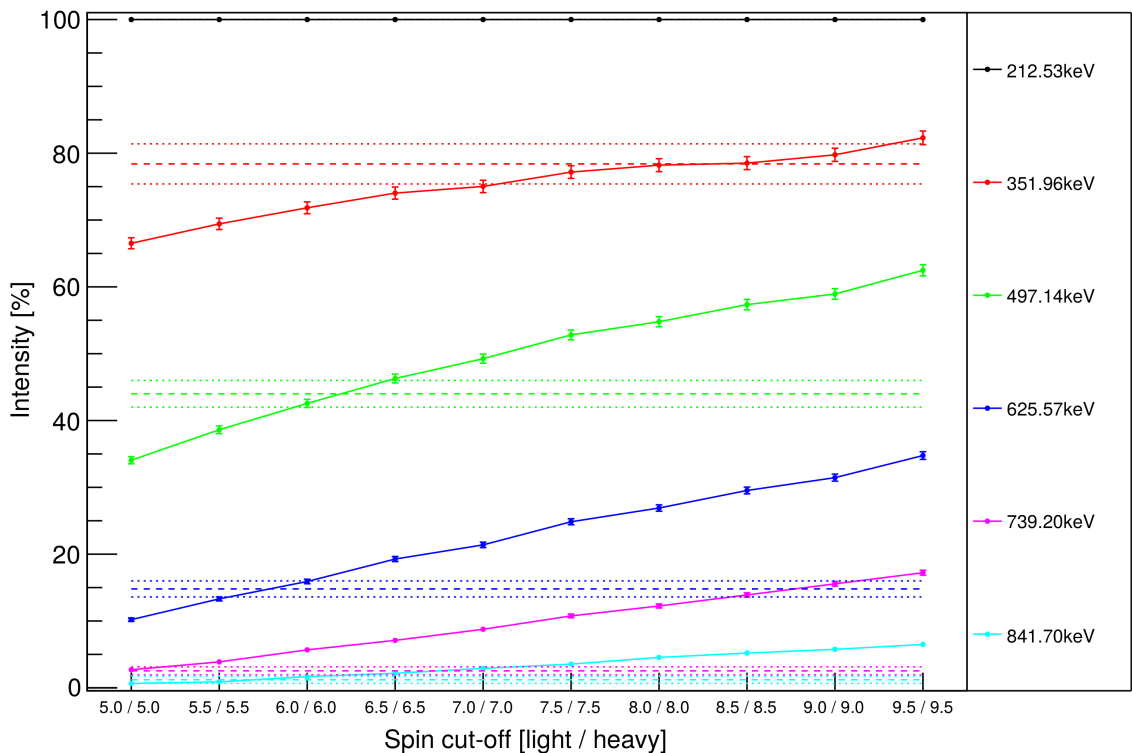


Figure 5.19: Evolution of simulated γ -transition intensities in ^{100}Zr depending on the spin cut-off value. The CONSTANT spin cut-off model was used. Dashed lines show intensity values from the EXILL experimental data, dotted lines errors on them.

Reducing the spin cut-off parameter decreases the initial spin of the fission fragments. The whole initial spin distribution is pushed towards lower values. As neutron cannot remove an indefinite amount of angular momentum, after neutron emission, a fragment with a high initial spin stays in a region of high spin. When the initial spin-distribution is decreased, the population of high-spin excited states is also reduced. This mechanism also affects lower spin transitions ($6^+ \rightarrow 4^+$, $4^+ \rightarrow 2^+$) as the initial spin distribution goes to lower spin values.

The analysis of Figure 5.19 shows that a lower spin cut-off parameter is required to reproduce the experimental data. To decide how small is the optimal value for the chosen set of the free parameters (Table 5.10), we compared their χ^2 values. For each simulation the χ^2 was calculated, as before, over the prompt γ -ray transition intensities coming from the main ground state band: 212.5 keV, 352.0 keV, 497.1 keV, 625.6 keV, 739.2 keV and 841.7 keV. The simulation with the spin cut-off parameter equal to 5.5

gives the lowest χ^2 value (Figure 5.20).

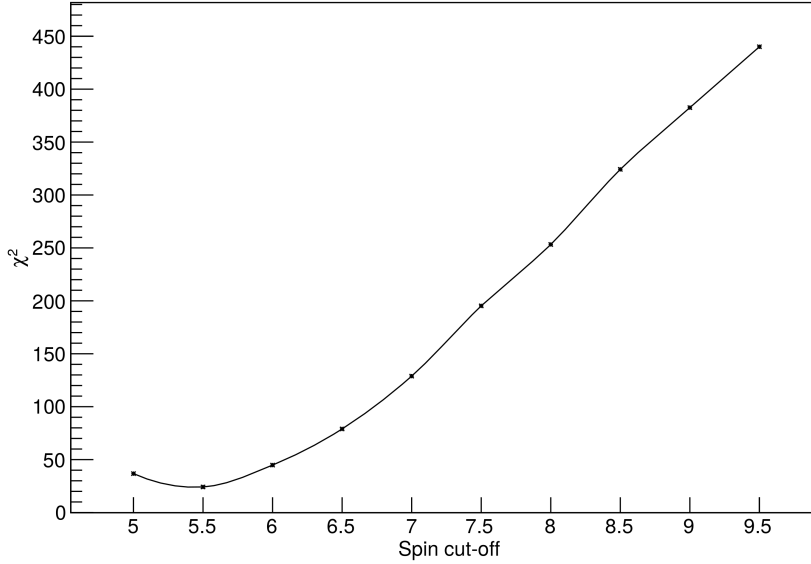


Figure 5.20: χ^2 values containing main band γ -ray transitions in ^{100}Zr for FIFRELIN simulations with different spin cut-off values. In each simulation $\bar{\sigma}_L$ was equal to $\bar{\sigma}_H$.

BSFG model

We also used the BSFG model coupled to the EGLO model for the photon strength functions and CTM for the level density and we modified the parameter called scaling factor (f_σ) (Section 2.2.2). The reference simulation parameters are given in Table 5.11. We kept R_T^{\min} and R_T^{\max} unchanged and we scanned f_σ between 0.9 to 1.8 with a step of 0.05.

Parameter	Used values
R_T^{\min}	0.75
R_T^{\max}	1.23
f_σ	1.8

Table 5.11: Parameters used to simulate $^{235}\text{U}(n_{th}, f)$ with the BSFG spin cut-off model giving the most accurate intensities and correct $\bar{\nu}_{Tot}$.

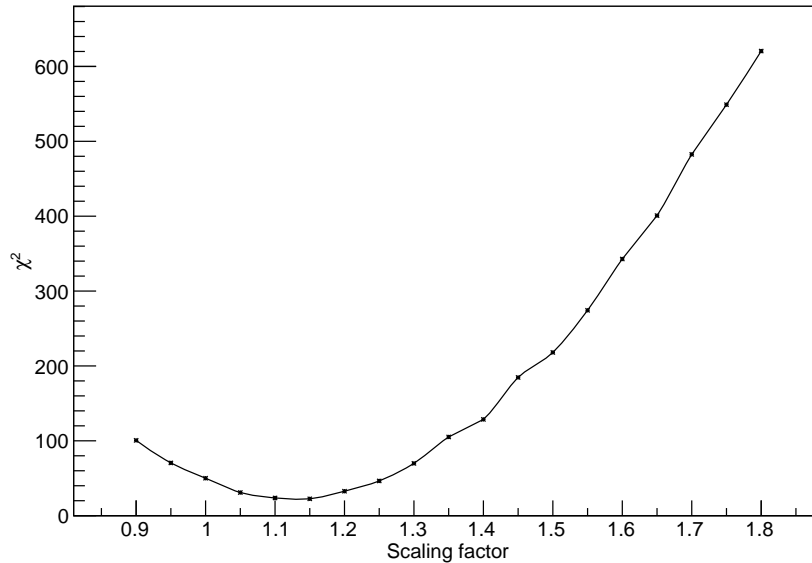


Figure 5.21: χ^2 value containing main band γ -transitions in ^{100}Zr for FIFRELIN simulations with different scaling factor values (f_σ).

Like in the previous study a drastic decrease of f_σ is required to reproduce the experimental data and the optimum is obtained for f_σ equal to 1.15 (Figure 5.21). f_σ chooses how far the primary fission fragment spin-distribution is from the mean spin distribution taking into account the nuclear level density. For a given excitation energy E it gives: $J(E) = f_\sigma \cdot J_{mean}(E)$. When f_σ equals 1, the spin of the primary fission fragment follows the mean of the nuclear spin-level density. One can compare for example the spin-distribution for $f_\sigma = 1.8$ (Figure 5.22) and for $f_\sigma = 1.15$ (Figure 5.23).

In our analysis we observed that the optimal f_σ was reduced from 1.8 to 1.15. It has a physical meaning and it could have been somehow expected. It means that the fission process prefers to populate the primary fission fragments with a spin close to their most probable spin value regarding their nuclear structure.

Let us now look closer at the impact of changing f_σ on each transition intensity. A large value of f_σ impacts mostly the discrete transitions between high-spin states. This is observed on the evolution of the transition intensities with f_σ in Figure 5.24. The reason is again the shape of the initial spin distribution as a function of the excitation energy. At low excitation energy, the spin is low and very close to the mean of the level density J_{mean} . At high energy, the spin of the primary fragments increases more than

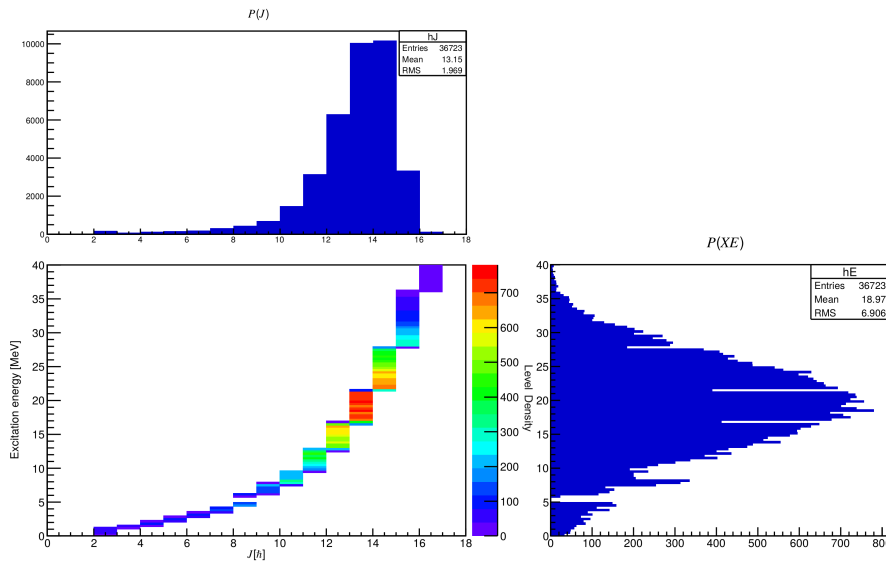


Figure 5.22: Initial distribution of excitation energy (XE) and spin (J) for light fission fragments when the BSFG spin cut-off model is used, $f_\sigma = 1.8$ and $R_T^{\max} = 1.23$.

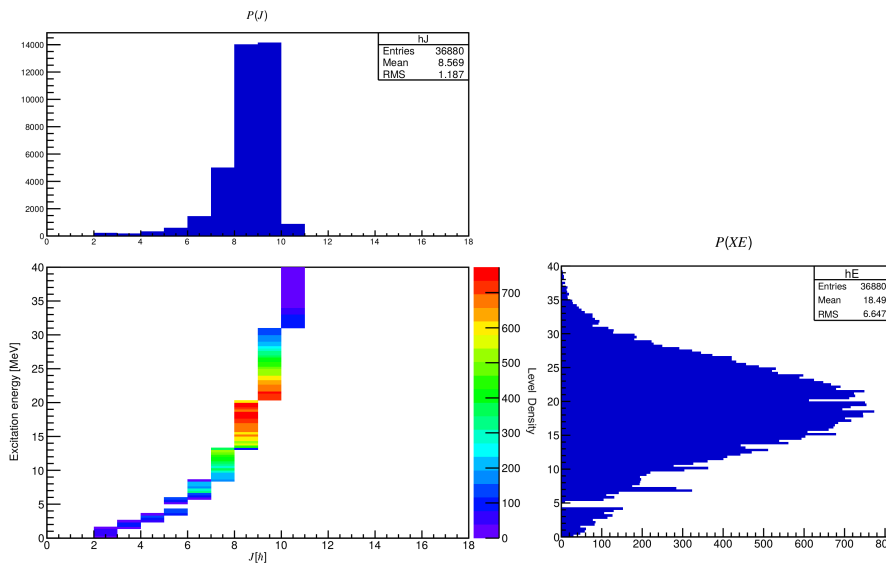


Figure 5.23: Initial distribution of excitation energy (XE) and spin (J) for light fission fragments when the BSFG spin cut-off model is used, $f_\sigma = 1.15$ and $R_T^{\max} = 1.23$.

J_{mean} . The effect of varying f_σ is thus more important at high energy and thus, here, for the transitions between high spin states.

The simulation which correctly reproduces the experimental intensity of the $12^+ \rightarrow 10^+$ (841.7 keV) transition uses f_σ equal to 1.50, this value is not far from the reference

simulation ($f_\sigma = 1.80$). On the other hand, f_σ needs to be reduced to only 0.95 for the $4^+ \rightarrow 2^+$ (352.0 keV) transition. It is a huge reduction in comparison to 1.80 from the reference simulation. At low excitation energy, the modification of f_σ needs to be large to see any difference in the population of the excited states.

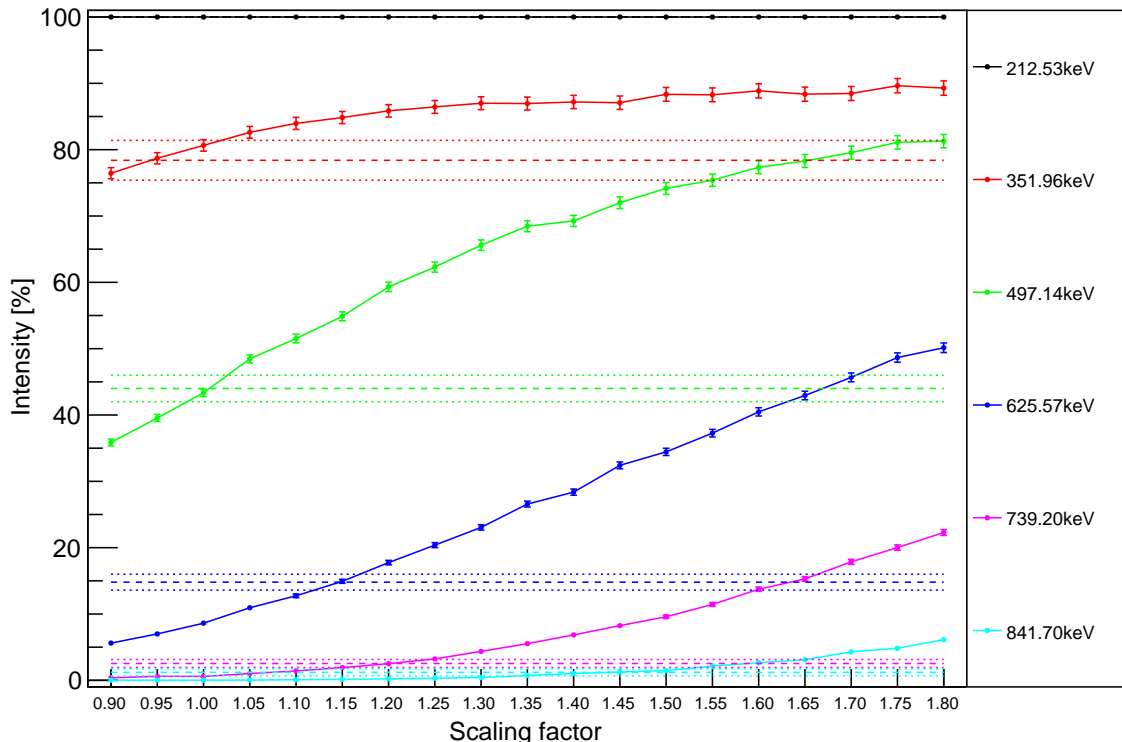


Figure 5.24: Evolution of simulated γ -ray transition intensities in ^{100}Zr depending on the spin cut-off value. The BSFG spin cut-off model was used. Dashed lines show intensity values from the EXILL experimental data, dotted lines errors on them.

5.4.3 Comparison of the two models

Table 5.12 compares γ -transitions intensities measured with EXILL, with the two optimal FIFRELIN simulations (lowest χ^2 value), the first one using the CONSTANT spin cut-off model with $\bar{\sigma}_L$ and $\bar{\sigma}_H$ both equal to 5.5, and the second one using the BSFG spin cut-off model with $f_\sigma = 1.15$.

The main observation is that the overall performances of both simulations are similar. They obtain around the same χ^2 values for the main band γ -transitions ($\chi^2 \approx 21$

E_γ (keV)	Transition	I_γ		
		EXILL data	FIFRELIN simulation CONSTANT	FIFRELIN simulation BSFG
Deformed Ground State Band (1)				
212.5	$2_1^+ \rightarrow 0_1^+$	100	100	100
352.0	$4_1^+ \rightarrow 2_1^+$	78(3)	69.4(9)	84.8(9)
497.1	$6_1^+ \rightarrow 4_1^+$	44(2)	38.6(6)	54.9(7)
625.6	$8_1^+ \rightarrow 6_1^+$	15(1)	13.3(3)	14.9(3)
739.2	$10_1^+ \rightarrow 8_1^+$	2.5(6)	3.9(2)	1.9(1)
841.7	$12_1^+ \rightarrow 10_1^+$	1.2(5)	0.89(7)	0.14(3)
Band (2)				
219.8	$(7_1^+) \rightarrow (6_3^+)$	4.1(6)	1.36(9)	2.1(1)
250.3	$(8_3^+) \rightarrow (7_1^+)$	1.8(4)	0.65(6)	1.14(8)
Band (3)				
267.3	$?^? \rightarrow ?^?$	0.8(4)	0.12(3)	0.11(2)
301.3	$?^? \rightarrow ?^?$	1.2(6)	0.03(1)	0.05(1)
Band (4)				
536.0	$4_2^+ \rightarrow 2_2^+$	1.5(8)	1.9(1)	2.2(1)
547.0	$(6_2^+) \rightarrow 4_2^+$	2.0(4)	0.65(6)	0.95(7)
Transitions between Bands				
845.2	$(6_3^+) \rightarrow 4_2^+$	3.0(6)	0.94(8)	1.7(1)
1695.2	$(6_3^+) \rightarrow 4_1^+$	2.8(4)	0.66(6)	0.83(7)
1464.2	$?^? \rightarrow 6_1^+$	0.6(3)	0.22(4)	0.18(3)
665.98	$2_2^+ \rightarrow 2_1^+$	1.9(7)	3.8(2)	2.3(1)
850.1	$4_2^+ \rightarrow 4_1^+$	5.0(6)	2.5(1)	2.9(1)
900.1	$(6_2^+) \rightarrow 6_1^+$	1.9(3)	0.45(5)	0.80(7)

Table 5.12: Relative intensities (I_γ) of the γ -ray transitions (keV) in ^{100}Zr , normalized to the strongest transition (212.5keV). Comparison of the EXILL experimental data with the simulations scanning the spin cut-off value or f_σ which gives the lowest χ^2 .

for the BSFG model and $\chi^2 \approx 22$ for the CONSTANT model), see Figures 5.20 and 5.21. It can be seen that the intensities of the prompt γ -rays are much closer to the EXILL data (Table 5.12) than in the reference cases (Table 5.9).

The BSFG model gives slightly better results for the γ -rays outside of the main bands, see Table 5.12. Another observation in Table 5.12 is that, in the main band, the feeding of the low-spin excited states is higher for the BSFG model than for the CONSTANT model while this trend reverses for the high-spin states. The reason should be linked to the different spin distributions but no simple explanation has been found for this effect.

5.5 Dependence with the temperature

As explained in Section 5.4.2, to explore the influence of the spin distribution model on the discrete γ -ray cascade, we remove the constraint that FIFRELIN must reproduce the average prompt neutron multiplicities.

Shifting the spin distribution of the primary fission fragments to lower a value allowed us to improve the reproduction of the γ -transition intensities and tremendously the χ^2 value calculated on the ground state band transitions. But it had an impact on the simulated values of the average prompt neutron multiplicities. Table 5.13 shows those values for the optimal FIFRELIN simulations. All of them are larger than the adopted experimental values.

Neutron multiplicity	CONSTANT	BSFG	Adopted experimental value
$\bar{\nu}_L$	1.52	1.53	1.41
$\bar{\nu}_H$	1.23	1.20	1.01
$\bar{\nu}_{Tot}$	2.75	2.73	2.42

Table 5.13: Average prompt-neutron multiplicities for the simulations which give the lowest χ^2 value. For CONSTANT, the spin cut-off parameter is equal to 5.5. For BSFG, f_σ is equal to 1.15. The adopted experimental values are taken from [Nis+98].

The reason is that by reducing the spin of the fission fragments, we reduced their rotational energy (E^{rot}), see Equation 2.17. But the distribution of the excitation

energy did not change. One can compare the distributions on the right plot of Figure 5.22 and 5.23. Therefore, the available energy to emit neutrons ($XE - E^{rot}$) increased and this is why the prompt neutron multiplicity went up.

We decided to look for a simulation which correctly reproduces the prompt-neutron multiplicities by scanning the R_T^{\min} and R_T^{\max} values which are closely related to the primary fission fragment temperature (see Section 2.2.3). This work was performed for a simulation using the BSFG spin cut-off model only.

We scanned R_T^{\min} between 0.5 to 0.95 and R_T^{\max} between 1 and 1.5 both with the step equal to 0.05, see Figure 5.25. f_σ , like in the optimal simulation from the previous analysis, was equal to 1.15.

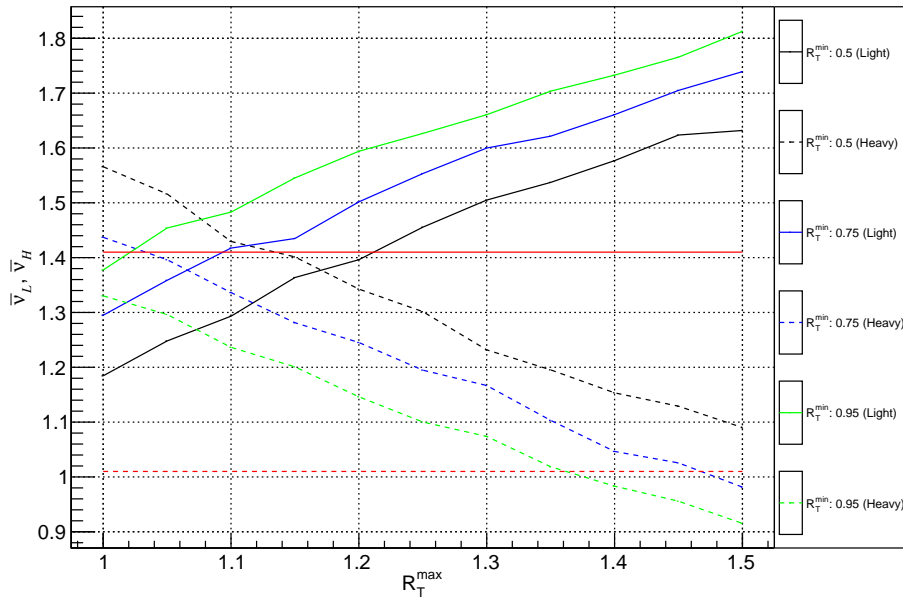


Figure 5.25: $\bar{\nu}_L$ and $\bar{\nu}_H$ obtained with FIFRELIN simulations as a function of R_T^{\max} and for different R_T^{\min} . Full lines show $\bar{\nu}_L$. Dashed lines show $\bar{\nu}_H$. Red lines show the experimental values. Only 3 different R_T^{\min} values are presented: minimum (0.5), maximum (0.95) and one from the analysis of the BSFG spin cut-off model (0.75).

We used only 10000 events per simulation to reduce the calculation time. From our experience this number is enough to find a correct prompt-neutron multiplicity, and we had observed only a slight difference between 10000 and 1000000 events in terms of $\bar{\nu}_L$, $\bar{\nu}_H$ and $\bar{\nu}_{Tot}$. We performed 110 simulations, none of them gave the correct average total prompt-neutron multiplicity equal to 2.42. The obtained $\bar{\nu}_{Tot}$ values were around

2.7. Even though the $\bar{\nu}_{Tot}$ is incorrect, some simulations gave correct $\bar{\nu}_L$ or $\bar{\nu}_H$ (Figure 5.25). Nevertheless, it was impossible to find a set of R_T^{\min} and R_T^{\max} values which correctly reproduces both $\bar{\nu}_L$ and $\bar{\nu}_H$ at the same time.

Since we know that the best agreement between the EXILL data and the FIFRELIN simulation is obtained for the rather low f_σ equal to 1.15, we decided to look for a simulation which will give the correct $\bar{\nu}(100)$ and the correct prompt γ -ray intensities for ^{100}Zr . This allows us to check if FIFRELIN is able to locally reproduce the experimental data. According to the published experimental neutron multiplicity as a function of a fission fragment mass (Figure 5.26), $\bar{\nu}(100)$ (for the mass of ^{100}Zr) is between 1.40 and 1.65. The experimental range (1.40 \div 1.65) is marked in Figure 5.27 and is compared with the results from the FIFRELIN simulations as a function of R_T^{\max} and for different R_T^{\min} .

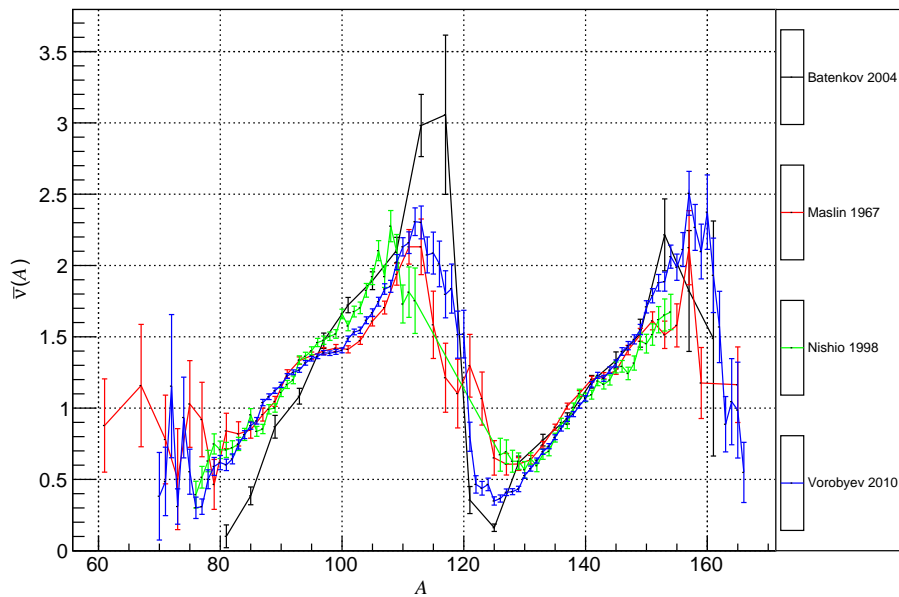


Figure 5.26: Prompt-neutron multiplicity sawtooth as a function of a fission fragment mass number, coming from the published experimental data [Bat+05; MRC67; Nis+98; Vor+10].

From Figure 5.27 we can conclude that some simulations correctly reproduce $\bar{\nu}(100)$ if R_T^{\max} is lower than 1.15. There is no strong dependence of $\bar{\nu}(100)$ with R_T^{\min} . This can be understood by looking at the fission fragment temperature correlation graph in Figure 5.28. In the $^{235}\text{U}(n_{th}, f)$ reaction, the fission fragment partners of ^{100}Zr have the

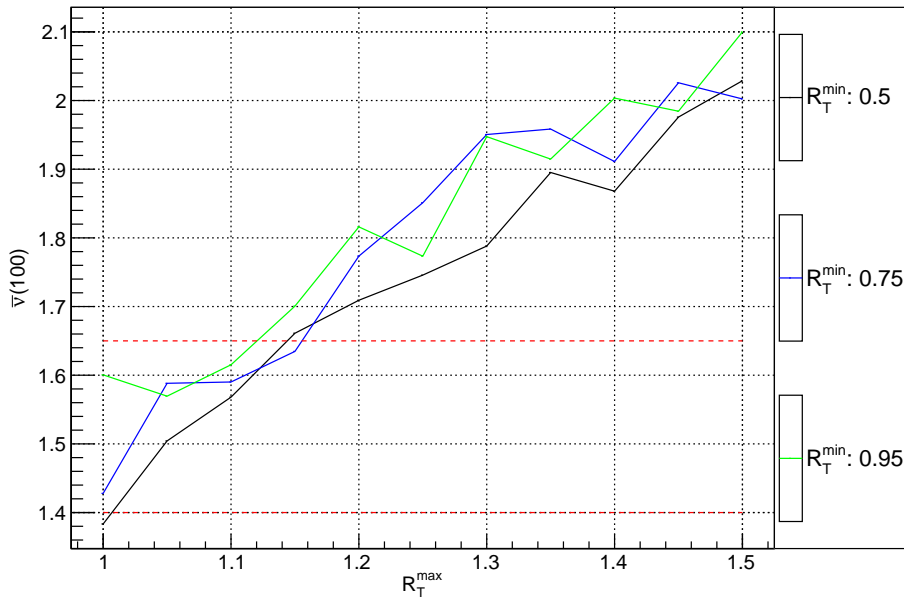


Figure 5.27: $\bar{\nu}(100)$ obtained with FIFRELIN simulations as a function of R_T^{\max} and for different R_T^{\min} . Only 3 different R_T^{\min} values are presented: minimum (0.5), maximum (0.95) and one which was used in the previous analysis of the BSFG spin cut-off model (0.75). Dashed, red lines mark minimal and maximal $\bar{\nu}(100)$ coming from the published experimental data (Figure 5.26).

mass around $A = 136$, which is close to $A = 132$ that corresponds to a doubly magic nucleus defining the R_T^{\max} position. Any change of R_T^{\max} in the simulation will have a much stronger influence on the ^{100}Zr temperature than adjusting R_T^{\min} .

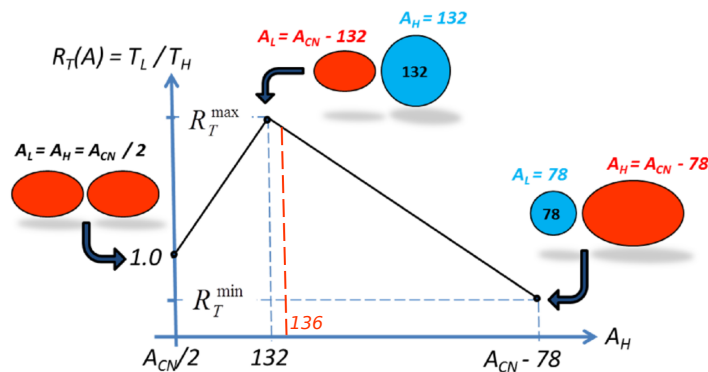


Figure 5.28: Temperature curve showing the relation between R_T^{\min} and R_T^{\max} . Dashed, red line marks a position of ^{100}Zr .

We decided to keep $R_T^{\min} = 0.75$ because it is the same as in the simulation which gives the best agreement with the EXILL data and the correct $\bar{\nu}_{Tot}$ (Table 5.11). Having the same R_T^{\min} as before allows us to study only the influence of R_T^{\max} on the FIFRELIN output. According to Figure 5.27, we decided to use $R_T^{\max} = 1.0$, for which $\bar{\nu}(100) = 1.43$. As before, we tried to determine the best f_σ by scanning its value around 1.15. The best χ^2 value was obtained for $f_\sigma = 1.2$ (Figure 5.29), which is not far from the optimal value obtained previously ($f_\sigma = 1.15$ for $R_T^{\max} = 1.23$). $\bar{\nu}(100) = 1.49$ is much better than 1.78 obtained when $R_T^{\max} = 1.23$. The new value fits in the range of the experimental neutron multiplicities (Figure 5.26).

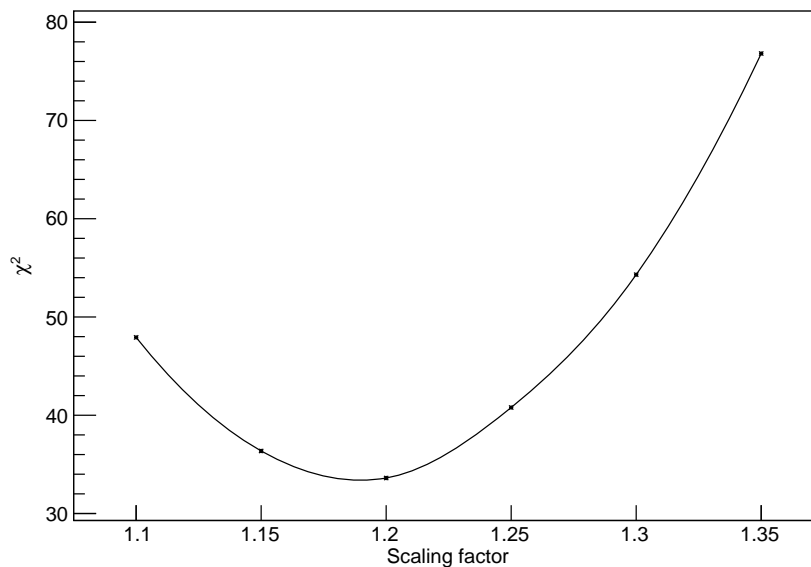


Figure 5.29: χ^2 value containing main band γ -transitions in ^{100}Zr for FIFRELIN simulations with different scaling factor values (f_σ) for $R_T^{\max} = 1.0$.

Due to the reduction of R_T^{\max} from 1.23 to 1.00, the temperature (the intrinsic excitation energy) of the light fission fragment in comparison to the heavy fission fragment becomes much lower (Equation 2.23). As a consequence the mean value of the initial excitation energy for the light fragments is also reduced (Equation 2.14) and is now close to 16.2 MeV (Figure 5.30), whereas it was around 18.5 MeV for $R_T^{\max} = 1.23$ (Figure 5.22).

To see the effect of changing the temperature on the γ -ray transitions, we calculated their intensities for two R_T^{\max} values ($R_T^{\max} = 1.23$ and $R_T^{\max} = 1.0$), see Table 5.14. The change of R_T^{\max} does not affect too much the prompt γ -ray intensities because $J(E)$

E_γ (keV)	Transition	I_γ		
		EXILL data	FIFRELIN simulation BSFG (R_T^{\max} 1.23)	FIFRELIN simulation BSFG (R_T^{\max} 1.00)
Deformed Ground State Band (1)				
212.5	$2_1^+ \rightarrow 0_1^+$	100	100	100
352.0	$4_1^+ \rightarrow 2_1^+$	78(3)	84.8(9)	86.3(9)
497.1	$6_1^+ \rightarrow 4_1^+$	44(2)	54.9(7)	57.7(7)
625.6	$8_1^+ \rightarrow 6_1^+$	15(1)	14.9(3)	14.9(3)
739.2	$10_1^+ \rightarrow 8_1^+$	2.5(6)	1.9(1)	1.61(9)
841.7	$12_1^+ \rightarrow 10_1^+$	1.2(5)	0.14(3)	0.11(2)
Band (2)				
219.8	$(7_1^+) \rightarrow (6_3^+)$	4.1(6)	2.1(1)	2.2(1)
250.3	$(8_3^+) \rightarrow (7_1^+)$	1.8(4)	1.14(8)	1.02(8)
Band (3)				
267.3	$?^? \rightarrow ?^?$	0.8(4)	0.11(2)	0.15(3)
301.3	$?^? \rightarrow ?^?$	1.2(6)	0.05(1)	0.07(2)
Band (4)				
536.0	$4_2^+ \rightarrow 2_2^+$	1.5(8)	2.2(1)	2.0(1)
547.0	$(6_2^+) \rightarrow 4_2^+$	2.0(4)	0.95(7)	1.14(8)
Transitions between Bands				
845.2	$(6_3^+) \rightarrow 4_2^+$	3.0(6)	1.7(1)	1.53(9)
1695.2	$(6_3^+) \rightarrow 4_1^+$	2.8(4)	0.83(7)	1.01(7)
1464.2	$?^? \rightarrow 6_1^+$	0.6(3)	0.18(3)	0.15(3)
665.98	$2_2^+ \rightarrow 2_1^+$	1.9(7)	2.3(1)	2.1(1)
850.1	$4_2^+ \rightarrow 4_1^+$	5.0(6)	2.9(1)	3.0(1)
900.1	$(6_2^+) \rightarrow 6_1^+$	1.9(3)	0.80(7)	0.79(7)

Table 5.14: Relative intensities (I_γ) of the γ -ray transitions (keV) in ^{100}Zr , normalized to the strongest transition (212.5 keV). Comparison of the EXILL experimental data with the simulations using BSFG which give the lowest χ^2 value for different R_T^{\max} .

stays about the same, close to $J_{mean}(E)$. Only a slight reduction in feeding the states with spin above 8^+ can be noticed.

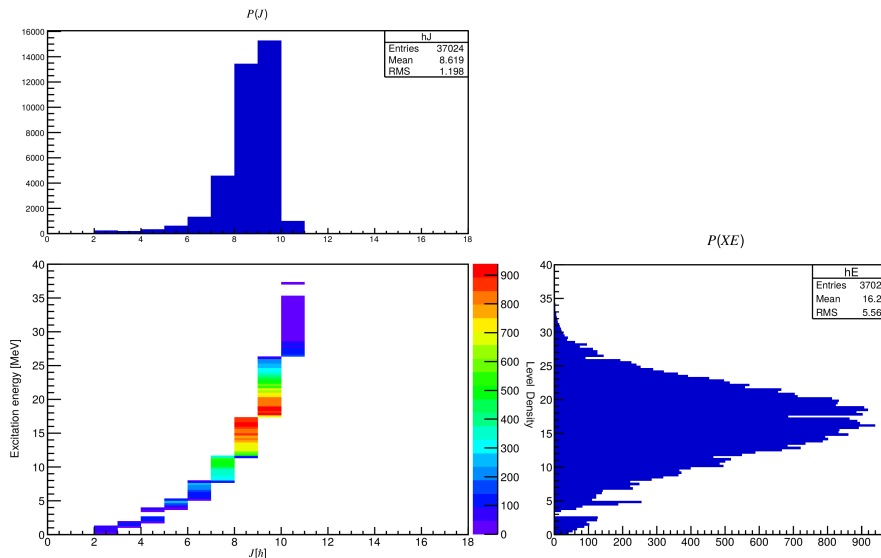


Figure 5.30: Initial distribution of excitation energy (XE) and spin (J) for light fission fragments when the BSFG spin cut-off model is used, $f_\sigma = 1.2$ and $R_T^{\max} = 1.0$.

5.6 Summary of the ^{100}Zr analysis

We have performed an extensive analysis on ^{100}Zr . In Section 5.2, the comparison of the prompt γ -ray cascade coming from the EXILL experiment to ^{248}Cm [Dur+95] and ^{235}U [Muk+12] data shows a good agreement. Nevertheless, there is a slight disagreement with the ^{252}Cf data [Hwa+06]. We concluded that it can be caused either by the difference in the distributions of the initial spin and excitation energy of the primary fission fragments or by a normalization problem in [Hwa+06].

A further ^{100}Zr analysis, in Section 5.3, was focused on a comparison of the EXILL data with results of the FIFRELIN simulations. We started with the simulations which at the same time correctly reproduce three average prompt-neutron multiplicities ($\bar{\nu}_L$, $\bar{\nu}_H$, $\bar{\nu}_{Tot}$). We compared two spin cut-off models: CONSTANT and BSFG. We observed that γ -ray transition intensities are rising with the atomic mass of Te (fission partner of ^{100}Zr) when the CONSTANT spin cut-off model is used. It causes an overpopulation of the high spin excited states. This phenomenon was entirely assigned to

the CONSTANT model. It was neither noticed in the simulations using BSFG model, nor in the EXILL experimental data.

Section 5.4 of the FIFRELIN analysis was devoted to finding the best set of models and free parameters. To compare the results we used a χ^2 test built on the intensities of γ -transitions in the ground state band when the fission partner is ^{134}Te (2 evaporated neutrons). The best results (the lowest χ^2 value) were generated by the simulations using the EGLO photon strength functions model and the CTM level density model. This is true for the simulations using CONSTANT and BSFG spin cut-off models. Even though, we had chosen the simulations with the lowest χ^2 values, in the direct comparison to the experimental data, feeding of the high spin states was too high. We concluded that this problem is caused by a too high simulated initial spin of the primary fission fragments.

We tackled the high initial spin of the primary fission fragment by scanning the free parameters: the spin cut-off of the light and heavy fission fragment groups (CONSTANT spin cut-off model) and the scaling factor (BSFG spin cut-off model). For both models significant reduction of these free parameters remarkably reduced the χ^2 , bringing the intensities of γ -rays closer to the experimental values (Table 5.12). Unfortunately, it also disturbed the prompt-neutron multiplicity values, which were far from experimental data (Table 5.13).

Section 5.5 was devoted to the improvement of the prompt-neutron multiplicity in the simulation with the decreased scaling factor. This analysis was conducted only with the BSFG spin cut-off model. This decision was taken because in this model, the initial spin distribution is excitation energy dependent and follows J_{mean} which makes more sense in view of the nuclear structure than the naive hypothesis of a distribution with a constant spin cut-off parameter.

To reduce the initial excitation energy of the primary fission fragments, and thus the prompt-neutron multiplicity, we scanned values of the free parameters: $R_{\text{T}}^{\text{min}}$ and $R_{\text{T}}^{\text{max}}$. It did not give us the expected outcomes. The average total prompt-neutron multiplicity stayed almost unchanged at around 2.7, which is much higher than the desirable 2.41. It proves that with the tested model setup, FIFRELIN is unable to simultaneously reproduce the γ -ray intensities and the prompt-neutron multiplicity averaged over all fission fragments.

We decided to test how correct FIFRELIN can be in the case of the single fission fragment - ^{100}Zr . To do that we looked for a $R_{\text{T}}^{\text{max}}$ which gives the correct prompt-

neutron multiplicity for the fission fragment with the atomic mass $A = 100$. We were able to find an R_T^{max} value which met our criteria. Its modification forces us to redo the scaling factor optimization. The lowest χ^2 value was found, whereas the correct neutron multiplicity for the mass $A = 100$ was preserved. This proved that when an iterative process of optimization of the free parameters is used, FIFRELIN is simultaneously able to deliver the correct neutron multiplicity for the fragment with a particular atomic mass and to correctly reproduce the γ -ray intensities emitted during its de-excitation process.

General conclusions and perspectives

Conclusions

My study of the nuclear fission fragments by spectrometry of the prompt γ -rays was motivated by a desire to deeper understand the fission process. We are convinced that a precise measurement of the discrete γ -ray cascade emitted by the fission fragments should help answering fundamental questions about the fission fragments de-excitation process. Additionally, such experimental information is essential to evaluate the codes that simulate the de-excitation process, and that will be used, in the future, to estimate the γ -heating process in nuclear reactors.

A large part of my thesis was concentrated on the data analysis of an experimental campaign performed at the ILL in 2012-2013 called EXILL. The experiment consisted in measuring, with a large array of HPGe detectors, the prompt γ -rays emitted by a ^{235}U target placed in an intense thermal neutron flux. I studied the γ -ray cascades in several fission fragments. In this manuscript, I presented the detailed results on ^{142}Ba and ^{100}Zr .

The large number of fission fragments and, as a result, the huge amount of transitions in the spectra, requests an analysis by a triple- γ coincidence technique. With this technique, two selected γ -rays identify the pair of fission fragments and the third γ -ray allows exploring their de-excitation cascade. In the course of my work, we found out that the standard analysis method, based on a simple background subtraction, which does not take into account the local landscape of the 2D coincidence matrix around the peak we want to study, fails to provide reproducible results. Some transition intensities could fluctuate up to 10% depending on the selection of the background region and/or the coincidence gates. Such additional uncertainty made it impossible to study some phenomena like e.g. the evolution of the de-excitation cascade in a fission fragment with its fission partner, which we expected to have the same order of magnitude.

In order to measure the number of coincidences between the three transitions $\gamma_1, \gamma_2, \gamma_3$, we developed a new analysis method, based on a scan of the coincidence gates in three directions. For each gate, we fit the peak associated to γ_3 in the coincidence spectrum. It results in a clean coincidence matrix with a two-dimensional peak centered on (γ_1, γ_2) . Different algorithms were then developed to estimate the volume of this 2D peak, according to the presence of contaminants, their positions and intensities. The new technique was automatized and became the main part of the EXILL data analysis software, that we called "EXILLANA".

The major advantage of the new method is that the final results are less contaminated than with the standard technique or, more exactly, that we can better identify contaminants and remove their contribution. As a consequence, uncertainties are better estimated and properly propagated.

The second part of my thesis was devoted to benchmarking the Monte-Carlo code FIFRELIN with the experimental results I extracted from the EXILL data. FIFRELIN simulates the fission process and the de-excitation of the fission fragments. I performed numerous simulations using different models which are implemented in this code. The goal was to find a set of them that best reproduces our experimental results and, at the same time, preserves correct averaged prompt-neutron multiplicities.

I have tested in particular the spin cut-off models implemented in FIFRELIN by studying the evolution of the de-excitation cascade in a fragment with its fission partner. It allows me to exclude the simple spin cut-off model which assumes that the spin distribution of the primary fragment does not vary with its excitation energy. Simulations were indeed found incompatible with the experimental results.

The next step was to reduce the discrepancies between the experimental and the simulated transitions intensities, especially for the transitions between high spin states. It was done by optimizing the initial spin and excitation energy of the primary fission fragments. This study showed however that FIFRELIN was unable to simultaneously provide correct average prompt-neutron multiplicities and reproduce well the experimental γ -ray intensities for the fission fragments which we compared.

In the last analysis, we aimed to obtain a correct prompt-neutron multiplicity and a correct description of the γ -transitions for a particular fission fragment. By adjusting the excitation energy partition between a fission fragment and its partner, and by using the BSFG spin cut-off model, we could successfully reproduce with a good precision both observables for ^{100}Zr .

Perspectives

Part of the problems which we encountered during the analysis of the EXILL data should be solved with the future experiments on the new instrument FIPPS installed at ILL. FIPPS is composed, like EXILL, of a large array of Compton suppressed HPGe detectors, but with a better energy resolution. It will improve the signal over background ratio. An important upgrade is the use of an active target, with the fissile actinide dispersed in a scintillator liquid. It allows tagging the fission events and thus clean the data from the large background coming from fission fragment β -decay and (n,γ) reactions on the target support. In a second phase, the addition of a fragment spectrometer to FIPPS is expected to improve significantly its performances.

The perspectives with FIPPS could be to study the de-excitation cascade dependence with the deformation of the fission partner and to see what could be the influence of the collectivity in the fission process. So far, our attempts to study this effect with EXILL data have not provided meaningful conclusions.

The new analysis method and the EXILLANA code can be further developed. One of the problems with using the narrow gates is the low statistics in the gated spectra. It reduces the possibility of analyzing weak γ -ray transitions. One can imagine to use asymmetric gates, such as 1 keV x 3 keV, for the horizontal gate scan and 3 keV x 1 keV for the vertical gate scan. In this way, we keep the same capability of precise contamination detection but we extract the area of the desired peak on 3 keV x 3 keV cumulative gate and thus gain in statistics by a factor of up to 9. This would improve both the ability to measure small peaks and reduce the uncertainty on the intensities of all peaks.

Another improvement could be the implementation of an algorithm which finds the best region of interest (ROI) for every spectrum separately. It could simplify and speed up the analysis and may improve the uncertainty on the area of the fitted peaks.

The experimental results on the de-excitation cascades of more fission fragments could accelerate the improvement of FIFRELIN. For that we should conduct analysis of the full cascade in both fission partners rather than extracting the strongest transition intensities in one of them. It would be a great constraint to check how well FIFRELIN is able to reproduce simultaneously different de-excitation cascades. It would facilitate the tuning of the implemented models and maybe the development of new models for the energy sharing and the spin distribution.

Based on my study of the FIFRELIN simulation results, I would propose several changes in this code. First of all, the implementation of the BSFG model should be corrected to provide a full distribution of spins instead of the mean value. Second of all, concerning the nuclear level schemes of the fission fragments, the RIPL-3 database used by FIFRELIN should be replaced by the more up-to-date ENSDF or XUNDL databases. We have analyzed several fission fragments (not presented in this manuscript) and for some of them, a comparison of our experimental results to FIFRELIN simulation results shows strong discrepancies, which can be reduced by an update of the level schemes. In some cases, only spins or parities were modified. In other cases, the update consists in completing the level scheme at high energy. Both changes have had a clear impact on the simulation results.

Bibliography

- [Alv93] C. R. Alvarez, *Nuclear Physics News*, vol. 3, pp. 10–13, 1993.
- [AP95] I. Ahmad and W. R. Phillips, *Reports on Progress in Physics*, vol. 58, pp. 1415–1463, 1995.
- [Aud+12] G. Audi *et al.*, *Chinese Physics C*, vol. 36, pp. 1287–1602, 2012.
- [AW95] G. Audi and A. Wapstra, *Nuclear Physics A*, vol. 595, pp. 409–480, 1995.
- [Axe62] P. Axel, *Physical Review*, vol. 126, pp. 671–683, 1962.
- [Aza99] F. Azaiez, *Nuclear Physics A*, vol. 654, pp. 1003–1008, 1999.
- [Bal+10] A. R. Balabekyan *et al.*, *Physics of Atomic Nuclei*, vol. 73, pp. 1814–1819, 2010.
- [Bat+05] O. I. Batenkov *et al.*, *AIP Conference Proceedings*, vol. 769, pp. 625–628, 2005.
- [BB89] J. Bocquet and R. Brissot, *Nuclear Physics A*, vol. 502, pp. 213–232, 1989.
- [Bec98] F. Becvar, *Nuclear Instruments and Methods in Physics Research Section A: Accelerators, Spectrometers, Detectors and Associated Equipment*, vol. 417, pp. 434–449, 1998.
- [Bet36] H. A. Bethe, *Physical Review*, vol. 50, pp. 332–341, 1936.
- [BG69] F. D. Becchetti and G. W. Greenlees, *Physical Review*, vol. 182, pp. 1190–1209, 1969.
- [BGM90] U. Brosa, S. Grossmann, and A. Müller, *Physics Reports*, vol. 197, pp. 167–262, 1990.
- [Bha+01] P. Bhattacharyya *et al.*, *Physical Review C*, vol. 64, no. 054312, 2001.
- [BL80] S. Bjørnholm and J. E. Lynn, *Reviews of Modern Physics*, vol. 52, pp. 752–932, 1980.

- [Bla+08] D. Blanchet *et al.*, *Annals of Nuclear Energy*, vol. 35, pp. 731–745, 2008.
- [Bla12] D. P. Blair, *PCSR - Sub-chapter 4.1 - Summary description*, <http://www.epr-reactor.co.uk/ssmod/liblocal/docs/PCSR/Chapter%20%204%20-%20Reactor%20and%20Core%20Design/Sub-Chapter%204.1%20-%20Summary%20description.pdf>, EDF and Areva, 2012.
- [Boy15] D. Boyes, *The HTMR-100 Modular High Temperature Gas Reactor program*, https://www-legacy.iaea.org/NuclearPower/Downloadable/Meetings/2015/2015-12-07-12-09-NPTDS/TM_Deep_Burn/A04-HTMR-Reactor_&Plant_Presentation_IAEA_2015.pdf, Steenkampskraal Thorium Limited, 2015.
- [Bri55] D. M. Brink, PhD thesis, Oxford University, Oxford, UK, 1955.
- [Bri63] D. M. Brink, ?Report ANL-6797?, in *International Conference on Nuclear Physics with Reactor Neutrons*, Argonne National Laboratory, USA, 1963, p. 194.
- [Cap+09] R. Capote *et al.*, *Nuclear Data Sheets*, vol. 110, pp. 3107–3214, 2009.
- [Cha32] J. Chadwick, *Nature*, vol. 129, p. 312, 1932.
- [CIZN16] B. S. C. I. Zhang and W. Nazarewicz, *Physical Review C*, vol. 94, no. 064323, 2016.
- [Col+13] A.-C. Colombier *et al.*, *EPJ Web of Conferences*, vol. 42, no. 04001, 2013.
- [dAn07] G. de Angelis, *Nuclear Physics A*, vol. 787, pp. 74c–83c, 2007.
- [Duc+99] G. Duchêne *et al.*, *Nuclear Instruments and Methods in Physics Research A*, vol. 432, pp. 90–110, 1999.
- [Dur+95] J. L. Durell *et al.*, *Physical Review C*, vol. 52, no. R2306(R), 1995.
- [ES08] J. Eberth and J. Simpson, *Progress in Particle and Nuclear Physics*, vol. 60, pp. 283–337, 2008.
- [Far10] G. Farkas, *From Gen I to Gen III*, https://inis.iaea.org/collection/NCLCollectionStore/_Public/44/078/44078368.pdf, IAEA, 2010.
- [FG94] P. Frobrich and I. I. Gontchar, in *2nd International Conference on Dynamical Aspects of Nuclear Fission*, Smolenice, Slovakia, 1994, p. 182.

- [FH18] M. Fawaz-Huber, *Going Long Term: US Nuclear Power Plants Could Extend Operating Life to 80 Years*, <https://www.iaea.org/newscenter/news/going-long-term-us-nuclear-power-plants-could-extend-operating-life-to-80-years>, Updated: 16-01-2018, IAEA, 2018.
- [Fra18] Framatome, *Taishan 1 & 2*, <http://www.framatome.com/FR/businessnews-320/framatome-grands-projets--taishan-1-et-2.html>, 2018.
- [GC56] A. Gilbert and A. G. W. Cameron, *Canadian Journal of Physics*, vol. 43, pp. 1446–1496, 1956.
- [GHK08] S. Goriely, S. Hilaire, and A. J. Koning, *Physical Review C*, vol. 78, no. 064307, 2008.
- [GK02] S. Goriely and E. Khan, *Nuclear Physics A*, vol. 706, pp. 217–232, 2002.
- [GKS04] S. Goriely, E. Khan, and M. Samyn, *Nuclear Physics A*, vol. 739, pp. 331–352, 2004.
- [Gor96] S. Goriely, *Nuclear Physics A*, vol. 605, pp. 28–60, 1996.
- [GSP07] S. Goriely, M. Samyn, and J. M. Pearson, *Physical Review C*, vol. 75, no. 064312, 2007.
- [GT48] M. Goldhaber and E. Teller, *Physical Review*, vol. 74, pp. 1046–1048, 1948.
- [GTR07] F. Gonnenuwein, I. Tsekhanovich, and V. Rubchenya, *International Journal of Modern Physics E*, vol. 16, pp. 410–424, 2007.
- [Gue+96] A. Guessous *et al.*, *Physical Review C*, vol. 53, pp. 1191–1196, 1996.
- [Gön14a] F. Gönenuwein, ?Neutron and Gamma Emission in Fission?, in *Fiesta 2014*, Tübingen, Germany: University of Tübingen, 2014.
- [Gön14b] F. Gönenuwein, ?Neutron-induced Fission?, in *l'Ecole Joliot Curie 2014*, Frejus, France, 2014.
- [Ham+03] F.-J. Hambsch *et al.*, *Nuclear Physics A*, vol. 726, pp. 248–264, 2003.
- [Ham+95] J. H. Hamilton *et al.*, *Progress in Particle and Nuclear Physics*, vol. 35, pp. 635–704, 1995.
- [Ham+97] J. H. Hamilton *et al.*, *Progress in Particle and Nuclear Physics*, vol. 38, pp. 273–287, 1997.
- [Hop+72] F. F. Hopkins *et al.*, *Physical Review C*, vol. 5, pp. 1015–1030, 1972.

- [Hot+91] M. A. C. Hotchkis *et al.*, *Nuclear Physics A*, vol. 530, pp. 111–134, 1991.
- [Hwa+06] J. K. Hwang *et al.*, *Physical Review C*, vol. 74, no. 017303, 2006.
- [IAE15] IAEA, *Advanced Large Water Cooled Reactors*, https://aris.iaea.org/Publications/IAEA_WRC_Booklet.pdf, 2015.
- [IGS79] A. Ignatyuk and K. I. nad G. Smirenkin, 'Role of collective effects in systematics of level density of nuclei?', Kernforschungszentrum Karlsruhe, Karlsruhe, Germany, Tech. Rep. KfK-tr-632, 1979.
- [IST75] A. Ignatyuk, G. Smirenkin, and A. Tishin, *Yadernaya Fizika*, vol. 21, no. 485, 1975.
- [Jen+17] M. Jentschel *et al.*, *Journal of Instrumentation*, vol. 12, no. P11003, 2017.
- [JLM74] J. Jeukenne, A. Lejeune, and C. Mahaux, *Journal de Physique Colloques*, vol. 35, no. C5, 1974.
- [Jon+05] E. F. Jones *et al.*, *Physics of Atomic Nuclei*, vol. 69, pp. 1198–1203, 2005.
- [Kal+02] V. Kalinin *et al.*, *Journal of Nuclear Science and Technology*, vol. 39, pp. 250–253, 2002.
- [KBM09] M. A. Kellett, O. Bernillon, and R. W. Mills, 'The Jeff-31/6311 radioactive decay data and fission yields sub-libraries Jeff report 20?', Nuclear Energy Agency, Tech. Rep., 2009.
- [KD03] A. Koning and J. Delaroche, *Nuclear Physics A*, vol. 713, pp. 231–310, 2003.
- [KHD08] A. Koning, S. Hilaire, and M. Duijvestijn, 'TALYS-1.0?', in *International Conference on Nuclear Data for Science and Technology*, Nice, France: EDP Sciences, 2008, p. 211.
- [Kor+00] A. Korgul *et al.*, *The European Physical Journal A*, vol. 7, pp. 167–176, 2000.
- [KU90] J. Kopecky and M. Uhl, *Physical Review C*, vol. 41, pp. 1941–1955, 1990.
- [KUC93] J. Kopecky, M. Uhl, and R. E. Chrien, *Physical Review C*, vol. 47, pp. 312–322, 1993.
- [Lee97] I. Y. Lee, *Progress in Particle and Nuclear Physics*, vol. 38, pp. 65–78, 1997.

- [Lem15] J. Lemaître, ?Etude des fragments de fission au point de scission avec le modèle SPY?, PhD thesis, Université Paris Sud - Paris XI, Saclay, France, 2015.
- [Lit+17] O. Litaize *et al.*, ?FIFRELIN-1.0 user guide?, CEA Cadarache, Tech. Rep., 2017.
- [Lon85] M. A. Lone, in *Neutron induced reactions, Proceedings of the 4th International Symposium*, Smolenice, Czechoslovakia, 1985, pp. 238–252.
- [LS10] O. Litaize and O. Serot, *Physical Review C*, vol. 82, no. 054616, 2010.
- [LSB15] O. Litaize, O. Serot, and L. Berge, *The European Physical Journal A*, vol. 51, no. 177, 2015.
- [MD98] S. F. Mughabghab and C. Dunford, *Physical Review Letters*, vol. 81, pp. 4083–4086, 1998.
- [MF39] L. Meitner and O. R. Frisch, *Nature*, vol. 143, pp. 239–240, 1939.
- [MRC67] E. E. Maslin, A. L. Rodgers, and W. G. F. Core, *Physical Review*, vol. 164, pp. 1520–1527, 1967.
- [MS71] U. Mosel and H. Schmitt, *Nuclear Physics A*, vol. 165, pp. 73–96, 1971.
- [Muk+12] S. Mukhopadhyay *et al.*, *Physical Review C*, vol. 85, no. 064321, 2012.
- [Möl+09] P. Möller *et al.*, *Physical Review C*, vol. 79, no. 064304, 2009.
- [Nai+97] H. Naik *et al.*, *Nuclear Physics A*, vol. 612, pp. 143–162, 1997.
- [NEA14] NEA, *Technology Roadmap Update for Generation IV Nuclear Energy Systems*, <https://www.gen-4.org/gif/upload/docs/application/pdf/2014-03/gif-tru2014.pdf>, OECD, 2014.
- [Nis+98] K. Nishio *et al.*, *Nuclear Physics A*, vol. 632, pp. 540–558, 1998.
- [Nob] *The Nobel Prize in Chemistry 1944*, <https://www.nobelprize.org/prizes/chemistry/1944/summary/>, Nobel Media AB, 2018.
- [NSI04] H. Naik, R. J. Singh, and R. H. Iyer, *Journal of Physics G: Nuclear and Particle Physics*, vol. 30, pp. 107–128, 2004.
- [Oku+18] S. Okumura *et al.*, ? $^{235}\text{U}(n, f)$ Independent fission product yield and isomeric ratio calculated with the statistical Hauser–Feshbach theory?, *Journal of Nuclear Science and Technology*, 2018, Published online.

- [Pas89] V. V. Pashkevich, in *International Conference on the 50th Anniversary of Nuclear Fission*, Leningrad, Russia, 1989, p. 241.
- [Paş+18] H. Paşca *et al.*, *Nuclear Physics A*, vol. 969, pp. 226–236, 2018.
- [Pom+18] K. Pomorski *et al.*, *Physical Review C*, vol. 97, no. 034319, 2018.
- [Por+06] M.-G. Porquet *et al.*, *The European Physical Journal A*, vol. 153-159, p. 28, 2006.
- [Ray94] J. Raynal, ?Notes on ECIS94?, CEA Saclay, Tech. Rep., 1994.
- [Reg13] D. Regnier, ?Contribution à l'étude des gammas prompts de fission?, PhD thesis, University of Grenoble, Grenoble, France, 2013.
- [Rim05] G. Rimpault, in *Proceedings of the Workshop On Nuclear Data Needs for Generation IV*, Antwerp, Belgium, 2005.
- [RLS12] D. Regnier, O. Litaize, and O. Serot, *Physics Procedia*, vol. 31, pp. 59–65, 2012.
- [RLS16] D. Regnier, O. Litaize, and O. Serot, *Computer Physics Communications*, vol. 201, pp. 19–28, 2016.
- [RU+00] T. Rząca-Urban *et al.*, *European Physical Journal A*, vol. 9, pp. 165–169, 2000.
- [RU+09] T. Rząca-Urban *et al.*, *Physical Review C*, vol. 79, no. 024319, 2009.
- [RU+17a] T. Rząca-Urban *et al.*, *Physical Review C*, vol. 95, no. 064302, 2017.
- [RU+17b] T. Rząca-Urban *et al.*, *Physical Review C*, vol. 95, no. 064302, 2017.
- [Ra15] M. Rapała, ?Study of the nuclear fission process of Uranium-235 by prompt gamma-ray spectrometry?, Master's thesis, Warsaw University of Technology, Warsaw, Poland, 2015.
- [Sah+01] S. K. Saha *et al.*, *Physical Review C*, vol. 65, no. 017302, 2001.
- [Sco+80] S. M. Scott *et al.*, *Journal of Physics G: Nuclear and Particle Physics*, vol. 6, pp. 1291–1317, 1980.
- [Sim+00] J. Simpson *et al.*, *Acta Physica Hungarica New Series Heavy Ion Physics*, vol. 11, pp. 159–188, 2000.

- [SJA14] K.-H. Schmidt, B. Jurado, and C. Amouroux, 'General Description of Fission Observables, GEF Model', Nuclear Energy Agency, Tech. Rep., 2014.
- [SLC17] O. Serot, O. Litaize, and A. Chebboubi, *EPJ Web of Conferences*, vol. 146, no. 04027, 2017.
- [Smi+02] A. G. Smith *et al.*, *Journal of Physics G: Nuclear and Particle Physics*, vol. 28, pp. 2307–2316, 2002.
- [Ste18] E. P. Steinberg, *Encyclopædia Britannica: Nuclear fission*, <https://www.britannica.com/science/nuclear-fission>, Updated: 06-07-2018, 2018.
- [Sud02] S. Sudar, 'TrueCoinc' software utility for calculation of the true coincidence correction', International Atomic Energy Agency, Tech. Rep., 2002, pp. 37–48.
- [TEKS99] L. V. D. nad T. E. Kuzmina and S. M. Soloviev, *Nuclear Instruments and Methods in Physics Research A*, vol. 438, pp. 116–118, 1999.
- [TLS16] L. Thulliez, O. Litaize, and O. Serot, *EPJ Web of Conferences*, vol. 111, no. 10003, 2016.
- [Urb+97] W. Urban *et al.*, *Nuclear Physics A*, vol. 613, pp. 107–131, 1997.
- [VC15] M. Verpelli and R. Capote, *International Nuclear Data Committee INDC (NDS)*, vol. 0702, 2015.
- [Vor+05] A. Vorobyev *et al.*, *AIP Conference Proceedings*, vol. 769, pp. 613–616, 2005.
- [Vor+10] A. Vorobyev *et al.*, *EPJ Web of Conferences*, vol. 8, no. 03004, 2010.
- [Vor+77] P. E. Vorotnikov *et al.*, *Nuclear Physics A*, vol. 281, pp. 295–309, 1977.
- [Wah+62] A. C. Wahl *et al.*, *Physical Review*, vol. 126, pp. 1112–1126, 1962.
- [Wah88] A. C. Wahl, *Atomic Data and Nuclear Data Tables*, vol. 39, pp. 1–156, 1988.
- [Wan+12] M. Wang *et al.*, *Chinese Physics C*, vol. 36, pp. 1603–2014, 2012.
- [WAT03] A. Wapstra, G. Audi, and C. Thibault, *Nuclear Physics A*, vol. 729, pp. 129–336, 2003.

- [Wes18] Westinghouse, *AP1000 PWR*, <http://www.westinghousenuclear.com/New-Plants/AP1000-PWR>, 2018.
- [Woh+86] F. K. Wohn *et al.*, *Physical Review C*, vol. 33, pp. 677–690, 1986.

Résumé en français

R.1 Introduction

R.1.1 Processus de fission

Une des thématiques de la physique nucléaire est de comprendre et d'étudier tous les phénomènes qui conduisent à la fission nucléaire et qui se produisent après la scission du noyau. Dans ce travail, je m'intéresse à la fission induite par les neutrons thermiques de l' ^{235}U (la réaction $^{235}\text{U}(n_{th}, f)$).

Le processus commence par la création du système fissionnant. Un noyau de ^{235}U , à l'état fondamental, capture un neutron et forme un noyau composé d' ^{236}U . Sa durée de vie est proche d'une femtoseconde [Vor+77]. Le noyau composé vibre et se déforme, jusqu'à atteindre une configuration où deux groupes de nucléons se retrouvent reliés par un col. Le point de selle est la déformation critique sans retour possible. A ce stade, le noyau composé surmonte une barrière de potentielle qu'on appelle la barrière de fission.

Partant du point selle, la force de répulsion Coulombienne entre les protons surpasse la force forte - la force attractive qui lie les nucléons ensemble. Le cou s'allonge. La scission se produit lorsque la déformation est si forte que le col joignant les deux proto-fragments devient instable et se brise. Dans la majorité des cas, deux noyaux excités sont créés à la scission, on les appelle les fragments primaires. La répulsion Coulombienne les accélère dans des directions opposées le long de l'axe de fission.

Lorsque les fragments de fission atteignent leur vitesse finale, la somme de leurs énergies cinétiques se situe entre 150 et 200 MeV; elle constitue la majorité de l'énergie libérée pendant le processus de fission. De plus, chaque fragment de fission a une énergie d'excitation entre 0 et 40 MeV [Reg13].

Pour éliminer cette énergie d'excitation et atteindre leur état fondamental, les frag-

ments de fission émettent durant, en général, quelques picosecondes d'abord des neutrons prompts et ensuite une cascade de rayons γ prompts. En dessous de l'énergie de séparation des neutrons (S_n), l'émission de neutrons devient énergétiquement impossible et un fragment de fission ne se désexcite que par émission de rayons γ . Les cascades γ peuvent être vues comme composées de différentes branches, réparties selon la structure nucléaire du fragment de fission.

La spectroscopie γ des fragments de fission, en fournissant de nouvelles données expérimentales, peut nous aider à comprendre le processus de fission. L'étude de l'évolution de la cascade γ dans un fragment de fission donné, en fonction de son partenaire de fission ou encore selon différents systèmes fissionnant, permet d'étudier la question de la distribution des moments angulaires des fragments de fission primaires. Une partie de ma thèse est consacrée à l'obtention de ce type de données pour la réaction $^{235}\text{U}(n_{th}, f)$.

R.1.2 L'échauffement γ

L'échauffement γ est un processus d'échauffement de la matière induit par les rayons γ qui la traversent. Elle est causée par un dépôt d'énergie des rayons γ via des interactions électromagnétiques avec les atomes composant les matériaux.

La volonté d'améliorer l'efficacité énergétique des réacteurs nucléaires et de prolonger leur durée de vie a motivé de nouvelles solutions dans leur conception. L'une d'elles est l'utilisation d'un réflecteur lourd, en acier inoxydable, dans les réacteurs de génération III+ et dans les futurs réacteurs de génération IV. En raison de son emplacement, très proche du cœur du réacteur, il est exposé à un rayonnement γ intense et constant. Plus de 90% de l'échauffement total dans les régions sans combustible d'un réacteur est causé par les rayons γ [Bla+08]. Une évaluation précise du spectre des rayons γ est donc obligatoire si l'on veut estimer correctement cet effet.

Pour assurer un très haut niveau de sûreté des nouveaux réacteurs nucléaires, les simulations de tous les processus nucléaires, et en particulier de ceux qui se déroulent autour du cœur du réacteur, doivent être effectuées avec une grande précision. Cela comprend la simulation de l'échauffement γ . Une incertitude maximale de 7,5% est considéré comme admissible dans le calcul du dépôt d'énergie dans les zones hors combustibles [Rim05]. Les incertitudes actuelles sur les calculs d'échauffement γ sont de l'ordre de 15-30% [Bla+08]. Les spectres moyens et les multiplicités sont mesurés

de plus en plus précisément, mais il manque des informations plus détaillées, comme les rayons γ prompts émis par les fragments pris individuellement.

R.1.3 Simulation du processus de désexcitation de fragments de fission

Un code de simulation Monte-Carlo - FIFRELIN [LS10] - est développé par les physiciens du laboratoire d'Études de Physique (DEN/DER/SPRC/LEPH) du CEA Cadarache. Ce code simule la désexcitation des fragments de fission en tenant compte de l'émission de neutrons prompts ainsi que de la cascade complète de rayons γ qui se produit pendant la désexcitation. Il pourrait donc être utilisé (intégré) à moyen terme dans les codes de simulation des réacteurs pour estimer l'échauffement γ .

Une partie importante de ma thèse a été dédiée à la comparaison des résultats provenant des données expérimentales mesurées à l'ILL lors de la campagne expérimentale EXILL avec ceux du code de simulation FIFRELIN. D'autres part, comme FIFRELIN propose une sélection de modèles différents pouvant être utilisés lors de la simulation, mon travail a également consisté à évaluer quelle configuration donnait les résultats les plus proches des données expérimentales. Plus précisément, l'étude a consisté à évaluer l'influence des modèles de distribution des moments angulaires et des variables telles que le spin cut-off et l'énergie d'excitation des fragments sur les résultats de la simulation. Cette comparaison a fourni un retour (feedback) important pour les concepteurs de FIFRELIN.

R.1.4 Plan du document

Dans ce travail de thèse, j'ai étudié la possibilité d'utiliser la spectroscopie γ d'une cible fissile pour fournir de nouveaux résultats expérimentaux qui peuvent être utilisés pour aborder des questions clés sur la modélisation du processus de fission.

La première partie de cette thèse est consacrée au code de simulation Monte-Carlo FIFRELIN. Les paramètres d'entrée requis, les observables possibles en sortie, les modèles utilisés et le fonctionnement de ce code sont décrits au chapitre 2. Ce chapitre explique également comment la simulation est préparée et comment nous avons utilisé FIFRELIN.

Les données expérimentales proviennent de la campagne EXILL. Elle est décrite dans le chapitre 3, qui contient également des informations sur le prétraitement des

données (la création du cube γ - γ - γ) et la description de la méthode standard pour l'analyse des coïncidences γ - γ - γ .

Dans le chapitre 4, je décris la nouvelle méthode d'analyse que nous avons développée afin d'améliorer la reproductibilité des résultats et obtenir une meilleure estimation des incertitudes. En particulier, je détaille le traitement du bruit de fond et des contaminations, qui constitue une amélioration notable par rapport à la méthode standard. Je décris également le processus d'ajustement semi-automatique des spectres et le calcul des intensités de transitions γ prompts. La question de leurs incertitudes est également abordée. Je discute aussi des limites de la méthode de spectrométrie γ en termes de statistiques et de contamination.

Une grande partie de mon travail a consisté dans l'analyse des données expérimentales sur $^{235}\text{U}(n_{th}, f)$ et plus particulièrement à extraire l'intensité des transitions γ produits lors de la désexcitation des fragments de fission. Ce travail a été réalisé pour un certain nombre de fragments et plus précisément pour ceux avec un rendement de fission important. L'étude de la paire (^{100}Zr - ^{134}Te) est présentée au chapitre 5. Le noyau de ^{100}Zr est un noyau pair avec une bande rotationnelle dominante. Sa grande déformation et un schéma de niveau simple nous ont permis de valider la méthodologie d'analyse que nous avons développée et de tester les fondements physiques de certains modèles utilisés dans FIFRELIN, en particulier les modèles de distribution de spin. L'évolutions de la cascade γ dans le ^{100}Zr en fonction de son partenaire de fission, selon différents modèles de distribution de spin est ainsi comparée aux données expérimentales. Nous avons également comparé nos résultats expérimentaux avec les autres données expérimentales disponibles (provenant de différents systèmes fissionnant). L'origine des écarts observés est abordée.

R.2 Le code de simulation Monte-Carlo FIFRELIN

R.2.1 Introduction

FIFRELIN (FISSION FRAGMENT EVAPORATION LEADING TO AN INVESTIGATION OF NUCLEAR DATA) est un code Monte-Carlo développé dans le laboratoire DEN/DER/SPRC/LEPH du CEA Cadarach [LS10; LSB15; Lit+17]. Il est utilisé pour simuler le processus de fission et la désexcitation des fragments de fission. Pour la fission induite par les neutrons et la fission spontanée, il peut simuler des observables tels que les spectres et les mul-

tiplicités des neutrons prompts et des rayons γ , les rendements post-neutron, l'énergie libérée mais aussi les cascades de rayons γ émises par les fragments de fission. La simulation du processus de désexcitation nucléaire pour un fragment de fission donné nécessite une grande quantité de données nucléaires : schémas de niveaux nucléaires, densités de niveau, fonctions de force des photons et coefficients de transmission neutronique.

R.2.2 Caractéristiques des fragments de fission primaires

Pour simuler la cascade de désexcitation d'un fragment, il faut d'abord connaître sa masse A , sa charge nucléaire Z , son énergie d'excitation E^* , son spin J et sa parité π . Au début du processus, ces caractéristiques sont donc échantillonnées pour les fragments de fission primaires avant la simulation de la désexcitation proprement dite.

Dans FIFRELIN, les distributions des masses et des énergies cinétiques des fragments, avant évaporation des neutrons, sont tirées de données expérimentales ou sont fournies par des codes externes comme GEF [SJA14].

Pour trouver les charges nucléaires des fragments, FIFRELIN tient compte de l'hypothèse UCD (Unchanged Charge Density) mais avec une modification par une fonction de polarisation de la charge qui dépend de la masse du fragment [Wah88; BB89; Nai+97; NSI04]. Cette hypothèse est utilisée pour dériver la charge nucléaire la plus probable qui est ensuite échantillonnée dans une gaussienne.

En première approximation, on suppose que les probabilités d'avoir une parité positive ou négative sont identiques. Une distribution de spin initialement dérivée par Bethe [Bet36] est utilisée pour échantillonner à la fois le spin initial des fragments de fission primaires et les spins impliqués dans le calcul des densités de niveaux nucléaires.

L'énergie libérée est calculée à partir de l'évaluation de masse atomique AME2003 [AW95; WAT03] ou AME2012 [Aud+12; Wan+12]. Pour calculer l'énergie d'excitation intrinsèque E^* , FIFRELIN utilise l'hypothèse d'un gaz de Fermi. FIFRELIN traite également la répartition de l'énergie d'excitation intrinsèque entre les deux fragments de fission. L'énergie est répartie selon une loi de rapport de température qui dépend de la masse des fragments. Cela suppose un couplage étroit entre les températures des deux fragments de fission. Cette loi est basée sur la fermeture des couches dans les noyaux sphériques (doublement magique). L'énergie d'excitation intrinsèque est calculée de manière itérative.

R.2.3 Le processus de désexcitation

FIFRELIN utilise le formalisme Hauser-Feshbach pour simuler le processus de désexcitation qui est mis en œuvre en utilisant la notion de réalisation nucléaire [Bec98].

Si le schéma de niveau complet (la vraie réalisation nucléaire) est connu pour tous les fragments de fission, la simulation consisterait en une désexcitation Monte Carlo des noyaux par évaporation des neutrons et émission des rayons gamma.

Cependant, la véritable réalisation du nucléaire est bien sûr inconnue. La plupart des schémas de niveau des fragments sont incomplets et aucun modèle de structure nucléaire n'est réellement capable de reproduire correctement les propriétés des états nucléaires à haute énergie. Pour faire face à ce problème, une solution consiste à générer un grand nombre de réalisations nucléaires (virtuelles), puis à simuler la cascade de désexcitation pour chacune d'entre elles. La réalisation nucléaire consiste donc à ajouter les informations existantes sur le noyau à un ensemble de niveaux virtuels produits en fonction de la densité du niveau (Section 2.5).

Comme la réalisation nucléaire a un caractère statistique, la valeur attendue de toute réalisation observable fluctue d'une réalisation à l'autre. Si le nombre de réalisations est suffisamment élevé, la valeur moyenne d'un observable sera stable.

Dans FIFRELIN, le système nucléaire est divisé en trois régions d'énergie. Dans la première région, le schéma de niveaux est considéré comme complètement connu. Les données expérimentales de la base de données RIPL-3 [Cap+09; VC15] déterminent la cascade jusqu'à l'état fondamental ou un état isomère. Dans la deuxième région, le schéma de niveaux est incomplet. Il n'y a que peu de niveaux expérimentaux et le schéma de niveaux est complété à l'aide de modèles de densité de niveaux. Dans la troisième région, les états excités ne sont plus séparés, ils sont traités comme un continuum. Le schéma du niveau nucléaire est décrit par des valeurs moyennes qui sont calculées à partir des modèles de densité de niveau. Dans FIFRELIN, la compétition entre l'émission de neutrons et de rayons γ est considérée dès le début de la cascade.

R.2.4 Les différents modèles implémentés dans FIFRELIN

Le schéma du niveau nucléaire expérimental n'étant pas entièrement connu, pour le compléter, FIFRELIN utilise des modèles de densité de niveau, des fonctions de force des photons et des coefficients de transmission neutronique. Différents modèles sont utilisés pour décrire la densité de niveau en fonction de l'énergie d'excitation, du spin

et de la parité.

FIFRELIN utilise également des modèles de spin cut-off pour compléter les caractéristiques insuffisamment connues (le spin et la parité) des fragments de fission primaires. Dans le modèle de de spin cut-off CONSTANT, les états d'entrée du fragment de fission primaire sont répartis autour d'un spin initial donné et d'une valeur d'énergie d'excitation initiale (Figure 5.18 page 142). La spin provient de l'échantillonnage de la distribution décrite par l'équation 2.7 à la page 20, avec une valeur de spin cutoff fixe. Cela signifie que dans ce modèle, la distribution des spins ne dépendra pas de l'énergie d'excitation. Un facteur d'échelle (f_σ) est utilisé dans le modèle Back-Shifted Fermi Gas (BSFG). Celui-ci permet de modifier le paramètre de spin cut-off qui dépend cette fois de l'énergie d'excitation du fragment. Pour une valeur de f_σ proche de 1, l'état d'entrée du fragment est en moyenne proche de la valeur moyenne de la densité au niveau.

Pendant le processus de désexcitation des fragments de fission, la majeure partie de l'énergie d'excitation est éliminée par émission de neutrons prompts. Pour simuler cette partie de la désexcitation (Equation 2.26 à la page 28) nous devons connaître les coefficients de transmission neutronique. Ils sont calculés avec les codes ECIS [Ray94] ou TALYS [KHD08] en utilisant différents potentiels de modèles optiques tels que Becchetti-Greenlees [BG69], Koning-Delaroche [KD03] ou Jeukenne-Lejeunce-Mahaux [JLM74].

Une estimation de l'émission de γ entre les niveaux simulés est réalisée avec les fonctions de forces des photons ou les fonctions de force radiatives. Les fonctions de force des photons sont différenciées selon leur type (électrique E ou magnétique M) et leur multipolarité (L).

Pour décrire les taux de transition des rayons γ , FIFRELIN utilise un des modèles basés sur le concept de résonance dipolaire géante. La GDR peut être considérée comme une vibration dipolaire collective des fluides de protons et de neutrons dans le noyau.

R.2.5 Multiplicité des neutrons prompts

La multiplicité des neutrons prompts est l'observable la plus importante dans une simulation FIFRELIN. On distingue la multiplicité moyenne des fragments de fission légers ($\bar{\nu}_L$) et lourds ($\bar{\nu}_H$) et la multiplicité moyenne intégrée sur tous les fragments de fission

($\bar{\nu}_{Tot}$). Les paramètres libres de la simulation sont optimisés de sorte que les écarts entre les multiplicités de neutrons prompts expérimentales et simulées ne dépassent pas 1%. Cette condition est la contrainte par défaut utilisée par les simulations FIFRELIN.

R.3 L'expérience EXILL

R.3.1 Introduction

Une expérience innovante a été menée dans le réacteur de recherche de l'ILL. Pour la première fois, un grand nombre de détecteurs HPGe a été utilisé pour étudier le processus de fission induit par les neutrons. Cette expérience a produit une grande quantité de données utiles sur la désexcitation des fragments de fission. Dans le chapitre 3, je décris en détail l'expérience et les différentes techniques réalisées pour traiter les données brutes. J'explique également la méthode que nous avons utilisée en première instance pour extraire la cascade de rayons γ émis par les fragments ainsi que ses limites.

R.3.2 Description de la campagne EXILL

L'expérience EXILL (**EX**OGAM at **ILL**) a été menée en 2012 et 2013 au réacteur de recherche de l'Institut Laue-Langevin (ILL) à Grenoble, France. Elle a été divisée en plusieurs campagnes qui utilisaient quatre configurations de détecteurs différentes. Trois d'entre elles ont été dédiées à spectroscopie γ classique et une d'elles à des mesures fast-timing (Tableau 3.1 page 48).

Pour cette campagne EXILL, une balle de détecteurs germanium de haute pureté (HPGe) a été placée pendant deux cycles du réacteur (50 jours chacun) auprès de l'installation PF1B de l'ILL qui dispose d'un faisceau intense de neutrons froids.

Notre laboratoire (IRFU, DRF, CEA Saclay), en collaboration avec des collègues du laboratoire DEN/DER/SPRC/LEPH du CEA Cadarache, a proposé d'étudier le processus de fission et la cascade des rayons γ prompts émis par les fragments de fission. L'idée était d'extraire deux types d'informations des données EXILL. La première concerne la distribution des paires de fragments de fission $Y(Z1,A1,Z2,A2)$. La mesure du rendement peut aider à déterminer comment l'énergie d'excitation est partagée entre les fragments de fission primaires. Les rendements des paires peuvent aussi être utilisés pour comparer des codes comme GEF ou FIFRELIN. La deuxième idée était

lié à la possibilité d'extraire précisément la cascade des rayons γ discrets émis par les fragments. L'intérêt est de vérifier dans quelle mesure des codes de désexcitation tels que FIFRELIN sont capables de reproduire correctement la cascade γ pour chaque fragment individuellement sachant qu'ils sont en général plutôt validés sur le spectre moyen; mais aussi de vérifier si la cascade γ change avec le système fissionnant ($^{235}\text{U}(n_{th}, f)$, $^{252}\text{Cf}(sf)$, $^{248}\text{Cm}(sf)$) ou encore si la cascade dans un fragment change selon son partenaire de fission.

Dans ce travail, nous nous sommes concentrés sur la spectroscopie γ des produits de fission de la réaction $^{235}\text{U}(n_{th}, f)$. Les données proviennent du premier cycle du réacteur, avec 16 jours de mesures avec de l' ^{235}U sur un support en Zr et 6 jours de mesures avec ^{235}U sur un support en Be, voir Tableau 3.1 page 48.

Les données proviennent d'une balle composée de 16 détecteurs HPGe : 8 clovers EXOGAM, 2 clovers venant de l'instrument LOHENGRIN et 6 détecteurs venant de GASP. Chaque clover étant constitué de 4 cristaux, cette configuration totalisait 46 cristaux de germanium. Tous les détecteurs HPGe, à l'exception des clovers de LOHENGRIN, étaient entourés d'un blindage anti-Compton actif basé sur des scintillateurs BGO. Les détecteurs étaient placés à environ 13 cm de la cible.

Un système de collimation dédié a été utilisé pour réduire le faisceau de neutrons initiale à un pinceau dont le diamètre est environ 1 cm. Le flux de neutrons après collimation était d'environ 10^8 n/cm²/s, ce qui se traduit par un taux de fission d'environ 10^5 par seconde dans les cibles d'uranium. L'énergie des neutrons était d'environ 4.5 meV [Jen+17].

Afin de fournir des conditions optimales pour la spectroscopie γ , les parois extérieures de la chambre contenant la cible étaient entourées d'une feuille de 1 mm d'épaisseur de ^6LiF afin d'éliminer les neutrons diffusés.

Lors de l'analyse des données, j'ai notamment calculé l'efficacité du système de détection et je l'ai corrigé pour tenir compte des effets de sommation.

R.3.3 Méthode de coïncidence γ - γ - γ

Au début de nos études, nous avons utilisé une méthode classique de coïncidence $\gamma\gamma$. Cette technique de spectroscopie de rayons γ est basée sur le fait que lors de la désexcitation d'un noyau de fragment de fission (Figure 3.7 à la page 61), les rayons γ sont émis en un temps limité (souvent en quelques picosecondes ou nanosecondes).

Les énergies des transitions sont uniques pour un élément particulier et leur émission dépend de l'état d'entrée des fragments de fission (énergie d'excitation, spin et parité). En sélectionnant une transition γ dans la cascade de désexcitation d'un fragment particulier et en regardant les rayons γ émis en coïncidence dans un court laps de temps avec cette transition, on peut filtrer les données expérimentales et découvrir les transitions provenant de la même cascade ou de la cascade du partenaire de fission. On peut également décider de regarder les rayons γ émis en coïncidence avec deux transitions appartenant à la cascade du fragment, ou encore une transition de la cascade et une transition dans celle du partenaire de fission, pour filtrer encore mieux les données. Cela permet de construire un schéma de niveaux qui contient ces transitions γ et les niveaux excités du fragment (Figure 3.7 page 61).

Les données expérimentales brutes (événements en "list mode") sont utilisées pour construire un histogramme 3D qu'on appelle le cube γ - γ - γ . Il contient les informations sur les coïncidences entre tous les événements mesurés pendant l'expérience et permet d'utiliser facilement la méthode des coïncidences $\gamma\gamma\gamma$.

Pour analyser la cascade de désexcitation d'un fragment de fission à partir d'un cube de coïncidence, il suffit de sélectionner une région d'énergie (une porte) autour du pic γ associé à une transition appartenant à sa cascade ou à celle de son partenaire de fission. On construit un histogramme contenant tous les rayons γ émis en coïncidence avec cette porte. Une deuxième porte autour d'une seconde transition est ensuite sélectionnée à partir de cet histogramme pour filtrer encore mieux les données. Le spectre obtenu permet d'identifier et d'ajuster les pics γ appartenant à la cascade sélectionnée. De cette façon, on peut calculer les intensités des transitions γ .

Dans le cas des données EXILL, l'utilisation de la méthode de coïncidence $\gamma\gamma\gamma$ est requise en raison de la forte contamination des spectres par 1) les rayons γ prompts produits après la capture neutronique par les éléments du setup ou des supports des cibles (Al, Zr) 2) les rayons γ émis suite à la désintégration β des fragments de fission 3) le fond Compton (Figure 3.8 sur page 65).

Dans la méthode standard, une région du spectre proche de la porte de coïncidence et que l'on considère comme caractéristique du bruit de fond sous le pic doit être choisie. Cette porte est utilisée pour trouver le spectre des γ en coïncidence avec le bruit de fond. La méthode consiste ensuite à soustraire ce spectre de bruit du spectre en coïncidence avec la transition. La même opération est effectuée pour la seconde porte de coïncidence.

Le problème de cette méthode est d'une part, que suite à la soustraction, des pics négatifs apparaissent dans les spectres finaux. Ils compliquent l'ajustement des pics. D'autre part, l'amplitude des pics et donc l'intensité des transitions varient avec le choix des portes de bruit de fond. Les résultats ne sont donc pas reproductibles et l'écart entre les analyses que j'ai effectuées a pu atteindre 10%.

R.4 Nouvelle technique d'analyse

R.4.1 Introduction

Nous avons testé différentes façons d'analyser les données et nous avons finalement décidé de développer un nouveau schéma d'analyse qui prend en compte le bruit de fond d'une manière plus correcte. Dans un sens, la méthode standard, très rapide, peut être vue comme une méthode "spectroscopique" dont l'objectif principal est de trouver de nouvelles transitions et de nouveaux états excités dans les noyaux. Pour étudier la désexcitation des fragments de fission, nous voulons mesurer précisément l'intensité de certaines transitions connues avec les meilleures incertitudes estimées. Nous avons besoin d'une méthode "spectrométrique".

Dans le chapitre 4, je décris l'idée générale et le schéma d'analyse utilisé dans cette nouvelle méthode. La section 4.4 explique brièvement comment nous avons automatisé l'ajustement d'un grand nombre de pics et comment nous avons calibré la fonction de réponse (ou fonction d'ajustement) du système de détection. La section 4.5 explique en détail les algorithmes utilisés pour extraire l'intensité des transitions en triple coïncidence, particulièrement dans le cas de contaminations. La dernière section fournit les performances et les limites de cette nouvelle méthode en montrant les cascades γ extraites pour les fragments de ^{142}Ba .

R.4.2 Concepts de la nouvelle méthode d'analyse

Dans la méthode standard, les difficultés d'ajustement des pics peuvent être attribuées au fait que le spectre en coïncidence est obtenu par soustraction de spectres.

Pour formaliser le concept, considérons un cas simple avec la méthode standard. Nous voulons étudier la cascade de transitions discrètes dans un fragment de fission F_2 . F_1 est l'un de ses partenaires de fission. Comme portes, nous utilisons la transition T_A , appartenant à la cascade de F_1 et la transition T_B , qui par exemple remplit l'état

fondamental du fragment F_2 . L'objectif est de mesurer l'intensité d'une transition γ dans la cascade de F_2 , que nous appelons T_X , en coïncidence avec T_A et T_B . Les transitions T_A , T_B et T_X ont respectivement les énergies E_A , E_B et E_X .

Nous construisons le spectre des coïncidences. C'est le spectre des rayons γ en coïncidence avec une petite région de rayons γ autour de T_A et une petite région de rayons γ autour de T_B ; ou sous une forme courte autour des énergies (E_A, E_B) .

Le problème est que, ce faisant, nous prenons également les événements en coïncidence avec les rayons γ du bruit de fond, c'est-à-dire avec les rayons γ qui appartiennent à la petite région autour de (E_A, E_B) mais qui ne sont pas reliés aux transitions T_A et T_B .

La méthode standard consiste à soustraire une portion équivalente d'événements en coïncidence avec une petite région autour d'une énergie E'_A un peu plus élevée que E_A et la même petite région autour de E_B . Puis, symétriquement, une portion équivalente d'événements coïncidant avec la même petite région autour de E_A et une petite région autour d'une énergie E'_B un peu plus élevée que E_B est soustraite.

Le fond sous le pic de T_A et T_B se compose cependant aussi de rayons γ qui n'ont aucun lien avec les noyaux A et B : diffusion Compton d'autres fragments, réactions (n, γ) dans la cible ou rayons γ du milieu environnant. Puisque nous le soustrayons deux fois dans le processus précédent, nous devons le compenser en ajoutant une portion équivalente d'événements en coïncidence avec la petite région de rayons γ autour de (E'_A, E'_B) . Le processus est illustré dans la Figure R.1. Δ_A est la largeur des régions (portes) autour de respectivement E_A et E'_A . Δ_B est la largeur des régions (portes) autour de respectivement E_B et E'_B .

La nouvelle méthode que nous avons développé est basée sur l'idée qu'il faudrait scanner les portes afin de mieux estimer le bruit de fond et qu'il faut éviter la soustraction des spectres.

Nous effectuons un balayage avec des portes étroites dans trois directions : le long du premier axe E_1 , cela définit un ensemble de portes horizontales ; le long du deuxième axe E_2 , les portes verticales et le long des deux axes E_1 et E_2 en même temps, les portes en diagonale, voir Figure R.2.

Comme précédemment, chaque mise en place de la porte se fait sur une petite région 2D d'énergies de tailles (Δ_A, Δ_B) . De nombreuses portes permettent de scanner la forme du pic et de détecter d'éventuelles contaminations.

Un spectre en coïncidence avec une petite région autour de (E_1, E_2) contient des

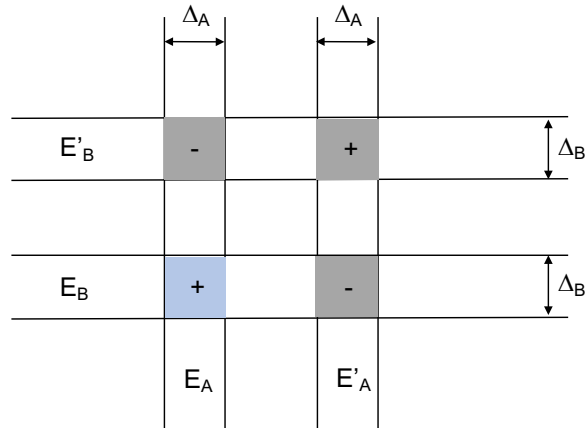


Figure R.1: Représentation schématique de la méthode standard d'analyse des données. Pour obtenir l'intensité d'une transition en coïncidence avec les transitions T_A et T_B , avec l'énergie E_A et E_B , on construit le spectre des rayons γ en coïncidence avec une petite région autour de (E_A, E_B) , puis on soustrait les rayons γ en coïncidence avec les régions autour de (E'_A, E_B) et autour de (E_A, E'_B) et ajoute les rayons γ en coïncidence avec une région autour (E'_A, E'_B) .

pics que l'on peut ajuster pour extraire leur amplitude. Ce spectre ne contient que des pics "positifs" puisqu'il n'y a pas de soustraction de spectres. Le processus consiste à trouver le pic associé à la transition T_X dans chaque spectre de coïncidence et à déterminer sa surface par un ajustement. A la fin de ce processus, nous aurons donc le nombre de coups associés à la transition T_X pour les différentes portes définies dans la Figure R.2. Cet ensemble de nombres peut être relié aux coupes horizontale, verticale et diagonale dans la matrice en coïncidence avec la transition T_X . Le volume du pic qui se dessine dans la matrice de coïncidence peut être obtenu à l'aide d'un ajustement de ces coupes. C'est une partie essentielle de la nouvelle technique d'analyse. Cette idée générale fonctionne pour le cas sans contamination. Nous avons également dérivé différents schémas de calcul qui traitent correctement les cas où des contaminations sont visibles, selon leur position et leur amplitude.

R.4.3 Analyse de ^{142}Ba

Pour évaluer la nouvelle technique d'analyse, j'ai comparé les intensités des transitions discrètes du ^{142}Ba extraites avec cette nouvelle technique d'analyse et la technique standard. Les deux ensembles de résultats ont été également comparés aux données

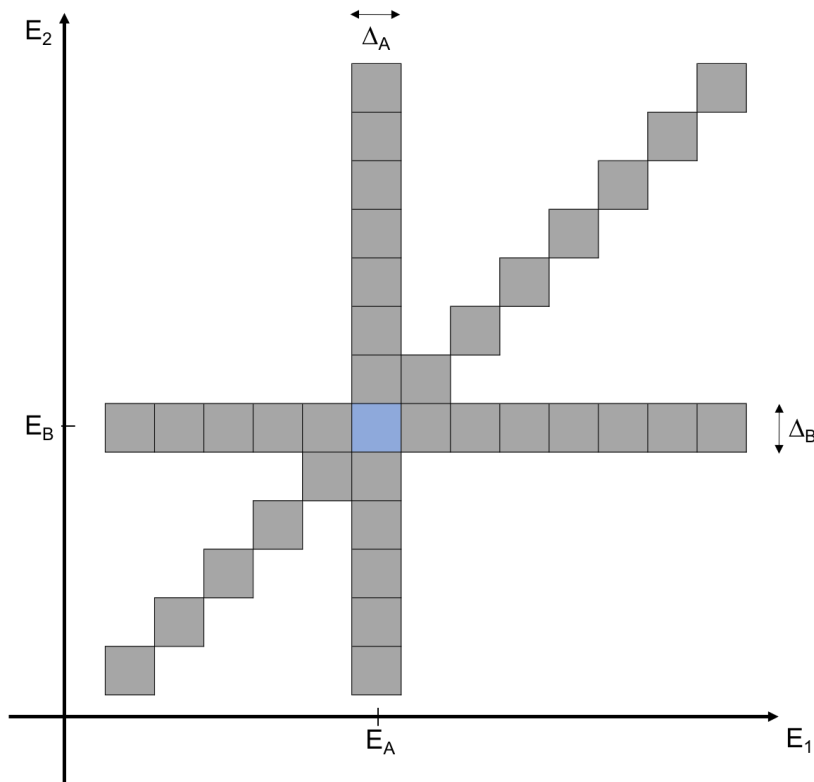


Figure R.2: Représentation schématique de la nouvelle façon de scanner les portes 2D autour de (E_A, E_B) . Chaque carré correspond à une porte 2D avec la taille (Δ_A, Δ_B) .

expérimentales existantes provenant de la fission spontanée du ^{248}Cm [Urb+97].

L'intérêt d'analyser le ^{142}Ba est que ce fragment ainsi que ses partenaires de fission (les isotopes de Krypton) appartiennent aux fragments les plus produits dans la réaction $^{235}\text{U}(n_{th}, f)$ (voir Tableau 5.1). Ses transitions sont donc facilement identifiées dans les spectres de coïncidence et ont des statistiques très élevées, ce qui nous a permis de garder de faibles incertitudes. Le noyau de ^{142}Ba est aussi un noyau pair-pair ayant une structure nucléaire relativement simple et bien étudiée, ce qui a facilité le processus de sélection des portes.

Le résultat de mon analyse est résumée dans le tableau 4.1 où je présente les transitions mesurées, leurs intensités et les incertitudes. Une caractéristique commune à presque toutes les intensités mesurées est qu'avec la nouvelle technique, les valeurs sont réduites. Une explication simple est qu'avec des portes beaucoup plus petites et un meilleur contrôle de la détection et du traitement des contaminations, les intensités des pics sont moins contaminées. Les écarts les plus importants sont observés pour

les transitions avec les intensités les plus faibles. Les transitions moins intenses sont proportionnellement beaucoup plus exposées à la contamination.

Si on compare la réaction $^{235}\text{U}(n_{th}, f)$ à la réaction $^{248}\text{Cm}(sf)$, l'état initial de ^{142}Ba dans les deux systèmes fissionnant semble être similaire. On s'attend donc à ce que sa cascade de désexcitation soit similaire dans les deux cas ; les intensités des transitions discrètes ne devraient pas beaucoup varier. Les différences relatives entre les intensités mesurées pour $^{248}\text{Cm}(sf)$ et notre résultats pour le $^{235}\text{U}(n_{th}, f)$, présentées dans le tableau 4.1, sont effectivement plus faibles lorsqu'on utilise la nouvelle méthode d'analyse.

Globalement, les incertitudes des intensités des transitions γ sont plus élevées avec la nouvelle technique. Néanmoins, nous sommes beaucoup plus confiants quant aux résultats et aux incertitudes obtenus car ils prennent en compte beaucoup plus de facteurs que la technique standard.

En conclusion, l'analyse ^{142}Ba a montré un impact direct de la nouvelle technique d'analyse sur les résultats et leur interprétation physique.

R.5 Études sur ^{100}Zr

R.5.1 Introduction

Le chapitre 5 présente l'étude de la cascade γ dans un fragment de fission bien produit, le ^{100}Zr , et la dépendance de sa cascade avec son partenaire de fission (avec le nombre de neutrons évaporés). L'intensité des transitions a été extraite des données EXILL avec la méthode expliquée au chapitre 4 et a été comparée aux résultats des calculs FIFRELIN.

Comme détaillé au chapitre 2, FIFRELIN est un code vivant et les développeurs ont mis en œuvre différentes options pour les états d'entrée des fragments primaires, plusieurs modèles pour les densités nucléaires, pour les fonctions de force des photons, etc. Cela reflète bien sûr le manque actuel de connaissances sur le processus de fission et la désexcitation des fragments ainsi que sur la structure nucléaire elle-même. L'un des objectifs initiaux de l'étude était de valider le code FIFRELIN, de trouver les modèles qui correspondent le mieux aux mesures et d'optimiser leurs paramètres. Plusieurs modèles dans FIFRELIN ont été testés pour voir lequel reproduit le mieux nos données expérimentales et en particulier, une étude plus poussée a été faite sur les modèles de

distribution de spin.

Nous avons décidé d'étudier le ^{100}Zr parce qu'avec ses partenaires de fission (les isotopes de Tellurium), il appartient aux fragments les plus produits dans la réaction $^{235}\text{U}(n_{th}, f)$ (voir Tableau 5.1). Le noyau de ^{100}Zr est aussi un noyau pair-pair, et son schéma de niveau est simple et bien étudié avec d'autres réactions.

Dans ce travail, notre intention n'était pas d'étudier la structure de ^{100}Zr et nous n'avons pas essayé de trouver de nouvelles transitions ou de nouveaux niveaux ou d'améliorer les rapports d'embranchement. Dans la section 5.2, je présente une comparaison de nos résultats sur la réaction $^{235}\text{U}(n_{th}, f)$ obtenue lors de l'expérience EXILL avec des données existantes sur le même système fissionnant et sur deux systèmes différents : la fission spontanée du $^{248}\text{Cm}_{152}$ et celle du $^{252}\text{Cf}_{154}$. Dans la même section, une comparaison de la réaction $^{235}\text{U}(n_{th}, f)$ et de la fission spontanée de $^{252}\text{Cf}_{154}$ est également effectuée à l'aide des simulations FIFRELIN. Dans la section 5.3, l'évolution de la cascade γ du $^{100}\text{Zr}_{60}$ avec son partenaire de fission a été examinée et comparée aux simulations FIFRELIN en utilisant différents modèles et paramètres. Cette étude nous a permis de proposer une optimisation du modèle permettant de décrire la distribution de spin du fragment primaire dans la section 5.4. Les simulations optimales ne fournissent pas les bonnes valeurs moyennes de multiplicité des neutrons prompts. Dans la section 5.5, j'ai présenté les résultats de l'optimisation de la multiplicité des neutrons rapides en modifiant les paramètres (R_T^{min} et R_T^{max}) responsables de la température des fragments de fission.

R.5.2 Résultats et interprétation

Nous avons fait une analyse approfondie des fragments de ^{100}Zr . Dans la section 5.2, la comparaison de la cascade γ provenant de l'expérience EXILL avec celle du ^{248}Cm [Dur+95] et celle du ^{235}U [Muk+12] montre un accord satisfaisant. Néanmoins, il y a un léger désaccord avec les données de ^{252}Cf [Hwa+06]. Nous avons conclu qu'il peut être causé soit par une différence dans la distribution des énergies d'excitation et des spin des fragments primaires, soit par un problème de normalisation dans [Hwa+06].

Une autre analyse, décrite dans la section 5.3, est axée sur une comparaison des données EXILL avec les résultats des simulations FIFRELIN. Nous avons commencé par les simulations qui reproduisent correctement les trois multiplicités moyennes de neutrons prompts ($\bar{\nu}_L$, $\bar{\nu}_H$, $\bar{\nu}_{Tot}$). Nous avons comparé deux modèles de distribu-

tion de spin : le modèle CONSTANT et le modèle BSFG. Nous avons observé que les intensités de transition discrètes augmentent avec la masse atomique de Te (le partenaire de fission du ^{100}Zr) lorsque le modèle CONSTANT est utilisé. Cela provoque une surpopulation des états excités dont le spin est élevé. Ce phénomène a été entièrement attribué au modèle CONSTANT. Elle n'a été remarquée ni dans les simulations utilisant le modèle BSFG, ni dans les données expérimentales EXILL.

La section 5.4 décrit le travail réalisé sur les simulations pour trouver le meilleur ensemble de modèles et de paramètres libres. Pour comparer les résultats, nous avons utilisé un test χ^2 basé sur les intensités des transitions γ dans la bande de l'état fondamental lorsque le partenaire de fission est le ^{134}Te (2 neutrons évaporés). Les meilleurs résultats (la valeur la plus faible de χ^2) ont été obtenus en utilisant le modèle de fonction force de photon EGLO et le modèle de densité au niveau CTM. C'est le cas des simulations utilisant les modèles CONSTANT et BSFG. Même en choisissant les simulations avec les valeurs χ^2 les plus basses, dans la comparaison directe avec les données expérimentales, l'alimentation des états de spin élevés reste trop élevée. Nous avons conclu que ce problème est causé par un spin initial trop élevée dans les simulations pour les fragments de fission primaires.

Nous avons traité cette question en scannant les deux paramètres libres des modèles : les spin cut-off des fragments de fission légers et lourds (pour le modèle CONSTANT) et les facteurs d'échelle des fragments légers et lourds (pour le modèle BSFG). Pour les deux modèles, une réduction significative de ces paramètres libres a remarquablement réduit le χ^2 , rapprochant les intensités des transitions γ des valeurs expérimentales (Tableau 5.12). Malheureusement, elle a également perturbé les valeurs de multiplicité des neutrons prompts, loin des données expérimentales (Tableau 5.13).

La section 5.5 décrit le travail consacré à l'amélioration de la multiplicité des neutrons prompts dans la simulation avec un facteur de mise à l'échelle réduit. Cette analyse n'a été effectuée qu'avec le modèle BSFG. Pour réduire l'énergie d'excitation initiale des fragments primaires, et donc la multiplicité des neutrons prompts, nous avons balayé les valeurs des paramètres libres $R_{\text{T}}^{\text{min}}$ et $R_{\text{T}}^{\text{max}}$ associés à la loi de répartition de l'énergie d'excitation entre les deux fragments. Cette action ne nous a pas donné les résultats escomptés. La multiplicité totale moyenne des neutrons rapides est restée pratiquement inchangée à environ 2.7, ce qui est beaucoup plus élevé que le chiffre souhaitable de 2.41. Cela prouve qu'avec le modèle testé, FIFRELIN n'est pas en mesure de reproduire simultanément les intensités des transitions γ discrètes et la

multiplicité moyenne de neutrons prompts sur tous les fragments de fission.

Nous avons décidé de tester comment FIFRELIN peut être correct dans le cas d'un fragment de fission unique - celui de ^{100}Zr . Pour ce faire, nous avons cherché un R_T^{max} qui donne la multiplicité de neutrons prompts correcte pour le fragment de fission avec la masse atomique $A = 100$. Nous avons pu trouver une valeur R_T^{max} qui correspondait à nos critères. Sa modification nous a obligé à refaire l'optimisation du facteur d'échelle. Une valeur plus basse de χ^2 a été trouvée, alors qu'une multiplicité de neutrons correcte pour la masse $A = 100$ a été conservée. Ceci prouve que lorsqu'un processus itératif d'optimisation des paramètres libres est utilisé, FIFRELIN est simultanément capable de délivrer la multiplicité de neutrons prompts correcte pour le fragment avec une masse atomique particulière et de reproduire correctement les intensités de transitions γ .

Appendix A

A.1 Experimental results - EXILL data analysis

Results of the analysis of EXILL experimental data presented in this appendix were obtained during the course of this thesis.

Our experimental results on ^{134}Te , ^{142}Ba , ^{94}Sr , ^{140}Xe , ^{104}Mo and ^{144}Ba are arranged in tables together with available experimental intensities measured in the $^{248}\text{Cm}(sf)$ or $^{252}\text{Cf}(sf)$ processes and with results of FIFRELIN simulations. For ^{134}Te and ^{142}Ba , the scaling factor (f_σ) of each of the corresponding FIFRELIN simulation was optimized to obtain the lowest χ^2 value. The optimization process was similar to the one used in the ^{100}Zr analysis, see Section 5.4.2.

^{92}Kr , ^{142}Ba , ^{94}Sr and ^{140}Xe evolutions of γ -transition intensities with the appropriate fission partner mass are presented.

For ^{92}Kr , ^{138}Xe and ^{130}Sn , only results of the EXILL data analysis and FIFRELIN simulation are presented.

The last section contains results of the analysis of γ -transition intensity dependence with the deformation of the fission partner. A presented fission fragment pair is: ^{87}Kr - ^{146}Ba . We have looked for changes in γ -transition intensities in Ba depending on deformation of Kr.

A.1.1 ^{134}Te

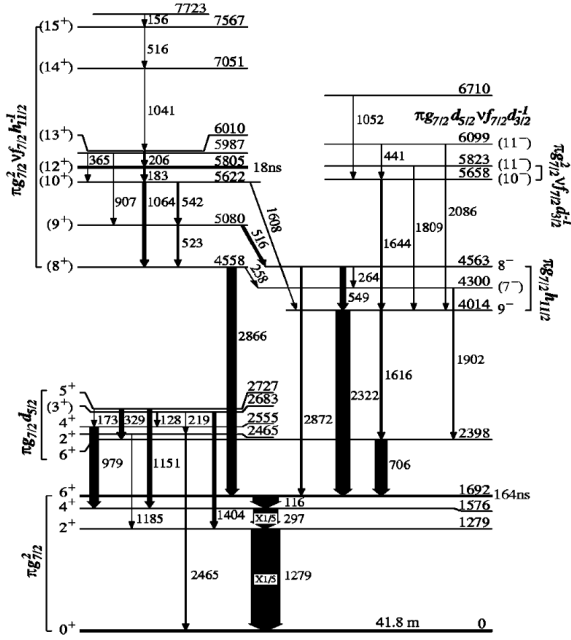


Figure A.1: Level scheme of ^{134}Te from [Sah+01].

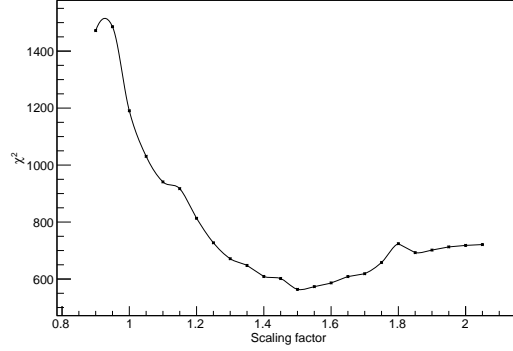


Figure A.2: χ^2 value containing γ -transitions: 115.7 keV, 297.1 keV, 706.3 keV, 978.5 keV, 2322.0 keV in ^{134}Te , for the FIFRELIN simulations with different scaling factor values (f_σ). The χ^2 was calculated according to Equation 5.1. Models and free parameters set used in the simulations: EGLO photon strength functions, CTM level density model, BSFG spin cut-off model, $R_T^{\min} = 0.75$, $R_T^{\max} = 1.23$.

The optimal scaling factor $f_\sigma=1.5$ (Figure A.2) is much higher than the one found in the ^{100}Zr analysis ($f_\sigma=1.15$ for $R_T^{\max}=1.23$, see Section 5.4.2). General agreement between the EXILL experimental results and the FIFRELIN simulation results is bad ($\chi^2 = 563.8$, see Figure A.2, reduced $\chi^2 = 112.8$). Many γ -transitions are not produced in the FIFRELIN simulation at all, see Table A.1.

E_γ (keV)	E_i^{level} (keV)	E_f^{level} (keV)	Transition	I_γ		
				^{248}Cm data	EXILL data*	FIFRELIN data
115.7	1692.1	1576.5	$6_1^+ \rightarrow 4_1^+$	19.4	16.5(8)	25.3(5)
182.6	5804.7	5622.1	$(12_1^+) \rightarrow (10_1^+)$	1.4	0.7(3)	
205.7	6010.4	5804.7	$(13_1^+) \rightarrow (12_1^+)$	1.3	2.0(4)	
218.5	2683.3	2465.2	$(3_1^+) \rightarrow 2_2^+$	0.1	3.6(5)	0.03(2)
297.1	1576.5	1279.4	$4_1^+ \rightarrow 2_1^+$	88.4	86(3)	92(1)
329.3	2727.5	2398.4	$5_1^+ \rightarrow 6_2^+$	3.3	1.4(5)	5.4(2)
516.3	5080.0	4563.7	$(9_1^+) \rightarrow (8_1^-)$	2	0.6(4)	0.07(2)
706.3	2398.4	1692.1	$6_2^+ \rightarrow 6_1^+$	9.2	7.3(7)	30.3(6)
978.5	2554.9	1576.5	$4_2^+ \rightarrow 4_1^+$	6.4	5.0(4)	8.5(3)
1040.6	7051.0	6010.4	$(14_1^+) \rightarrow (13_1^+)$	0.3	1.1(3)	
1064.4	5622.1	4557.6	$(10_1^+) \rightarrow (8_1^+)$	2.4	0.9(3)	0.009(9)
1150.8	2727.5	1576.5	$5_1^+ \rightarrow 4_1^+$	3.7	2.1(2)	6.1(2)
1185.9	2465.2	1279.4	$2_2^+ \rightarrow 2_1^+$	0.1	1.8(4)	0.009(9)
1279.3	1279.3	0.0	$2_1^+ \rightarrow 0_1^+$	100	100	100
1403.8	2683.3	1279.4	$(3_1^+) \rightarrow 2_1^+$	2.1	2.4(3)	1.2(1)
1607.9	5622.1	4014.2	$(10_1^+) \rightarrow 9_1^-$	0.4	1.3(4)	
1615.6	4014.2	2398.4	$9_1^- \rightarrow 6_2^+$	1.8	0.6(4)	0.11(3)
1644.3	5658.5	4014.2	$(10_1^-) \rightarrow 9_1^-$	1.2	1.4(4)	0.009(9)
2322.0	4014.2	1692.1	$9_1^- \rightarrow 6_1^+$	10.4	4.5(5)	1.2(1)
2865.6	4557.6	1692.1	$(8_1^+) \rightarrow 6_1^+$	6.9	1.7(7)	1.01(9)

Table A.1: Relative intensities (I_γ) of the γ -ray transitions (keV) in ^{134}Te , normalized to the $2_1^+ \rightarrow 0_1^+$ transition (1279.3 keV). ^{248}Cm data comes from [Sah+01]. The fission partner of ^{134}Te for the EXILL data was ^{100}Zr , for [Sah+01] it was ^{110}Ru , ^{111}Ru or ^{112}Ru . For ^{248}Cm data, except for the weakest lines, the intensities should be accurate within 20% [Sah+01]. Models and free parameters set used in the FIFRELIN simulation: EGLO photon strength functions, CTM level density model, BSFG spin cut-off model, $R_{\text{T}}^{\text{min}} = 0.75$, $R_{\text{T}}^{\text{max}} = 1.23$, $f_\sigma = 1.5$ (optimized, see Figure A.2). *The γ -transition intensities were not corrected to take into account that the excited state at 1692.1 keV is long-lived (164 ns).

A.1.2 ^{92}Kr

The level scheme of ^{92}Kr can be seen in Figure 3.11. FIFRELIN seems to strongly overfeed the excited state at 1803.0 keV, which causes too high intensity of the γ -transition at 1034.0 keV. The γ -transitions which feed this excited state and have too high intensity as well, are at 688.1 keV and 849.5 keV, see Table A.2.

E_γ (keV)	E_i^{level} (keV)	E_f^{level} (keV)	Transition	I_γ	
				EXILL data	FIFRELIN data
677.3	1446.3	769	$2_2^+ \rightarrow 2_1^+$	1.5(6)	1.3(1)
688.1	2491.1	1803.0	$(6_1^+) \rightarrow (4_1^+)$	5.1(7)	26.4(5)
769.0	769.0	0.0	$2_1^+ \rightarrow 0_1^+$	100	100(1)
849.5	2652.5	1803.0	$(6_2^+) \rightarrow (4_1^+)$	1.2(3)	32.5(6)
1032.1	2835.1	1803.0	$?^? \rightarrow (4_1^+)$	8.5(9)	1.7(1)
1034.0	1803.0	769.0	$(4_1^+) \rightarrow 2_1^+$	38(2)	87(1)
1106.0	3171.7	2065.7	$(6_4^+) \rightarrow (4_3^+)$	2.9(5)	0.58(7)
1112.3	3178.1	2065.7	$(6_5^+) \rightarrow (4_3^+)$	1.8(5)	0.45(6)
1232.2	3035.2	1803.0	$(6_3^+) \rightarrow (4_1^+)$	8.1(6)	6.9(2)
1296.7	2065.7	769.0	$(4_3^+) \rightarrow 2_1^+$	13(7)	6.7(2)
1368.7	3171.7	1803.0	$(6_4^+) \rightarrow (4_1^+)$	2.3(4)	1.2(1)

Table A.2: Relative intensities (I_γ) of the γ -ray transitions (keV) in ^{92}Kr , normalized to the $2_1^+ \rightarrow 0_1^+$ transition (769.0 keV). The fission partner of ^{92}Kr for the EXILL data and the FIFRELIN data was ^{142}Ba . Models and free parameters set used in the FIFRELIN simulation: EGLO photon strength functions, CTM level density model, BSFG spin cut-off model, $R_{\text{T}}^{\text{min}} = 0.75$, $R_{\text{T}}^{\text{max}} = 1.23$, $f_\sigma = 1.8$. These parameters were used in the reference FIFRELIN simulation (Table 5.7) which gave the correct prompt-neutron multiplicity.

The evolutions of γ -transition intensities in ^{92}Kr with the Ba mass number are fitted well with the constant functions, see Figure A.3. It seems that there is no dependence.

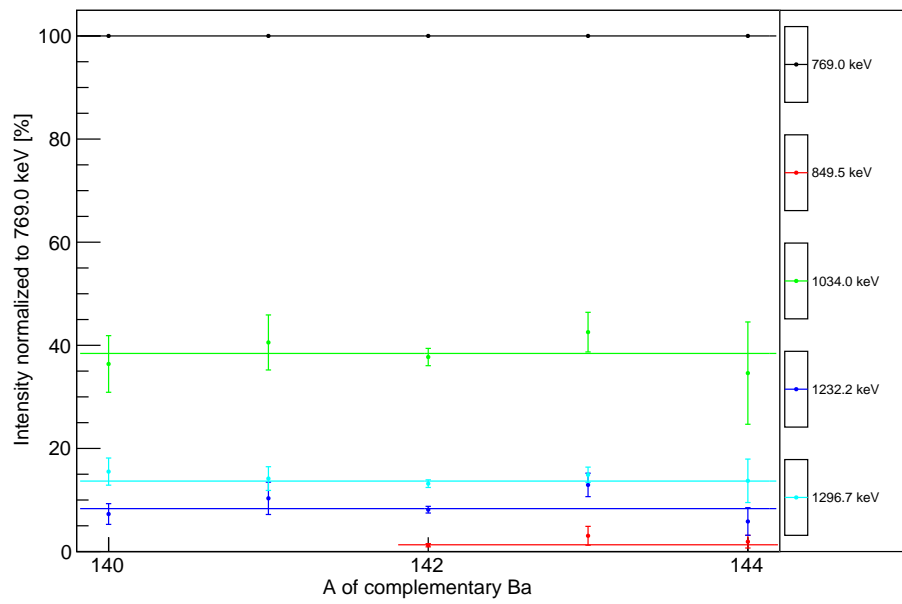


Figure A.3: Evolution of γ -transition intensities in ^{92}Kr with Ba mass number obtained from the EXILL experiment data. Lines show the fits with the constant function.

A.1.3 ^{142}Ba

The level scheme of ^{142}Ba can be seen in Figure 3.12. The optimal scaling factor $f_\sigma=1.05$ (Figure A.4) is close to the one found in the ^{100}Zr analysis ($f_\sigma=1.15$ for $R_{\text{T}}^{\text{max}}=1.23$, see Section 5.4.2). The reduced f_σ (thus reduced initial spin) causes over-feeding of the low-spin excited states ($J \leq 6$) thus intensities of the γ -transitions in this spin region are too high. A good example are the ground state band transitions at 475.0 keV and 631.1 keV. General agreement between the EXILL experimental results and the FIFRELIN simulation results is good ($\chi^2 = 31.5$, see Figure A.4, reduced $\chi^2 = 7.9$).

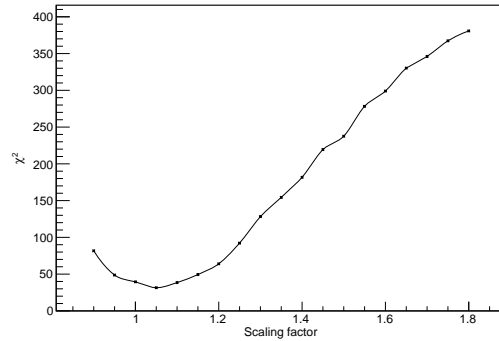


Figure A.4: χ^2 value containing γ -transitions: 359.7 keV, 475.3 keV, 631.5 keV, 693.4 keV in ^{142}Ba , for the FIFRELIN simulations with different scaling factor values (f_σ). The χ^2 was calculated according to Equation 5.1. Models and free parameters set used in the simulations: EGLO photon strength functions, CTM level density model, BSFG spin cut-off model, $R_{\text{T}}^{\text{min}} = 0.75$, $R_{\text{T}}^{\text{max}} = 1.23$.

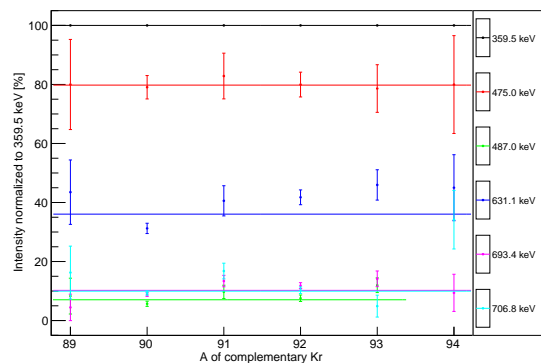


Figure A.5: Evolution of γ -transition intensities in ^{142}Ba with Kr mass number obtained from the EXILL experiment data. Lines show the fits with the constant function.

E_γ (keV)	E_i^{level} (keV)	E_f^{level} (keV)	Transition	I_γ		
				^{248}Cm data	EXILL data	FIFRELIN data
205.8	1747.0	1541.1	$5_1^{(+)} \rightarrow 5_1^-$	1.3(3)	0.6(4)	2.1(1)
276.8	2229.1	1952.6	$8_2^+ \rightarrow 7_1^-$	2.3(3)	1.8(4)	1.2(1)
306.9	1848.1	1541.1	$6_2^+ \rightarrow 5_1^-$	4.0(4)	4.7(4)	3.7(2)
323.2	2070.0	1747.0	$7_1^{(+)} \rightarrow 5_1^{(+)}$	1.5(3)	1.5(6)	1.3(1)
354.3	2513.5	2159.2	$9_1^- \rightarrow 8_1^+$	5.1(4)	4.4(5)	2.1(1)
359.5	359.5	0.0	$2_1^+ \rightarrow 0_1^+$	100	100	100
380.9	2229.1	1848.1	$8_2^+ \rightarrow 6_2^+$	6.5(8)	4.0(6)	3.2(2)
382.4	1848.1	1465.7	$6_2^+ \rightarrow 6_1^+$	1.0(5)	2.7(6)	1.1(1)
412.1	2925.6	2513.5	$(10_2^+) \rightarrow 9_1^-$	1.0(2)	1.4(7)	0.29(5)
451.0	2679.9	2229.1	$(9_1^+) \rightarrow 8_2^+$	4.5(5)	2.3(9)	1.2(1)
475.0	834.5	359.5	$4_1^+ \rightarrow 2_1^+$	85(5)	80(4)	95(1)
487.0	1952.6	1465.7	$7_1^- \rightarrow 6_1^+$	18(2)	7.6(1)	11.6(30)
560.9	2513.5	1952.6	$9_1^- \rightarrow 7_1^-$	4.5(4)	4.0(5)	2.1(1)
585.7	2814.6	2229.1	$(10_1^+) \rightarrow 8_2^+$	5.5(5)	4(1)	0.93(9)
609.8	2679.9	2070.0	$(9_1^+) \rightarrow 7_1^{(+)}$	3.8(8)	4(1)	1.06(9)
631.1	1465.7	834.5	$6_1^+ \rightarrow 4_1^+$	40(3)	42(3)	53.3(8)
640.1	3153.6	2513.5	$(11_1^-) \rightarrow 9_1^-$	5(1)	2(1)	0.42(6)
655.4	2814.6	2159.2	$(10_1^+) \rightarrow 8_1^+$	1.3(3)	0.6(4)	0.26(5)
693.4	2159.2	1465.7	$8_1^+ \rightarrow 6_1^+$	13(2)	12(1)	10.9(3)
706.8	1541.1	834.5	$5_1^- \rightarrow 4_1^+$	6.0(6)	10(1)	16.8(4)
766.5	2925.6	2159.2	$(10_2^+) \rightarrow 8_1^+$	2.3(3)	2.4(7)	1.1(1)
912.6	1747.0	834.5	$5_1^{(+)} \rightarrow 4_1^+$	3.5(5)	4.6(5)	6.0(2)
932.8	1292.3	359.5	$3_1^{(-)} \rightarrow 2_1^+$	2(1)	1.1(4)	1.5(1)
1013.6	1848.1	834.5	$6_2^+ \rightarrow 4_1^+$	2.9(4)	2.9(9)	2.8(2)

Table A.3: Relative intensities (I_γ) of the γ -ray transitions (keV) in ^{142}Ba , normalized to the $2_1^+ \rightarrow 0_1^+$ transition (395.5 keV). ^{248}Cm data comes from [Urb+97]. The fission partner of ^{142}Ba for the EXILL data measured with the new analysis technique (EXILL data) was ^{92}Kr , for [Urb+97] it was a complementary Zr fragment. Models and free parameters set used in the simulations: EGLO photon strength functions, CTM level density model, BSFG spin cut-off model, $R_{\text{T}}^{\text{min}} = 0.75$, $R_{\text{T}}^{\text{max}} = 1.23$, $f_\sigma = 1.05$ (optimized, see Figure A.4).

E_γ (keV)	E_i^{level} (keV)	E_f^{level} (keV)	Transition	I_γ		
				^{248}Cm data	EXILL data	FIFRELIN data
298.8	3155.7	2857.0	$6_1^+ \rightarrow 5_1^-$	51(6)	27(2)	51(1)
677.7	2604.1	1926.3	$4_1^- \rightarrow 3_1^{(-)}$	43(4)	42(2)	31.7(7)
767.3	3923.0	3155.7	$7_1^- \rightarrow 6_1^+$	28(2)	38(2)	14.8(5)
837	837.0	0.0	$2_1^+ \rightarrow 0_1^+$	286(20)	319(11)	194(3)
1009.8	3155.7	2146.0	$6_1^+ \rightarrow 4_1^+$	34(3)	39(2)	33.9(7)
1089.4	1926.3	837.0	$3_1^{(-)} \rightarrow 2_1^+$	83(6)	77(2)	53(1)
1308.9	2146.0	837.0	$4_1^+ \rightarrow 2_1^+$	100	100	100

Table A.4: Relative intensities (I_γ) of the γ -ray transitions (keV) in ^{94}Sr , normalized to the $4_1^+ \rightarrow 2_1^+$ transition (1308.9 keV). ^{248}Cm data comes from [RU+09]. The fission partner of ^{94}Sr for the EXILL data measured with the new analysis technique (EXILL data) was ^{140}Xe . [RU+09] results were obtained from spectra doubly gated in ^{94}Sr on different γ -ray peaks. Models and free parameters set used in the simulations: EGLO photon strength functions, CTM level density model, BSFG spin cut-off model, $R_T^{\text{min}} = 0.75$, $R_T^{\text{max}} = 1.23$, $f_\sigma = 1.8$.

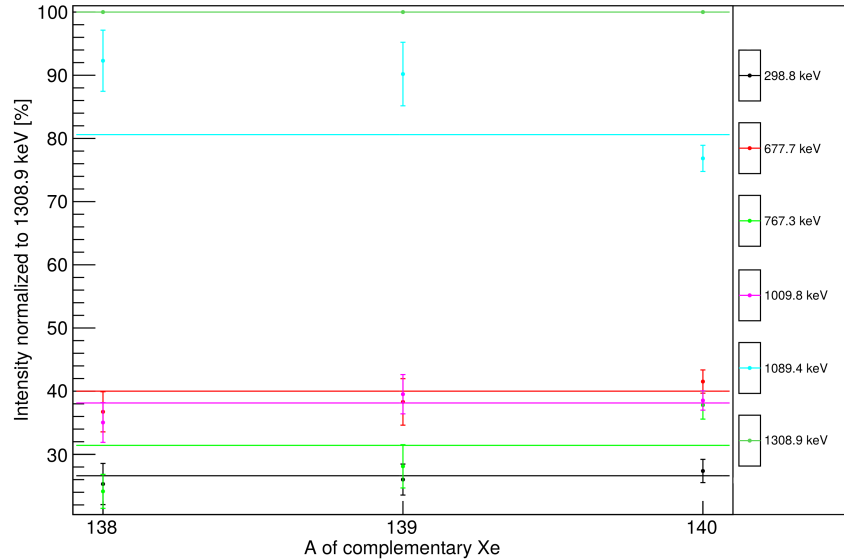


Figure A.7: Evolution of γ -transition intensities in ^{94}Sr with Xe mass number obtained from the EXILL experiment data. Lines show the fits with the constant function.

A.1.5 ^{140}Xe

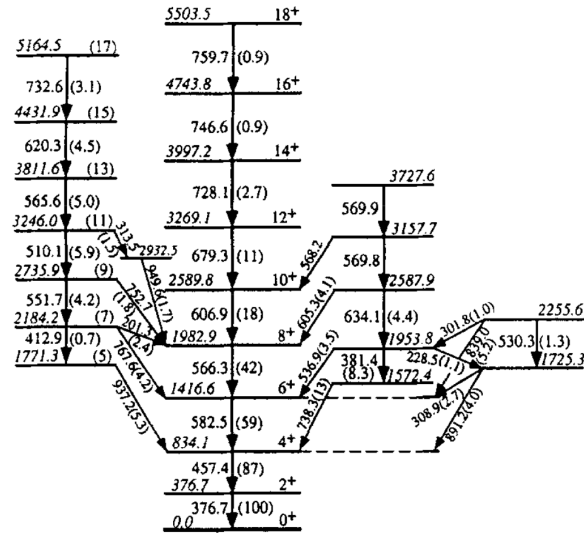


Figure A.8: Level scheme of ^{140}Xe from [Ham+97].

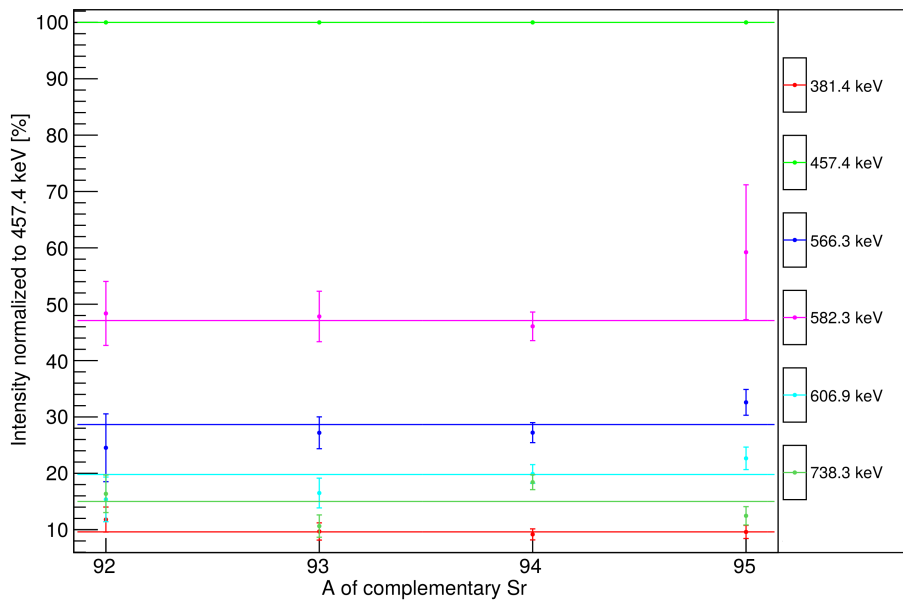


Figure A.9: Evolution of γ -transition intensities in ^{140}Xe with Sr mass number obtained from the EXILL experiment data. Lines show the fits with the constant function.

E_γ (keV)	E_i^{level} (keV)	E_f^{level} (keV)	Transition	I_γ		
				^{252}Cf data	EXILL data	FIFRELIN data
308.9	1725.3	1416.6	$?^? \rightarrow 6_1^+$	4.6	3.4(7)	0.42(5)
376.7	376.7	0.0	$2_1^+ \rightarrow 0_1^+$	115	106(4)	101(1)
381.4	1953.8	1572.4	$?^? \rightarrow ?^?$	9.4	9(1)	1.37(9)
412.9	2184.2	1771.3	$7_1^- \rightarrow 5_1^-$	1.7	1.7(8)	1.6(1)
457.4	834.1	376.7	$4_1^+ \rightarrow 2_1^+$	100	100	100
510.1	3246.0	2735.9	$11_1^- \rightarrow 9_1^-$	6.3	6(1)	16.0(3)
536.9	1953.8	1416.6	$?^? \rightarrow 6_1^+$	4.7	4.3(4)	0.62(6)
551.7	2735.9	2184.2	$9_1^- \rightarrow 7_1^-$	5.9	5.1(7)	15.1(3)
566.3	1983.0	1416.6	$8_1^+ \rightarrow 6_1^+$	40	27(2)	77.9(9)
582.3	1416.6	834.1	$6_1^+ \rightarrow 4_1^+$	62	46(3)	95(1)
605.3	2587.9	1983.0	$?^? \rightarrow 8_1^+$	3	4(3)	0.42(5)
606.9	2589.8	1983.0	$10_1^+ \rightarrow 8_1^+$	21	20(2)	47.9(7)
634.1	2587.9	1953.8	$?^? \rightarrow ?^?$	6.8	6(1)	0.58(6)
679.3	3269.1	2589.8	$(12_1^+) \rightarrow 10_1^+$	7.7	4(2)	24.1(4)
738.3	1572.4	834.1	$?^? \rightarrow 4_1^+$	12.2	18(1)	2.4(1)
752.7	2735.9	1983.0	$9_1^- \rightarrow 8_1^+$	3	3.4(9)	6.6(2)
891.2	1725.3	834.1	$?^? \rightarrow 4_1^+$	3.7	3(1)	0.72(7)
927.7	1304.3	376.7	$?^? \rightarrow 2_1^+$	3	2(1)	2.0(1)
937.2	1771.3	834.1	$5_1^- \rightarrow 4_1^+$	4.3	5(1)	1.6(1)
1136.4	1513.0	376.7	$3_1^- \rightarrow 2_1^+$	1.4	3(2)	0.08(2)

Table A.5: Relative intensities (I_γ) of the γ -ray transitions (keV) in ^{140}Xe , normalized to the $4_1^+ \rightarrow 2_1^+$ transition (457.4 keV). ^{252}Cf data comes from [Ham+97], intensity uncertainties are around 15%. The fission partner of ^{140}Xe for the EXILL data measured with the new analysis technique (EXILL data) was ^{94}Sr , for [Ham+97] it was a complementary Ru fragment. Models and free parameters set used in the simulations: EGLO photon strength functions, CTM level density model, BSFG spin cut-off model, $R_T^{\min} = 0.75$, $R_T^{\max} = 1.23$, $f_\sigma = 1.8$.

A.1.6 ^{138}Xe

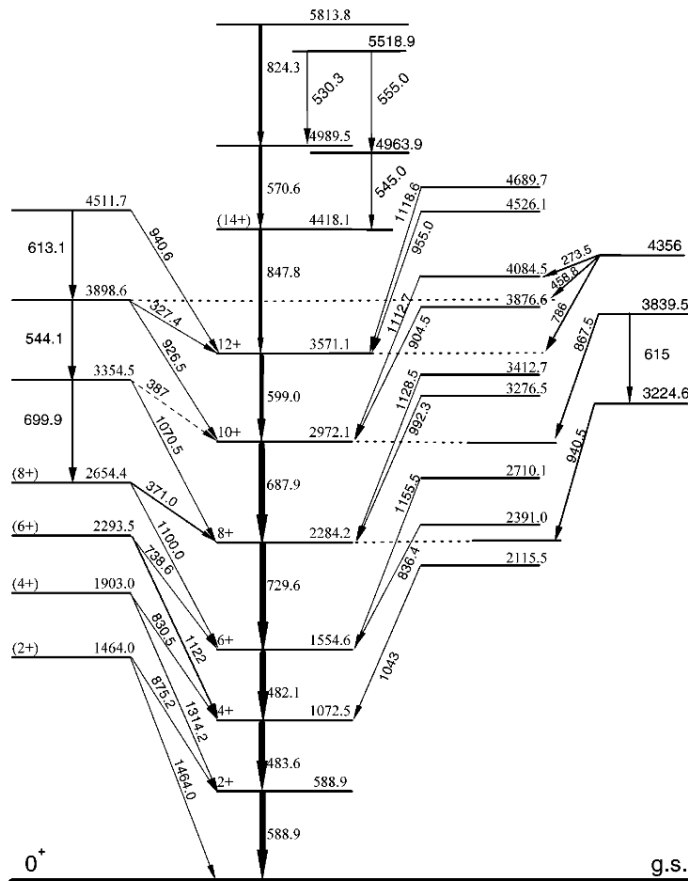


Figure A.10: Level scheme of ^{138}Xe from [Kor+00].

E_γ (keV)	E_i^{level} (keV)	E_f^{level} (keV)	Transition	I_γ	
				EXILL data	FIFRELIN data
212.2	2543.7	2331.5	? [?] → ? [?]	4(1)	0.02(1)
318.6	2334.0	2015.4	? [?] → ? [?]	5(1)	
370.9	2655.1	2284.2	(8 ₂ ⁺) → 8 ₁ ⁺	5(3)	1.9(1)
482.1	1554.6	1072.5	6 ₁ ⁺ → 4 ₁ ⁺	118(24)	129(2)
483.6	1072.5	588.9	4 ₁ ⁺ → 2 ₁ ⁺	393(30)	132(2)
621	2952.5	2331.5	? [?] → ? [?]	4(2)	0.10(3)
687.9	2972.1	2284.2	10 ₁ ⁺ → 8 ₁ ⁺	58(4)	62.3(9)
729.6	2284.2	1554.6	8 ₁ ⁺ → 6 ₁ ⁺	100	100
738.6	2293.2	1554.6	(6 ₂ ⁺) → 6 ₁ ⁺	3.5(7)	0.27(5)
771.1	2674.3	1903.2	? [?] → ? [?]	4(2)	
778.9	2794.3	2015.4	? [?] → ? [?]	7(3)	
830.5	1903.0	1072.5	(4 ₂ ⁺) → 4 ₁ ⁺	3(1)	0.04(2)
836.4	2391.0	1554.6	? [?] → 6 ₁ ⁺	5(3)	0.48(6)
837.9	2952.6	2114.7	? [?] → ? [?]	9(6)	0.19(4)
875.2	1464.0	588.9	(2 ₂ ⁺) → 2 ₁ ⁺	5.3(6)	0.82(8)
942.9	2015.4	1072.5	? [?] → 4 ₁ ⁺	2.9(3)	
1043	2115.5	1072.5	? [?] → 4 ₁ ⁺	8(2)	
1155.5	2710.1	1554.6	? [?] → 6 ₁ ⁺	4(1)	
1210.3	2674.3	1464.0	? [?] → ? [?]	3.5(9)	
1314.2	1903.0	588.9	(4 ₂ ⁺) → 2 ₁ ⁺	143(14)	0.05(2)

Table A.6: Relative intensities (I_γ) of the γ -ray transitions (keV) in ^{138}Xe , normalized to the $8_1^+ \rightarrow 6_1^+$ transition (729.6 keV). The fission partner of ^{138}Xe for the EXILL data and the FIFRELIN data was ^{96}Sr . Models and free parameters set used in the FIFRELIN simulation: EGLO photon strength functions, CTM level density model, BSFG spin cut-off model, $R_T^{\min} = 0.75$, $R_T^{\max} = 1.23$, $f_\sigma = 1.8$.

A.1.7 ^{104}Mo

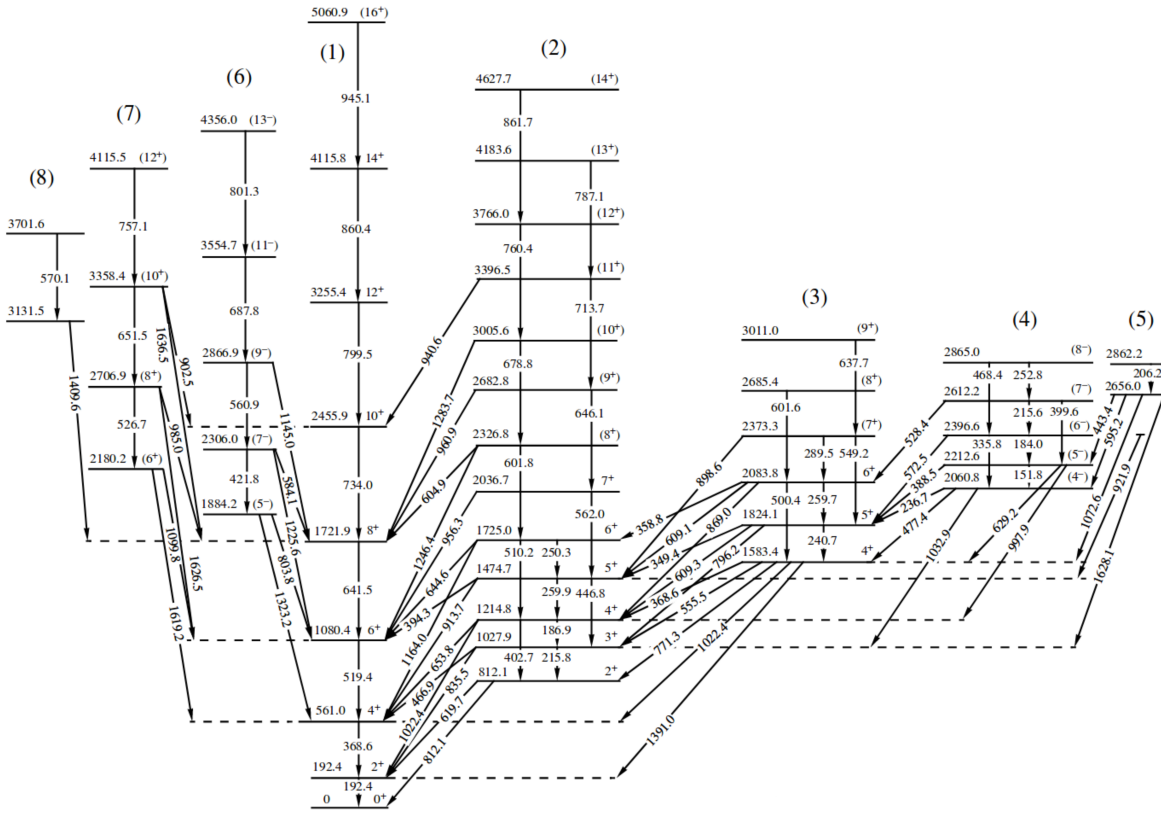


Figure A.11: Level scheme of ^{104}Mo from [Jon+05]. Different fission bands are denoted by the numbers in brackets at the top of each band.

E_γ (keV)	E_i^{level} (keV)	E_f^{level} (keV)	Transition	I_γ		
				^{248}Cm data	EXILL data	FIFRELIN data
192.0	192.1	0.0	$2_1^+ \rightarrow 0_1^+$	100	100	100
240.6	1824.1	1583.4	$5_2^+ \rightarrow 4_3^+$	20(2)	13(6)	0.11(5)
252.7	2864.1	2611.3	$?^? \rightarrow ?^?$		17(4)	0.09(4)
259.3	2083.4	1824.1	$(6_3^+) \rightarrow 5_2^+$	32(4)	31(4)	0.07(4)
368.5	560.7	192.1	$4_1^+ \rightarrow 2_1^+$	16(3)	61(4)	105(2)
447.6	1475.6	1028	$5_1^+ \rightarrow 3_1^+$	35(2)	16(4)	0.8(1)
467.4	1028	560.7	$3_1^+ \rightarrow 4_1^+$	11(1)	10(2)	0.13(5)
509.8	1724.4	1214.8	$6_2^+ \rightarrow 4_2^+$	45(3)	16(2)	2.7(2)
519.4	1080.1	560.7	$6_1^+ \rightarrow 4_1^+$		45(5)	99(2)
601.7	2326.3	1724.4	$(8_2^+) \rightarrow 6_2^+$	82(4)	13(3)	5.5(4)
641.7	1721.9	1080.1	$8_1^+ \rightarrow 6_1^+$		12(2)	81(2)
654.1	1214.8	560.7	$4_2^+ \rightarrow 4_1^+$	49(7)	9(3)	1.5(2)
835.8	1028	192.1	$3_1^+ \rightarrow 2_1^+$	89(1)	13(3)	1.1(2)
868.6	2083.4	1214.8	$(6_3^+) \rightarrow 4_2^+$	41(5)	4(3)	0.38(9)
1022.7	1214.8	192.1	$4_2^+ \rightarrow 2_1^+$	26(5)	7(6)	1.7(2)

Table A.7: Relative intensities (I_γ) of the γ -ray transitions (keV) in ^{104}Mo , normalized to the $2_1^+ \rightarrow 0_1^+$ transition (192.0 keV). ^{248}Cm data comes from [Gue+96; Smi+02]. The fission partner of ^{104}Mo for the EXILL data measured with the new analysis technique (EXILL data) was ^{130}Sn , for [Gue+96] it was ^{140}Xe . [Smi+02] results were obtained from spectra doubly gated in ^{104}Mo on different γ -ray peaks. Models and free parameters set used in the simulations: EGLO photon strength functions, CTM level density model, BSFG spin cut-off model, $R_{\text{T}}^{\text{min}} = 0.75$, $R_{\text{T}}^{\text{max}} = 1.23$, $f_\sigma = 1.8$.

A.1.8 ^{130}Sn

E_γ (keV)	E_i^{level} (keV)	E_f^{level} (keV)	Transition	I_γ	
				EXILL data	FIFRELIN data
261.3	2257	1995.6	$(6_1^+) \rightarrow (4_1^+)$	9(3)	65(3)
602.1	2597.7	1995.6	$?^? \rightarrow (4_1^+)$	8(4)	
774.4	1995.6	1221.2	$(4_1^+) \rightarrow (2_1^+)$	100	100
1221.2	1221.2	0	$(2_1^+) \rightarrow 0_1^+$	190(15)	106(4)
2028.3	2028.3	0	$(2_2^+) \rightarrow 0_1^+$	6(1)	

Table A.8: Relative intensities (I_γ) of the γ -ray transitions (keV) in ^{130}Sn , normalized to the $(4_1^+) \rightarrow (2_1^+)$ transition (774.4 keV). The fission partner of ^{130}Sn for the EXILL data measured with the new analysis technique (EXILL data) was ^{104}Mo . Models and free parameters set used in the simulations: EGLO photon strength functions, CTM level density model, BSFG spin cut-off model, $R_T^{\min} = 0.75$, $R_T^{\max} = 1.23$, $f_\sigma = 1.8$.

E_γ (keV)	E_i^{level} (keV)	E_f^{level} (keV)	Transition	I_γ		
				^{248}Cm data	EXILL data	FIFRELIN data
196.6	2863.4	2666.8	$13_1^- \rightarrow 12_1^+$	1.7(4)	4.1(6)	3.0(2)
271.4	2044.0	1772.7	$10_2^+ \rightarrow 9_1^-$	4.4(6)	3.8(5)	9.5(3)
302.1	1772.7	1470.6	$9_1^- \rightarrow 8_1^+$	24(3)	23(2)	33.4(7)
316.5	1355.0	1038.6	$7_1^- \rightarrow 5_1^-$	5.6(8)	2(1)	4.5(2)
330.7	529.9	199.2	$4_1^+ \rightarrow 2_1^+$	100	100	100
388.0	2666.8	2278.8	$12_1^+ \rightarrow 11_1^-$	2.2(4)	4(1)	8.3(3)
393.7	1355.0	961.3	$7_1^- \rightarrow 6_1^+$	25(3)	20(2)	23.6(6)
417.7	1772.7	1355.0	$9_1^- \rightarrow 7_1^-$	15(1)	11(1)	19.9(5)
431.3	961.3	529.9	$6_1^+ \rightarrow 4_1^+$	88(8)	73(6)	97(1)
506.1	2278.8	1772.7	$11_1^- \rightarrow 9_1^-$	20(3)	22(2)	34.0(7)
508.7	1038.6	529.9	$5_1^- \rightarrow 4_1^+$	12(3)	19(10)	5.0(2)
509.3	1470.6	961.3	$8_1^+ \rightarrow 6_1^+$	47(6)	35(4)	67(1)
573.5	2044.0	1470.6	$10_1^+ \rightarrow 8_1^+$	13(1)	13(1)	27.6(6)
584.6	2863.4	2278.8	$13_1^- \rightarrow 11_1^-$	11(1)	18(2)	17.7(5)
622.8	2666.8	2044.0	$12_1^+ \rightarrow 10_1^+$	3.2(6)	5.0(9)	12.0(4)
638.8	838.0	199.2	$3_1^- \rightarrow 2_1^+$	3(1)	2.6(4)	
723.1	4241.8	3518.7	$(17_1^-) \rightarrow (15_1^-)$	1.3(3)	2.4(7)	0.42(7)

Table A.9: Relative intensities (I_γ) of the γ -ray transitions (keV) in ^{144}Ba , normalized to the $4_1^+ \rightarrow 2_1^+$ transition (330.7 keV). ^{248}Cm data comes from [Urb+97]. The fission partner of ^{144}Ba was ^{90}Kr gated at 655.6 keV. Most of the transitions from [Urb+97] were measured in the spectra double-gated in ^{144}Ba . Models and free parameters set used in the simulations: EGLO photon strength functions, CTM level density model, BSFG spin cut-off model, $R_T^{\min} = 0.75$, $R_T^{\max} = 1.23$, $f_\sigma = 1.8$.

We wanted to check if the intensities of the γ -rays stay unchanged when we set a gate in the different fission band of the fission partner. ^{87}Kr was a good fission partner for that study because it has two fission bands going to the ground state. Additionally, according to [Por+06], the γ -transition at 1577.5 keV can have a different character (dipole or quadrupole) than the γ -transition at 1419.8 keV (quadrupole).

E_γ (keV)	E_i^{level} (keV)	E_f^{level} (keV)	Transition	I_γ	
				Gated at 1577.5 keV (main band)	Gated at 1419.8 keV
198.2	2389.3	2191.3	$(10_1^-) \rightarrow 9_1^-$	7(5)	13(3)
203.4	1024.7	821.2	$5_1^- \rightarrow 3_1^-$	17(6)	13(4)
298.7	2389.3	2090.5	$(10_1^-) \rightarrow 8_1^-$	12(6)	5(2)
307.5	821.2	513.8	$3_1^- \rightarrow 4_1^+$	21(5)	16(2)
332.7	513.8	181.1	$4_1^+ \rightarrow 2_1^+$	100	100
428.5	1777.7	1349.3	$9_1^- \rightarrow 7_1^-$	27(4)	12(4)
444.7	958.4	513.8	$6_1^+ \rightarrow 4_1^+$	45(10)	41(7)
507.1	3297.9	2790.8	$(14_1^-) \rightarrow (12_1^-)$	11(6)	10(2)
524.2	1482.7	958.4	$8_1^+ \rightarrow 6_1^+$	41(6)	25(6)
569.4	2052.1	1482.7	$10_1^+ \rightarrow 8_1^+$	10(8)	8(3)
607.9	2090.5	1482.7	$8_1^- \rightarrow 8_1^+$	29(10)	8(6)

Table A.10: Relative intensities (I_γ) of the γ -ray transitions (keV) in ^{146}Ba , normalized to the $4_1^+ \rightarrow 2_1^+$ transition (332.7 keV). The fission partner of ^{146}Ba was ^{87}Kr . In both presented measurements one of the gates was at 181.1 keV ($2_1^+ \rightarrow 0_1^+$) transition in ^{146}Ba , second either at 1577.5 keV or at 1419.8 keV in ^{87}Kr . Transitions at 1577.5 keV and at 1419.8 keV go to the ground state of ^{87}Kr but they belong to different bands, see Figure A.14.

Appendix B

B.1 Uncertainty calculation

B.1.1 Uncertainty on an intensity from gate slices fitting

As described in Section 4.4.2, the detection system response $R(E)$ (see Equation 4.4) is composed of three Gaussians and a smooth step function that takes into account the Compton scattering. The Gaussians have the same center position, proportions of amplitude between each Gaussian and their widths are fixed thus during fitting with this response function, uncertainties come only from the peak position c and the amplitude A . By modifying Equation 4.4 we obtain:

$$R(E) = A \cdot f(E - c) \quad (\text{B.1})$$

where $f(E - c)$ is the shape function composed of three Gaussians and a smooth step function.

To obtain the components (N_H , N_V and N_D) needed to calculate the intensity of the desired peak (see Section 4.5), the fit of each of the gate slices (horizontal, vertical and diagonal) is averaged over the gate positioned at the energy E_X having the width Δ (Equation 4.20). It can be written as:

$$N(E) = \frac{1}{\Delta} \int_{E_X - \frac{\Delta}{2}}^{E_X + \frac{\Delta}{2}} R(E) dE = \frac{1}{\Delta} \int_{E_X - \frac{\Delta}{2}}^{E_X + \frac{\Delta}{2}} A \cdot f(E - c) dE \quad (\text{B.2})$$

The uncertainty on $N(E)$ will be then:

$$\delta N(E) = \sqrt{\left(\frac{\partial N(E)}{\partial A} \delta A\right)^2 + \left(\frac{\partial N(E)}{\partial c} \delta c\right)^2 + 2 \cdot COV(A, c) \frac{\partial N(E)}{\partial A} \frac{\partial N(E)}{\partial c}} \quad (\text{B.3})$$

where $COV(A, c)$ is the covariance between A and c . δA , δc and $COV(A, c)$ are taken from the fit.

Derivation of $N(E)$ over A is:

$$\begin{aligned}
\frac{\partial N(E)}{\partial A} &= \frac{\partial}{\partial A} \frac{1}{\Delta} \int_{E_X - \frac{\Delta}{2}}^{E_X + \frac{\Delta}{2}} A \cdot f(E - c) dE \\
&= \frac{\partial}{\partial A} \frac{A}{\Delta} \int_{E_X - \frac{\Delta}{2}}^{E_X + \frac{\Delta}{2}} f(E - c) dE \\
&= \frac{1}{\Delta} \int_{E_X - \frac{\Delta}{2}}^{E_X + \frac{\Delta}{2}} f(E - c) dE \\
&= \frac{N(E)}{A}
\end{aligned} \tag{B.4}$$

Derivation of $N(E)$ over c is:

$$\begin{aligned}
\frac{\partial N(E)}{\partial c} &= \frac{\partial}{\partial c} \frac{1}{\Delta} \int_{E_X - \frac{\Delta}{2}}^{E_X + \frac{\Delta}{2}} A \cdot f(E - c) dE \\
&= \frac{\partial}{\partial c} \frac{1}{\Delta} \int_{E_X - \frac{\Delta}{2}}^{E_X + \frac{\Delta}{2}} A \cdot f(E - c) dE \left\| \begin{array}{l} t = E - c \\ E = t + c \\ dE = dt \\ t_1 = E_X - \frac{\Delta}{2} - c \\ t_2 = E_X + \frac{\Delta}{2} - c \end{array} \right\| \\
&= \frac{\partial}{\partial c} \frac{1}{\Delta} \int_{E_X - \frac{\Delta}{2} - c}^{E_X + \frac{\Delta}{2} - c} A \cdot f(t) dt \left\| \begin{array}{l} \frac{\partial}{\partial c} = \frac{\partial}{\partial t} \frac{\partial t}{\partial c} \\ \frac{\partial t}{\partial c} = \frac{\partial E - c}{\partial c} = -1 \end{array} \right\| \\
&= -\frac{1}{\Delta} \frac{\partial}{\partial t} \int_{E_X - \frac{\Delta}{2} - c}^{E_X + \frac{\Delta}{2} - c} A \cdot f(t) dt = -\frac{1}{\Delta} A \cdot f(t) \Big|_{E_X - \frac{\Delta}{2} - c}^{E_X + \frac{\Delta}{2} - c} \\
&= -\frac{1}{\Delta} R(t) \Big|_{E_X - \frac{\Delta}{2} - c}^{E_X + \frac{\Delta}{2} - c} = -\frac{1}{\Delta} R(E) \Big|_{E_X - \frac{\Delta}{2}}^{E_X + \frac{\Delta}{2}} \\
&= -\frac{1}{\Delta} \left(R(E = E_X + \frac{\Delta}{2}) - R(E = E_X - \frac{\Delta}{2}) \right)
\end{aligned} \tag{B.5}$$

Since we know the value of A and c from the fit, $R(E = E_X + \frac{\Delta}{2})$ and $R(E = E_X - \frac{\Delta}{2})$

can be easily calculated. Finally, the uncertainty on $N(E)$ takes the form:

$$\delta N(E) = \left\{ \left(\frac{N(E)}{A} \delta A \right)^2 + \left(\frac{1}{\Delta} \left(R(E = E_X - \frac{\Delta}{2}) - R(E = E_X + \frac{\Delta}{2}) \right) \delta c \right)^2 + 2 \cdot COV(A, c) \frac{N(E)}{A} \frac{1}{\Delta} \left(R(E = E_X - \frac{\Delta}{2}) - R(E = E_X + \frac{\Delta}{2}) \right) \right\}^{1/2} \quad (\text{B.6})$$

B.1.2 Uncertainty on a background from gate slices fitting

The backgrounds B'_H , B'_V , B_D (see Section 4.5) are fitted in the appropriate gate slice with the linear function:

$$B(E) = a \cdot E + b \quad (\text{B.7})$$

where a and b are the linear function parameters.

Uncertainty on $B(E)$ comes from uncertainties on both parameters a and b :

$$\begin{aligned} \delta B(E) &= \sqrt{\left(\frac{\partial B(E)}{\partial a} \delta a \right)^2 + \left(\frac{\partial B(E)}{\partial b} \delta b \right)^2 + 2 \cdot COV(a, b) \frac{\partial B(E)}{\partial a} \frac{\partial B(E)}{\partial b}} \\ &= \sqrt{(E \cdot \delta a)^2 + (\delta b)^2 + 2 \cdot COV(a, b) \cdot E} \end{aligned} \quad (\text{B.8})$$

B.1.3 Uncertainty on a number of events coming from the desired γ -transition in the restricted 2D region of the central gate

The number of events N_X coming from the desired γ -transition in the restricted 2D region of the central gate is obtained according to the calculation schemes presented in Section 4.5. Here, I will consider just the calculation scheme in a situation when the contamination is on the horizontal slice. N_X is calculated then from Equation 4.19 which has the form:

$$N_X = N_H - B'_V + B_D$$

Since it is just a simple subtraction and addition equation, the uncertainty on N_X is:

$$\delta N_X = \sqrt{(\delta N_H)^2 + (\delta B'_V)^2 + (\delta B_D)^2} \quad (\text{B.9})$$

Other calculation schemes also consist of subtraction and addition only and have analogical simple method of uncertainty calculation.

B.1.4 Uncertainty on the absolute efficiency

The absolute efficiency is calculated from the Equation 3.7 which has the form:

$$\epsilon(E) = \exp^{A+B \cdot \ln(E)+C \cdot \ln^2(E)}$$

The parameters A , B and C were fitted (see Section 3.2.4) and they are correlated. The variance/covariance matrix was calculated during the fit of the absolute efficiency curve. The uncertainty on the absolute efficiency contains thus correlations between all parameters:

$$\begin{aligned} \delta\epsilon(E) = & \left\{ s_A^2 \left(\frac{\partial\epsilon(E)}{\partial A} \right)^2 + s_B^2 \left(\frac{\partial\epsilon(E)}{\partial B} \right)^2 + s_C^2 \left(\frac{\partial\epsilon(E)}{\partial C} \right)^2 \right. \\ & + 2 \cdot s_{AB} \left(\frac{\partial\epsilon(E)}{\partial A} \right) \left(\frac{\partial\epsilon(E)}{\partial B} \right) + 2 \cdot s_{AC} \left(\frac{\partial\epsilon(E)}{\partial A} \right) \left(\frac{\partial\epsilon(E)}{\partial C} \right) \\ & \left. + 2 \cdot s_{BC} \left(\frac{\partial\epsilon(E)}{\partial B} \right) \left(\frac{\partial\epsilon(E)}{\partial C} \right) \right\}^{1/2} \end{aligned} \quad (\text{B.10})$$

where s_A , s_B and s_C are the variances, s_{AB} , s_{AC} and s_{BC} are the covariances.

Derivation of $\epsilon(E)$ on A is:

$$\frac{\partial\epsilon(E)}{\partial A} = \exp^{A+B \cdot \ln(E)+C \cdot \ln^2(E)} \cdot 1 = \epsilon(E) \quad (\text{B.11})$$

Derivation of $\epsilon(E)$ on B is:

$$\frac{\partial\epsilon(E)}{\partial B} = \exp^{A+B \cdot \ln(E)+C \cdot \ln^2(E)} \cdot \ln(E) = \epsilon(E) \cdot \ln(E) \quad (\text{B.12})$$

Derivation of $\epsilon(E)$ on C is:

$$\frac{\partial\epsilon(E)}{\partial C} = \exp^{A+B \cdot \ln(E)+C \cdot \ln^2(E)} \cdot \ln^2(E) = \epsilon(E) \cdot \ln^2(E) \quad (\text{B.13})$$

Finally the uncertainty on the absolute efficiency is:

$$\begin{aligned} \delta\epsilon(E) = & \epsilon(E) \left\{ s_A^2 + s_B^2 (\ln(E))^2 + s_C^2 (\ln^2(E))^2 + 2 \cdot s_{AB} \cdot \ln(E) \right. \\ & \left. + 2 \cdot s_{AC} \cdot \ln(E) \cdot \ln(E) + 2 \cdot s_{BC} \cdot \ln(E) \cdot \ln^2(E) \right\}^{1/2} \\ = & \epsilon(E) \left\{ s_A^2 + s_B^2 \cdot \ln^2(E) + s_C^2 \cdot \ln^4(E) + 2 \cdot s_{AB} \cdot \ln(E) \right. \\ & \left. + 2 \cdot s_{AC} \cdot \ln^2(E) + 2 \cdot s_{BC} \cdot \ln^3(E) \right\}^{1/2} \end{aligned} \quad (\text{B.14})$$

During the calculation of the uncertainty on the normalized intensity some terms from the equation above are crossed out.

Titre: Etude de la fission nucléaire par spectrométrie des rayons gamma prompts

Mots clés: échauffement γ , simulation Monte-Carlo, spectroscopie γ , fission, désexcitation des fragments de fission

Résumé: La volonté d'améliorer l'efficacité énergétique des réacteurs nucléaires a motivé de nouvelles solutions dans leur conception. L'une d'elles est l'utilisation d'un réflecteur lourd dans les réacteurs de génération III+ et les futurs réacteurs de génération IV. Lorsque la matière est traversée par des rayons γ , les excitations induites entraînent une élévation de sa température. Ce processus, appelé échauffement γ , est responsable de plus de 90% de la production de chaleur dans la région hors combustible d'un réacteur nucléaire. C'est également le cas dans le réflecteur. Pour simuler l'effet de l'échauffement γ en fonction de la composition du combustible, il faut disposer de données précises sur les γ prompts émis par les différents fragments produits dans le processus de fission.

En 2012, une campagne d'expériences inédite, EXILL, a été menée au réacteur de recherche de l'ILL. Un grand nombre de détecteurs HPGe a été placé autour d'une cible fissile et a mesuré les rayons γ émis par la cible alors qu'elle était irradiée par un faisceau intense de neutrons froids. Dans ce travail, nous avons analysé les données obtenues avec des cibles ^{235}U . Elles nous ont permis d'étudier la désexcitation de plusieurs fragments de fission et plus globalement le processus de fission induite par des neutrons.

Dans un premier temps, nous avons utilisé la méthode standard d'analyse par coïncidence γ - γ - γ . Nous avons pu filtrer les données expérimentales, identifier les transitions γ dans des fragments bien produits et calculer leur intensité relative. Les problèmes que nous avons rencontrés concernent le bruit de fond. Les résultats obtenus dépendent de ce choix et présentent donc des problèmes de reproductibilité. Nous avons développé et testé une nouvelle méthodologie d'analyse. Son principe est un balayage des portes de coïncidence selon trois directions, ce qui permet de trouver le bruit de fond le mieux adapté. L'idée principale était finalement de passer d'une méthode "spectroscopique", dont le but est de trouver de nouvelles transitions et des états excités dans un noyau, à une méthode "spectrométrique", qui nous permet d'obtenir plus précisément l'intensité de transitions γ connues, avec une meilleure estimation de leur incertitude. Cela nous a amené à développer un logiciel d'analyse semi-automatique d'ajustement des pics. Divers schémas de calcul de l'intensité des transitions γ ont été également élaborés pour tenir compte des contaminations possibles, selon leur emplacement dans la matrice de coïncidence et leur intensité. La méthode standard et la nouvelle méthode d'analyse ont été comparées pour l'analyse du ^{142}Ba .

Dans ce travail, nous avons également comparé nos résultats sur quelques noyaux, tel que le ^{100}Zr , avec des simulations réalisées avec le code FIFRELIN. Ce dernier est un code Monte-Carlo qui simule le processus de fission et la désexcitation des fragments de fission. FIFRELIN utilise plusieurs modèles différents pour décrire ces processus. Nous avons testé le comportement des différents modèles, trouvé les valeurs optimales des paramètres de simulation et testé comment ces configurations reproduisaient les résultats expérimentaux. FIFRELIN n'a pas été en mesure de reproduire simultanément les intensités des transitions γ émises par les fragments de ^{100}Zr et la multiplicité de neutrons prompts moyennée sur tous les fragments de fission. Cependant, avec des paramètres modifiés, FIFRELIN a fourni localement une multiplicité de neutrons prompts correcte pour les fragments de masse atomique $A = 100$ et des intensités de transition γ bien reproduites pour les noyaux de ^{100}Zr .

Nous avons également comparé nos résultats expérimentaux sur les fragments de ^{100}Zr provenant du processus $^{235}\text{U}(n_{th}, f)$ avec les autres données expérimentales disponibles provenant des expériences sur $^{248}\text{Cm}(sf)$ et $^{252}\text{Cf}(sf)$, et une autre expérience sur $^{235}\text{U}(n_{th}, f)$.



Title: Study of nuclear fission by spectrometry of the prompt gamma rays

Keywords: γ -heating, Monte-Carlo simulation, γ -ray spectroscopy, fission, fission fragment de-excitation

Abstract: The desire to improve the fuel efficiency of nuclear reactors has motivated new solutions in their design. One of them is the heavy reflector used in the generation III+ and in the future generation IV reactors. γ -rays passing through matter cause its excitation and temperature rise. It is a process called γ -heating, and it is responsible for more than 90% of the heat production in the non-fuel region of the nuclear reactor. This is also the case of the heavy reflector. To simulate the γ -heating effect in every state of the nuclear reactor it is necessary to have precise data on the prompt γ -rays emitted by different fission fragments produced in the course of the nuclear chain reaction.

In 2012, at the research reactor of the ILL, an innovative experiment, called EXILL, was conducted. It produced a large amount of useful data on the de-excitation of the fission fragments. A large number of HPGe detectors were used to study the neutron induced fission process by measuring the emitted γ -rays. Fissile targets were irradiated by an intense cold neutron beam. In this work we analyzed the ^{235}U targets. We studied several fission fragments and more generally the fission process by using high-resolution γ -ray spectroscopy.

At the beginning, we used the standard γ - γ - γ coincidence analysis method. We were able to filter experimental data, identify the well produced γ -rays, and calculate their relative intensities. The problems we have encountered are related to the background. The results obtained with this method were background dependent and thus presented some problems with reproducibility. We therefore developed and tested a new analysis methodology. Its crucial feature is a coincidence gates scanning in three directions which helps to find the most suitable background. The idea was to move from a “spectroscopic” method, which main purpose is finding new transitions and excited states in a nucleus, to a “spectrometric” method, which allows us to obtain more precise γ -ray intensities. We developed a semi-automatic analysis software which facilitates fitting of the chosen γ -ray peak, the contamination and the background. Various γ -ray intensity calculation schemes were derived to take into account different contamination strengths and placements. The results of the analysis with the new technique are reproducible and more reliable. The standard and the new analysis method were compared in the ^{142}Ba analysis.

In this work, we also compared our experimental results on some nuclei, such as ^{100}Zr , with the simulation results performed with the FIFRELIN code. It is a Monte-Carlo code which simulates the fission process and the de-excitation of the fission fragments. It uses various models to describe these processes. We were able to test the behavior of different models implemented in FIFRELIN to find the optimal simulation parameter values and to test how well these setups reproduce the experimental results. FIFRELIN was unable to simultaneously reproduce the γ -ray intensities of ^{100}Zr and the prompt-neutron multiplicity averaged over all fission fragments. However, with modified simulation parameters, FIFRELIN locally provided correct prompt-neutron multiplicity for the fission fragment with the atomic mass $A = 100$ and well reproduced γ -ray intensities of ^{100}Zr .

We also compared our experimental results on ^{100}Zr coming from the $^{235}\text{U}(n_{th}, f)$ process with the other available experimental data coming from the experiments on $^{248}\text{Cm}(sf)$ and $^{252}\text{Cf}(sf)$, and another experiment on $^{235}\text{U}(n_{th}, f)$.